Metal Oxide Nanostructures for DNA Analysis

Paul Cannon, B.Sc. (Hons)

School of Physical Sciences

Dublin City University

A thesis submitted to Dublin City University for the degree of
Doctor of Philosophy (Ph.D.)

Research Supervisors

Dr. Jennifer Gaughran, Prof. Enda McGlynn, and Dr. Brian Freeland

August 2024

Declaration

I hereby certify that this material, which I now submit for assessment on the programme of study leading to the award of Doctor of Philosophy is entirely my own work, and I have exercised reasonable care to ensure that the work is original, and does not to the best of my knowledge breach any law of copyright, and has not been taken from the work of others save and to the extent that such work has been cited and acknowledged within the text of my work.

Signed: Paul Cannon (Paul Cannon, Candidate)

ID No.: 16322566

Date: 26th August 2024

For my parents,

Breda and Joe

Acknowledgements

Words cannot describe the depth of my gratitude to my parents, Breda and Joe Cannon. Without the sacrifices they made and their unwavering support and belief in me, I would never have made it to university, let alone completed a PhD. This achievement is theirs as much as it mine, and I thank them from the bottom of my heart. I would also like to thank my siblings, Shane, Ciara, and Stephen, for their encouragement and the moments of levity that they have brought into my life which have been invaluable.

A special thanks to my partner and best friend, Sama Al-Shammari, for being my biggest supporter and being a beacon of hope and strength for me. You have always made me feel like I could achieve anything.

I've made friends for life here in DCU, but a special thanks to Stephen Durkan, my friend, housemate, and sounding board for the last seven years. Your friendship and shared experiences have been a cornerstone of my PhD experience.

Thank you to all the members of DCU's School of Physical Sciences. A special thanks to Pat Wogan for answering and solving every technical question I ever had, and for all those lovely coffees you made me, and Darragh O'Neill, for being so helpful and indulging in far too many of my "one last XPS measurement" requests.

Last, but definitely not least, I express my deepest gratitude to my supervisors Dr. Jennifer Gaughran, Prof. Enda McGlynn, and Dr. Brian Freeland, for giving me this opportunity and the tools to excel and get the absolute most out of it by being the best mentors one could hope for. I am eternally grateful for everything you've done for me through these four years.

Finally, I would like to acknowledge the Irish Research Council for the financial support of this work.

List of Publications

Journal Articles

1. **Paul Cannon**, Brian Freeland, Margaux Jaquiery, Enda McGlynn, Jennifer Gaughran. *Single-step functionalization of silicon nanoparticles providing efficient DNA binding*. Colloids and Surfaces A: Physicochemical and Engineering Aspects, 129217, 2022. (Chapter 4, Sections 4.1 - 4.3)
2. **Paul Cannon**, Enda McGlynn, Brian Freeland, Jennifer Gaughran. *Development and optimisation of a SiO_2 PVD technique based on the thermal decomposition of PDMS*. New Journal of Chemistry 47 (8), 3734-3744, 2023. (Chapter 3, Section 3.3)
3. **Paul Cannon**, Enda McGlynn, Darragh O'Neill, Conor Darcy, Erin Rouse, Robert O'Connor, Brian Freeland, Barry O'Connell, Jennifer Gaughran. *Deposition of high-quality, nanoscale SiO_2 films and 3D structures*. Applied Materials Today 38, 102175, 2024. (Chapter 3, Sections 3.4 – 3.6; Chapter 5, Section 5.1)
4. **Paul Cannon**, Enda McGlynn, Brian Freeland, Jennifer Gaughran. *Nanostructured deposits on piezoelectric microbalances for enhanced DNA detection*. [In preparation] (Chapter 5, Section 5.2)
5. Amulya Kotamraju, **Paul Cannon**, Enda McGlynn, Samantha Fahy, Dylan Doherty, Jennie O'Loughlin, Purabi Bhagabati, Jennifer Gaughran, Susan M. Kelleher, Keith D. Rochefort, Brian Freeland. *Silicon nanoparticle surface coatings of poly-lactic-acid (PLA) discs as a model prototype for increased functionality biocompatible human implants*. [In preparation] (Chapter 4, Section 4.4; Chapter 5, Section 5.3)

Conference Manuscripts

1. **Paul Cannon**, Enda McGlynn, Darragh O'Neill, Brian Freeland, Jennifer Gaughran. *Deposition of ultra-thin SiO_2 layers to enable core-shell nanostructure architectures for biosensing applications*. 2023 IEEE Nanotechnology Materials and Devices Conference (NMDC), Paestum, Itaty, pp. 508-509. (Oral)

Poster Presentations

1. **Paul Cannon**, Enda McGlynn, Jennifer Gaughran. *Nanoforest-on-a-Chip: Oxide Nanostructures for DNA analysis*. BOC School of Physical Sciences, Postgraduate Poster Competition, Dublin City University, 2020.

2. **Paul Cannon**, Brian Freeland, Margaux Jaquiery, Enda McGlynn, Jennifer Gaughran. *Single-Step Functionalization of DNA to Silicon Nanoparticles by Pulsed Laser Ablation in Liquids*. 10th International Colloids Conference, Online, 2020.
3. **Paul Cannon**, Enda McGlynn, Darragh O'Neill, Briand Freeland, Jennifer Gaughran. *Core-Shell ZnO-SiO_2 Nanorod Array Synthesis for Biosensing Applications*. BOC School of Physical Sciences, Postgraduate Poster Competition, Dublin City University, 2023.
4. **Paul Cannon**, Enda McGlynn, Brian Freeland, Jennifer Gaughran. Nanostructured *Quartz Crystal Microbalance for Enhanced DNA Detection*. Institute of Physics Ireland, Annual Meeting, Dublin, 2024
5. **Paul Cannon**, Enda McGlynn, Brian Freeland, Jennifer Gaughran. Nanostructured *Quartz Crystal Microbalance for Enhanced DNA Detection*. BOC School of Physical Sciences, Postgraduate Poster Competition, Dublin City University, 2024.

Awards

1. Junior Category Winner of DCU Physics' annual BOC Postgraduate Poster Competition 2020.
2. Recipient of Government of Ireland Postgraduate Scholarship Award 2021.
3. Winner of Young Investigator Award, IEEE Nanotechnology Materials and Devices Conference 2023.
4. Runner-Up in DCU's Tell-It-Straight Competition 2024.
5. Overall Winner of DCU Physics' annual BOC Postgraduate Poster Competition 2024.
6. Winner of DCU's Faculty of Science and Health Outstanding Graduate Researcher Award 2024.

Table of Contents

Glossary

AFM	Atomic Force Microscopy
ALD	Atomic Layer Deposition
ATR	Attenuated Total Reflection
BF	Bright Field
BSE	Backscatter Electron
CTRVPT	Carbothermal Reduction Vapour Phase Transport
CBD	Chemical Bath Deposition
CVD	Chemical Vapour Deposition
CP	Contact Profilometry
DI	Deionised
DF	Dark Field
DLS	Dynamic Light Scattering
DNA	Deoxyribonucleic Acid
dsDNA	Double stranded Deoxyribonucleic Acid
EDX	Energy Dispersive X-Ray Spectroscopy
ELISA	Enzyme Linked Immunosorbent Assay
FTIR	Fourier Transform Infrared Spectroscopy
GATR	Grazing Angle Attenuated Total Reflection
HAEC	Human Aortic Endothelial Cells
IFMP	Inelastic Mean Free Path
IR	Infrared
LDH	Lactate Dehydrogenase
LASiS	Laser Ablation Synthesis in Solution
MTS	3-(4,5-dimethylthiazol-2-yl)-5-(3-carboxymethoxyphenyl)-2-(4-sulfophenyl)-2H-tetrazolium
n	Number of repeats
NA	Nucleic Acid
NR	Nanorod
NS	Nanostructure
PCR	Polymerase Chain Reaction

PDMS	Polydimethylsiloxane
PLA	Polylactic Acid
PMMA	Polymethyl Methacrylate
POC	Point of Care
PTFE	Polytetrafluorethylene
PVD	Physical Vapour Deposition
QCM	Quartz Crystal Microbalance
RNA	Ribonucleic Acid
SE	Secondary Electrons
SEM	Scanning Electron Microscope
SiNP	Silicon Nanoparticle
ssDNA	Single stranded DNA
STEM	Scanning Transmission Electron Microscope
TEM	Transmission Electron Microscope
UV	Ultraviolet
Vis	Visible
XPS	X-Ray Photoelectron Spectroscopy
XRD	X-Ray Diffraction

List of Figures

Abstract

Metal Oxide Nanostructures for DNA Analysis

Paul Cannon, B.Sc. (Hons)

Nucleic acids are excellent biomarkers for disease identification; however, their isolation and detection are laborious and time-consuming, requiring specialised techniques which pose significant challenges when integrating into microfluidic devices for point-of-care diagnostics. In this work, the synthesis and characterisation of novel SiO_2 nanostructures for nucleic acid isolation and detection is demonstrated. Nanomaterials have emerged as promising candidates for functional materials that can be incorporated into these small portable devices; however, these structures come with costly and complex synthesis procedures, reducing their compatibility with the themes of low-cost diagnostics, and limiting their adoption by the wider research community that don't have access to the required instrumentation. This work outlines the synthesis and characterisation of SiO_2 nanostructures synthesised using low-cost techniques, enabling both DNA isolation and detection within a microfluidic device. A novel and straightforward SiO_2 deposition system was developed, based on the thermal decomposition of polydimethylsiloxane at > 450 °C, and a systematic investigation into the effect of the system parameters on the deposition morphology was studied. The ability to produce high quality, 2D thin films (1 - 18 nm thickness) and 3D nanostructures was demonstrated. Additionally, an investigation into the efficient production of both ligand-free and DNA-functionalised SiO_2 nanoparticles by the well-established but traditionally inefficient method of laser ablation synthesis in solution (LASiS) was carried out. The LASiS technique demonstrated the ability to produce biocompatible SiO_2 nanoparticle surface coatings which were used as a model prototype for increased functionality biocompatible implants. The DNA isolation capabilities of each SiO_2 nanostructure morphology were investigated within microfluidic channels using standard fluorescence spectroscopy, followed by the development of a label-free DNA detection mechanism by growing these SiO_2 nanostructures on piezoelectric quartz crystal microbalance substrates. By measuring the change in frequency and dissipation of the crystal oscillations, DNA binding events were analysed and quantified. These nanostructures show significantly enhanced DNA capture capabilities compared to planar substrates, which was verified by both fluorescence spectroscopy and changes in piezoelectric resonance frequency.

This work not only provides a breakthrough in low-cost, accessible SiO_2 deposition techniques but also significantly enhances the functionality and biocompatible of surfaces and biosensors, paving the way for more widespread adoption of point-of-care diagnostics.

1. Introduction

1.1. Point-of-Care Diagnostics

Now more than ever, the importance of rapid and easily accessible disease detection has been recognised by not just the scientific community, but the worldwide population as well. However, even prior to the COVID-19 pandemic, there had been a shift in the priority for disease detection, moving away from the traditional centralised laboratory approach to a Point-of-Care (POC) approach [1], [2]. POC systems are laboratory standard tests which are designed to be used outside of the lab setting, right at the point of patient care. Traditionally, diagnostic systems were located in well-funded laboratories in highly regulated and quality-assessed environments, using bulky and expensive equipment and chemical agents while requiring highly skilled workers to carry out the manual diagnostic procedures [1]. POC systems are designed to be used outside of these environments, in locations like a physician's office, patient's homes, and in poorer and more disadvantaged regions of the world that don't have access to modern healthcare facilities. Especially with diseases like bacterial meningitis and sepsis for example, where early detection of disease can make all the difference [3], [4], [5], the ability to run tests and obtain results immediately will allow for better and more tailored treatment of disease. Additionally, with the growing dangers of antibiotic-resistant bacteria, fast, reliable disease detection mechanisms can combat antibiotic over-prescription. The final major benefit of POC systems is the reduction of cost compared to traditional diagnostic systems, which comes from the reduction in sample and reagent consumption, time spent in healthcare settings like emergency rooms, and the reduced cost of detection equipment that arises from miniaturization.

The WHO Sexually Transmitted Diseases Diagnostics Initiative have developed a generic set of requirements/criteria to consider when designing POC diagnostic systems, particularly when focusing on those for the developing world [6]. They should be:

1. Low cost and affordable for those at risk of infection.

2. Highly specific to the target disease/biomarker with good sensitivity.

3. User friendly and simple to perform with minimal training, ideally having as much automation as possible and requiring minimal user input.

4. Robust manufacturing with rapid results to enable treatment at first visit.

Three commonly known and utilised POC diagnostic devices are, glucose test strips to measure glucose levels for the management of diabetes [7], pregnancy tests which utilise lateral flow microfluidic channels and colloidal metals to detect the presence of human chorionic gonadotropin hormone, which is produced in the body around a week after fertilisation [8], and, most recently, SARS-CoV-2 lateral flow assays for the detection of coronavirus antigens [9]. It is well understood that the COVID-19 antigen tests, while useful for initial screening, do not qualify as a true (or official) diagnosis. The current gold standard for definitive diagnosis is the detection of viral nucleic acids (NAs) using the polymerase chain reaction (PCR), a centralised laboratory technique. PCR-based testing centres were rapidly established worldwide to meet the demands of the COVID-19 pandemic, with the single goal of detecting of detecting COVID-19, proving highly effective in documenting and controlling the spread of the virus. However, this centralised approach is not sustainable for long-term health monitoring, especially if multiple diseases become widespread simultaneously. The PCR technique involves several intricate steps, first requiring the isolation of DNA (which itself is a multi-step process that is described in section 1.2.2.), which is then amplified/multiplied through thermal cycling, and detection using fluorescence spectroscopy [10]. Each step requires precise control and highly trained staff to ensure accuracy, and the process demands sophisticated equipment to manage the thermal cycling and detect the fluorescent signals of labelled NAs, making PCR challenging to perform outside of centralised laboratories. This specialised nature of PCR therefore presents significant challenges for integration into POC systems, highlighting the need for innovative solutions that maintain diagnostic accuracy while being adaptable to POC settings.

To satisfy these WHO criteria [6], two emerging fields have shown promise in their attempt to address these issues in miniaturising biomolecule diagnostics. The first are microfluidic systems, which offer the capability to condense complex fluidic handling processes, using small amounts of samples, into simple automated devices. The second is the use of nanomaterials, which due to their small size and unique physicochemical properties, offer highly specific and sensitive biomolecule capture and detection capabilities. Nanomaterials show great promise in biomedical settings, with many receiving approval from the U.S. Food and Drug Administration, and the European Medicines Agency, in the areas of nanomedicine and enhancing laboratory based diagnostic techniques [11]. Most recently, antibody functionalised gold nanoparticles (NPs) incorporated into microfluidic devices have achieved emergency authorization worldwide for COVID-19 antigen testing

[12], paving the way for further research into nanotechnologies for POC diagnostics and their approval for real world use [13], [14], [15], [16], [17].

1.2. Nucleic Acids

1.2.1. Molecular Structure

Nucleic acids (NAs) are long polymeric molecules made up of a chain of nucleotide monomers, with the most well-known relevant NAs being ribonucleic acid (RNA) and deoxyribonucleic acid (DNA). Nucleotides consist of a phosphate group, a carbon sugar (ribose or deoxyribose), and a nitrogenous base [18]. NAs encode the instructions for cells to carry out specific functions, and these instructions are encoded by the nitrogenous base sequences of the NA strands. These codes are given a sense of direction, as the "top" of a DNA strand is terminated a 5' phosphate group, and the end of the chain is terminated with a 3' hydroxyl group, with a "5" and "3" denoting the number of carbon atoms in the deoxyribose sugar molecule that are bonded with the phosphate groups [18]. This directionality is related to the current gold standard for DNA detection discussed in section 1.2.2. [19]. The molecular structure is illustrated below in Figure 1.1.

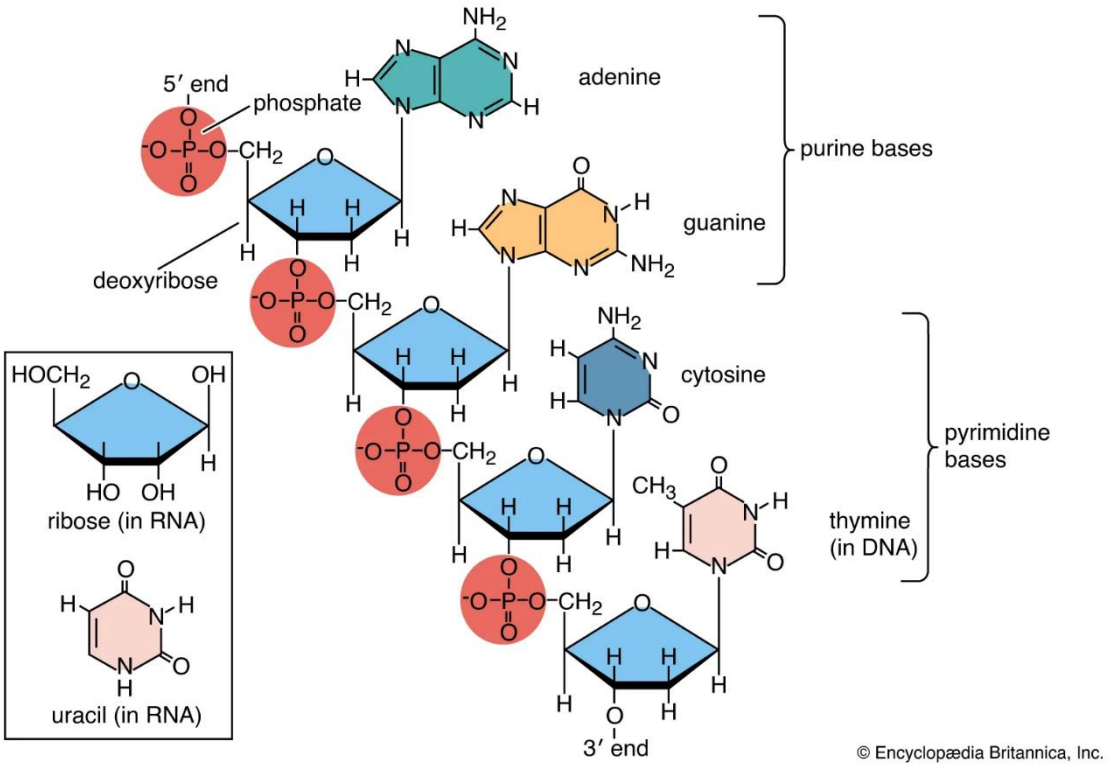

Figure 1.1: Molecular structure of NAs, including the phosphate group (red) and pentose sugar (blue) backbone and the nitrogenous bases of both DNA and (inset) RNA. [20]

The phosphate group and sugar make up the negatively charged backbone of the NAs, and the nitrogenous bases on one nucleotide connect to the complementary nitrogenous bases on another nucleotide by hydrogen bonding to create the characteristic double helix coil shape. This is the natural case for DNA, which is the NA of focus in this work, whereas RNA tends to exist in single strand form, but it can conform to this double stranded arrangement when introduced to its complementary strand. Both DNA and RNA have four nitrogenous bases, which are adenine, cytosine, guanine, and thymine in DNA, with uracil replacing thymine in RNA. Adenine can only bind to thymine (and uracil) by hydrogen double bonds, and cytosine will only bind to guanine by hydrogen triple bonds, giving rise to the complementary strand specificity which is crucial for specific NA recognition and detection. The sequence of nitrogenous bases is unique to each function of the cell or organism the NAs belong to, making NAs an unparalleled biomarker for disease.

To put his into real world context, viral infections are diagnosed by detecting the presence of NAs of the target virion by reading the nitrogenous base sequence required for it to replicate itself inside human cells. Taking COVID-19 as an example, the nitrogenous base sequence of SARS-CoV-2 RNA is entirely specific to that virion, and observing this base-pair sequence within human cells is therefore definitive proof of infection. In order to read these sequences, a complex, multi-step procedure is required, and the general workflow is described in the following section to allow comparison with the state-of-the-art extensions proposed by this research work.

1.2.2. Testing Stages

NA testing consists of three distinct stages; first is the extraction of NAs from the complex samples, second is the cleaning or purification of extracted NAs, and third is the detection of specific NA strands of interest. NA testing often follows the well-established Boom chemistry method to extract and purify the NAs [21], with numerous viable detection mechanisms emerging in recent years. This work hopes to minimise the NA testing workflow into microfluidic devices, overcoming bottlenecks associated with capture and detection in microfluidic channels, and to use low cost, label-free detection mechanisms.

1.2.2.1. Extraction

Extraction involves the lysing or rupturing of sample cells in order to expose, capture, and collect the NAs. The lyses method depends on the cell type due to differences in cell-wall structures, but typically mechanical shear force and/or chemical lysing reagents are used

to accomplish this. After the cellular components have been extracted, the NAs must be isolated and then purified for detection.

1.2.2.2. Purification

Following lysis, the sample is passed, by centrifugation, through a filter or membrane containing silica beads, which have a strong affinity for NA binding [22]. The lysed sample is mixed with a high ionic strength binding buffer containing a chaotropic agent (typically guanidinium thiocyanate). The chaotropic agent disrupts the surrounding hydrogen shell of NAs (i.e. break the hydrogen bonds between NA backbone and water) exposing the negatively charged DNA backbone. The silica membrane surfaces are also negatively charged, but the positively charged ions from the binding buffer form a bridge between both the negatively charged DNA and negatively charged silica, allowing extraction of only NAs from complex biological samples. While the NAs remain on the silica beads after mixing, so do a multitude of other contaminants. Therefore, the beads are washed multiple times with organics solutions of isopropanol and ethanol, removing contaminants while leaving behind the strongly bound NAs. Then the bound NAs are removed from the silica with an elution buffer which has a low salt concentration and higher pH (> 7) which encourages NA-

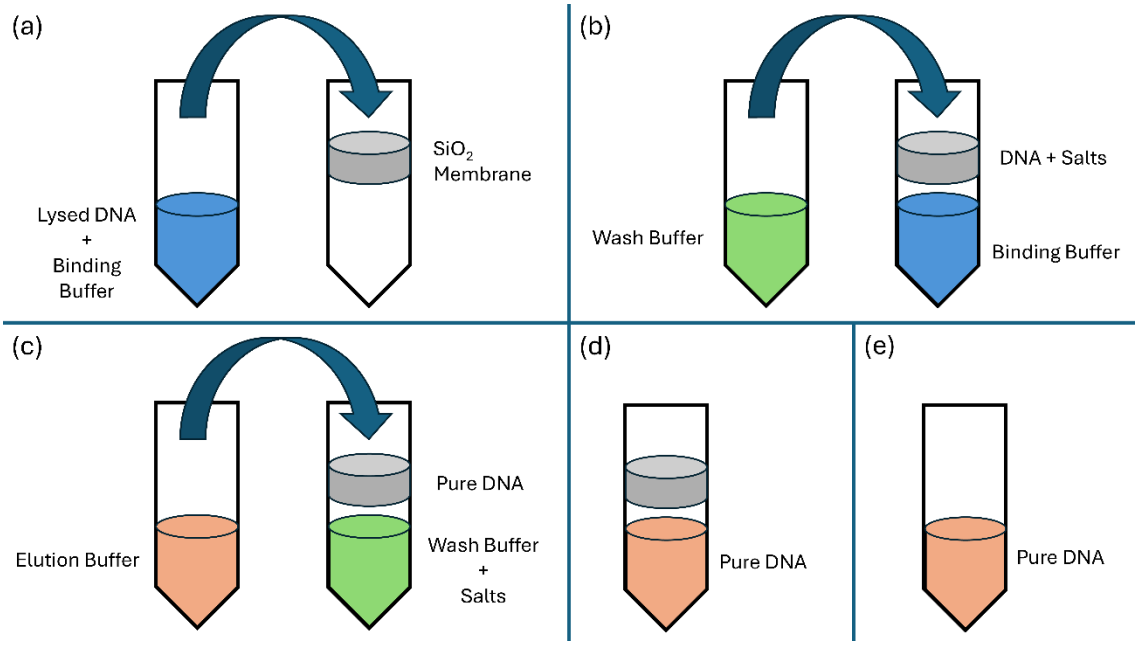

Figure 1.2: Illustration of steps involved to isolate and purify DNA from lysed samples. (a) First the DNA is isolated through binding to an SiO_2 membrane under the high ionic strength conditions of the binding buffer. (b) Next, the bound DNA is cleaned with a wash buffer, removing contaminants while DNA remains bound to the SiO_2 membrane. (c) Lastly, the DNA is removed from the SiO_2 membrane with an elution buffer so that it can be collected ((d) and (e)) for further analysis.

silica separation, and the NAs are re-suspended in solution to be prepared for detection. The process is illustrated in Figure 1.2.

1.2.2.3. Detection

The most widely utilised detection method is the polymerase chain reaction (PCR) [23]. This technique amplifies the number of NA strands, being able to take a single strand of target NA and generating thousands or millions of copies of that one target sequence. Amplification through thermal cycling involves repeatedly heating and cooling the NAs, denaturing and renaturing them, to enable the enzymatic replication of the target DNA sequence [24]. DNA is heated to 95 °C, denaturing it by dissociating the hydrogen bonds between complementary base pairs of the double stranded NA, reducing the double stranded NA to two single NA strands. Immediately following denaturation, synthetic primers (i.e. short single-stranded sequences of DNA of ~ 15 – 30 nucleotides in length, designed to be complementary to the regions either side the target sequence) are introduced which bind to the complementary sequences on the single-stranded target DNA when annealed [10]. Then the sample is annealed at a temperature ranging from 37 – 72 °C (depending on the primers used) allowing for the hydrogen bonds to reform between the sample NA strand and the primers. Primers are essential for this process as DNA polymerase cannot synthesise DNA from nothing, they can only attach new DNA nucleotides to existing strands of nucleotides, and to create a primer that covers the entire target sequence would be impractical, expensive, and challenging, as target sequences can be hundreds or thousands of nucleotides long [25]. After annealing, the sample is kept at 75 – 80 °C to enable optimal activity of DNA polymerase, and this step is known as elongation. DNA polymerase attaches to the annealed primers, and begins extending the primer across the target sequence, synthesising DNA in a 3' to 5' direction, producing strands identical to the target sequence. The primers are then removed, and the gaps are filled by the DNA polymerase, resulting in a complete replication of the single-stranded DNA and duplication of the number of target NA strands present before the thermal cycling. An illustration of a single PCR cycle is shown in Figure 1.3.

These cycles are repeated 10s to 100s of times to amplify the target NA to a concentration that is detectible by fluorescence spectroscopy. PCR is coupled with a fluorescently labelled hybridization probe (i.e. a synthetically synthesised complementary strand) that will only bind to the target sequence, enabling the detection of that specific DNA sequence by fluorescence spectroscopy which will be described in detail in section 2.2.

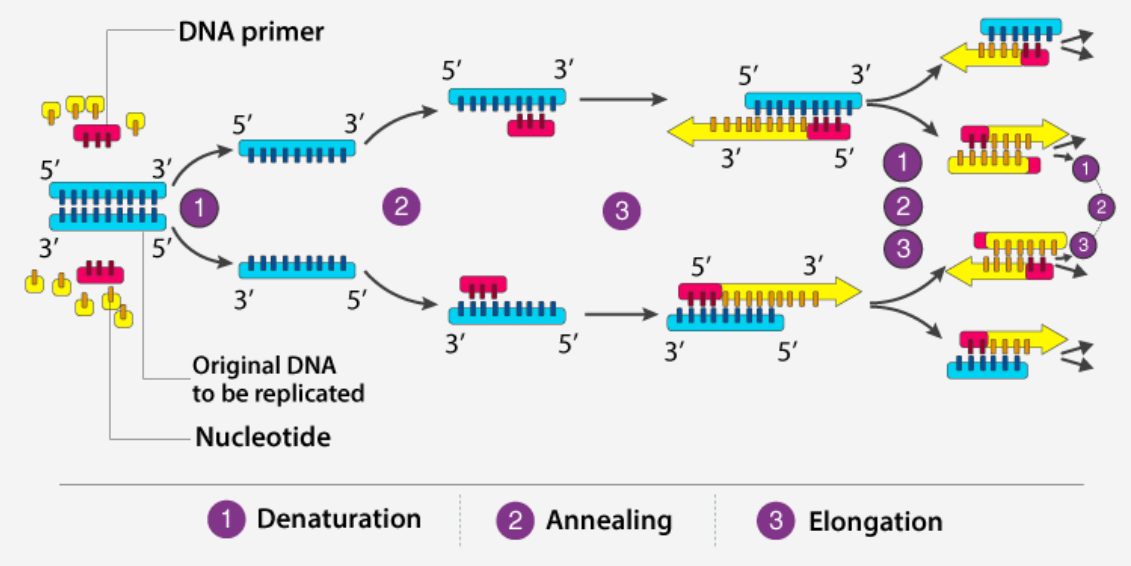

Figure 1.3: Illustration of the three steps involved in PCR DNA replication for specific DNA strand detection. [26]

Each of these PCR steps demands specialised reagents, equipment, and highly trained personnel to carry out the exhaustive procedures and ensure accuracy and reliability, making PCR challenging to integrate into portable, user-friendly POC systems. It is therefore necessary that further research is conducted into the design and implementation of alternative techniques for capturing and detecting NAs on POC devices.

1.3. Motivation & Objectives

There are two major roadblocks preventing true NA diagnosis on POC devices. The first is related to the sample preparation process, specifically the inability to reproducibly capture and clean DNA in microfluidic devices. The current state-of-the-art sample preparation process is the well-established Boom chemistry method, which is lengthy and labour-intensive [21]. This process utilises silica beads to capture DNA, but they are difficult to incorporate into microfluidic channels. The second roadblock is the current need for large and expensive equipment and reagents required to analyse the NAs. The ultimate goal of this work is to utilise SiO_2 nanomaterials, whose small dimensions are highly compatible with microfluidic channels and biomolecular interactions, to address both of these roadblocks. In particular, this work focuses on:

1. The synthesis and physicochemical characterisation of novel SiO_2 nanostructure morphologies.
2. Employment of SiO_2 nanostructures for DNA capture and detection.

1.4. Nanomaterials for Sensing Applications

Nanomaterials are objects that have at least one dimension in the nanoscale (1 - 100 nm). Metal and semiconductor nanostructures host an abundance of material- and morphology-dependant properties that make them highly desirable for not only diagnostics, but sensing applications in general. The high surface to volume ratio of NSs offers greater reactivity, and altered optical, electrical, and catalytic properties than their bulk counterparts, allowing for a broad range of detection capabilities [27]. These properties can be fine-tuned by modifying their size, morphology, and composition (through doping) [28], [29], [30]. This work looks at two different types of NSs; namely ZnO and SiO_2, to utilise their high surface to volume ratios to increase the amount of DNA capture, isolation and detection that can be achieved in microfluidic channels.

1.4.1. Zinc Oxide

ZnO is widely studied metal oxide semiconductor, particularly in relation to its applications in electronic and optoelectronic devices. ZnO is an intrinsically n-type, group II – IV compound semiconductor with a wide bandgap energy of 3.37 eV at room temperature and pressure in its most stable wurtzite crystal structure [31]. This structure arranges the atoms such that each electronegative-ion (O) is surrounded by four electropositive-ions (Zn) at the corner of the tetrahedron and vice versa. The Zn and O ions are arranged alternatively along the c-axis or c-plane resulting in positive and negative polar planes in the vertical direction (see Figure 1.4). The lateral a-plane and m-plane are terminated with both Zn and O atoms and are therefore non-polar.

It is this combination of a polar vertical plane and non-polar lateral planes that allows for the preferential 1-dimensional growth of ZnO NSs along the c-axis [32], [33]. This propensity for controlled growth along the c-axis is exploited for this work. ZnO is often characterised by the relative ease with which nanostructured morphologies can be synthesised by bottom-up, self-organised methods. High surface to volume ratio ZnO NSs can be synthesised using low-cost, facile techniques compared to the much more complex and specialised synthesis of SiO_2 nanostructures. Therefore, for the work presented in this thesis, 1D ZnO nanorods were grown to act as a nanoscaffold to be coated with a thin SiO_2 film, with the subsequent core-shell structure mimicking the effects of pure SiO_2 nanorods.

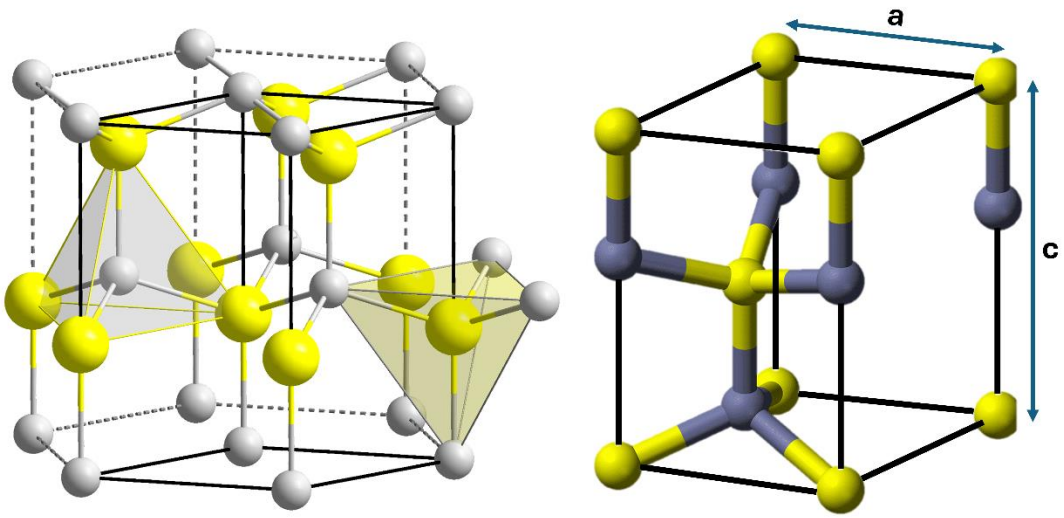

Figure 1.4: Wurtzite crystal structure of ZnO. Yellow indicates Zn atoms and grey indicates O atoms. Source: [34], public domain.

1.4.2. Silicon Dioxide

Silica, otherwise known as silicon dioxide (SiO_2), is one of the most abundant materials on the earth's surface, existing in a variety of forms, either amorphous or crystalline, with a well-known allotrope being quartz. There are countless allotropes of silica, but α-quartz is

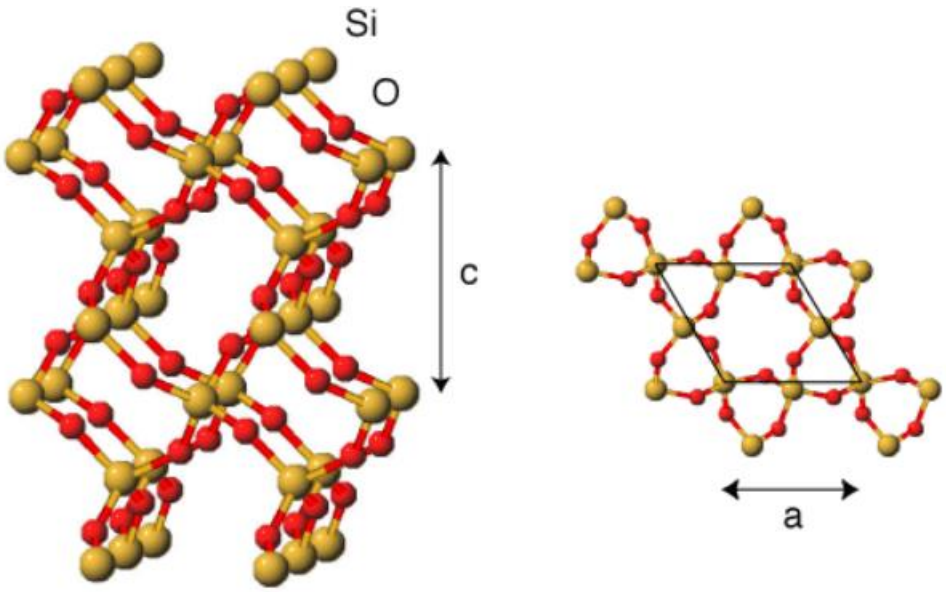

Figure 1.5: α-quartz crystal structure. Red indicates oxygen atoms and yellow indicates silicon atoms. [35]

the most stable form of solid silica. Crystalline quartz has each Si atom surrounded by four pairs of electrons at tetrahedron corners, which act as bonds connecting it to four equidistant oxygen atoms. Each O atom is also surrounded by four tetrahedrally oriented electron pairs, two of which serve as bonds connecting the O and Si atoms [36]. This orientation can be seen in Figure 1.5, and is anisotropic in nature, giving rise to the

piezoelectric effect along certain crystallographic directions that will be discussed in more detail in section 2.13 [37]. Silica is the current state-of-the-art capture mechanism for DNA isolation as stated in section 1.2 due to its well-established affinity for DNA adsorption and inherent biocompatibility [22].

1.4.3. Nanomaterial-Based Point-of-Care Diagnostics

Nanomaterials have been widely used for detecting biomolecules. Although this work uses the NSs as capture mechanisms with detection achieved by other means, NSs often come with inherent sensing properties that can be utilised for detection, which could be a focus of future work. The most common of which are Au nanomaterials, who obtain unique optoelectronic properties at the nanoscale. As discussed earlier, AuNPs have been approved for use in over-the-counter COVID-19 POC diagnostic tests [12]. However, these tests provide purely qualitative results, indicating the presence or absence of infection by a single colourimetric indicator. AuNPs exhibit a property called localised surface plasmon resonance, which gives rise to the brilliant red colour seen in the COVID-19 lateral flow assay, also provides a quantitative measurement of biomolecule detection. LSPR is caused by the displacement and coherent oscillations of the conduction electrons on the NP surface when excited by incident light of a particular resonance frequency. This frequency strongly depends on the NP size, morphology, and surrounding dielectric mediums. When biomolecules bind to the AuNP surface, this causes local refractive index changes around the NP which in turn changes the LSPR resonance frequency. The relative change in LSPR wavelength depends on the amount of biomolecule binding, providing quantitative measurements [38]. This principle has been utilised in many POC diagnostic tests, for detecting nucleic acids and antigens [38], [39]. However, AuNPs come with costly raw material costs and complex synthesis procedures [40]. This work pursues low-cost and facile NS synthesis techniques that can provide similar capture and detection capabilities as the current gold standard.

ZnO nanomaterials are often employed in photoelectrochemical-based biomolecule sensing [41]. This high isolectric point of 9.5 (i.e. the pH at which no net migration takes place in an electric field) provide ZnO with strong adsorption ability for low isoelectric point biomolecules like enzymes and proteins. One such enzyme is glucose oxidase, and by coating electrode surfaces with these ZnO-enzyme hybrids, glucose detection can be achieved [42], [43], [44]. When glucose comes into contact with glucose oxidase in the presence of O_2, it undergoes an oxidation reaction facilitated by the enzyme. The enzyme catalyses the transfer of electrons from glucose to O_2, which acts as an electron acceptor.

This reaction produces gluconic acid and more importantly, hydrogen peroxide (H_2O_2) as a by-product. The ZnO NSs detect the presence of this H_2O_2 byproduct through an electrochemical reaction. Given ZnOs semiconducting nature and good electron mobility, when H_2O_2 is adsorbed onto the electrically biased ZnO surface, the electrons from H_2O_2 are transferred to the ZnO electrode, generating an increased current under an applied voltage. The high surface area of ZnO NSs provides significantly increased binding sites for glucose and H_2O_2 interactions, enhancing the overall sensitivity of the sensor. This sensor response can additionally be enhanced by photoactivation. When exposed to UV wavelengths with energies greater than the ZnO bandgap, electron-hole pairs are generated which can participate in electrochemical reactions, increasing the rate of the reaction and further improving the glucose sensing response. This principle can be applied for detecting a variety of other molecules, from human health biomarkers to food safety and environmental monitoring markers [45]. However, the surface properties of ZnO differ significantly from SiO_2, and hence their interaction with biological species such as NAs and proteins is quite different to that of SiO_2.

Si-based biosensors provide a wide range of detection technologies for different types of biomolecule sensing. An emerging tool is the use of Si cantilever arrays, typically used in atomic force microscopy, as highly sensitive sensors, capable of not only static biomolecule sensing, but for also studying the dynamics of biomolecule binding [46]. Typically, the top of each cantilever is functionalised with the appropriate capture molecules (antibodies or DNA probes) designed to bind target molecules. When a target molecule binds to the functionalized surface, the induced stress or mechanical loading causes changes in the resonance frequency of the piezoelectric cantilever (detected either optically or electrically), and the magnitude of this change provides a quantitative measure of the binding interaction between capture and target molecules. A key advantage of these arrays is the ability to provide simultaneous detection of multiple analytes on different cantilevers in parallel, enabled by their small physical dimensions, making them highly suitable for multiplexed biosensing applications [47]. An additional benefit of these arrays is the ability to use a reference cantilever placed amongst the sensing cantilever, which reduces the noise and compensates for non-specific changes such as an environmental variations in temperature, humidity, or mechanical drift, improving the accuracy of these sensors.

Nanostructured SiO_2 does not have inherent optical or electronic properties for direct biomolecule sensing. However, SiO_2 is still widely incorporated into microfluidic devices

and has been used to enhance currently researched diagnostic techniques, such as the aforementioned LSPR sensing. LSPR sensing relies on the LSPR propagation along the Au/dielectric interface, where the dielectric is the layer of immobilised capture molecules such as antibodies or enzymes for the specific target analyte. A relatively new enhancement of this technique involves the creation of symmetric dielectric-metal-dielectric structures to increase the sensitivity of LSPR sensing [48]. SiO_2 thin films have been identified as a promising dielectric, due to their tuneable refractive index that is similar to most water-based sensing mediums and biological fluids, which allows for better matching with the interface of the metal and sensing medium [49], [50]. The increased sensitivity arises from constructive interference between the surface plasmon waves occurring at the two identical metal-dielectric interfaces separated by the thin, usually ≤ 20 nm, Au film, providing much higher signal-to-noise ratios compared to normal SPR.

SiO_2 NPs have often been used for biosensing, as their surface can be easily functionalised with capture molecules, and these have been used to enhance laboratory-based techniques like ELISAs. Typical sandwich ELISA testing involves the immobilisation of a capture antibody or single stranded DNA (ssDNA) on a chamber surface which captures the target analyte or its complementary DNA strand. Then more antibodies, or the same capture DNA strand, each functionalised with a single fluorophore, specific to the analyte are added to the chamber. These detection antibodies/DNA only bind to the analyte immobilised by the capture antibodies/DNA, and everything else is washed away. Porous SiO_2 NPs have been used to increase the detection signal, by encapsulating multiple fluorophores within their SiO_2 matrix [51]. Instead of the detection antibodies/DNA being functionalised with a single fluorophore, they are functionalised with SiO_2 NPs encapsulating multiple fluorophores, providing a much higher fluorescence signal for the same concentration of target analyte. This sandwich assay principle is how the POC lateral flow assays work, with the colourimetric red line indicator arising from AuNP-functionalised detection antibodies.

As mentioned in section 1.2, SiO_2 has a high affinity for DNA binding, and is used as the capture medium for DNA isolation and purification for subsequent detection. Nanostructured SiO_2 has a significantly larger surface area, and therefore available binding sites than its bulk counterpart, enabling higher efficiency DNA capture and isolation, and ultimately higher detection sensitivity. Incorporating free SiO_2 microbeads like those used for lab-based PCR into microfluidic channels results in inconsistent and irreproducible capture and isolation efficiencies [52]. Instead, SiO_2 micropillars are being incorporated

into microfluidic channels to overcome these challenges with high binding efficiencies [53], [54]. However, the creation of these SiO_2 nanostructured deposits is quite challenging, due to the complexity of SiO_2 deposition and structuring methods, often involving etching and physical/chemical vapour deposition under high vacuum conditions which are highly-specialised and expensive techniques [55].

This work explores novel routes for the creation of nanostructured SiO_2 deposits using relatively simple laboratory-based methods to enable high efficiency DNA capture and detection. This should enable significant advances in research areas such as biosensors and biomedical devices, reducing the barrier and limitations preventing widespread SiO_2 nanostructure growth and to enable point-of-care DNA isolation and label-free detection.

1.5. Outline of Thesis

This thesis describes the synthesis of novel SiO_2 nanostructures to enable reproducible DNA isolation and detection within microfluidic devices. The SiO_2 NSs were used to capture DNA, and their DNA binding efficiencies were analysed. A brief outline of each chapter is as follows:

Chapter two describes the theoretical principles that underpin each of the experimental techniques used to characterise the NSs and their DNA binding capabilities. The instruments and general procedures used are included.

Chapter three details the development and optimisation of a novel SiO_2 deposition technique for producing 2D thin films and high surface to volume ratio NSs. The experimental setup is shown, alongside a systematic investigation into the effect the controllable variables have on the resultant SiO_2 deposit characteristics. The ability of the system to produce ultrathin conformal thin films with high controllability, alongside "3D" nanostructures with high surface-to-volume ratios depending on the chosen system parameters is demonstrated.

Chapter four details the synthesis and characterisation of SiO_2 nanoparticles and an investigation into dynamic flow conditions to enable high efficiency nanoparticle production and surface functionalisation using DNA as a model biomolecule. The chapter concludes with the characterisation of a novel nanoparticle drop casting technique used to produce uniform SiO_2 nanoparticle coatings for bioapplications.

Chapter five demonstrates a number of bioapplications of the SiO_2 nanomaterials. Firstly, traditional fluorescence spectroscopy techniques were used to compare the DNA binding

capabilities of planar SiO_2 surfaces, SiNPs, ZnO NRs, SiO_2 nanodendrites, and ZnO-SiO_2 NRs nanostructures. This was done in both microwell plates and as part of microfluidic channels for DNA isolation and subsequent detection. SiO_2 nanostructures are then grown on piezoelectric QCM substrates to enable label-free DNA detection. The chapter concludes with preliminary work using SiO_2 nanoparticle coatings to promote cell growth for biocompatible implant applications.

Chapter six outlines the final general conclusions of the thesis and includes some suggestions for further work for each topic covered in the thesis.

2. Experimental Techniques

The results showcased in this thesis were obtained using a large range of well-established experimental equipment and techniques, and this chapter outlines the theoretical principles of each technique and the instruments and procedures used.

This chapter begins with a description of well-established synthesis techniques adopted for this work. ZnO nanorods were synthesised to act as scaffolds for novel SiO_2 deposition, and physical vapour techniques were used to deposit thin Au layers to enable of electrical characterisation and electron imaging of insulating samples.

A major focus of this work was the investigation of the effects of nanostructure (NS) morphology on DNA binding ability. NS morphologies were imaged using various electron microscopy (EM) techniques. EM provides high magnification images beyond the resolution capable of optical microscopy, allowing direct observation of nanometre scale structures and features. EM enables measurement of NS height, width, and interspacing by capturing images at various angles (0-90°).

Novel synthesis techniques were utilised to create both homogenous (single-component) and core-shell (dual-component) NSs. To determine the chemical properties of these structures, such as elemental makeup, stoichiometry and chemical bonding, x-ray photoelectron spectroscopy (XPS), energy-dispersive x-ray spectroscopy (EDX), and Fourier transform infrared spectroscopy (FTIR) were utilised. XPS and EDX in particular provided information about composition of samples, with XPS allowing depth profiling, i.e. chemical characterisation of the first ~ 10 nm of sample. FTIR was used to complement these results as it is capable of identifying the various molecular bonds present within samples.

Thin film thicknesses were measured using spectroscopic ellipsometry and contact profilometry (CP) and complemented by XPS depth profiling and EM. The roughness of these films was characterised using atomic force microscopy (AFM) and CP. The dielectric breakdown characteristics of thin films were determined using current – voltage sweeps and analysed using Weibull statistics.

This chapter concludes with a description of the techniques used to quantify DNA. DNA binding efficiencies of NSs were assessed through a combination of traditional fluorescence spectroscopy techniques and quartz crystal microbalance (QCM) measurements.

2.1. Nanostructure Synthesis

2.1.1. ZnO Nanorod Growth

As mentioned in section 1.4.3, the growth of silica micro- and nanostructures requires the use of complex and specialised top-down techniques such as photolithography, etching, and vacuum based deposition technologies. In this work, the goal was to use facile, substrate independent techniques to produce ZnO structures *via* bottom-up techniques to act as nano-scaffolds for the development of core-shell ZnO-silica nanostructures, where the silica shell mimics the effects of silica nanorods whose production is far more challenging. This section details the growth technique for the ZnO nanorods using well established methods, with chapter 3 discussing the design and optimisation of the novel silica coating mechanism.

2.1.1.1. Chemical Bath Deposition

Chemical bath deposition (CBD) techniques are relatively inexpensive and highly versatile techniques, especially for the low temperature growth (< 100 °C) of ZnO nanostructures and thin films. There are many different combinations of materials and precursor compounds that can be used, but generally it involves the use of Zn salts such as Zn acetate, nitrate, formate, sulphate, or chloride as a source of Zn ions. These Zn salt precursors are paired with a base chemical as a source of O or hydroxide ions that can form a partially soluble Zn hydroxide [56]. Under the right conditions, this Zn hydroxide can be decomposed to form ZnO or Zn2+ which may then become ZnO through oxidation [57]. A wide range of substrates, bases, precursors, solvents, and surfactants can be used in different combinations to provide precise control over resultant morphology. In this work, the predominant CBD growth method used was the direct thermal decomposition of zinc acetate in aqueous solution. The lower temperature and relatively neutral pH of the reaction is much more suitable for a wide range of substrates as more commonly used CBD conditions can result in etching of various templates or masks. However, while this CBD technique will create ZnO nanostructures, without appropriate nucleation sites, ZnO nanostructures will form in solution and deposit randomly on the substrate. For our application, we require highly ordered, vertically aligned nanorods to efficiently and reproducibility capture DNA by flowing a solution through them. The technique used was adopted from Greene *et al*., using a facile seeding process that allows vertically aligned growth without the need for epitaxial matching [32]. The chemical pathway for the seed layer was unravelled by Byrne *et al.*, and is illustrated in Figure 2.1 [58].

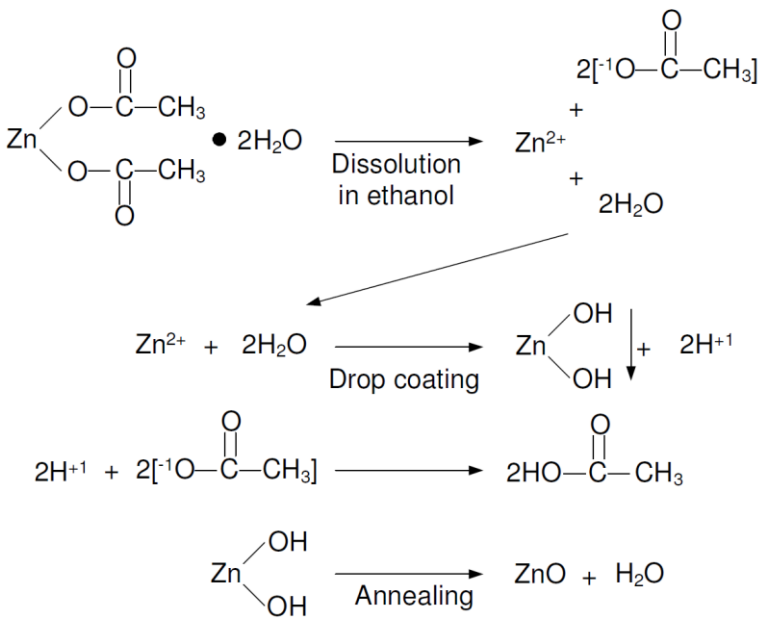

Figure 2.1: Chemical pathway to the formation of ZnO crystal seeds by drop-coating a solution of zinc acetate in ethanol. [33]

A 5 mM zinc acetate solution is prepared by dissolving zinc acetate dihydrate in anhydrous ethanol. 3.5 µL/cm^2 of this solution is drop coated onto a clean substrate (polished Si wafer) and is allowed to spread evenly across the substrate surface. After 20 seconds have elapsed, the substrate is thoroughly rinsed in absolute ethanol and gently dried with a nitrogen stream. Typically, this process is repeated four more times, but it is strongly dependent on the relative humidity of the room as water vapour in the atmosphere drives the reaction that produces ZnO seed crystals. More drop coatings are required at low humidity (< 20%) and less at higher humidity (> 45%). In our lab, five dropcoats were typically used. The reaction is additionally dependent on the hydroscopic nature of the ethanol in the zinc acetate solution. Under high enough humidity, water from the atmosphere diffuses into the drop coated solution and reacts with the zinc acetate, forming an insoluble zinc acetate hydroxide precipitate which deposits onto the substrate in 4 - 5 nm crystals. After sufficient drop coats, the seeded substrate is annealed at 350 °C for 30 minutes. Here the zinc hydroxide becomes ZnO and water, with the latter being evaporated off leaving behind only small ZnO nucleation sites. These seed crystals lie with their basal planes parallel to the substrate surface, allowing well textured growth, given ZnOs preferential growth along the c-axis. It is this seeded substrate that is placed in a CBD reaction to facilitate vertically aligned ZnO nanorod growth, and the reaction is illustrated in Figure 2.2.

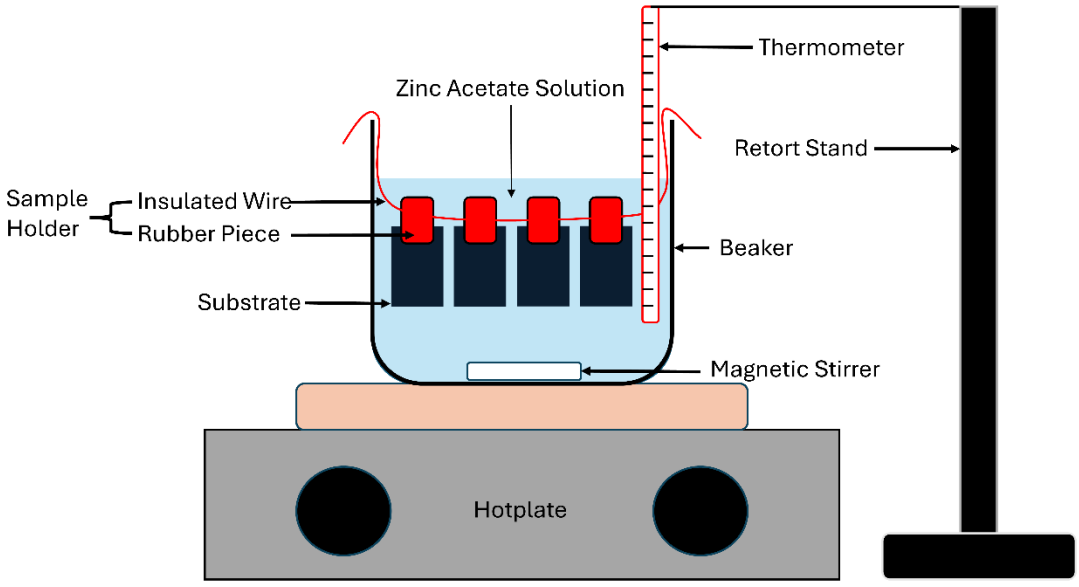

Figure 2.2: CBD deposition of ZnO nanorods on seeded substrates illustration.

The Zn acetate CBD reaction involves dissolving Zn acetate in deionised (DI) water to create a 25 mM solution, or 5.28 mg Zn acetate per mL of solution, and heating to (65 ± 5) °C. Similar to the seeding process, zinc acetate reacts with water to form zinc hydroxide, which decomposes into ZnO which deposits on ZnO seeds. Heating zinc acetate results in the loss of the acetate anion leading to the formation of partially soluble zinc hydroxide. The sample is submerged in the solution and is left for 1 - 3 hours to produce nanorods of a reasonable length (approximately 400 nm every 90 minutes). Constant agitation throughout the deposition is required to prevent precipitation build-up on the surface, and this is achieved with magnetic stirring. Due to the hexagonal wurtzite crystal structure, ZnO will grow preferentially along the c-axis to minimise the free energy which is why ZnO nanorods are the predominant ZnO structure. The top or basal c-plane surface of ZnO is a polar face, alternately terminated in either Zn or O, whereas the side faces are nonpolar, allowing ZnO to be easily grown in nanowire form. When the CBD growth stage is performed on a substrate seeded using the method mentioned above, the nanorods will be aligned with the c-axis normal to the substrate surface. SEM images of CBD nanorods grown for this work are shown in Figure 2.3.

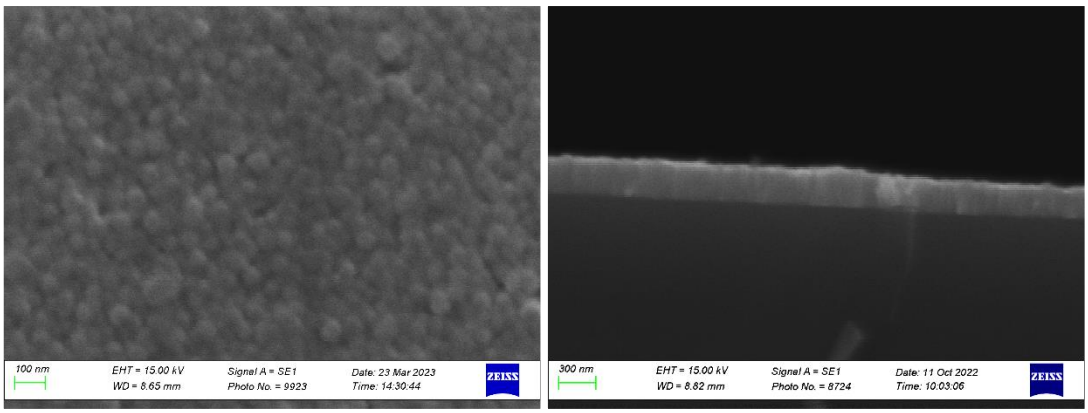

Figure 2.3: (Left) Plan-view and (Right) cross-section view of ZnO CBD buffer layers grown on Si substrates.

2.1.1.2. Carbothermal Reduction Vapour Phase Transport

It is from this CBD buffer layer that high aspect ratio carbothermal reduction vapor phase transport (CTRVPT) NRs were grown. ZnO will not readily deposit on SiO_2 (the native oxide of Si substrates), and the lattice mismatch between ZnO and Si will generally result in randomly aligned nanorods [59]. The previous ZnO buffer layer serves two crucial functions; it provides energetically favourable sites for ZnO nucleation, and the crystallographic texture allows for the growth of vertically aligned ZnO nanorods along the c-axis from the already c-axis aligned buffer NRs [60], [61], [62]. This growth method is based on the reduction of a metal oxide by a carbon-based reducing agent at high temperatures. ZnO powders are reduced by graphite to produce a Zn vapour and carbon monoxide.

$$ZnO(s) + C(s) \rightarrow Zn(g) + CO(g)$$

The Zn vapour is then re-oxidised into ZnO which will deposit on energetically favourable sites provided by the aligned ZnO buffer layer.

$$Zn(g) + \frac{1}{2}O_2(g) \rightarrow ZnO(s)$$

In this work, CTRVPT depositions were carried out in a quartz tube (length: 1.15m, diameter: 3.7 cm) positioned with the hot zone of a single temperature zone horizontal tube furnace (Lenton Thermal Designs). The quartz tube was connected to a high purity argon (99.999%) flow controlled by a mass flow controller (MFC Analyt GFC 17). A schematic diagram of the tube furnace is shown in Figure 2.4.

For this work, 60 mg of high purity ZnO powder (99.9995%) and 60 mg of graphite powder (99.9999%) were carefully mixed *via* mortar and pestle to create a homogenous mixture and increase the contact area for CTR. This ground powder mixture was spread across a 2 cm length of an alumina crucible. Substrates coated in the buffer layer were suspended

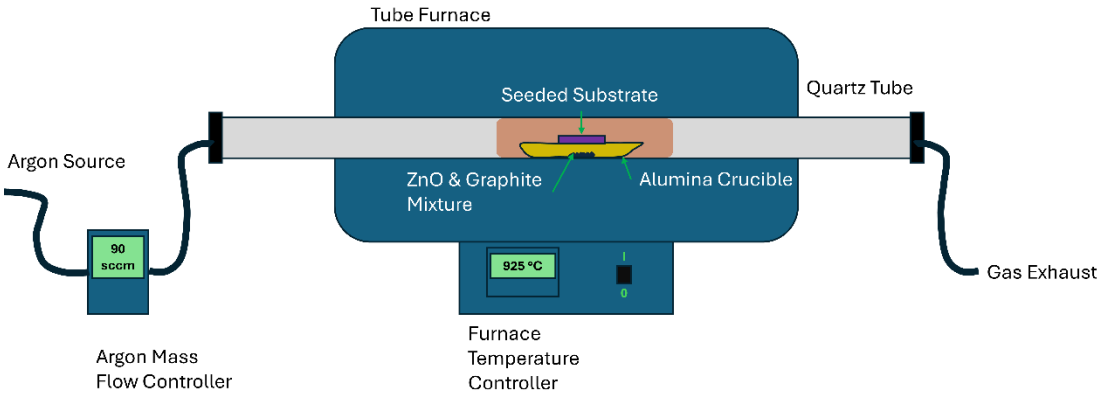

Figure 2.4: Schematic diagram of tube furnace used for CTRVPT ZnO NR growth.

directly above the ZnO-graphite mixture, with the buffer layer facing down towards the powder, and the alumina boat containing sample and powder was loaded into the quartz tube so that the powder and substrate were in the centre of the furnace hot zone. The ends of the quartz tubes were enclosed, and argon was flowed at a rate of 90 sccm for 5 minutes to purge the tube. Once purged, the system was heated to 925 °C, maintaining argon flow for the whole growth process. This temperature was kept for 40 minutes, after which the temperature is reduced, and the system allowed to cool for 1 -2 hours to < 400 °C before

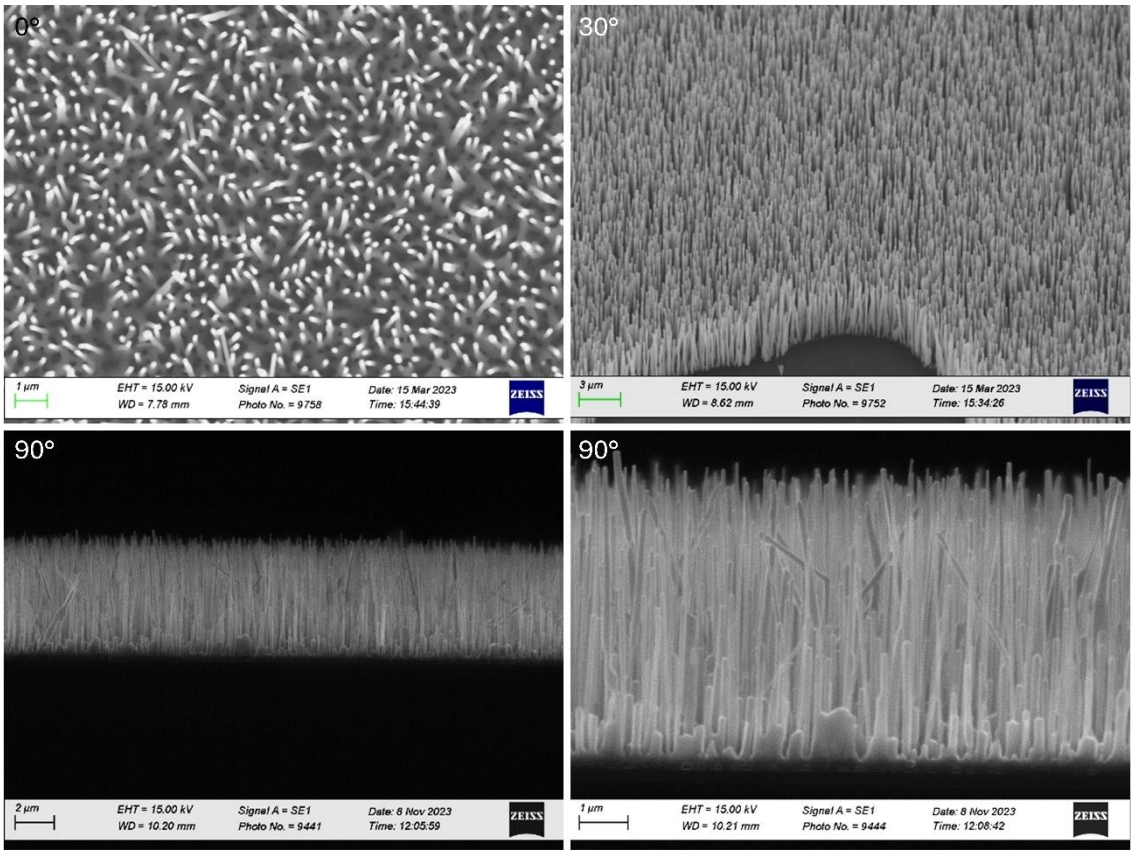

Figure 2.5: SEM images of CTRVPT ZnO NRs at (a) 0°, (b) 30°, (c & d) 90° viewing angles.

argon flow is stopped, and the alumina boat is removed. In spite of the argon purging, there is enough residual O_2 present in the tube to enable ZnO NR growth. SEM images of these CTRVPT NR arrays are shown in Figure 2.5.

2.1.2. Physical Vapour Deposition

Physical vapour deposition (PVD) techniques were used in this work to deposit Au films to act as electrodes for dielectric breakdown testing of SiO_2 thin films, and to deposit Au layers onto insulating sample surfaces to allow for SEM analysis. Two techniques were used in this work depending on sample dimensions and deposition chamber compatibilities. Au electrodes were deposited on SiO_2 coated substrates using electron-beam evaporation, and 3D printed PLA stents were coated in a thin 15 nm Au layer by magnetron sputtering.

2.1.2.1. Electron Beam Evaporation

Electron beam evaporation uses a focused beam of electrons to heat and evaporate target materials in a high vacuum environment [63]. The deposition material is loaded into a crucible inside a vacuum chamber, and the crucible is placed near a tungsten wire. A large current is passed through the wire to cause thermionic emission of electrons. The emitted electrons are accelerated towards the target deposition material by a high voltage, heating the material to its evaporation or sublimation point. The target material atoms or molecules become vaporised and travel in straight lines towards the substrate positioned above the

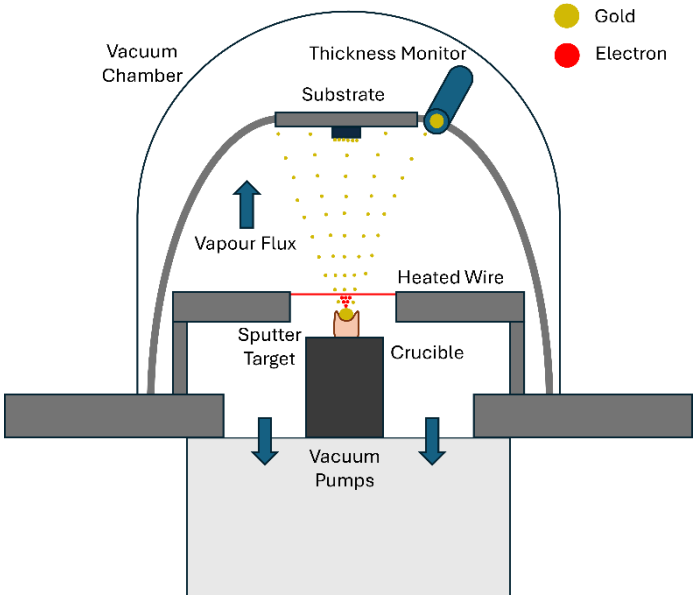

Figure 2.6: Schematic diagram of the electron-beam evaporator used in this work. The crucible containing the sputter target, in this work an Au foil, is located underneath the tungsten wire electron source (red), and the substrate is positioned directly above the sputter target. A high voltage accelerates electrons emitted from the wire towards the Au sputter target, vaporising the target atoms which then travel towards the substrate where they condense, forming a thin film.

crucible. The vaporised atoms/molecules condense onto the cooler substrate, forming a thin film. The thickness is monitored with a piezoelectric crystal monitor, using the known density and acoustic impedance of the evaporated material, and the electron source current and accelerating voltages are turned off when the desired thickness is achieved [64]. A typical schematic is shown in Figure 2.6. This work utilised an Edwards Auto 306 vacuum coater. The deposition was performed under a ~ 1 – 3 keV accelerating voltage for the electron beam and ~ 25 mA current in the filament. The values varied depending on the deposition rate and total thickness required.

2.1.2.2. Magnetron Sputtering

Magnetron sputtering utilises a plasma to eject atoms from a solid target material and deposit them onto a substrate. A working gas, in this case argon, is introduced into the vacuum at low pressure. The cathode contains an arrangement of magnets, in such a way that one pole is positioned at the central axis of the target and the second pole is formed by a ring of magnets around the outer edge of the target. A high voltage is applied to the cathode (which is covered by the sputter target), causing electrons to spiral around the magnetic field lines with a well-defined frequency and radius, which is dependent on the strength of the magnetic field [65]. These spiralling electrons ionise the argon gas to create an argon plasma, and the argon ions are accelerated towards the sputter target. This ion bombardment causes the removal of sputter target atoms/molecules, which are then

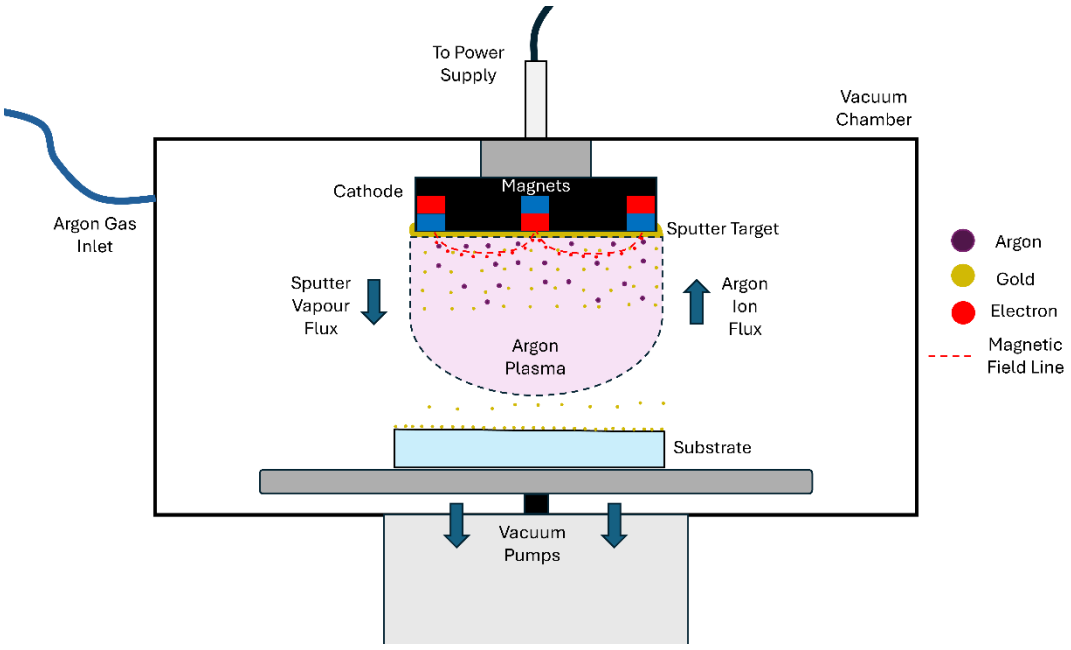

Figure 2.7: Schematic diagram of magnetron sputter coater used in this work. A gold foil is wrapped around the cathode and is sputtered by an argon plasma and deposited on a substrate lying beneath the gold foil. The argon gas is ionised by electrons spiralling around the magnetic field lines along the surface of the gold foil generated by the alternating arrangement of magnets within the cathode.

deposited on the substrate. The process is illustrated in Figure 2.7. This work utilised a Quorum Technologies K650X Magnetron Sputter Coater. The desired deposition thicknesses were achieved by following manufacturer guidelines. Au coating was performed at an argon pressure of 1 x 10^{-1} mbar and a deposition current of 20 mA, resulting in a deposition rate of 7.5 nm/min.

2.2. Nanostructure Characterisation

2.2.1. Electron Microscopy

Electron microscopy (EM) was the primary tool for NS analysis, due to the scale of the features under investigation. According to the Rayleigh criterion, two-point sources of light are considered resolvable if the central maximum bright spot of the diffraction pattern produced by one source overlaps with the first minimum dark spot of the diffraction pattern produced by the second source. This yields a resolution limit which is linearly proportional to the wavelength of light. Due to the scale of the features under investigation being similar to, and often smaller than the wavelength of visible light, optical microscopy was not suitable for examining the morphology of these structures.

This resolution limit can be overcome by the use of radiation with smaller wavelengths. The deBroglie wavelength, i.e. the wavelength associated with a massive particle, is given by:

$$\lambda = \frac{h}{p} = \frac{h}{mv} = \frac{h}{\sqrt{2me(U)}} \qquad (Eqn.\,2.1)$$

Where λ is the DeBroglie wavelength of the particle, h is the Planck constant, and p, v, m, e and U are the momentum, velocity, charge, and accelerating voltage of the particle respectively. Since electrons have a very small rest mass (~ 9.11x10^{-31} kg), even relatively modest velocities can result in significant momenta, leading to very small deBroglie wavelengths [66], [67]. In scanning electron microscopy (SEM), electrons are typically accelerated to 1 - 30 kV energies, resulting in deBroglie wavelengths of 0.039 – 0.007 nm, much smaller than the wavelengths of visible light (400-700 nm). EM must be performed under vacuum due to high electron scattering and absorption probabilities with gaseous air molecules. EM works by directing a beam of these high energy electrons at the sample, and in this work, two different EM techniques were utilised, SEM and scanning transmission electron microscopy (STEM). A schematic diagram representing a typical SEM is shown in Figure 2.8 alongside an illustration of the various processes that occur during electron beam bombardment.

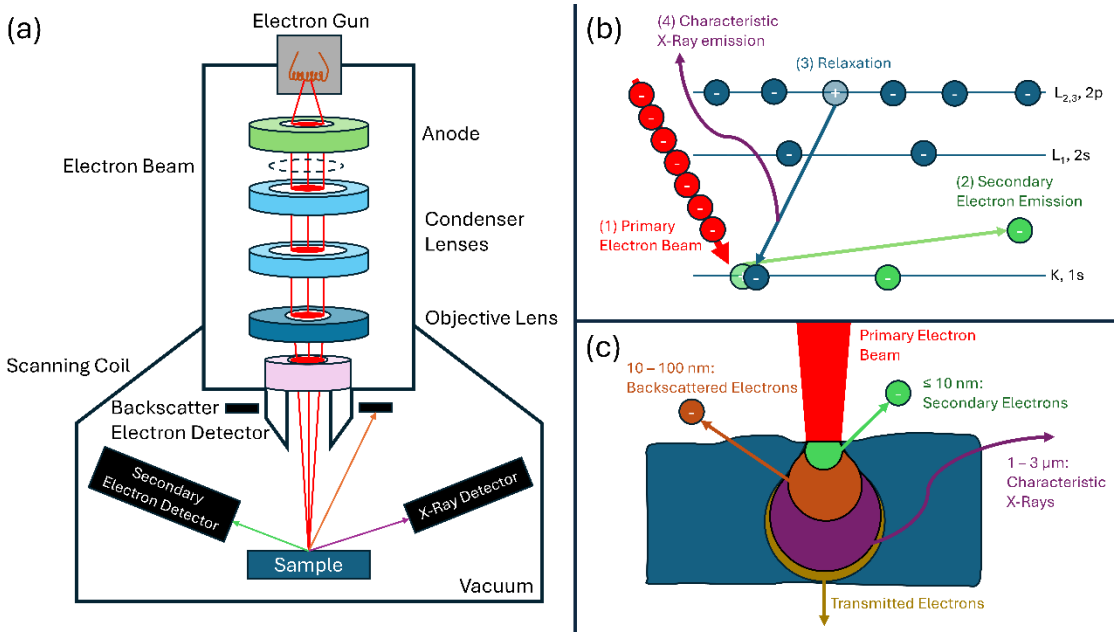

Figure 2.8: SEM setup-up and information arising from a sample under e-beam bombardment. (a) Typical schematic diagram of a SEM instrument. (b) Illustration of the atomic processes and sample interactions with the primary electron beam that give rise to the topological and chemical information obtained from SEM analysis. (c) Electron beam interaction volume and escape depth of the various signals from within the sample. The interaction volume is proportional to the energy of the incoming primary electrons.

2.2.1.1. Scanning Mode

The SEMs used in this work were primarily based on the principle of thermionic emission. Current is passed through a cathode, known as the electron gun, which is either a tungsten, or in the case of this work, a lanthanum hexaboride filament, and electrons are emitted by thermionic emission. Below the electron gun is an anode to accelerate the electrons and direct them down the column and towards the sample. The beam is directed, shaped, and focused by a system of apertures and magnetic lenses by utilising the Lorentz force. A condenser lens adjusts the spot size and beam current, and an objective lens focuses the beam on the sample surface. These lenses also allow the beam to raster scan over the sample and the resultant interactions and emitted species are measured by a variety of detectors. Applying small currents to the scanning coil induces a magnetic field that can move the beam depending on the direction of the scanning current. The system must be operated under high vacuum to reduce scattering of the electron beam from anything other than the sample surface. In SEM systems, secondary electron (SE) detectors, backscatter electron (BSE) detectors, and x-ray detectors are each used to provide different information about the sample under analysis.

The incoming electrons from the electron-beam interact with the target material in a variety of ways which produce different signals that are picked up by the aforementioned detectors. The most commonly used detector in this work was the SE detector. When

electrons in the beam undergo inelastic scattering with the target material, they can cause the ejection of electrons in its outer shell. These ejected electrons from the target material are called SEs. Due to the inelastic scattering, they are low energy electrons (~ < 50 eV) and therefore have short escape depths, meaning only electrons close to the surface escape a sample. This provides high surface sensitivity, and these SEs are used to form images of the sample surface and visualise topography. The number of SEs produced by the sample at each scanned point are plotted to give a two-dimensional image, with the number of scattered electrons being proportional to the brightness of the pixel. To detect these electrons, they must be accelerated by a positive bias to activate a scintillator, after which they are multiplied by a photomultiplier tube to produce the signal used to create the image.

The second type of electrons used for sample analysis are elastically scattered electrons from the original electron beam, known as backscattered electrons. This process is strongly dependent on the atomic mass of the atoms in the target material, with higher atomic masses resulting in greater numbers of backscattered electrons. These electrons therefore contain information about the elemental composition of the sample, with the image contrast arising from differences in atomic mass. The higher energy of these electrons allows them to escape from much deeper than SEs, so they do not provide as much topological information and are used primarily for compositional information. Because of this, they do not need to be accelerated towards the detector, and most of them travel back up the optical axis to a circular scintillator surrounding the beam emission point for detection.

In this work, a Karl Zeiss Evo LS15 was used for SE imaging, and Jeol JSM-IT 100 InTouchScope SEM was used for SE and BSE imaging.

2.2.1.2. Scanning Transmission Mode

The second type of EM used in this work was scanning transmission electron microscopy (STEM). Rather than detecting electrons that are emitted or scattered from a sample, STEM detects electrons that have been passed through a thin sample in a method more analogous to standard light microscopy [68]. Typically, in STEM, the electron beams are produced by field emission rather than thermionic emission to produce a more coherent, monochromatic, and narrow beam to enable higher resolution imaging and provide superior energy control for elemental analysis. Field emission sources are sharp metal tips (~ <100 nm diameter), and electrons are extracted by applying a high voltage at the anode, causing electrons to overcome the metal work function and tunnel through the vacuum

barrier. The emission can be precisely regulated by adjusting the applied voltage allowing for a highly coherent, monochromated, and narrow beam which contributes to a high brightness and spatial resolution. Higher voltages are typically used in STEM compared to SEM as electrons need to pass through the samples to generate images.

Since STEM detects transmitted electrons, the image contrast is provided primarily by both differences in atomic weight and the thickness of samples. Higher Z values will result in greater absorption and scattering of the electron beam, and thicker regions will reduce the transmission of electrons. There are two contrast and detection mechanisms in STEM, namely bright field (BF) and dark field (DF) imaging. BF imaging detects electrons that are directly transmitted through the specimen. Bright regions correspond to areas where more electrons are transmitted through the specimen, while darker regions correspond to areas of higher absorption or thickness. DF imaging is not the exact inverse of BF, but instead the BF detector collects electrons that are scattered to high angles and are not transmitted directly through the specimen. Not only does DF provide contrast based on sample thickness and Z-value, but also on crystal orientation and defects.

In this work a Hitachi S5500 Field Emission SEM was used for STEM imaging.

2.2.1.3. Energy-Dispersive X-Ray Spectroscopy

During the elastic interaction that creates the SEs, another signal is produced consequently. When SEs are emitted from the sample, a vacant hole is left behind which is filled by another electron from a higher orbital of that atom. This relaxation from a higher energy position to the lower energy vacancy is mediated by the emission of a characteristic x-ray. These x-rays have discrete energies corresponding to the exact energy difference between the two orbital states it transitions between. Each element has a unique electron configuration, and as a result, the energy levels, and transitions between them are unique to each element. Therefore, the characteristic x-rays serve as a fingerprint for identifying different elements in the target material. By coupling an x-ray detector to an EM instrument, spatially resolved chemical information can be obtained in a complementary fashion [69]. This technique is known as energy-dispersive x-ray spectroscopy (EDX), and the process of characteristic x-ray emission is illustrated in Figure 2.8b.

In this work, both the Karl-Zeiss LS15 and Hitachi S5500 were equipped with oxford instruments x-ray detectors to enable EDX imaging alongside electron imaging.

2.2.2. X-Ray Photoelectron Spectroscopy

X-ray photoelectron spectroscopy (XPS) is a surface sensitive characterisation technique that provides chemical information of the first ~ 10 nm of sample [70]. XPS utilises the photoelectric effect to eject valence band electrons from surface atoms. When incident x-rays ionise target atoms, a free electron is ejected (a photoelectron) with a kinetic energy K_e:

$$K_e = h.v - B_e \qquad (Eqn.\,2.2)$$

Where *h* is the Planck constant, v is the frequency of the incident photon (hv = incident photon energy) and B_e is the binding energy of the emitted photoelectron. When the absorbed photon energy is greater than the electron binding energy, the electron is ejected with a kinetic energy equal to the difference between the photon and binding energies. The lower the binding energies, the more kinetic energy the photoelectron will have upon emission [71]. As discussed in section 1.1.3, the energy of each core electron is unique to every element, and this variation in kinetic energy allows for unique fingerprinting of the different elements present in a sample. An illustration of the typical XPS experimental setup and the photoemission processes that take place on x-ray irradiation is shown in Figure 2.9.

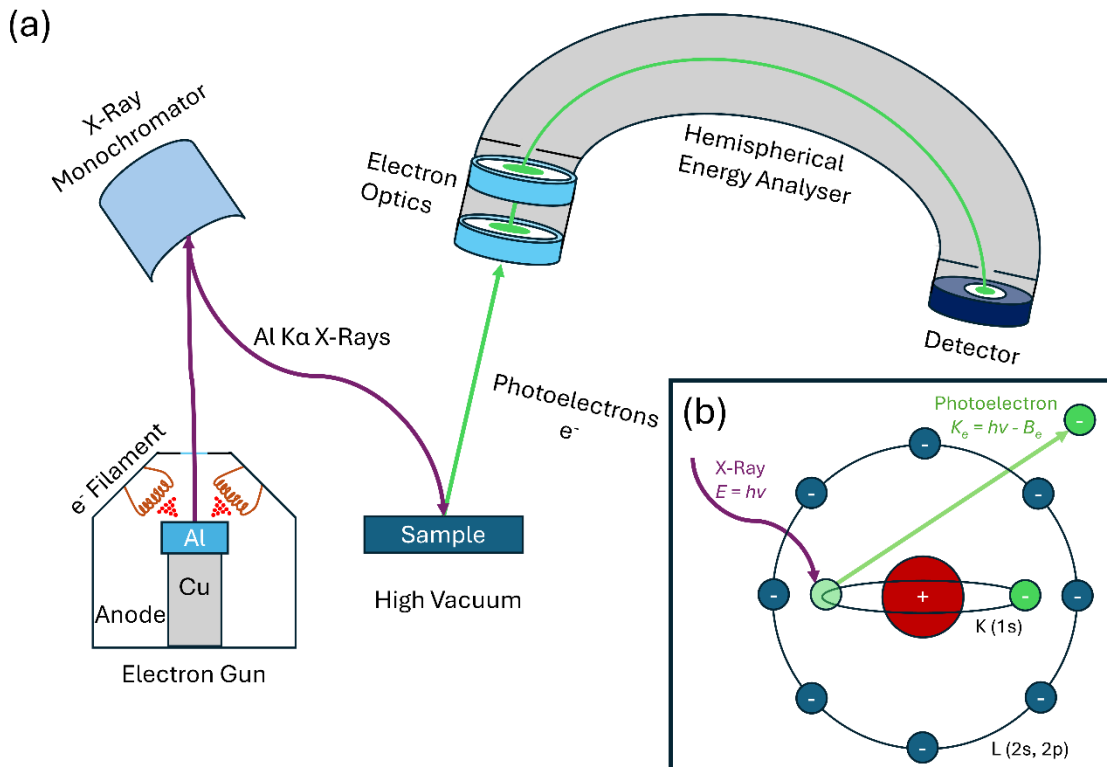

Figure 2.9: XPS setup-up and information arising from a sample under x-ray irradiation. (a) Typical schematic diagram of a XPS instrument. (b) Illustration of the process of photoelectron emission after x-ray absorption which allows for chemical identification.

XPS provides information on composition, chemical bonding, and depth profiling. Composition can be determined from the binding energy spectra obtained and comparing the results to standardised libraries of known binding energies. Samples are irradiated with a monochromatic x-ray beam, and photoelectrons with Ke ranging from 0 eV to the incident *hv* are emitted and detected, which can be easily converted to a binding energy spectrum using Eq. 2.2 above. Additionally, the shift in kinetic energy is of value as this provides information regarding the chemical bonding of the atom. Shifts in kinetic energy from expected values for pure atoms arise from interactions with neighbouring atoms. In this work, a key shift observed is from the oxidation of the Si 2p electrons. In crystalline Si, the Si 2p binding energy is 99.4 eV. However, when Si is bonded with O in a SiO_2 stoichiometry, the Si 2p orbital shifts to 103.5 eV. The electronegativity of the oxygen atom results in the increased binding energy of the Si 2p electron, and this shift is used to identify the presence of SiO_2 from pure Si crystals.

X-rays are produced by bombarding a metal target, typically Al, with electrons (emitted by thermionic emission) that have been accelerated with > 10 kV voltages. The anode is made of copper and is coated with an x-ray generating material, and in this work this coating was Al. The x-rays are monochromated (1486.7 eV Al Kα emission) before being focused on the sample at a spot size of about 100 μm^2. The electrons are emitted and then collected by an electron energy analyser consisting of three main components: the electrostatic collector lens, concentric hemispherical energy analyser, and the detector [72].

The surface sensitivity of XPS arises from the inelastic mean free path (IMFP) of the photoelectrons, which is defined by the distance electrons can travel in a solid before undergoing an inelastic scattering event. Although the Al Kα x-rays have a penetration depth on the order of microns, the inelastic mean free path (IFMP) of photoelectrons is approximately 10 nm [73]. XPS must be carried out in ultra-high vacuum (< $1x10^{-8}$ mbar) to detect these low energy photoelectrons.

In this work, XPS was carried out using a Scienta Omicron x-ray photoelectron spectrometer. XPS measurements were performed by Mr. Darragh O'Neill at the School of Physical Sciences in Dublin City University.

2.2.3. Ellipsometry

Ellipsometry was used in this work to determine the thickness and refractive index of < 20 nm thin films by measuring the changes in polarisation state of light when it interacts with a sample. Light is directed from a source, through a polariser, generating two

orthogonal waves of linearly polarised light, one oscillating parallel to the plane of incidence (P-waves) and one oscillating perpendicular to the plane of incidence (S-waves) that are in phase with one another. When this light interacts with the sample, it undergoes changes in its polarisation state dependant on the thickness and optical properties of the material it has interacted with [74]. Upon reflection from the sample, the two orthogonal waves will have a different relative amplitude and phase than their initial states. It is this difference between initial and final polarisation that can be used to infer optical properties and the thickness of materials. The change in polarisation is given by:

$$\rho_r = \frac{r_s}{r_p} = tan\Psi e^{\Delta_p} \qquad (Eqn.\,2.3)$$

Where ψ is the amplitude component and Δ_p is the phase difference which are measured by the ellipsometer, r_s and r_p represent the complex reflection coefficients of the s and p polarised light respectively. A schematic diagram is shown in Figure 2.10.

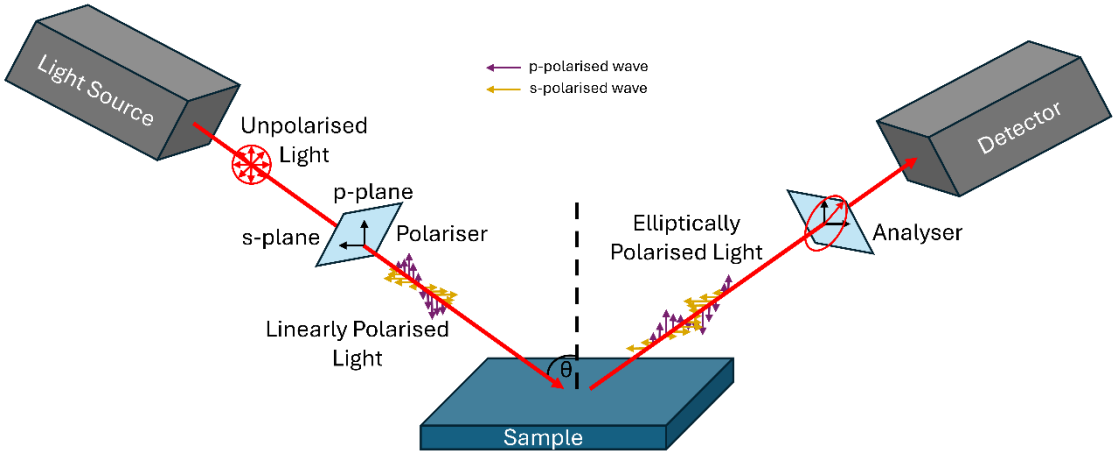

Figure 2.10: Ellipsometry setup illustration. The sample is irradiated with two orthogonally polarised light waves, and changes in polarisation occur after sample interaction which is measured by the polarisation analyser and detector.

By applying the Fresnel equations, which describe each material with its thickness and optical constants, experimental data is compared to mathematical models that calculate the predicted response of the sample material to determine the thickness and refractive indices which provide the closest fit, using parameters such as the mean squared error to ensure the quality of the fit [75]. In this work, SiO_2 films on Si substrates were analysed using ellipsometry. Cauchy models, which can be used for optically transparent materials, were used to ensure refractive indices close to the expected values for SiO_2, within the wavelength region SiO_2 is transparent in, but prebuilt SiO_2 on Si models were used for accurate thickness determination across the entire wavelength region utilised by the

instrument (245 – 1700 nm) as this model produced lower fit mean squared errors than the Cauchy models, likely due to minor absorption characteristics at ultraviolet (UV) and infrared (IR) wavelengths. In this work a J.A. Woollam M-2000UI spectroscopic ellipsometer was used and data was analysed using the Woolam CompleteEASE software.

2.2.4. Contact Profilometry

Contact profilometry (CP) is a technique used to measure the surface topography over relatively large scan areas compared to AFM (cm^2 vs μm^2 areas), providing 2D line profiles of the surface with nanometre sensitivity. CP consists of passing a mechanical diamond-tipped stylus across a surface with a constant force [76]. The movement of the stylus as it traces the sample topography is sensed electromechanically using a linear variable differential transformer (LVDT). The stylus is linked to a moveable coil of the LVDT with an AC current provided by a primary coil to generate a magnetic field, and any vertical movement of the stylus causes this core to move up or down. Within the LVDT are fixed secondary coils, and as the stylus coil moves up and down, it induces voltages in these secondary coils proportional to the displacement of the stylus and therefore the coil. Changes in the voltage output correspond to changes in the height of the sample. A schematic is shown in Figure 2.11.

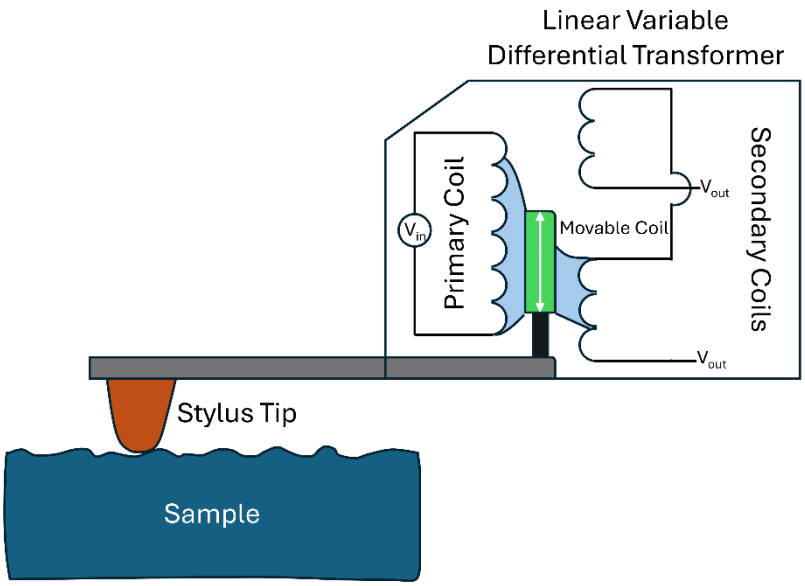

Figure 2.11: Contact profilometer setup showing the stylus tip that traces the sample surface and the LVDT which measures the change in height by inducing voltages (light blue) in secondary coils. (Stylus and LVDT are not to scale).

An important detail to remember about CP is that the obtained step heights are a convolution of the tip shape and diameter with the step heights and feature dimensions of

the sample [77]. In this work, a Bruker Dektak XT Profilometer with a 2.5 µm radius stylus was used. Sample scan parameters varied depending on scan length, but all scan speeds were ≤ 100 µm/s, often chosen to produce 300 nm/pt resolutions.

2.2.5. Atomic Force Microscopy

Atomic Force Microscopy (AFM) measures surface topography over relatively small areas with much higher vertical and lateral resolution than CP, providing 3D profiles of the surface with sub nanometre sensitivity [78]. AFMs consist of a laser focused onto the upper surface of a flexible cantilever, with the light reflected onto a four-quadrant photodetector. The cantilever is mounted on a piezoelectric crystal in a tripod configuration to enable movement in 3-Dimensions. At the end of the cantilever is a small (≤ 10 nm radius) probe tip, which is traced over the sample surface in a raster scan. As the cantilever is moved across the surface, it will move up and down with changes in the surface topography due to interactions with the probe and surface, deflecting the laser towards different quadrants of the photodetector which is used to measure variations in surface height [79]. A schematic diagram of a typical AFM instrument and the beam deflection detection mechanism is shown in Figure 2.12.

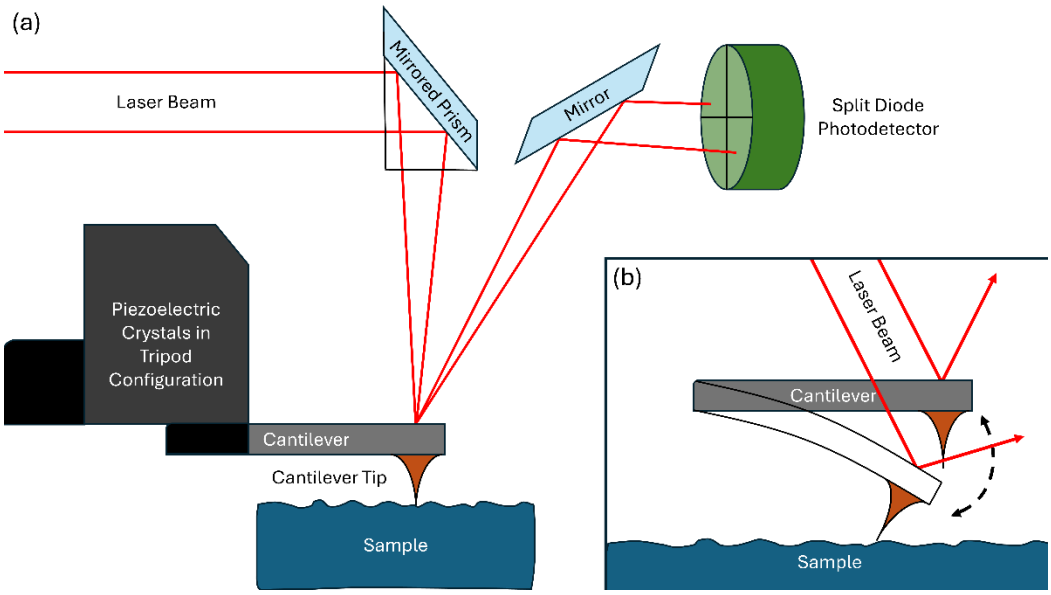

Figure 2.12: AFM set-up and operation. (a) Schematic diagram of a typical AFM instrument. (b) Illustration of cantilever movement determination by measuring beam deflection during tapping mode oscillations.

There are different modes of operation available with AFM, but this work only utilised a variation of tapping mode which is the only mode which will be discussed here [80]. This mode involves vibrating the cantilever close to its resonant frequency (which is typically tens to hundreds of kHz depending on the material) while bringing it close to the sample

such that it makes intermittent contact with the surface. As the tip approaches the surface, the interatomic forces between the tip and sample cause changes to the cantilever's oscillation and phase [81]. A feedback loop is employed to maintain a constant oscillation amplitude by adjusting the height of the tip above the sample surface. This change in height is detected by deflection of the cantilever which provides the imaging data.

In this work, a Bruker ICON AFM system was used to measure 3D surface topography using their proprietary variation of tapping mode called PeakForce Tapping ScanAsyst mode [82]. The same principles as tapping mode apply, but the cantilever is driven at frequencies significantly below resonance. AFM measurements were performed with a scan rate of 0.5 Hz and with 512 samples per line across areas of 1 μm^2.

2.2.6. X-Ray Diffraction

X-ray diffraction (XRD) is used to determine the crystalline structure of materials. By irradiating a sample with x-rays, two distinct processes occur. First is the absorption of x-rays, which can cause ejection of electrons if the incident energy exceeds that of the electron binding energy, which is the basic principle of XPS discussed in section 1.2. The second process is the incident x-rays can be scattered both elastically and inelastically. It is the elastic scattering of monochromatic x-rays that enable the probing of crystalline structures. Elastic scattering results in the scattered x-rays being partially coherent, and they can interfere with one another under certain conditions, with the condition for constructive interference described by the Bragg equation [83], [84]:

$$2d.sin\theta = n\lambda \qquad (Eqn. 2.4)$$

Where d is the interatomic distance of the material, θ is the incident angle and λ is the wavelength of the x-rays, and n is an integer representing the order of the reflection. The incident x-rays strike the crystal planes of the material and are elastically scattered at an angle θ, with each plane separated by a distance d. When the path length between x-rays scattered from each of the adjacent planes differs by an integer multiple of the incident x-ray wavelength, constructive interference occurs. By analysing these interference patterns, crystallographic information can be obtained.

The Bragg condition and typical experimental configuration are illustrated in Figure 2.13. Experientially in the so-called θ-2θ method, the beam source is fixed, and the sample is rotated by θ while the detector is rotated by 2θ which simultaneously measures the intensity of scattered x-rays, creating the interference pattern. In doing so, the angles incidence and reflection with respect to the surface normal remain equal during the entire

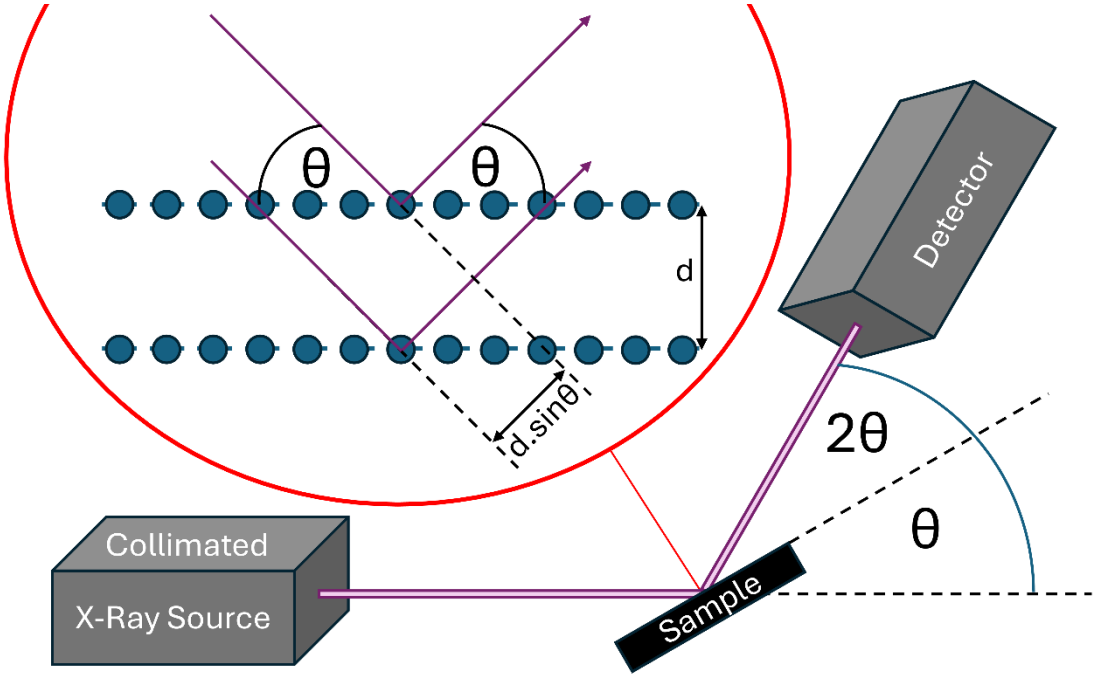

Figure 2.13: XRD setup and operation showing the θ-2θ geometric configuration for XRD measurements and the Bragg diffraction condition.

scan. The intensity peaks in this pattern are located at θ which satisfy the Bragg equation, which allows the interatomic spacing of each of the crystal planes, "d", to be calculated. This in turn enables XRD to achieve material and phase identification, which is one of the primary uses of XRD in this work. By comparing measurements to standardised databases and theoretical calculations, materials and their crystallographic structure can be identified.

The second used mode of operation in this work is the rocking curve, which is used to determine the degree of alignment or texture of nanostructures. This allows us to measure how well vertically aligned our ZnO nanorods are with respect to the substrate. This is done by keeping the position of the detector constant (on the 2θ angle at which the desired crystal plane was detected) and rotating the sample about the θ angle (sometimes called the ω angle), measuring the change in peak intensity for angles within ~ ±15 degrees of the detected peak in the interference pattern. A narrow rocking curve peak shows well aligned and ordered nanostructures, whereas a broad peak indicates more random orientations.

In this work, a Bruker AXS D8 Advance Texture Diffractometer was used to obtain XRD measurements.

2.2.7. Absorption Spectroscopy

2.2.7.1. UV-Vis

Ultraviolet-visible (UV-Vis) spectroscopy is a technique used to measure the concentration of a substance based on the absorption of ultraviolet and visible wavelengths of light, typically in the range of 200-800 nm. It involves the excitation of atomic energy levels of the sample atoms/molecules, which results in the absorption of that excitation wavelength and is used to detect the presence and quantity of the desired substance. Since the energy of atomic orbitals is quantised, when light of energy equal to the energy difference between these orbitals is incident on the atom, it is absorbed. This results in an electron from the lower energy orbital becoming excited to the higher energy orbital. The Lambert-Beer law describes this absorption [85]:

$$A = \varepsilon cl = l\,n\left(\frac{I_0}{I_T}\right) \qquad (Eqn.\,2.5)$$

Where A is the absorbance [%], ε is the molar absorptivity coefficient of the sample [moles.cm^{-1}], c is the molar concentration of the sample [moles], l is the optical path length [cm], I_0 is the light intensity detected through the reference cell, and I_T is the transmitted light intensity measured through the sample.

A spectrophotometer consists of a light source, a monochromator (prism or grating), a beam splitter, a sample cell, and a detector. This is a facile technique, simply measuring the reduced intensity of incoming light as it passes through a sample cuvette, and this can be related back to sample concentration by Eqn. 3 since the path length is known. The spectrophotometers can be used to scan a sample for a specific absorption wavelength, or the grating can be rotated continuously, so the full 600 nm range of wavelengths is scanned across the sample A schematic diagram of the setup is shown in Figure 2.14.

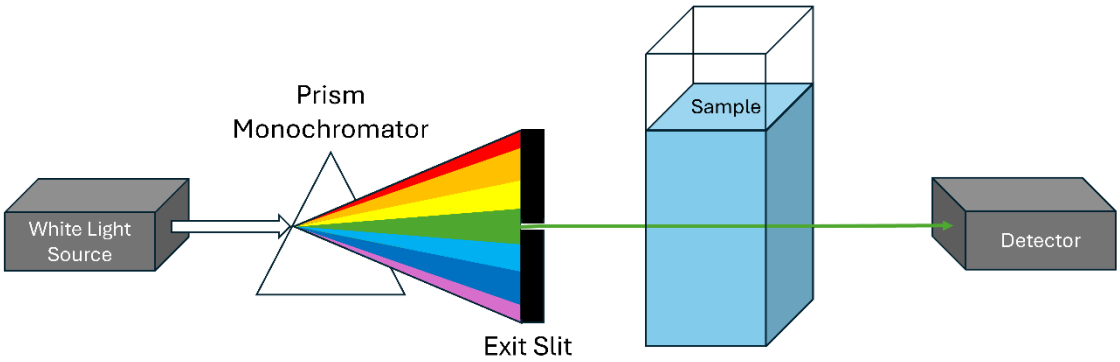

Figure 2.14: UV-Vis spectroscopy setup showing the white light source and monochromatic wavelength selection via a dispersive element, in this case a prism.

This technique is ubiquitous for DNA and RNA detection, as Nucleic Acids (Nas) have an absorbance maximum at 260 nm [86]. The technique is also used to determine the purity of a sample, using a ratio of the absorbance of 260 nm to 280 nm. The five nucleotides of DNA and RNA exhibit widely different 260/280 spectral intensity ratios. Therefore, the weighted average of each 260/280 nucleotide ratio is taken to get the overall ratio for either DNA or RNA as one of their nucleotide bases varies (DNA contains Thymine and RNA contains Uracil). The commonly used rule of thumb is that pure DNA has a ratio of 1.8, and pure RNA has a ratio of 2.0. Various factors can affect this ratio, such as the acidity of the solution, wavelength accuracy of the instrument, contamination of the sample and low concentrations of DNA. On the other hand, absorbance at 230 nm is generally due to some sort of contamination within the sample, so the 260/230 ratio can also provide more information. The strong absorbance of DNA in this ultraviolet region is due to the π → π* transitions of the pyrimidine and purine ring systems of the nucleobases. UV-Vis spectroscopy is a calibrated tool used for the determination of DNA concentrations by the following equation:

$$C_{sample} = A_{260}\ x\ 50 \frac{\mu g}{mL} \qquad (Eqn. 2.6)$$

Where C_{sample} is the concentration of sample DNA [µg/mL] and A_{260} is the absorption at 260 nm [0 - 1 a.u.]. This work utilised a Biochrom Libra S22 UV/Vis Spectrophotometer and quartz cuvettes with a 1 cm pathlength.

2.2.7.2. FTIR

Fourier Transform Infrared (FTIR) spectroscopy operates on similar principles as UV-Vis spectroscopy, but infrared radiation is used to study molecular vibrations. Rather than probing electronic transitions, IR absorption probes the vibrational energies of molecules and is influenced by the structural characteristics of molecules such as the strength of interatomic bonds and the environment around the molecule. These vibrations are associated with a change in the dipole moment of the molecule and are classified into either bending or stretching vibrations. Stretching represents the continuous change of distance between two bonded atoms, and bending represents a change in angle between the bonds in the molecule. Stretching vibrations can be further categorised into symmetric (in-phase) stretching or asymmetric (out-of-phase) stretching [87], [88].

The experimental setup differs quite significantly to that of UV-Vis spectroscopy, using an interferometer to modulate the intensity of the IR source which is passed through the sample. The typical experimental setup for FTIR can be seen in Figure 2.15, with the most

common optics configuration being the Michelson interferometer. The Fourier transform operation is applied to the resultant transmitted intensity variations with moving mirror path length in the interferometer and an absorption vs wavelength spectrum is generated by taking the ratio of a blank (reference) spectrum to a sample spectrum.

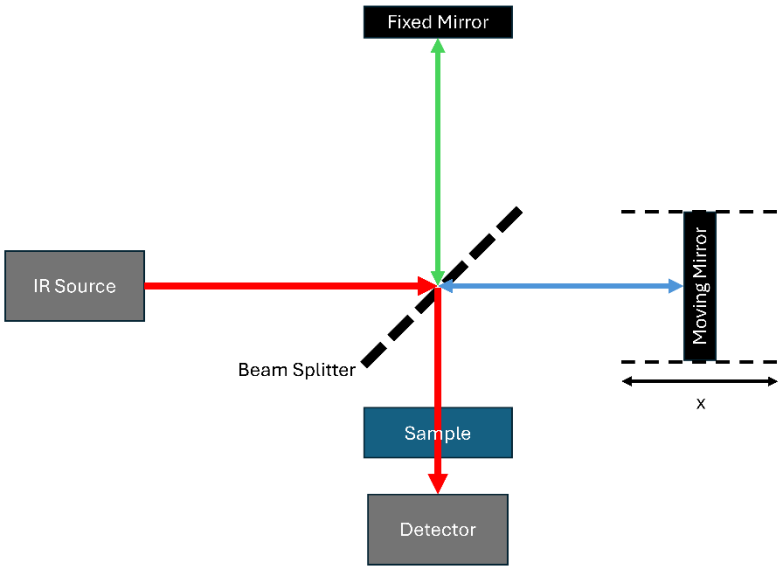

Figure 2.15: Schematic diagram of a typical interferometer arrangement for FTIR spectroscopy.

However, due to the nanoscale dimensions of the features studied in this work, standard "single pass" transmission FTIR was often not used, as the resultant absorption of such thin samples is too weak to be detected. To overcome this issue, attenuated total reflection FTIR (ATR-FTIR) was used. This technique passes light through the sample multiple times, increasing the amount of interaction between light and sample [89]. The multiple passes are achieved by exploiting total internal reflection. Total internal reflection occurs when light propagates from a more optically dense medium (higher refractive index) to an optically rare medium (lower refractive index) at an incidence angle greater than the critical angle. At the interface between both media where reflection occurs, a portion of the electromagnetic field penetrates the lower refractive index media caused by the constructive interference of the incoming and outcoming beams. This portion of the field extends only a short distance beyond the interface and decays exponentially with distance from the interface, and this decaying field is known as an evanescent wave. The depth of penetration of this evanescent wave is on the order of 10s of nanometres, allowing probing of ultrathin structures. The beam is internally reflected multiple times across the sample before reaching the detector, with the evanescent wave undergoing small amounts of absorption each time, ultimately leading to a detectable attenuation of the totally reflected

beam and allowing for the determination of absorbed wavelengths and identification of chemical bonding. This process is illustrated in Figure 2.16.

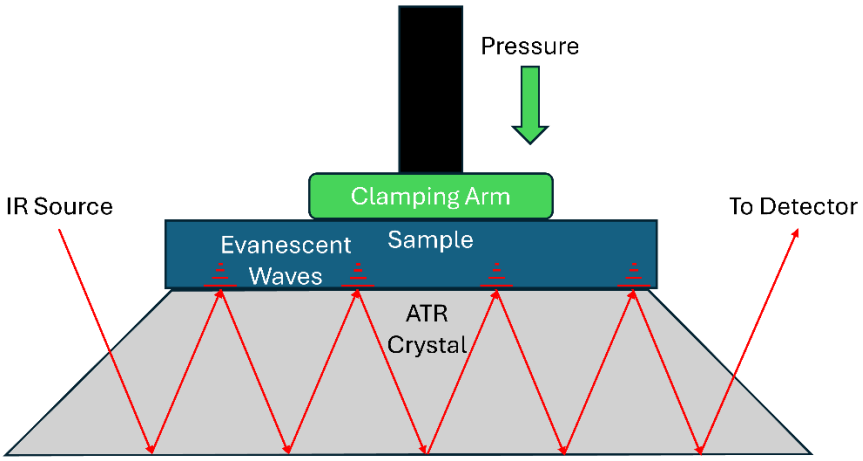

Figure 2.16: Illustration of total internal reflection of IR radiation within a crystal of high refractive index in contact with a sample containing a thin film of rarer refractive index. Pressure is applied via a clamping arm to ensure contact of sample with the ATR crystal.

This work utilised a Perkin Elmer Two FT-IR system in both transmission and ATR mode.

2.2.8. Dielectric Characterisation

This work reports the development a novel SiO_2 deposition system, capable of producing 2D thin films. The dielectric breakdown strength of these novel SiO_2 films were analysed and compared to industrial thermal oxides of the same thickness to determine the electrical quality of PDMS-based SiO_2. All electrical measurements were made on devices that resemble a metal oxide semiconductor capacitor. The SiO_2 films serves as the dielectric medium, with the silicon substrate serving as one conducting plate, and a

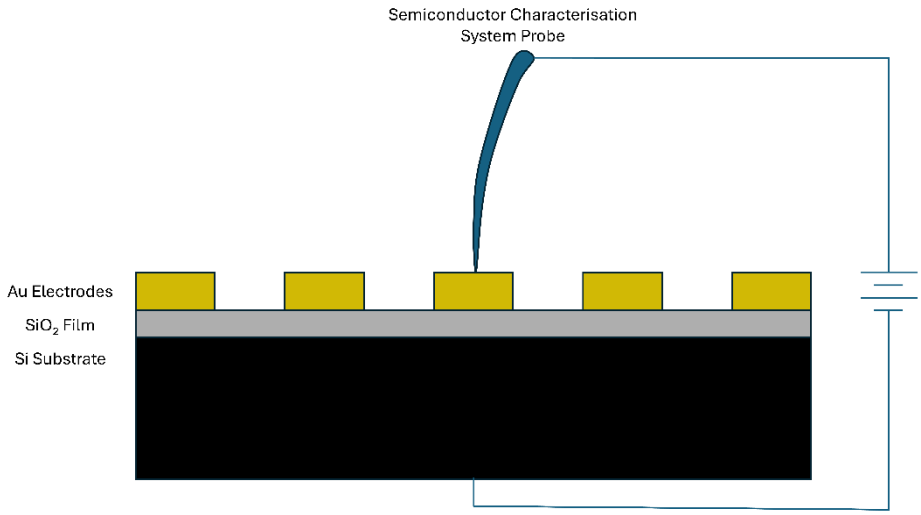

Figure 2.17: Illustration of metal oxide semiconductor capacitors developed and tested in this work to determine the dielectric breakdown characteristics of SiO_2 thin films.

deposited Au film serving as the other conducting plate. An illustration of this structure is shown in Figure 2.17.

Electrical breakdown characterisation was performed by an in-house system based on a Keithley 4200 semiconductor characterisation system.

2.2.8.1. Current – Voltage Sweeps

Current – Voltage (I – V) sweeps are used to characterise the electrical properties of dielectric films by applying varying voltage across the dielectric material and measuring the resulting current. Eventually, as the applied voltage increases, the insulating properties of the dielectric film will breakdown at a certain value (V_b). At and above this breakdown voltage, the dielectric film is no longer an insulator, allowing the flow of current through it. The dielectric remains permanently damaged as a result. Before breakdown, there is negligible current flow, and at and beyond the breakdown voltage, current readily flows through the dielectric. The voltage at which breakdown occurs at for each capacitor is recorded and analysed by Weibull statistics to determine the dielectric strength and failure characteristics of the film. If the thickness of the oxide is known, the breakdown voltage V_b [V] can be converted to its breakdown field E_b [V/nm], which is used for this work as oxides of known thicknesses are compared.

2.2.8.2. Weibull Statistics

Measuring I-V curves on multiple capacitors on single samples and identical samples will result in a range of breakdown voltages being recorded. To quantify this spread of results, the Weibull distribution is commonly employed, especially in the electrical characterisation of dielectrics[90], [91]. For current – voltage sweeping, the Weibull distribution is described by the following equation:

$$F = 1 - e^{\left(\frac{E_b}{\eta}\right)^{\beta}} \qquad (Eqn.\,2.7)$$

Where F represents the cumulative probability of failure (i.e. the fraction of failed devices), β is the shape parameter or Weibull slope, E_b is the measured electric field strength at which breakdown occurred, and η is the scale parameter (i.e. the electric field value at which 63% of the sample capacitors have undergone dielectric breakdown).

To determine the two fit parameters (β and η), one can rearrange equation (2.7) to give 1 – *F* on the left hand side, and then take the natural log of both sides of equation 2.8, which gives:

$$\ln\left[-\ln\left(1-F(E_b)\right)\right] = \beta \ln(E_b) - \beta \ln(\eta) \qquad (Eqn.\,2.8)$$

A plot of ln[-ln(1-F(E_b))] versus ln(E_b) provides a straight-line graph where β is the slope, and the y-intercept represents – β.ln(η). A low β value indicates a poorer quality film with a wide range of E_b values, and a high β indicates a more reliable device with a narrower range of expected breakdown values [92]. The parameter η is the scale parameter or 63 % value, i.e. the breakdown field (Eb) when ~ 63 % of the sample set have undergone dielectric breakdown. This is a measure of the breakdown field for the sample. The cumulative distribution function F(E_b) is estimated by first sorting the measured breakdowns from smallest to largest, followed by the application of a ranking algorithm. In this work, a median ranking was employed, through the use of the Benard approximation:

$$F(i) = \frac{i - 0.3}{n + 0.4} \qquad (Eqn.\,2.9)$$

Where F(i) is the failed device number and n is the total number of tested devices [93].

2.2.9. Contact Angle

Contact angle measurements are used to assess the wettability of a solid surface by a liquid, typically DI-H_2O. The contact angle is the angle formed at the interface between a solid surface, a liquid droplet, and the surrounding gas or vapour phase, and is measured at the point where the liquid meets the solid surface. The angle is formed by the tangent to the liquid surface at the three-phase (solid, liquid, vapour) boundary (see Figure 2.18) and indicates the degree of wettability.

The wettability of a material is dependent on the surface tension between the solid substrate, liquid, and vapour, and the interatomic forces between the liquid and solid surface [94]. A low contact angle, close to 0° indicates high wettability (hydrophilicity), meaning the liquid spreads easily over the surface. A high contact angle, greater than 90°, indicates low wettability or hydrophobicity, where the liquid tends to form a well-defined droplet on the surface. For a material to be highly wetting, the substrate surface energy must exceed that of the cohesive forces within the liquid, causing the liquid to spread across the substrate surface. For non-wetting surfaces, the cohesive forces within the liquid are much greater than the surface energy of surface, and the liquid forms a well-defined droplet instead of spreading across the surface.

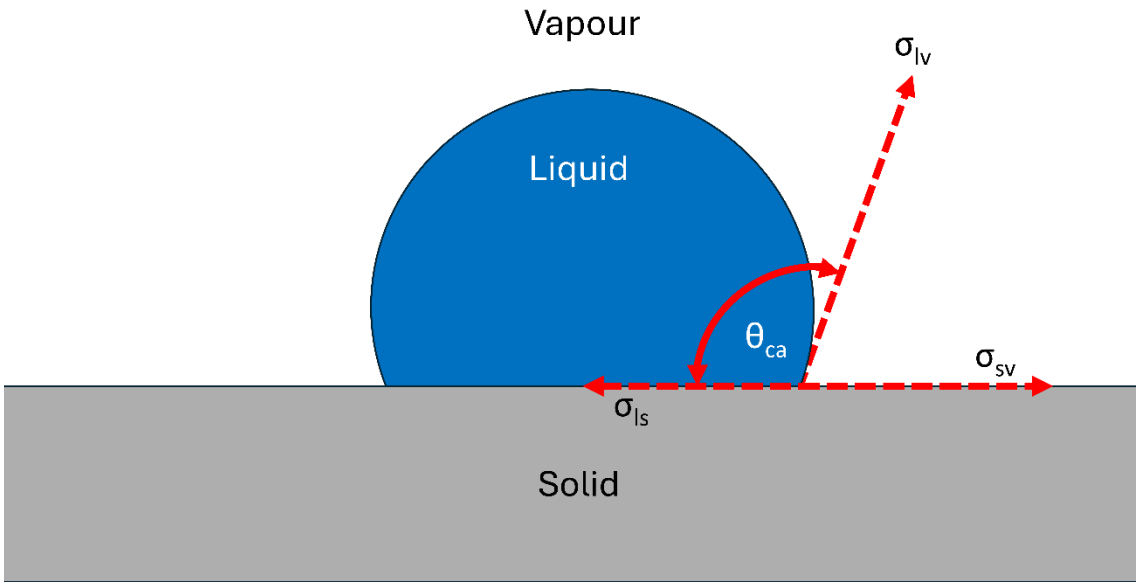

Figure 2.18: Illustration of the quantities involved in the calculation of contact angle.

Contact angle measurements can be used to calculate the surface energy of a solid surface using known surface tensions and the Young-Laplace equation:

$$cos\theta_{ca} = \frac{\sigma_{sv} - \sigma_{sl}}{\sigma_{lv}} \qquad (Eqn. 2.10)$$

Where θ_{ca} is the contact angle, and σ_{sv}, σ_{sl}, and σ_{lv}, are the surface tension between the solid and vapour, solid and liquid, and liquid and vapour, respectively. In biomedical applications, contact angle measurements help assess the biocompatibility of materials. For example, surfaces with specific contact angles may promote or inhibit the adhesion of cells or biomolecules, influencing the performance of medical devices or implants [95].

This work utilised a Dataphysics OCA 35 contact angle instrument to provide contact angle measurements.

2.2.10. Dynamic Light Scattering

Dynamic light scattering (DLS) measures time-dependent fluctuations in the scattering intensity that arise from particles undergoing random Brownian motion, i.e. smaller particles move faster, and larger particles move slower [96]. Particle size information can be extracted from analysing these fluctuations. These time-dependent fluctuations in the intensity of scattered light are analysed using vendor-specific curve-fit algorithms to estimate a size distribution. The speed of the Brownian motion is measured, which provides the translational diffusion coefficient 'D.'

This diffusion coefficient is related to the hydrodynamic diameter by the following Stokes-Einstein equation:

$$D_H = \frac{kT}{3\pi\eta D} \qquad (Eqn.\ 2.11)$$

Where D_H is the hydrodynamic diameter [m], k is the Boltzmann constant [J.K^{-1}], T is the temperature [K], η is the dynamic viscosity [Pa.s], and D is the diffusion coefficient [m^2.s^{-1}].

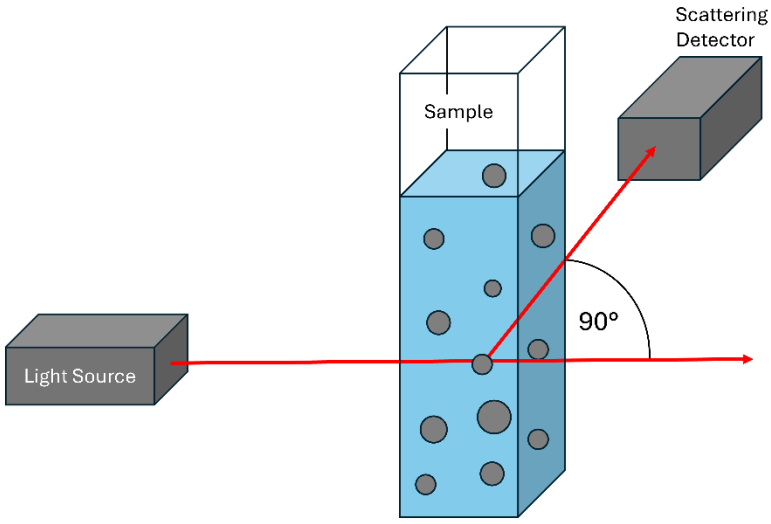

Figure 2.19: Schematic diagram of a typical DLS system. The scattering detector, positioned at an angle of 90° detects time dependent fluctuations in the intensity of light scattered from small particles within a solution.

The basic setup is shown in Figure 2.19. A monochromatic laser is directed at the sample in a cuvette. If there are particles in the sample, this incident laser light gets scattered in all directions due to the random motion of the particles. The scattered light is detected at a specific angle over time, and the signal is then analysed with an autocorrelation function to determine the size distribution. The autocorrelation function correlates the intensity of the scattered light at one point in time with its intensity at another point in time. These intensity fluctuations decay over time, and the rate of this decay is related to the motion of the particles, i.e. the faster the particles are moving, the quicker the decay. This decay time is therefore related to the diffusion coefficient. For size analysis, this angle of scattered light detection is usually 90 degrees (side-scattering), or 175 degrees (back-scattering) for smaller particles at low concentrations [97].

This work utilised a NANO-flex® 180° DLS Size from Microtrac Ltd.

2.2.11. Zeta Potential

The zeta potential is a property that arises from colloidal particles in a solvent, and that magnitude of this property is an indicator of the potential stability of the colloid. If a charged

particle with a given surface potential is dispersed in a liquid, counter ions will be strongly bound to the particle surface. These counter ions form the Stern layer or potential, with the opposite charge to the surface layer. This Stern layer is strongly bound, but additional ions are attracted the particle outside of the Stern layer, although these are less firmly associated, forming the diffuse layer or the slipping plane. These layers can be seen in Figure 2.20 and are known together as the electric double layer [98].

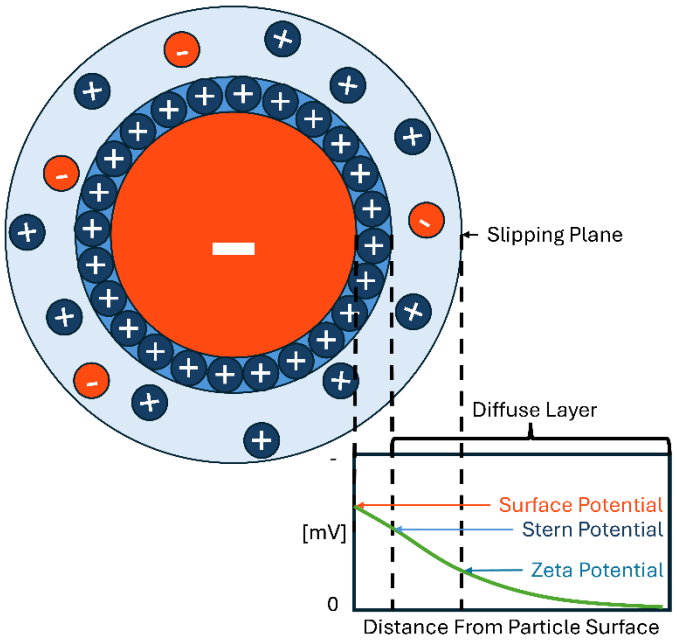

Figure 2.20: Various electrostatic layers of a colloidal particle with a negative surface charge in suspension.

Although these outer ions are less firmly associated, these ions will move with the general motion particle with which they are loosely bound to. The zeta potential is a measure of the potential at this slipping plane boundary and is therefore dependant not only on the colloidal surface material, but the surrounding solvent as well. Large zeta potentials indicate strong electrostatic repulsion between particles, and therefore higher stability. The lower the repulsive electrostatic force, the easier it is for particles to aggregate. In literature, particles with zeta potentials outside of the range of – 30 mV to +30 mV are considered stable [99], [100]. Zeta potential of colloidal particles is measured by placing them under an external electric field. For example, negatively charged particles will move towards the positively charged electrode and vice versa. The tightly bound counterions of the Stern layer will move with the particle under the strong electric field, however those ions in the diffuse layer will "slip" off when a certain potential is reached as the drag force will exceed their relatively weak electrostatic attractive force compared to those of the Stern layer. To determine the zeta potential, particles are accelerated at different electrode potentials,

and a laser beam is incident on the sample cuvette which indirectly measures the particle speed by measuring the Doppler frequency shift in scattered light from the moving particles. This particle velocity determined from frequency shift is converted into a value for electrophoretic mobility using equation 2.12:

$$\mu_e = \frac{v}{E} \qquad (Eqn.\ 2.12)$$

Where μ_e is the electrophoretic mobility [$m^2.V^{-1}.s^{-1}$], v is particle velocity [$m.s^{-1}$], and E is the electric field magnitude [$V.m^{-1}$]. Electrophoretic mobility is then used to calculate zeta potential using equation 2.13:

$$\zeta = \frac{\epsilon_r \epsilon_0}{\mu_e \eta} \qquad (Eqn.\ 2.13)$$

Where ζ is the zeta potential [V], ε_r is the relative permittivity of the liquid medium [$F.m^{-1}$], ε_0 is the electric permittivity of vacuum [$F.m^{-1}$], and η is the viscosity of the liquid medium [Pa.s]. Zeta potential can be measured using the same system used for DLS measurements described previously, albeit requiring a capillary cuvette with electrodes on either side. A voltage is applied across the capillary, and a laser is incident on the particles. The scattering pattern is related back to particle velocity as previously described. Zeta potential measurements were only performed on ligand free SiNPs in DI water, as the presence of ligands significantly reduces the reliability of zeta potential measurements as indicators of particle charge and stability [64]. The ligands induce a drag force, slowing down the particles which now invalidates the relationship between electrophoretic mobility and zeta potential. Additionally, ligands have steric stabilization effects, and zeta potentials only consider electrostatic effects. Surface ligands can provide low zeta potential particles with high stability, which is the typical case for polymer-stabilised particles which display ~ 0 mV zeta potentials yet display high stability.

This work utilised a Malvern Zetasizer Ultra.

2.3. DNA Analysis

2.3.1. Fluorescence Spectroscopy

Fluorescence spectroscopy involves the use of fluorophores, which are molecules that emit light upon excitation, to tag biomolecules. Fluorophores have three general types: organic dyes, naturally fluorescent biological molecules, or quantum dots. Specially

selected fluorophores are mixed with the sample so that they only bind to the specific target analyte, which is known as fluorescent labelling. A light source is used to excite the fluorophore by stimulated absorption, and its electrons are stimulated to a particular excited state. After absorption, the molecule enters an excited state with higher energy. However, the excited state is not stable, and the molecule undergoes rapid vibrational relaxation. During vibrational relaxation, the excess energy is rapidly dissipated as heat through collisions with neighbouring molecules. Then it relaxes back down to the ground state *via* radiative recombination, emitting a photon of light with energy slightly lower than the excitation energy and this process is illustration in Figure 2.21 [101].

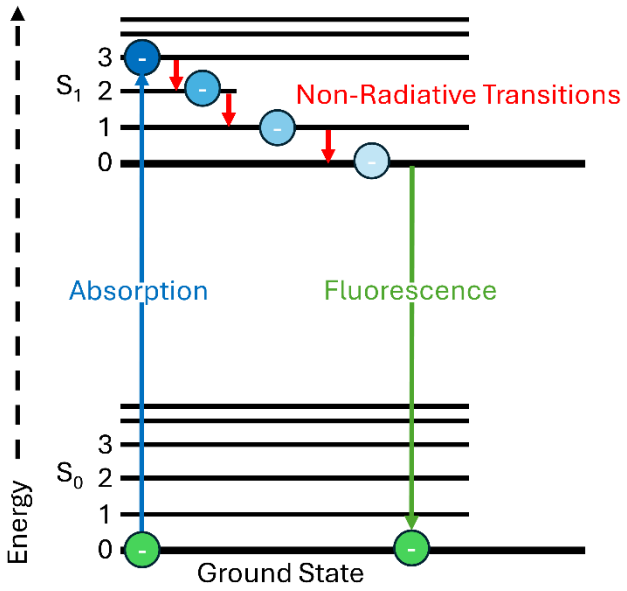

Figure 2.21: Photon absorption from an electron in a ground state (S_0) to an excited state (S_1), followed by vibrational relaxation, and then photon emission by radiative relaxation leading to fluorescence.

This difference in energy is known as the Stokes shift. The larger the Stokes shift, the more spectrally distinguishable the excitation signal is which reduces background noise due to less spectral overlap between excitation and emission wavelength signals. These emitted photons are measured with a detector and are used to determine the presence of the analyte. The intensity of the total emitted light is a measure of the concentration of the analyte. Typically, known concentrations of the target analyte are measured simultaneously to produce a standard curve of intensity vs known concentration, and the intensity of the unknown sample concentration is compared to the standard curve to calculate the sample concentration.

The fluorophores used in this work were cyanine dyes, a class of organic dyes that selectively bind only to double stranded DNA (dsDNA). Cyanine dyes contain a central

chromophore structure consisting of a chain of carbon atoms with alternating single and double bonds, often with heterocyclic rings at each end. This conjugated system is responsible for the absorption and emission of light, giving cyanine dyes their fluorescent properties. A PicoGreen dye consists of a cyanine dye molecule that is attached to a quaternary ammonium group which intercalates between the base pairs of the DNA double helix. The intercalation affects the probability of certain energy transitions occurring, giving rise to fluorescence emission over other energy loss pathways [102].

The operating principle of this technique involves using a light source that emits light of a specific excitation wavelength, which causes excitation of the fluorophore. The excitation light is passed through the sample cuvette, which causes the emission of photons. The photons are passed through an optical filter, which only allows wavelengths equal to the known fluorophore emission wavelength through, which are then incident on a detector. In this work a Tecan Safire 2 spectrofluorometer and a Tecan Infinite Pro 200 M Plex spectrofluorometer were used with Quant-iT Picogreen dsDNA assay fluorophores to quantify DNA concentrations ≤ 2 µg/mL, with a limit of detection of ~ 25 pg/mL. The excitation (λ_{ex}) and emission (λ_{em}) wavelengths were 480 nm and 520 nm respectively.

2.3.2. Piezoelectric Effect for Small Mass Detection

Quartz crystal microbalances (QCMs)se were used in this work for the label-free detection of DNA. Quartz is a piezoelectric material, meaning mechanical deformation of the quartz along certain crystallographic orientations produces a voltage across it, generating electricity. This is a reversible process and conversely, applying a voltage across a piezoelectric material causes physical deformation of that material [103]. Quartz is piezoelectric in many orientations, especially along its c-axis, but the AT-cut of α-quartz is the most commonly used in sensing applications. In an AT-cut quartz crystal, the crystallographic orientation is such that the angle between the c-axis and surface normal is ~ 35.25°. After cutting, a pair of Au electrodes are directly evaporated on the top and bottom faces of the quartz disc. The measurement principle of QCMs is based on the application of an alternating voltage across the quartz crystal leading to an oscillatory deformation, producing acoustic waves within the quartz [104]. At certain frequencies, the mechanical vibrations of the quartz become amplified, and these are the resonance frequencies of the quartz which are dependent on the thickness, physical dimensions, and mechanical properties of the quartz crystal. The AT-cut gives rise to a pure thickness shear mode oscillation, reducing lateral motion of the crystal and focusing the mechanical deformation primarily in the thickness direction, allowing for more direct coupling between

resonance frequency and mass deposition, allowing quartz crystals to be used as accurate mass transducers.

In 1959, Gunter Sauerbrey discovered that upon adding mass to the surface of a QCM, the resonance frequency decreases proportional to the amount of mass added so long as the mass is small compared to the total weight of the crystal (< 2%). An illustration of this frequency response upon mass loading is shown in Figure 2.22.

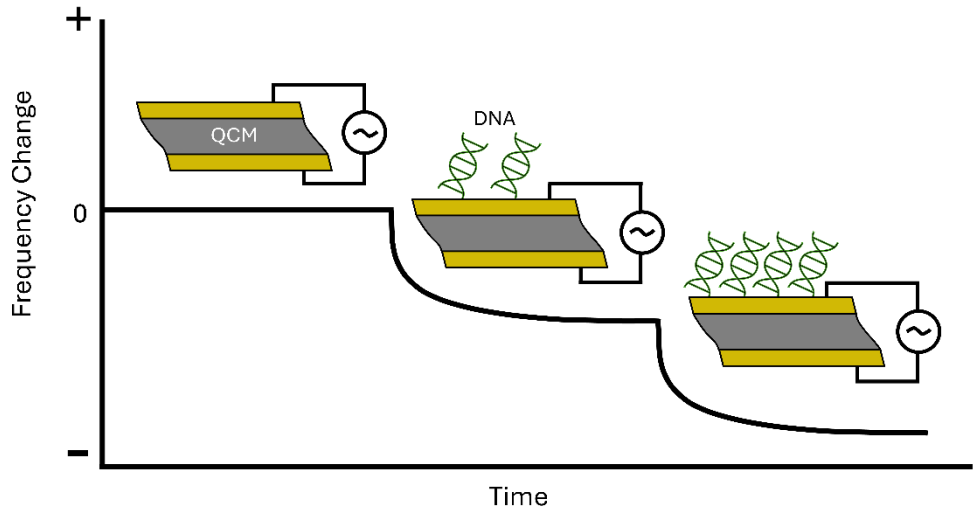

Figure 2.22: Frequency response with increasing mass loading on QCM illustration.

The exact relationship between changes in resonance frequency and deposited mass are defined by the Sauerbrey equation [105]:

$$\frac{\Delta f}{n} = -\frac{2.f_0^2}{A.\sqrt{\rho_q.\mu_q}}\Delta m \qquad (Eqn.2.14)$$

Where Δf is the frequency shift [Hz], n is the overtone number (1, 3, 5, 7, etc.), f_0 is the resonance frequency of the fundamental mode [Hz], A is the piezoelectrically active area of the electrodes [cm^2], ρ_q is the density of quartz [2.648 $g.cm^{-3}$], and μ_q is the shear modulus of AT-cut quartz [2.947 x 10^{11} $g.cm^{-1}.s^{-2}$]. As most of these values are material dependant constants, the equation is commonly rewritten in the form:

$$\Delta m = -C.\frac{\Delta f}{n} \qquad (Eqn.2.15)$$

Where C is the thickness dependant mass sensitivity constant [4.42 $ng.Hz^{-1}.cm^{-2}$ for 10 MHz quartz]. This equation is valid under three conditions: (1) the added mass is small compared to the mass of the crystal itself, (2) the added mass is rigidly adsorbed, and (3) the mass is evenly distributed over the active area of the crystal. The second condition is particularly important for liquid biosensing, as many polymers and lipids result in

viscoelastic films, violating the Sauerbrey condition of requiring rigidly bound material. These viscoelastic films cause dissipation of oscillation energy due to mechanical losses in the flexible mass, often resulting in underestimation of the amount of absorbed mass. Therefore, it is important to take dissipation into account during liquid biosensing to determine the validity of the Sauerbrey equation [106].

The dissipation can be measured using a ring-down approach [107]. The quartz is excited to its resonance frequency for a short period by an applied voltage, which is then turned off, and the number of oscillations and time taken to reach 50% of the original amplitude is counted, i.e. the decay time constant. The decay time depends on the rigidity or softness of the absorbed mass. Rigid materials couple strongly to the oscillating quartz, and the oscillation takes longer to decay. However, viscoelastic materials have a poor coupling with the quartz, significantly damping the oscillation and causing a rapid decay. This is illustrated in Figure 2.23.

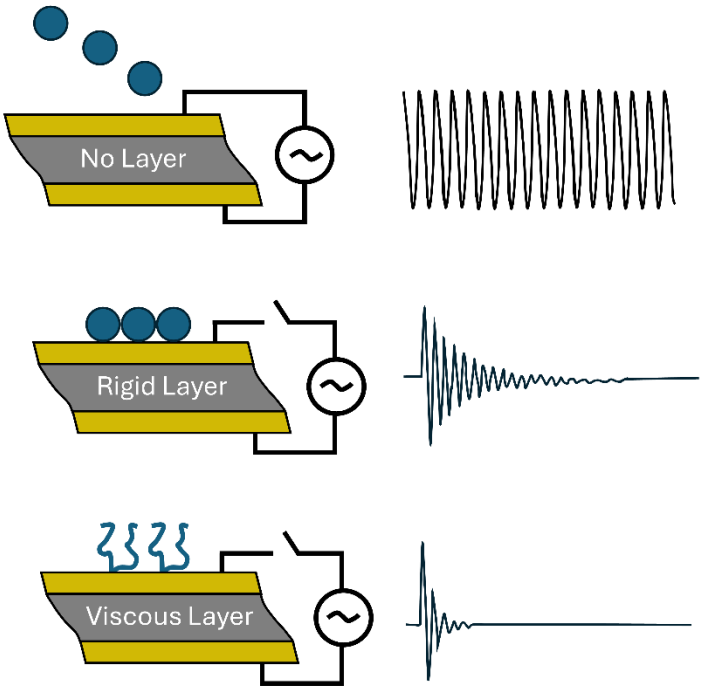

Figure 2.23: Dissipation measurement of an unloaded QCM, a rigidly bound material, and a viscoelastic material bound to the QCM surface.

However, the frequency response of a QCM is not only sensitive to changes in the surface mass loading but also the viscoelastic properties of the medium in contact with the QCM surface [108]. When a viscoelastic layer or viscous layer is in contact with the QCM, the frequency response can also decrease due to viscous drag from the liquid, described by the Kanazawa-Gordon equation:

$$\Delta f = -f_0^{\frac{3}{2}} \sqrt{\frac{\eta_L \rho_L}{\pi \rho_q \mu_q}} \qquad (Eqn. 2.16)$$

Where Δf is the frequency shift [Hz], n is the overtone number (1, 3, 5, 7, etc.), f_0 is the resonance frequency of the fundamental mode [Hz], η_L is the absolute viscosity of the liquid [$g.cm^{-1}.s^{-2}$], ρ_L is the density of the liquid [$g.cm^{-3}$], ρ_q is the density of quartz [2.648 $g.cm^{-3}$], and μ_q is the shear modulus of AT-cut quartz [2.947x10 11 $g.cm^{-1}.s^{-2}$].

QCMs have been successfully employed in a variety of biosensing applications, and have shown to be promising tools for the rapid detection of infectious diseases [109]. QCMs have been used to detect antibody-antigen interactions, as well nucleic acid hybdridization for the detection of disease [110], [111]. However, regarding NA detection, NAs are often amplified *via* PCR to obtain a sufficient concentration of analyte that can be detected by the QCM-based sensor [109]. The reliance on laboratory procedures prevents their applicability for on-site point-of-care applications. Additionally, the NAs are often bound with heavy molecules, such as Au NPs to produce a measurable frequency response, which is similar to requiring fluorescent or colorimetric labels, further increasing the complexity of the device [111]. This work aims to enhance the frequency response of QCMs for biosensing without the need for NA mass enhancement *via* amplification or binding to heavier molecules.

This work utilised the Novaetech S.r.l. openQCM Q-1 sensing module capable of simultaneous frequency and dissipation monitoring for DNA binding studies.

The changes in frequency and dissipation can be monitored simultaneously in real time by the careful design of the associated QCM electronics. The changes in resonance frequency are monitored by measuring the phase difference between the driving signal and the QCM's oscillation. At exact resonance, the QCM oscillations will be in phase with the driving signal, but changes in resonance frequency due to mass loading will induce a phase shift between them. When a phase shift is measured, the driving signal frequency is adjusted to re-align the phases, keeping the QCM at resonance. The dissipation is then measured by momentarily turning off the driving voltage to allow the QCM to oscillate without external excitation. This oscillation decay can be measured on very short timescales (μs to ms), meaning the oscillation doesn't come to a complete stop and enabling the system to quickly resume resonance. This allows the QCM system to rapidly switch between measuring frequency and dissipation without disrupting the oscillation.

3. Novel PDMS-Based SiO_2 Deposition

In this chapter SiO_2 thin films and nanostructures (NSs) grown by thermal degradation of polydimethylsiloxane (PDMS) in air are examined. First, a description of the thermal degradation of PDMS and subsequent generation of SiO_2 vapour is described. This is followed by the initial exploitation of this degradation to produce SiO_2 coatings from mm to nm dimensions before a thorough investigation into the optimisation of this process to produce nanoscale and nanostructured SiO_2 coatings in the second half of the chapter. Three primary variables were investigated, i.e. the amount of PDMS source mass used, the steady-state deposition temperature, and the heating rate up to the steady-state deposition temperature. The coatings were deposited on planar and nanostructured substrates, and the deposited morphologies were studied. The physicochemical and dielectric breakdown properties of the PDMS-based coatings were measured to ensure that the deposited material was indeed SiO_2.

3.1. Degradation Mechanism of PDMS

This work was possible due to the foundations laid by Camino *et al*. who studied the thermal degradation mechanisms of PDMS in nitrogen and air environments [112], [113]. Their ultimate goal was to understand the nature of the solid residue formed during PDMS thermal degradation which seemed to be dependent on the rate at which PDMS is heated. The molecular structure of PDMS is shown below, consisting of alternating Si and O atoms, with Si bonded to two methyl groups. It is well known that the thermal degradation of PDMS results in depolymerization over the range of 400 - 650 °C to produce cyclic oligomers, although this was studied in inert atmospheres and under vacuum [114], [115]. The thermally weakest bond in PDMS is the C-Si bond of 78 $kcal.mol^{-1}$, however kinetic simulations from Camino *et al*. found that in order to generate these cyclic oligomers, it is the Si-O bond of 108 $kcal.mol^{-1}$ that must break instead [116]. This suggests that the molecular structure and chemical kinetics of PDMS are the main factors governing depolymerization rather than solely the bond energies.

As PDMS is heated, Si-O bond scission leads to siloxane bond rearrangement, generating volatile cyclic oligomers. This rearrangement eliminates the cyclic dimethyl siloxane, resulting in a shortening of the residual chain length. This bond splitting repeats until the residual structure is too short to further cyclise. In the presence of air, the volatile oligomers

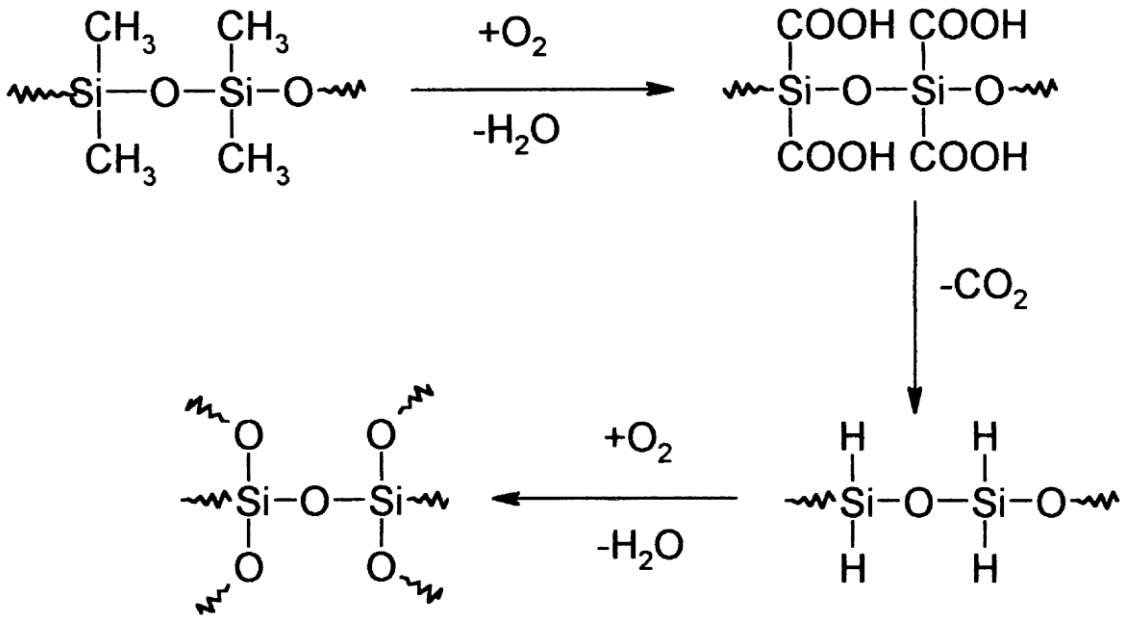

Figure 3.1: Proposed reaction of PDMS with O_2 to produce SiO_2. [112]

oxidise, leading to a gaseous silica species which will deposit on solid surfaces [112]. The chemical reaction is illustrated in Figure 3.1.

Two groups have used this to create nanostructures by coating the inner walls of a hollow alumina template [117], [118]. Our goal was to exploit this process to instead coat the outer surface of our solid ZnO NRs as a means of creating facile, low-cost SiO_2 NSs. In doing so, this approach could open a pathway to a cost-effective and accessible method for SiO_2 deposition performed entirely in ambient air at relatively low temperatures.

3.2. Materials & Methods

3.2.1. Synthesis of PDMS

PDMS was synthesised using the Sylgard 184 silicone elastomer kit from Dow Corning Corporation. The PDMS base and curing agent were mixed well in a 10:1 ratio by weight (40:4 g), respectively, and this mixture was poured into a clean petri dish. The petri dish was placed inside a desiccator and a vacuum was applied until all air bubbles were removed. The degassed PDMS mixture was allowed to cure at room temperature for at least 48 hours.

3.2.2. SiO_2 Deposition

The SiO_2 deposition was carried out in a Nabertherm Muffle Furnace LT 3/11/B410. The furnace allows careful control of temperatures from ambient to 1100 °C and heating rates from 1-9999 °C/hour, although with the temperatures used in this work (450 - 650 °C) the

heating rates would not exceed 2400 °C/hour (i.e. 40 °C/min) before reaching the set deposition temperature even if heating rates up to 9999 °C/hour were set.

The depositions were performed on cleaned Si substrates. Si wafers were cleaved into individual samples, typically with lengths and widths between 1.5 – 2.5 cm, and 0.5 – 2.0 cm, respectively. Once cleaved to the desired size, the substrates were blown under a nitrogen stream to remove any silicon fragments remaining on the sample after cleaving. Immediately before deposition, these substrates were cleaned by sonication in acetone for ten minutes, followed by rinsing fresh acetone, then sonication in absolute ethanol for ten minutes, followed by rinsing in absolute ethanol, and lastly, drying under a nitrogen stream.

ZnO films and NRs were synthesised on the same cleaned Si substrates described above using CBD and CTRVPT methods detailed in section 2.1.1.

3.2.3. Deposition Characterisation

The SiO_2 depositions were analysed using a wide variety of techniques for complete characterisation.

Film thicknesses were measured using contact profilometry (CP), electron microscopy (SEM, FESEM, STEM, and EDX), spectroscopy ellipsometry and x-ray photoelectron spectroscopy (XPS). CP was used to measure films greater than 20 nm in thickness, with ellipsometry and XPS used to study films from 0 – 20 nm and 0 – 10 nm respectively. EM and EDX data were used in conjunction with these techniques to verify film thickness measurements, and to image the various nanostructure morphologies.

Deposited film roughness was measured using CP and AFM. CP was used to measure roughness across much larger 2D line scan lengths (0.5 – 20 mm), with AFM providing much higher lateral resolution with shorter scan areas (~ 1 μm^2). The difference in lateral resolution is provided by the difference in probe diameter (CP ~ 2.5 µm, AFM ~ 10 nm).

Physicochemical properties were analysed using XPS, grazing angle attenuated total reflection FTIR spectroscopy (GATR-FTIR), and EDX. EDX and FTIR were the primary tools used for measuring stoichiometry and chemical bonding, with chemical identification *via* XPS supporting these measurements.

Dielectric characterisation was carried out by performing current-voltage sweeps on Au electrodes on each SiO_2 sample and analysing the data using a 2-parameter Weibull distribution. A 12 x 12 array of 100 nm thick Au electrodes (determined by the piezoelectric crystal monitor) were deposited by e-beam evaporation of an Au target through a copper

mask. The electrode area was (4.8 ± 0.8) x 10^{-3} mm^2 which was measured from SEM data of the electrodes after deposition. The probe of the Keithley 4200 was carefully positioned on each electrode using a built-in microscope, with care being taken not to damage the electrode. The voltage was then swept from 0 – 21 V in 0.1 V intervals and the subsequent current was measured, and the voltage at which breakdown occurred was recorded.

3.3. Initial Investigation

To begin, the setup of Hu *et al*. was adopted in an attempt to produce nanoscale SiO_2 coatings on bare Si wafer substrates before attempting to coat ZnO nanorods, whose characterisation would be more challenging. First, the PDMS block was loaded into an alumina boat and the substrate was placed vertically above the PDMS, across the top opening of the boat. This boat, containing both PDMS and substrate, was placed in the centre of the muffle furnace and heated in air to 650 °C (the steady-state deposition temperature) at a rate of 12 °C/min, remaining at this temperature for 2 hours. Three different deposition configurations were investigated throughout this subsection, which will be discussed in order, but they are shown here in Figure 3.2 for clarity.

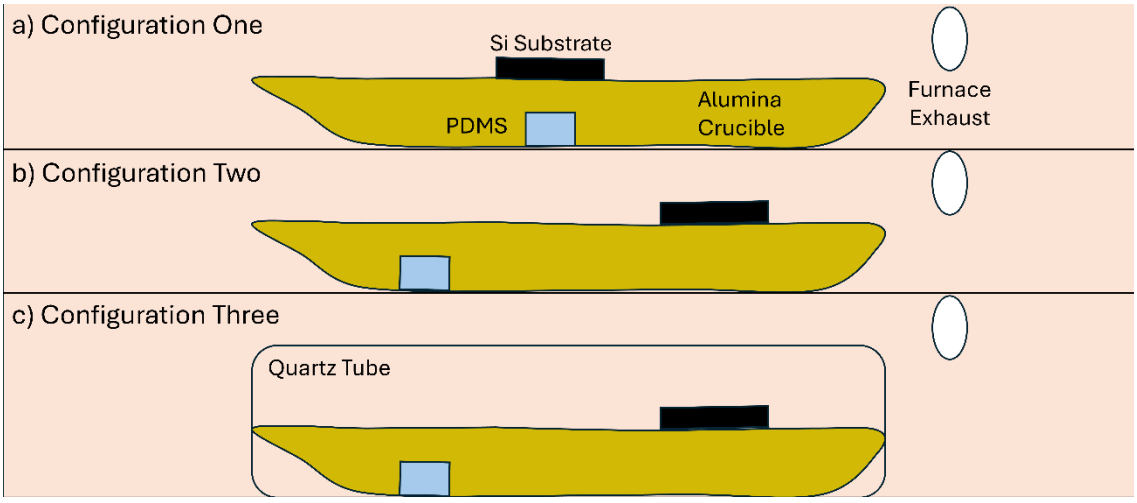

Figure 3.2: Configurations used to investigate PDMS-based SiO_2 deposition. In (a) the substrate is placed directly above the PDMS block whereas (b) has the substrate placed at a lateral distance of 5.5 cm away from the PDMS block and is positioned between the PDMS and furnace exhaust. (c) is the same as (b) except the entire crucible is placed within a hollow quartz tube to contain the SiO_2 vapour.

This first setup described, which is refered to as “configuration one” from this point onwards, resulted in coatings that were millimetres, rather than nanometres, thick (Figure 3.3). This is because our solid, nonporous substrate caused build-up of the material due to its impermeable nature and close proximity to the vapour source. Additionally, it was found that the PDMS expands greatly during the thermal cycling and physically came into contact

with the substrate, which drastically reduced the quality of the deposited coating. These issues were not relevant to the work of Hu *et al*. who were coating only the internal walls of a porous anodic aluminium oxide template, which would allow only a fraction of the vapour to enter and coat the nanopores [117].

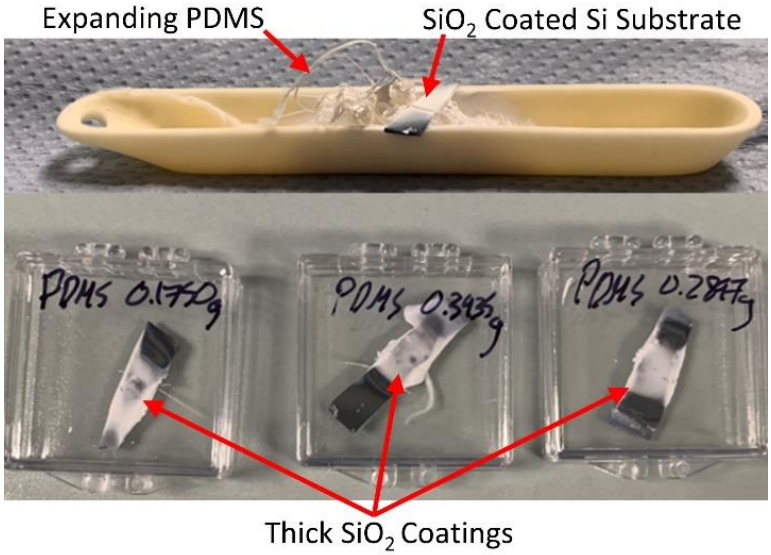

Figure 3.3: Photograph of SiO_2 deposition following the procedure of Hu et al. i.e. configuration one, showing the thick coatings and expansion of PDMS during heating.

To overcome the issues of PDMS expansion and to reduce coating thickness, the substrate was placed downstream from the PDMS, 5.5 cm away and facing the exhaust of the muffle furnace. This setup was called "configuration two" and is illustrated in Figure 3.2b. However, while this produced a significantly thinner coating, it was very uneven across the sample surface (Figure 3.4a).

A review of the literature showed the work of Favours *et al*. who aimed to utilise the same nanotubes as Hu *et al*. but noted that their setup resulted in significant SiO_2 deposits on the faces of the alumina templates [118]. This SiO_2 deposition on the faces of the template required thorough sanding to be removed before the templates could be dissolved and the nanotubes extracted. To overcome these issues, they modified the setup to include a tube furnace, sub-atmospheric pressures, and controlled gas flows to produce nanometre thickness coatings on all faces of the alumina template. Their technique also required significantly less PDMS, using 50 mg compared to the 600 mg used in the original work. For the novel approach to the work described here, their approach was modified to one which requires neither a tube furnace nor a vacuum pressures and controlled gas flow to achieve

conformal nanometre coatings in a standard muffle furnace/oven, which is also open to air at atmospheric pressure.

By simply placing the alumina boat containing PDMS with the sample downstream, all inside a hollow cylindrical quartz tube with similar length to the alumina boat, the vapour is confined and directed entirely over the sample surface, resulting in more deposition and uniformity of silica (Figure 3.4c). This was called “configuration three” (Figure 3.2c). Given that the entire vapour is directed over the sample, the coating for configuration three was

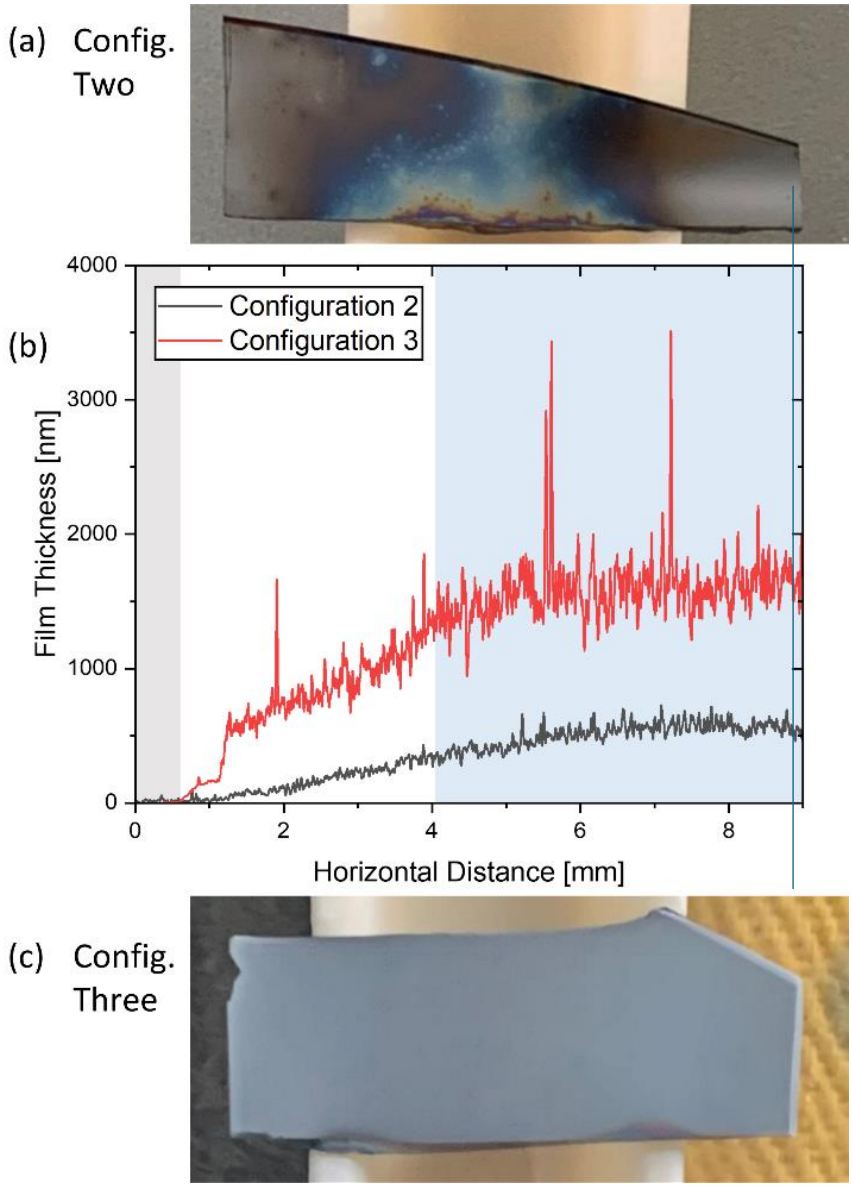

Figure 3.4: (a) Photograph of SiO_2 deposition by PVD configuration two i.e., alumina boat without quartz tube. The regions of visible light colours observed on the substrate arise from thin film interference effects due to areas of SiO_2 deposition with thicknesses equal to n.λ/2. (b) SiO_2 film thickness measurements across samples (a) and (c). (c) Photograph of SiO_2 deposition by configuration three i.e., the alumina boat contained within a hollow quartz tube configuration. Both depositions were carried out under the same conditions (~47.5 mg PDMS, 650 °C steady-state deposition temperature, 12 °C/min heating rate). Both samples are ~ 2 cm in length.

much thicker than it was when using the same setup without the quartz tube (configuration two), going from an average thickness of 500 nm to ~1700 nm in the centre region. Samples were photographed immediately after deposition, which can be seen in Figure 3.4, to better illustrate each setup.

The configuration three results show full sample coverage when compared to the deposition performed without the quartz tube (i.e. configuration two), however the profilometry results show large variations in thickness of the order of microns over length scales of microns. The contact profilometry results in isolation would suggest the quartz tube gives rise to significantly poorer quality coatings, but the visual images show a clear difference in sample coverage and uniformity on across the whole sample (Figure 3.4). These results indicated the benefit of the quartz tube method, however also showed the likelihood that significantly too much PDMS was being used. A more detailed schematic diagram of the furnace and configuration three used for the remainder of the SiO_2 deposition investigation are shown in Figure 3.5.

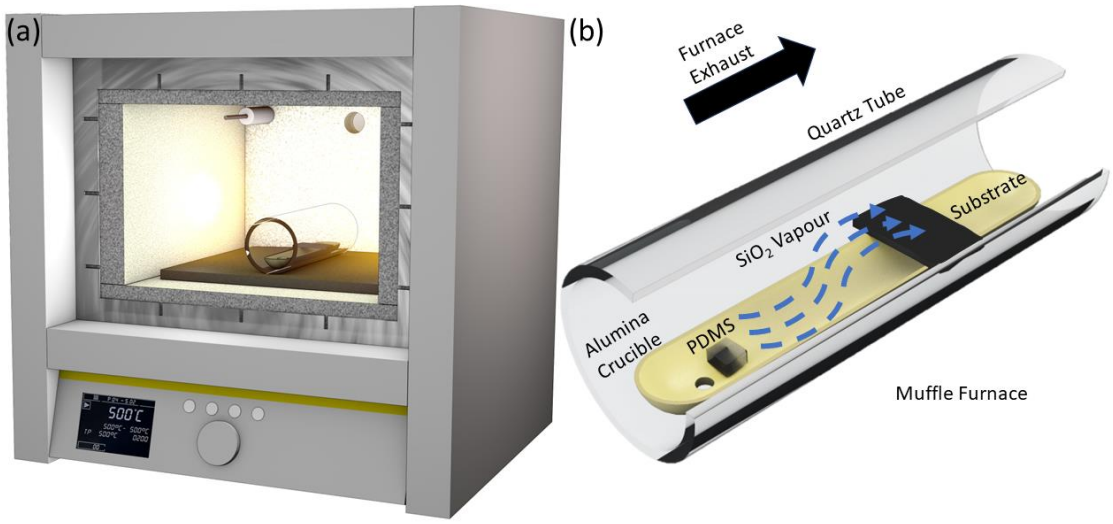

Figure 3.5: (a) Schematic diagram of PDMS-based SiO_2 deposition. (b) Labelled components of PDMS-based SiO_2 deposition.

The sample grown using configuration three was imaged under SEM (Figure 3.6) to better understand the large roughness observed in Figure 3.4. EDX was also performed to confirm that a pure SiO_2 coating was being obtained. By using a relatively low accelerating voltage (9.00 keV) and given that the coating thickness was ~ 1-2 µm, EDX spectra were obtained without signals from the substrate due to a ~ 300 nm penetration depth for the primary electron beam. The SEM image in Figure 3.6a shows clear island growth which is consistent with the contact profilometry results observed. Calculating the atomic percentages from

the weighted EDX results in Figure 3.6b gives a (69.3 ± 1.1 % : 30.7 ±1.1 %) or 2.26:1 ratio of oxygen to silicon, which is again consistent with the result expected for silicon dioxide and is in agreement with the values obtained by Favors *et al*. [118].

Hu *et al*. found that the SiO_2 thickness was linearly dependant on the amount of PDMS used, so the next step was to significantly reduce the amount of PDMS used in the process to produce thinner coatings of nanometre dimensions [117]. Depositions were performed

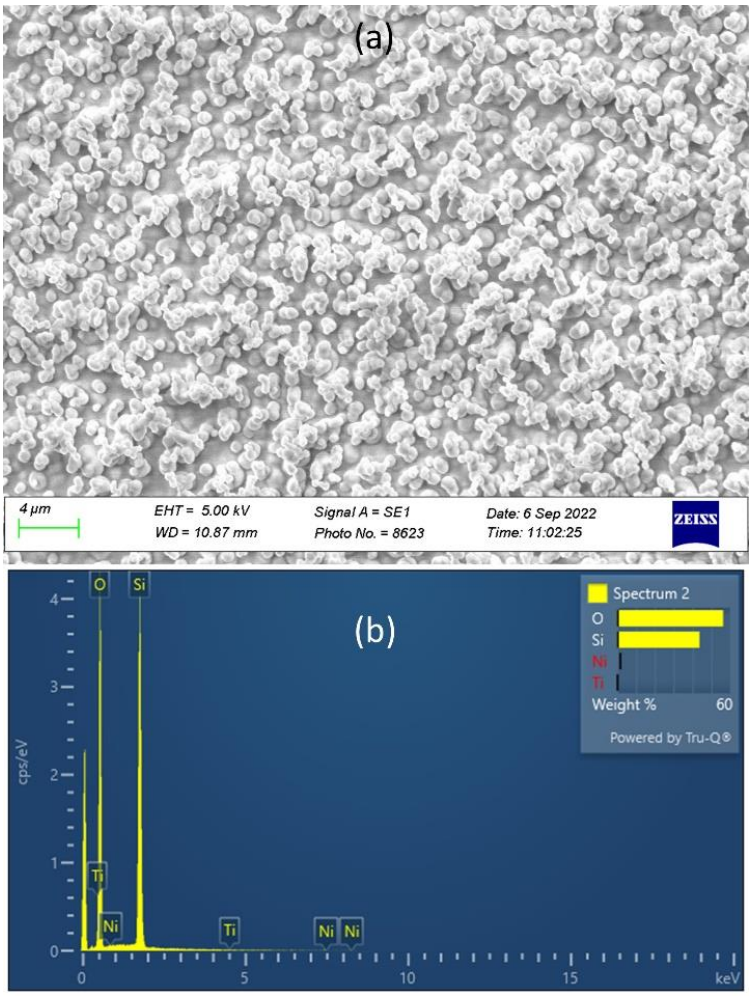

Figure 3.6: (a) SEM image of the sample grown using 47.5 mg of PDMS via configuration three, as shown in Figure 3.4c. The coating displays island-type growth, characteristic of SiO_2 on Si using PVD, with individual islands of ~1 µm in size, alongside multi-island structures. (b) EDX spectra of the same sample imaged in (a) showing the weight percentages of Si and O signals.

using 47.5, 30.6, 12.0, 6.0, and 1.5 mg of PDMS source material and measured the resulting thicknesses. The results are shown in the next subsection (3.3.1.). An important point to note for the remainder of section 3.2 is that, in order to measure the film thickness using

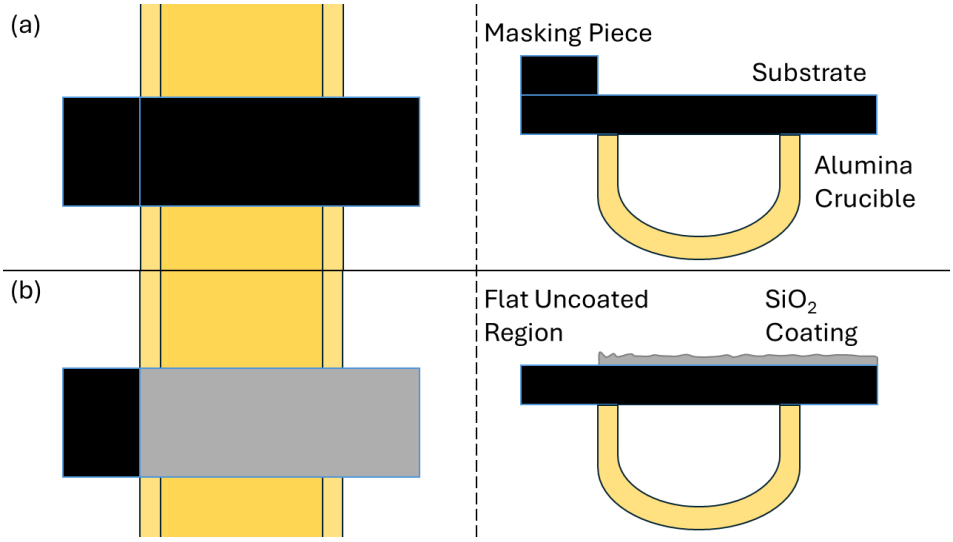

Figure 3.7: Illustration of (a) masked substrate before deposition, and (b) the SiO_2 film coated substrate with the masking piece removed. Left shows a top-down view and right shows a cross-sectional view. The Si substrates are coloured black and the SiO_2 coating is coloured grey.

CP, a section of the substrate was masked during deposition in order to provide a zero-point that the film thickness could be measured against. The masking was achieved by placing a small silicon substrate on the top of the sample. A diagram illustrating the masked substrate before deposition, and the SiO_2 film coated substrate with the masking piece removed is shown in Figure 3.7.

3.3.1. Effect of PDMS Source Mass on Film Thickness

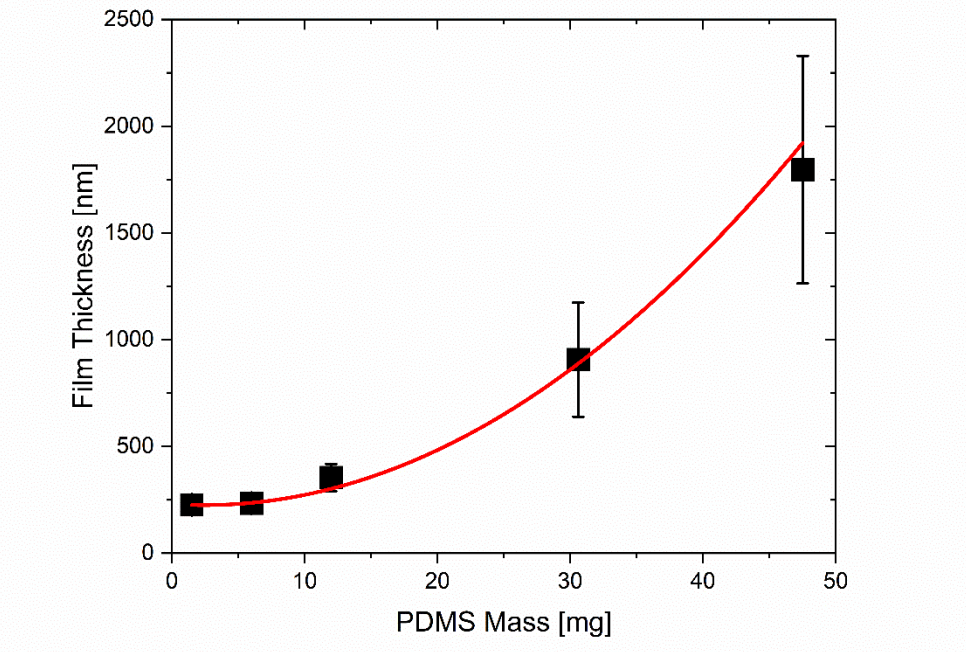

Figure 3.8: Film thickness vs. PDMS mass using a 12 °C/min heat rate, and a steady-state deposition temperature of 650 °C. The red line is a guide to the eye, using a parabolic form with a constant offset. Data points are mean ± 1 standard deviation, n = 3.

A rough linear trend in thickness vs source material was seen in Figure 3.8 for larger PDMS masses, however, there was only a 4% reduction in film thickness when reducing the PDMS mass from 6.0 to 1.5 mg (i.e. a 75% reduction). A nonlinear relationship is seen for smaller source masses, with the film thickness seeming to plateau at 6 mg of PDMS and below. The reasoning for this result was not clear initially, so the next step was to investigate the influence of both furnace steady-state deposition temperature and heating rate on the resultant film thickness to shed some light on the process.

3.3.2. Effect of Steady-State Deposition Temperature

Keeping the mass of PDMS constant at 12 mg, SiO_2 depositions were initially performed using a large range of steady state deposition temperatures (450 – 650 °C, in 50 °C intervals). The lower point of the range chosen was the minimum threshold temperature required to initiate the degradation mechanism for PDMS, and the largest temperature was the one used by both Hu *et al*. and Favors *et al*. [117], [118]. Each sample was heated at a rate of12 °C/min and maintained at the steady-state temperature for two hours to ensure complete degradation of PDMS. Figure 3.9 shows the effect of the steady-state temperature on the SiO_2 deposition process. The most obvious result is that lower temperatures give

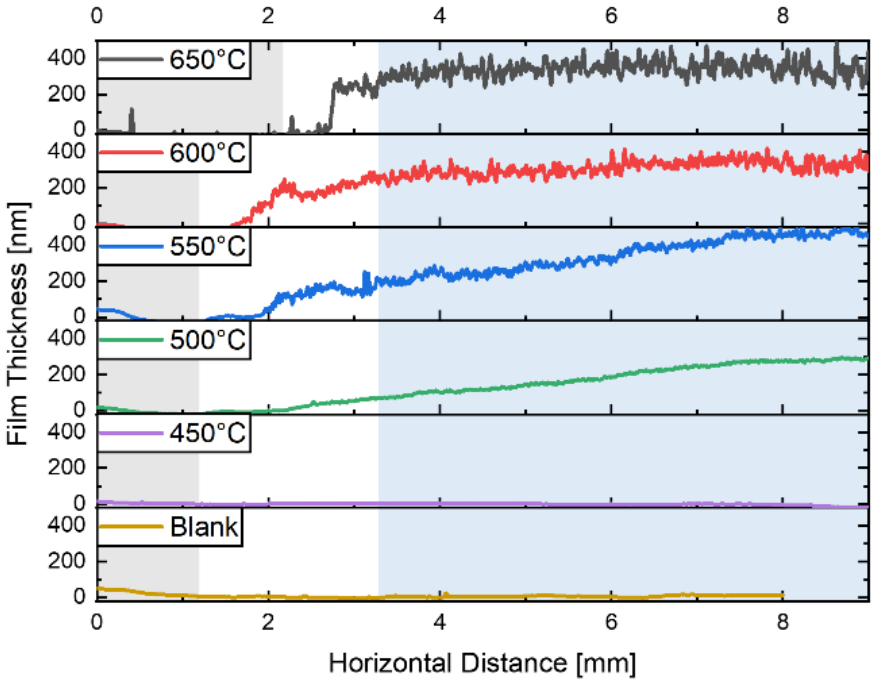

Figure 3.9: Steady-state deposition temperature dependence of SiO_2 film thickness using 12 mg of PDMS at a heating rate of 12 °C/min. Grey highlighted areas indicate uncoated substrate regions, and blue highlighted areas indicate where thickness measurements were taken from.

much less surface roughness, although the coatings themselves do not visually appear flat and are continuing to increase in thickness across the substrate, whereas the higher temperature samples have much rougher surfaces, but the thicknesses seem to plateau. Surface roughness measurements, as determined by the Dektak XT software, give surface roughness values of 34.7, 15.8, 16.9, 8.3, and 0.4 nm from higher to lower temperature, with the bare Si wafer reference sample (with no deposition) having a roughness of 0.1 nm.

Upon further investigation, it became apparent that the additional piece of Si placed on top of the sample (Figure 3.7), may have been affecting the SiO_2 deposition thickness. This is used to provide a flat measurement of the bare Si surface, and this "masked'' region can be seen as the flat region highlighted in grey on the lefthand side of Figure 3.9. The higher temperature coatings appear relatively unaffected by this, given the step edge between the flat region and the coated region. More gradual changes are seen between the flat and coated regions at lower temperatures. This was believed to be caused by the large Si piece deflecting the vapour more at lower deposition temperatures, causing thicker coatings to occur as the distance is increased from this piece.

To investigate this effect further, a 500 °C deposition was performed without this Si piece (Figure 3.10, black line) and the SiO_2 film was significantly flatter compared to the data illustrated in Figure 3.9, showing only an average 50 nm increase in thickness in the substrate centre. The thickness increases between 5 – 15 mm. This region corresponds to the area of the wafer directly above the alumina boat. These positions are where the silicon contacts the boat, so it is expected that an increase in coating thickness would be seen in the centre of the boat.

The standard "Scotch Tape'' test was performed (Figure 3.10) on this same sample to qualitatively measure the strength of adhesion, alongside repeated washing with isopropyl alcohol and deionised water, and the coating appeared unaffected, indicating good adhesion. A sticky residue remained after the test, which can be seen on the right-hand side of the profilometry data of Figure 3.10. For all subsequent tests, this masking Si piece was cleaved to be as small as possible and the substrates to be coated were increased in length from their initial size, equal to the width of the alumina boat (1 – 1.2 cm), to over double the width (2.5 cm) of the boat in order to have the Si piece as far from the boat centre as possible (Figure 3.11b).

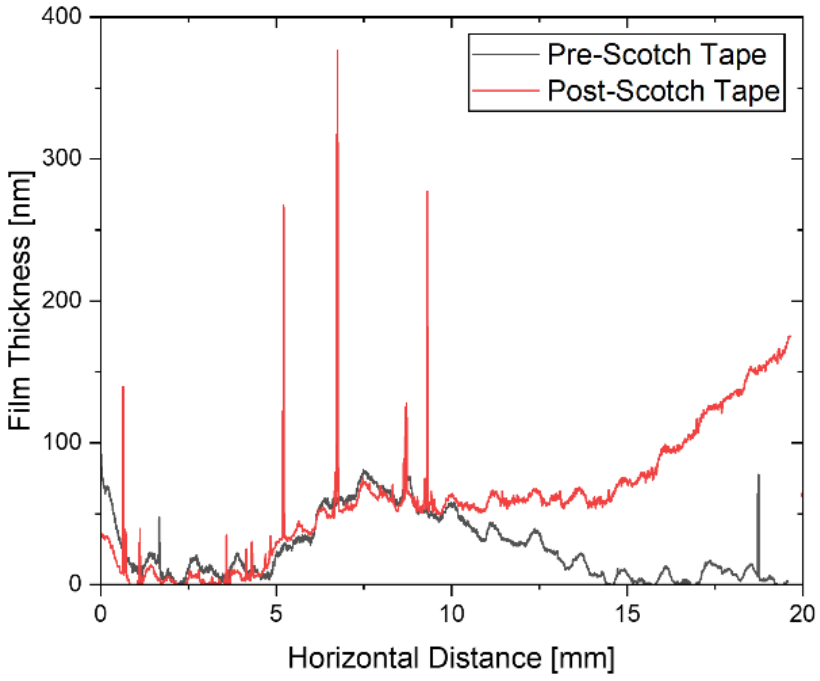

Figure 3.10: SiO_2 coating without Si piece to mark uncoated areas alongside a scan across the same sample after the "Scotch-Tape" test performed on the latter half of the surface (10–20 mm).

By applying the above sample modifications, further depositions were performed between 460 – 500 °C using only 6 mg of PDMS (Figure 3.11). No evidence of SiO_2 deposition was observed at 450 °C, given that this is the threshold temperature required for the bond scission of cyclic oligomers. This temperature must be exceeded to generate the SiO_2 vapour. Figure 3.11a shows there is no significant dependence of the film thickness on the steady-state deposition temperature in this temperature range. Findings from Camino *et al*. suggest that there could be a temperature dependence, as the weight of the PDMS block gradually decreases with increasing temperature after thermal degradation begins, until it eventually plateaus at a higher temperature [112], [113]. However, the steady-state deposition temperature was maintained for two hours, whereas they measured the change in mass with increasing temperature without maintaining each temperature for a set amount of time. Our lower temperature deposition for longer periods of time may be broadly equivalent to increasing the temperature until the PDMS has been completely degraded.

The steep incline seen at the left-hand side of Figure 3.11a (~ 2 – 7.5 mm) occurs between the silicon piece and the nearest contact point between the sample Si and the alumina boat, and the flat central region of the coating (~ 7.5 – 15 mm) corresponds to the centre of the alumina boat (illustrated in Figure 3.11b). The thickness of the coating begins to vary beyond this, starting roughly at the second contact point between sample and alumina

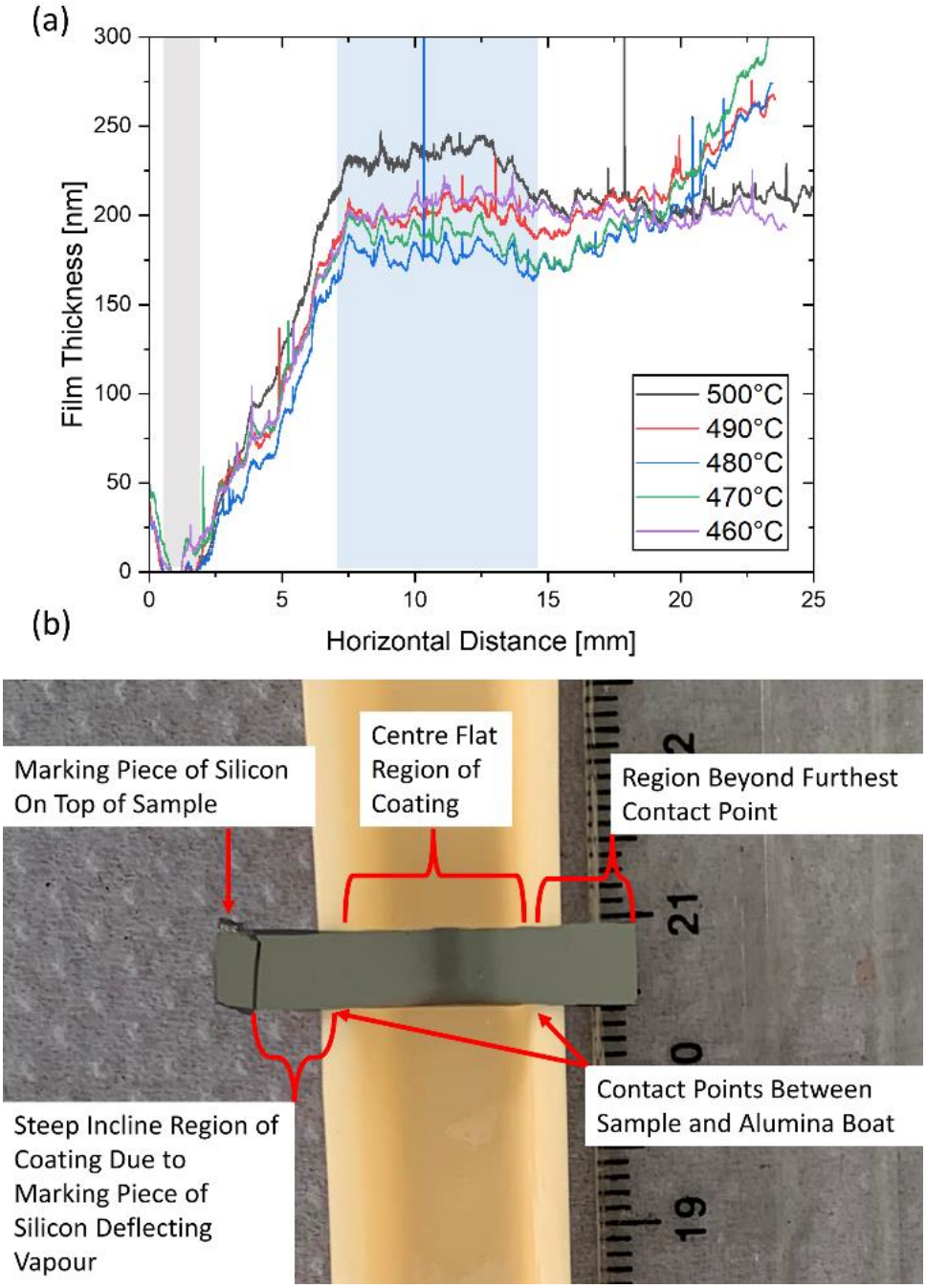

Figure 3.11: (a) Steady-state deposition temperature dependence of SiO_2 coating using 6 mg PDMS at a heating rate of 12 °C/min using updated sample preparation. (b) Annotated top-down photograph of SiO_2 PVD sample highlighting the different coating regions observed in (a). Grey highlighted areas indicate uncoated substrate regions, and blue highlighted areas indicate where thickness measurements were taken from.

(located at ~15 mm), and continuing along the sample in the region overhanging the alumina. It was believed that the upward thickness trend after the horizontal position labelled 15 mm onwards seen for some of the samples is a result of a slight tilt of the sample/boat during the deposition process.

3.3.3. Effect of Heating Rate

While reducing the size of the masking piece allowed us to produce flat and more uniform coatings across the substrate centre, they were still ~ 200 nm thick. To further reduce the coating thicknesses, the work done by Camino *et al*. was consulated, who studied the thermal degradation mechanisms/kinetics of PDMS [112], [113].They discovered that the products of the thermal degradation of PDMS depend on the heating rate, as this strongly affects the degree of depolymerization. Lower heating rates and steady-state temperatures produce the volatile cyclic oligomers required as the precursors for SiO_2 vapour generation. However, the lower the heating rate is, the lower the degree of depolymerization is and hence less SiO_2 vapour will be produced in this case. Rapid heating rates result in increased depolymerization, but these cyclic oligomers are then accompanied by linear oligomers, with the latter dominating the reaction products. Here, a radical mechanism occurs through homolytic Si–CH_3 bond scission. Cross-linking of macro-radicals here decreases the flexibility of the PDMS chain and hinders the splitting of cyclic oligomers. So rather than getting more SiO_2 vapour, bond reorganisation takes place with the formation of ceramic silicon oxycarbide, which represents the majority of the reactant product, producing less SiO_2 vapour.

SiO_2 coatings were performed at three different heating rates under a steady-state deposition temperature of 500 °C; the original 12 °C/min used by Hu *et al*. and Favours *et al*., and also at the minimum (1 °C/min) and maximum (40 °C/min) rates achievable with our system [117], [118]. A non-monotonic relationship is observed in Figure 3.12, with 1 and 40 °C/min heating rates producing significantly thinner coatings than a heating rate of 12 °C/min. The film thickness for the 1 °C/min deposition peaks at 60 nm and ranges consistently between 25–50 nm in the centre of the boat. These results provide additional context for those observed during the initial film thickness vs. PDMS mass investigation. The 1.5 mg blocks of PDMS are very small, with a significantly higher surface to volume ratio than the other blocks used. These smaller blocks undergo more rapid depolymerisation at high heating rates as a result of their small size and high surface to volume ratio, resulting in an altered reactant product compared to the larger PDMS masses.

Considering the results of each deposition parameter alongside the thermogravimetric analysis of PDMS at different heating rates performed by Camino *et al*., the effect of steady-state deposition temperature on film thickness is likely more apparent at lower heating rates than the 12 °C/min utilised here. At large heating rates, there is rapid degradation of PDMS per unit temperature above the decomposition threshold, whereas slower heating

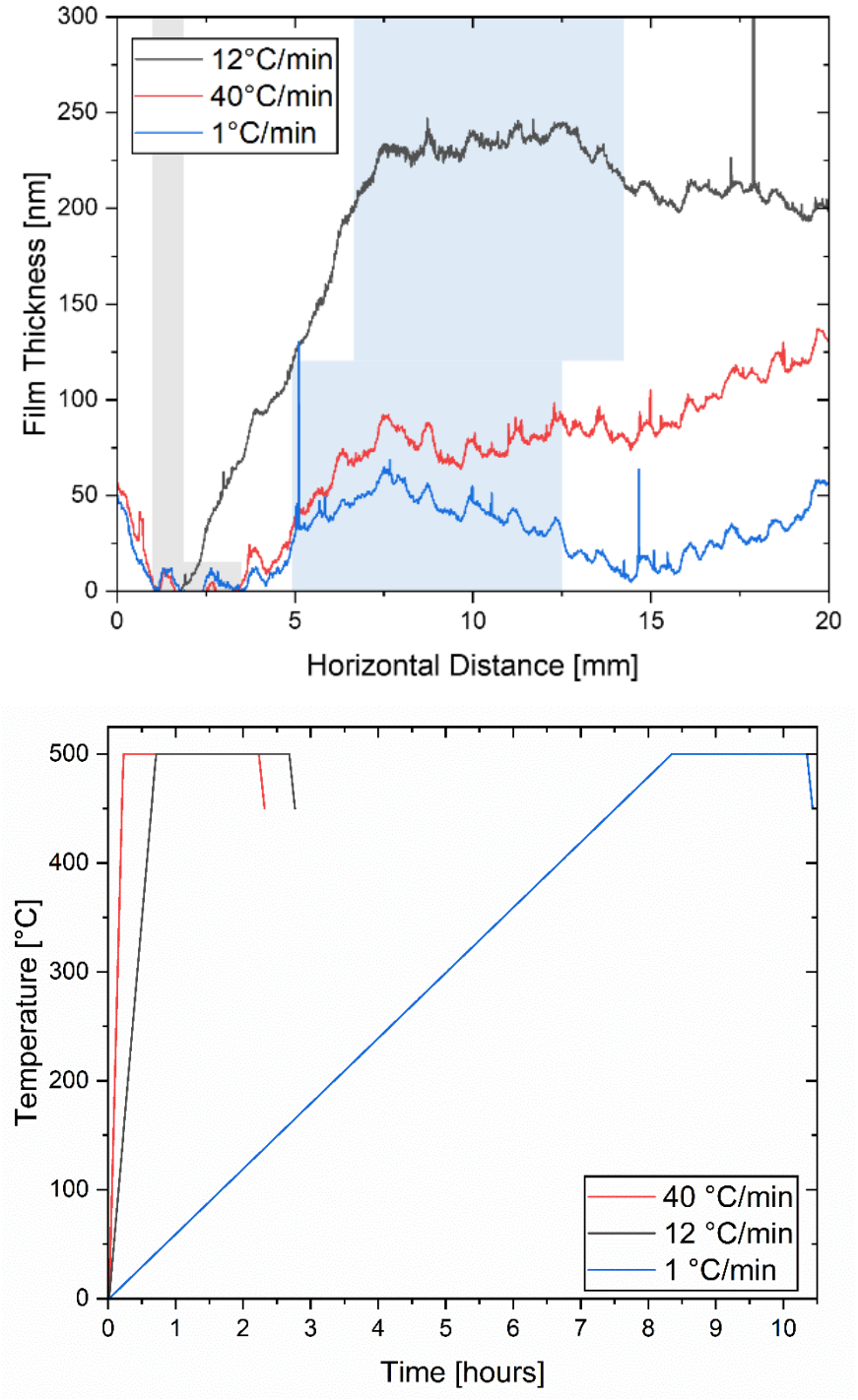

Figure 3.12: (Top) SiO_2 thickness dependence on heating rate for a steady-state deposition temperature of 500 °C using 6.0 mg of PDMS. Grey highlighted areas indicate uncoated substrate regions, and blue highlighted areas indicate where thickness measurements were taken from. (Bottom) Graph of temperature versus time for each heating rate used. Deposition occurs during the two-hour period at 500 °C.

rates than the 12 °C/min utilised here. At large heating rates, there is rapid degradation of PDMS per unit temperature above the decomposition threshold, whereas slower heating rates show a much lower amount of degradation per unit temperature, with two distinct stages of degradation emerging. However, this was not investigated further due to the tunability already available from varying the PDMS mass and heating rate alone.

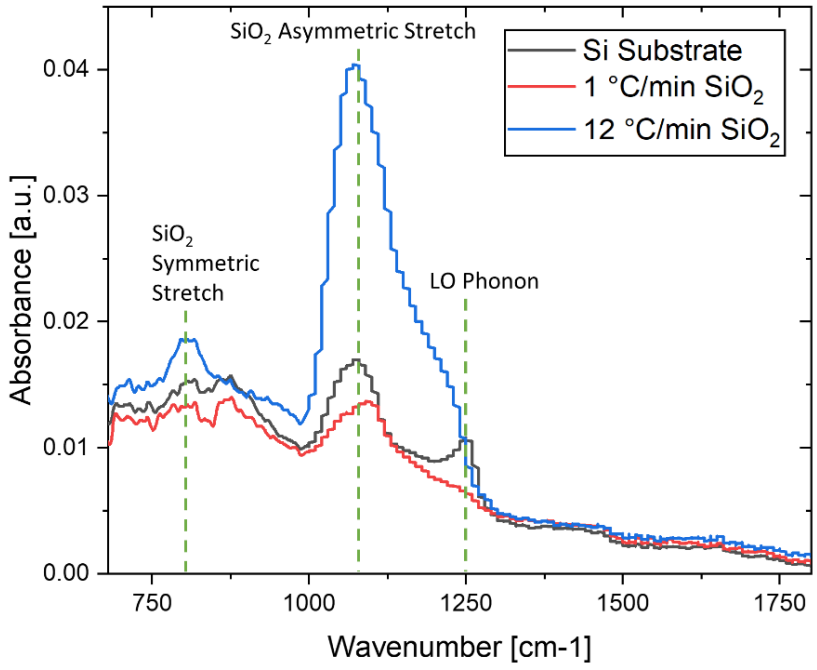

Figure 3.13: FTIR spectra of the SiO_2 coatings at varying thicknesses (the same samples analysed in Figure 3.12), showing the symmetric and asymmetric stretching vibrations of Si–O–Si at 800 and 1100 cm^{-1} respectively, and longitudinal optical phonons of the crystalline silicon wafer and its native oxide at 1250 cm^{-1} in the uncoated substrate.

Finally, these thinner samples were analysed using GATR-FTIR spectroscopy to confirm SiO_2 bonding to complement the SiO_2 stoichiometry confirmed by EDX. GATR-FTIR data (Figure 3.13) shows the increased intensity of the symmetric and asymmetric stretching vibrations of Si–O–Si, at 800 and 1100 cm^{-1} respectively, indicative of the presence of an increased deposit of SiO_2 in the thickest sample. The sharp peak at 1250 cm^{-1} observed in the uncoated Si sample is caused by longitudinal optical phonons of the crystalline silicon wafer and its native oxide [119], [120].

While CP profilometry was required to analyse the relatively thick coatings, now that the coatings had been reduced to tens of nanometres, the masking Si piece was removed as it had a clear effect on the deposited thickness and uniformity, and the coatings were analysed using spectroscopic ellipsometry and XPS instead of CP. The uniformity and thinness of the 1 °C/min heating rate films enables the use of ellipsometry and XPS.

3.4. 2D Films

3.4.1. Physical Characterisation

Keeping the heating rate at 1 °C/min, the SiO_2 thickness versus PDMS mass relationship was investigated using spectroscopic ellipsometry, and the results can be seen below.

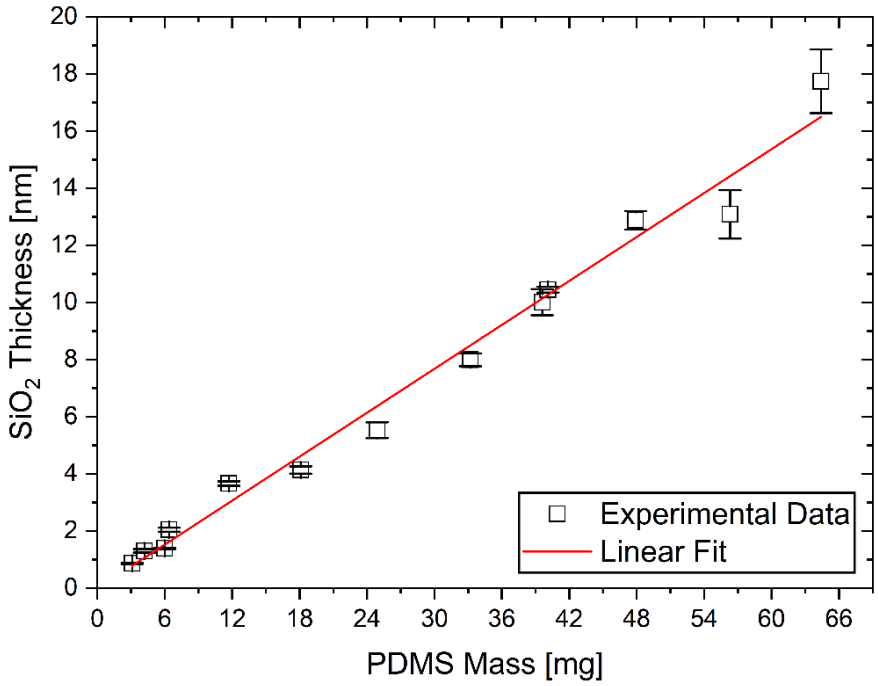

Figure 3.14: Thickness vs PDMS source mass determined via spectroscopic ellipsometry. The slope is 0.256 ± 0.010 nm/mg, and the intercept is -0.015 ± 0.335 nm, with an r^2 value of 0.984. The error bars represent the standard deviation from five independent measurements of each sample.

Figure 3.14 shows a regression plot of the thickness of the SiO_2 films deposited at a heating rate of 1 °C/min versus the mass of PDMS source material used. There is an excellent correlation, and one can see that ultra-thin SiO_2 films with thicknesses down to ~ 1 nm can be reliably and reproducibly grown using this method. The results in Figure 3.14 demonstrate a high degree of thickness controllability at an individual nanometre scale. Large increases in source mass are required to increase the SiO_2 deposition by sub-nanometre thicknesses. The removal of the masking Si pieces has had a significant effect on the vapour flow close to the substrate and had led to a significantly reduced deposition rate, allowing much thinner films to be deposited. An example of the ellipsometry data and the model fit obtained for a 1 °C/min 6.0 mg PDMS deposition is shown in Figure 3.15.

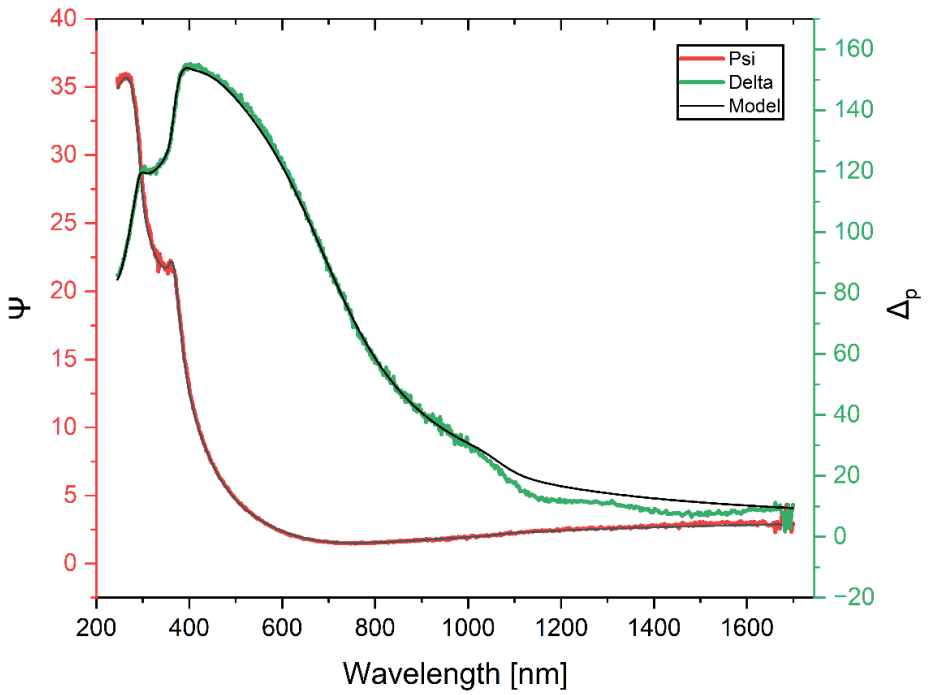

Figure 3.15: Example spectra of Ψ and Δ_p values recorded from a 1 °C/min 6.0 mg PDMS deposition on a clean silicon substrate with a 1.5 nm thick native oxide. The SiO_2 on Si model was applied to the spectra, with the best fit determining the PDMS-based SiO_2 thickness as 1.3 nm. The mean squared error of the fit was 5.3. The native oxide thickness was known prior to measurement.

The films display relatively uniform thicknesses, indicated by the low variations in thickness across the entire substrate surface (5 independent SE measurements over a 2 cm^2 area). AFM data of one of these films is shown in Figure 3.16 alongside data from a thermal oxide provided by an industrial partner in the microelectronics manufacturing sector. The data for PDMS-based depositions are quite featureless, speaking to the flat, thin film morphology, which is in agreement with the ellipsometry data of Figure 3.14. This was confirmed by cross-sectional FESEM data of the Au/SiO_2 structure shown in Figure 3.17. To obtain sufficient contrast to separate the SiO_2 films from the Si substrate, SiO_2 layers (using 15 mg and 45 mg PDMS) were instead deposited between three layers of Au rather than directly onto the Si substrate which was the case for the SE measurements. The residual roughness in these images arises from the granularity of the Au layers rather than the SiO_2 itself.

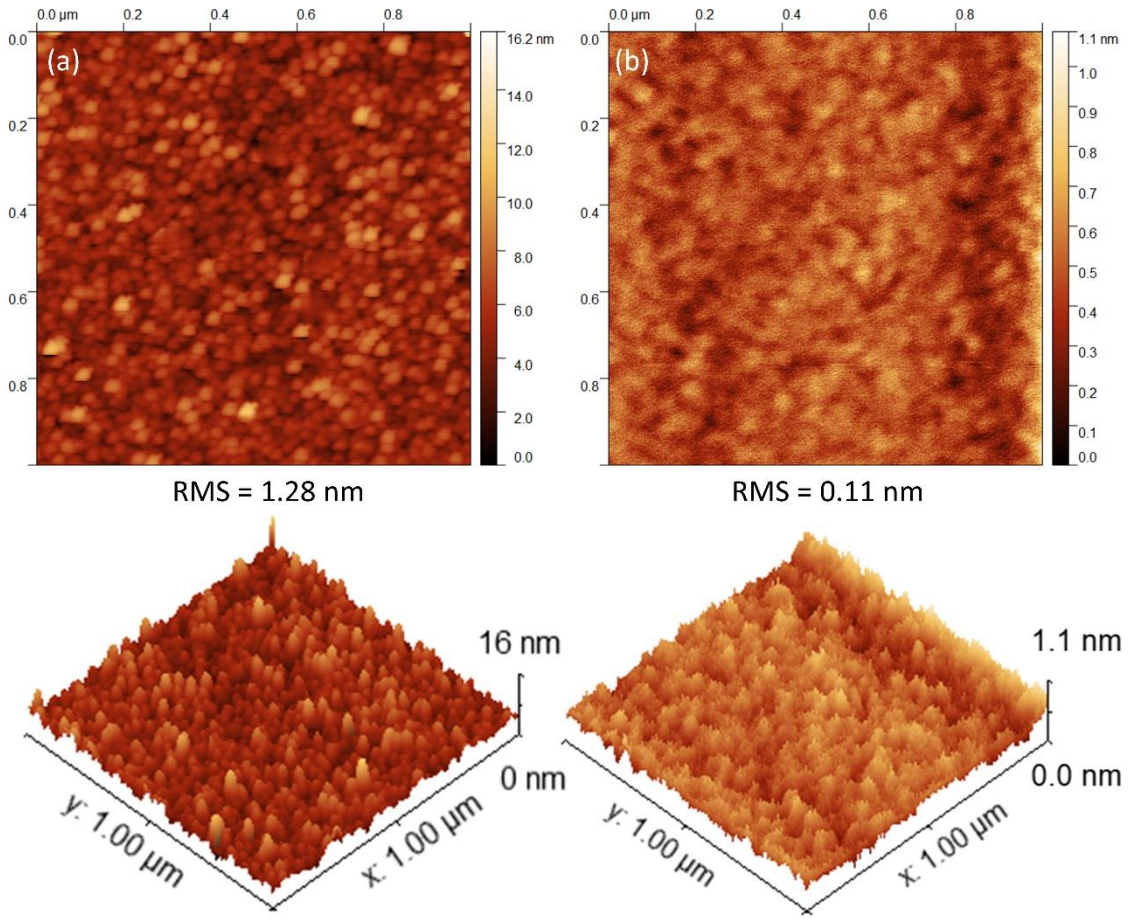

Figure 3.16: AFM data of nominal 11.5 nm SiO_2 films. (a) PDMS-Based SiO_2 and (b) industrial thermal oxide.

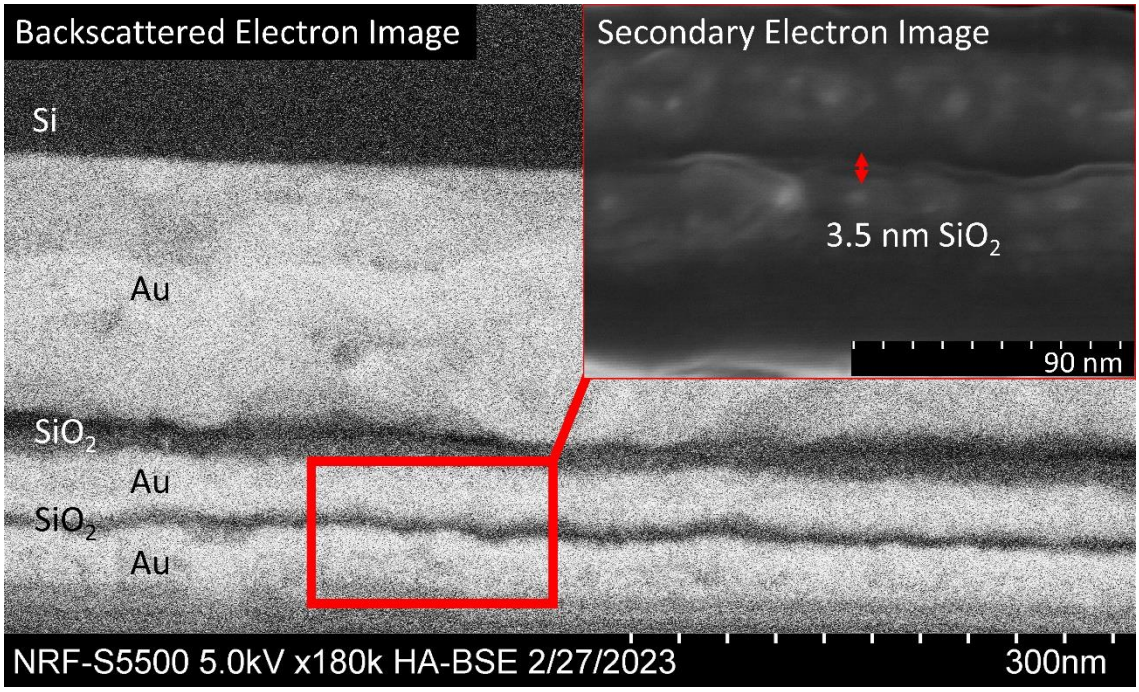

Figure 3.17: Cross-sectional FESEM data of planar SiO_2 films. PDMS-based SiO_2 films (dark regions) were deposited between e-beam evaporated Au layers (bright regions) to obtain sufficient contrast for imaging. The substrate is at the top of the image.

3.4.2. Dielectric Properties

The dielectric properties of these PDMS-based films were investigated, as the ultimate goal of this work was to coat conductive core ZnO nanorods, and the core-shell structure using conductive oxide cores such as ZnO may enable additional device functionality and selectivity by the use of voltages applied to the network of core nanostructures. The electric breakdown characteristics of the PDMS deposited films were investigated and compared to high-quality thermal oxide films of the same thickness. To do so, a 12x12 array of rectangular Au contact pads (area (4.8 ± 0.8) x 10^{-3} mm^2) were deposited onto the SiO_2-coated Si substrates through a copper mask *via* thermal evaporation of an Au wire in an Edwards AUTO 306 vacuum coater. These data were analysed using a 2-parameter Weibull distribution. The data and fits to the linear regions of the datasets are shown in Figure 3.18

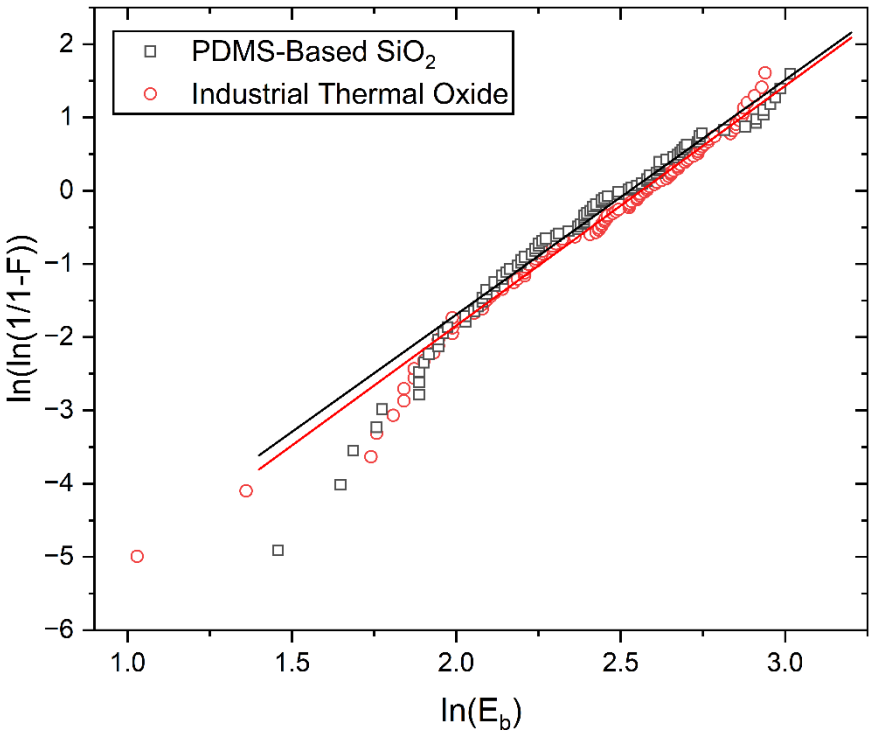

Figure 3.18: Weibull distribution plots of breakdown field comparing different 11.5 nm SiO_2 films. F indicates the cumulative probability of failure and E_b indicates the breakdown field (in MV/cm). The best fit lines are indicated by solid lines of the appropriate colour in the linear fitted regions of the two data sets. The r^2 values are 0.982 and 0.991, for the PDMS and thermal oxide films, respectively.

for the PDMS deposited films and high-quality thermal oxide films. The film thicknesses are 11.5 nm ± 0.5 nm in both cases, enabling meaningful comparison of the films' electrical stability. The breakdown strengths of the PDMS deposited SiO_2 and the industrial thermal oxide can be found from the slopes and intercepts of the linear portion of the data in Figure

3.18 using the two parameter Weibull distribution mentioned in section 2.2.8.2. The slope and intercept values of the linear fits are shown below in table 3.1.

	PDMS	Thermal oxide
Slope, β	3.21 ± 0.05	3.27 ± 0.03
Intercept, –βln(η)	-7.65 ± 0.11	-7.93 ± 0.08
η (MV/cm)	10.89 ± 0.05	11.28 ± 0.03

Table 3.1: Fit parameters from Weibull distribution plots comparing different 11.5 nm SiO_2 films.

Based on the fits, the values of η for the PDMS and thermal oxide films were found to be 10.84 ± 0.05 MV/cm and 11.30 ± 0.03 MV/cm, respectively. These values are quite close to each other and are also very close to the expected breakdown field of SiO_2 of ~ 10 MV/cm [121]. The PDMS-based film displays similar leakage current to the thermal oxide at electric fields of 6.5 MV/cm and lower. Above this field strength, the leakage current steadily increases to a single order of magnitude greater at ~ 11.5 MV/cm, at which point breakdown occurs, as shown in Figure 3.19. This leakage current is lower than values from the literature for SiO_2 as-deposited by atomic layer deposition (ALD) and comparable to annealed ALD samples and is much lower than SiO_2 films grown by chemical vapour deposition (CVD) methods (as-deposited and post anneal) [122], [123].

These measurements confirm that the breakdown strength of the PDMS films is comparable to that of high-quality industrial thermal oxides and that these ~ 11.5 nm thick films can sustain applied voltages of the order of 10 V at least as well as the industrial thermal oxide films. Hence the core-shell structure using conductive oxide cores such as ZnO could utilise voltages of this magnitude applied to the network of core nanostructures to enable additional device functionality such as selective attraction or repulsion of charged species in solution in a biosensor device, with this functionality further boosted by virtue of local field enhancement effects due to the high aspect ratio nanostructures [124], [125].

While this technique enables the deposition of ultra-thin conformal films between 0.8 – 18 nm, using PDMS masses greater than ~ 65 mg results in reduced uniformity which can be detected using spectroscopic ellipsometry and SEM. Spectroscopic ellipsometry fits to the data in Figure 3.14 result in mean squared errors of < 10, but using greater masses results in much greater mean squared errors and poorer fits to the data.

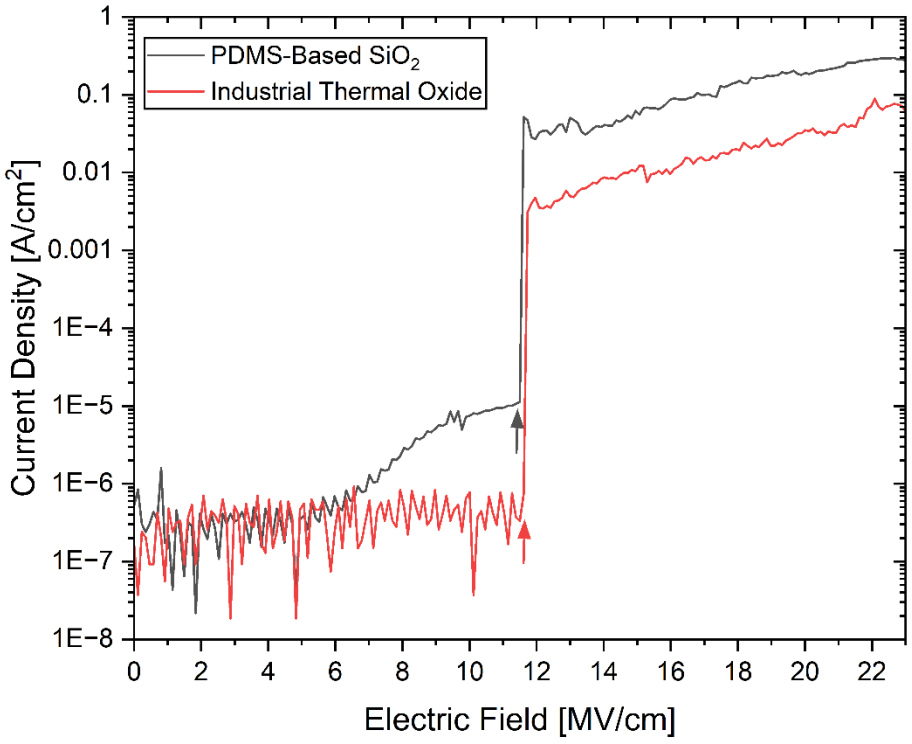

Figure 3.19: Current density vs electric field strength for various SiO_2 thin films. The arrows indicate the position of the breakdown field for each sample.

3.5. SiO_2 Coated ZnO

While the technique described above can successfully coat Si substrates with a high degree of controllability, SiO_2 coatings were deposited onto flat ZnO buffer layers under similar conditions to those deposited on Si substrates to provide elemental discrimination between film and substrate. This investigation was to determine if the coatings were pinhole free, and if similar levels of controllability were obtainable on non-Si substrates. Using XPS, the electron inelastic mean free path of ~ 1–2 nm means that for uniform and full coverage films the Zn 2p signal should be virtually undetectable for thicknesses ≥ 10 nm given our Al Kα x-ray source [73], [126], [127]. The XPS results for depositions on planar ZnO layers can be seen in Figure 3.20.

The XPS results show the full coverage and conformality of our PDMS based deposition. The PDMS deposition shows clear suppression of both Zn peaks located at 1022 and 1045 eV with coating thicknesses of ~ 10 nm, which is at the limit of XPS sensitivity for electrons with a kinetic energy of < 500 eV. In a conformal, uniform, dense and pinhole-free coating, the concentration of photoelectrons emanating from an underlying layer of this thickness will be beyond the detection limits of conventional XPS, which is what was seen in the samples

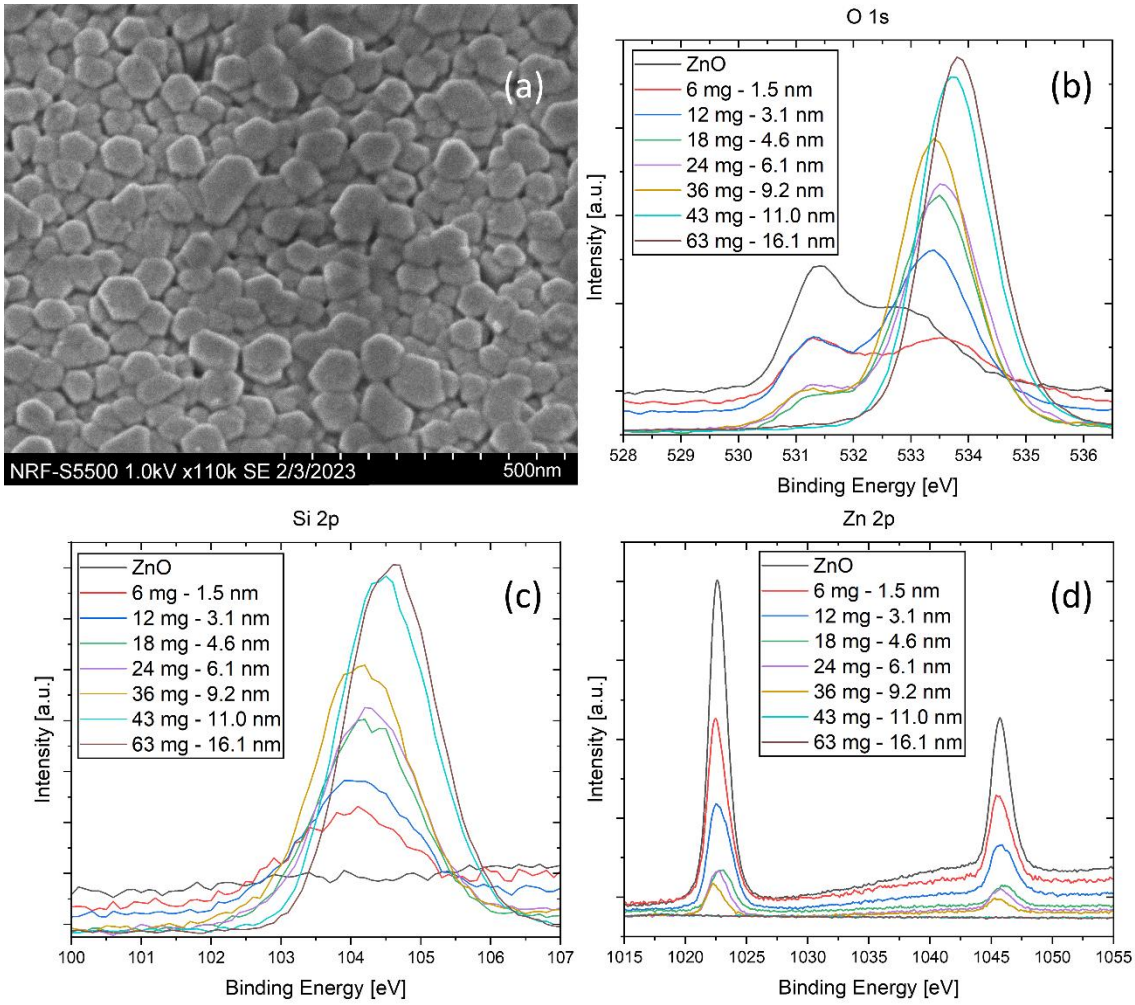

Figure 3.20: (a) FESEM image of compact CBD ZnO planar NR films used to study SiO_2 deposition on non-Si substrates. (b) XPS spectra of the O 1s orbital region of sample (b) coated using varying amounts of PDMS. (c) XPS spectra of the Si 2p orbital region (d) XPS spectra of the Zn 2p orbital region.

coated with PDMS deposited SiO_2. This effect is further illustrated by the O 1s spectra which shows two peaks, with the lower energy peak (531.5 eV) indicating the metal oxide bonding of ZnO, and the higher energy peak (533.5 eV) being that of the insulating SiO_2. With increasing PDMS mass, a decrease is seen in the 531.5 eV peak intensity and an increase in the 533.5 eV peak intensity. Quantitative elemental analysis of the PDMS based deposited films in Figure 3.20 is shown in Figure 3.21, which shows the atomic percentage of Zn continually decreases from 19.81% in uncoated ZnO, to eventually 0.00% with 10+ nm of SiO_2. Corresponding Si 2p signals show 0.00% in the uncoated ZnO, which increases continually to ~ 38 % with 10+ nm of SiO_2. The Zn and Si 2p atomic percentages are approximately equal for 11 and 16 nm of SiO_2 which is expected given the surface sensitivity of the system.

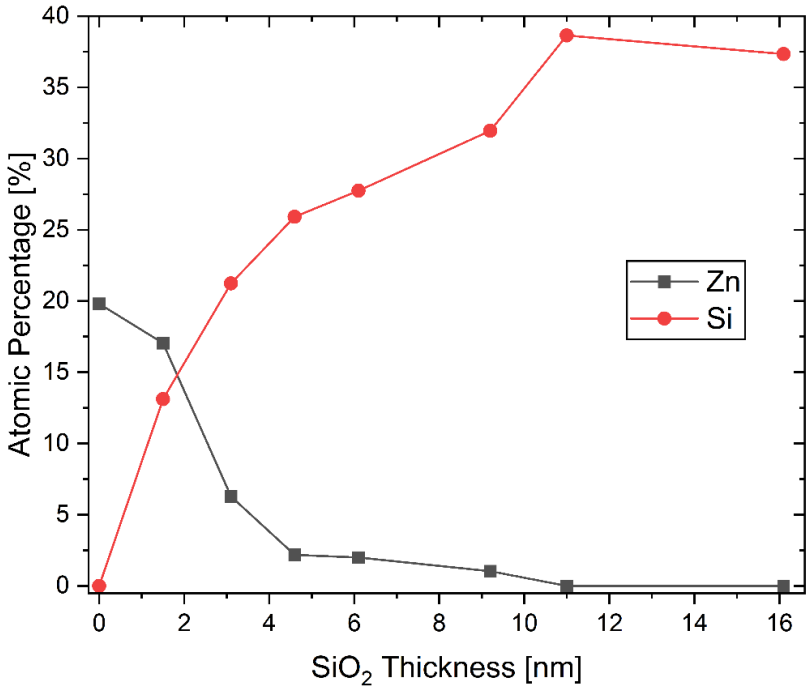

Figure 3.21: Atomic percentage of Zn and O vs SiO_2 thickness for PDMS-Based SiO_2 films deposited on ZnO layers. Data is from quantitative analysis of XPS data from Figure 3.20.

Now that a comparable thickness versus mass relationship was confirmed to occur on planar ZnO surfaces, the next step was to coat the high aspect ratio CTRVPT ZnO NRs that will be used for DNA capture. A CTRVPT NR array was coated using 43.6 mg of PDMS, which our regression line in Figure 3.14 predicts will result in a coating of 11.2 nm. The FESEM and EDX results of an SiO_2 coated ZnO NR are shown in Figure 3.22. By measuring the widths of the Si and Zn signals and subtracting the latter from the former, the SiO_2 shell thickness can be calculated.

The data in Figure 3.22 show an excellent conformal coating morphology at the single NR level on structures than are very different to the two planar substrates previously coated. The average nominal shell thickness of 11.2 nm predicted by the regression line in Figure 3.14 is in excellent agreement with the measured shell thicknesses on individual NRs determined using the EDX data from the FESEM system (10.5 ± 3.0 nm). This again indicates that the deposition technique is not strongly dependent on the substrate material. STEM data of another NR of the same array is shown below in Figure 3.23, which is also in agreement with the FESEM and EDX data. XPS was also performed on the same NR array before the NRs were removed for STEM analysis, and the results confirm complete coverage and suppression of the Zn 2p signal, showing the technique provides a similar level of controllability on a wide variety of substrate materials and morphologies.

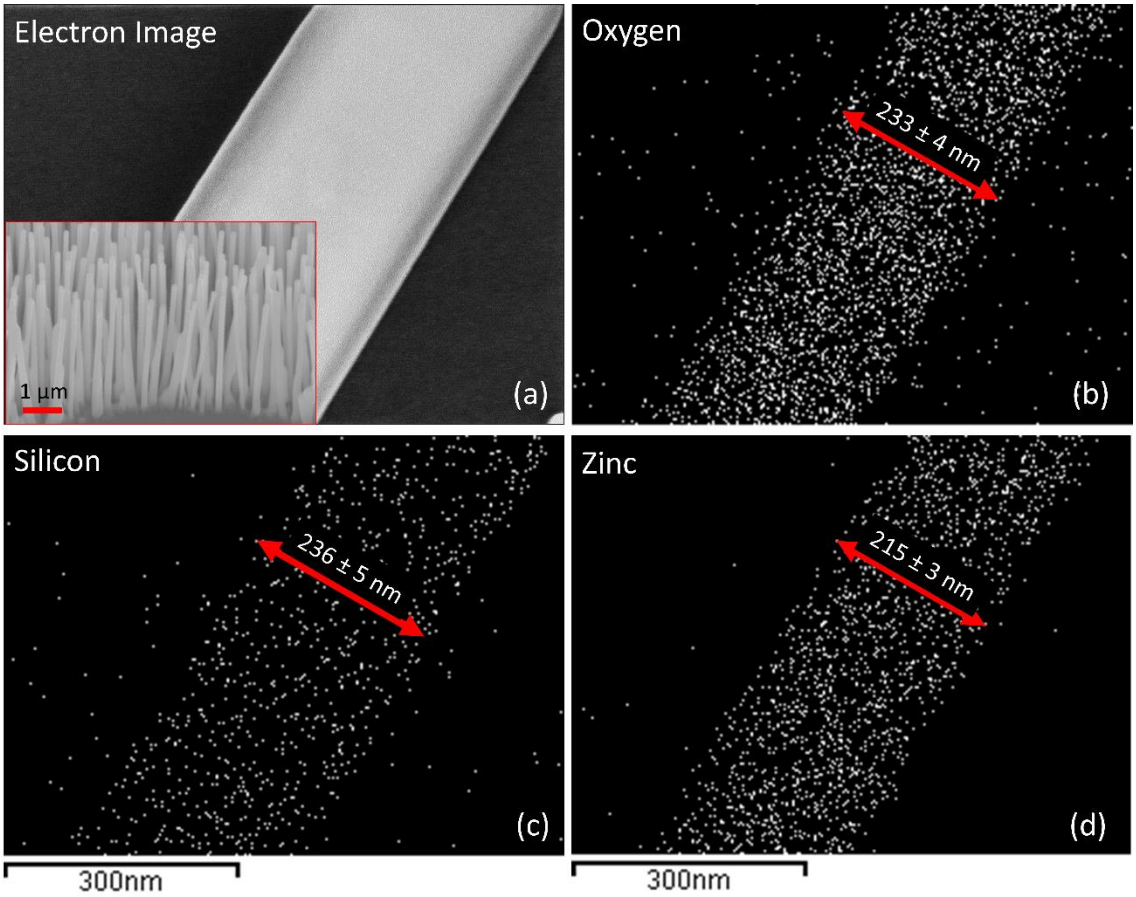

Figure 3.22: (a) FESEM image of a core-shell ZnO-SiO_2 NR with an aspect ratio of 20 (Inset: Lower magnification SEM image of vertically aligned CTRVPT ZnO NR array tilted by 30°). (b), (c), and (d) corresponding EDX images of the characteristic O, Si, and Zn x-ray emission from (a).

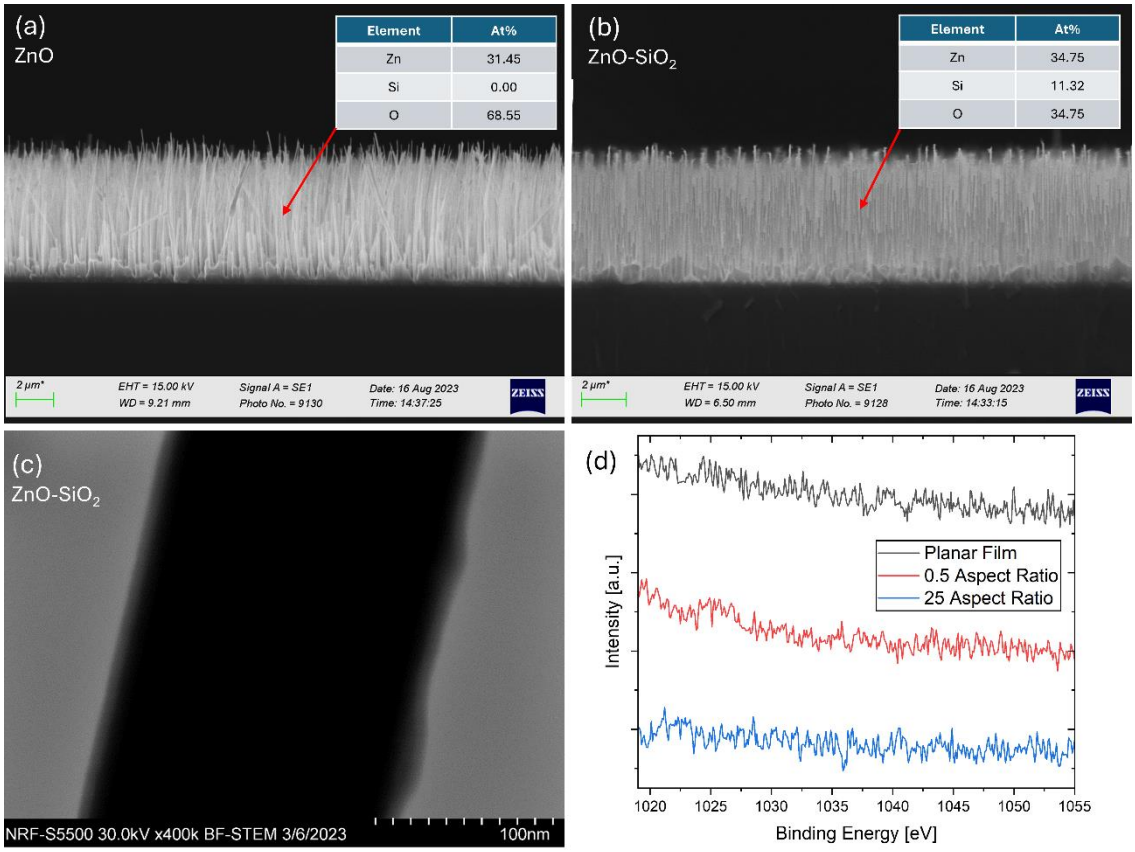

Figure 3.23: Cross-sectional SEM and EDX of CTRVPT ZnO NRs before (a) and after (b) 10.5 nm SiO_2 coating. (c) STEM image of ZnO NR coated in 10.5 nm SiO_2 (d) and XPS of Zn 2p intensity of ZnO NSs of various aspect ratios after 10.5 nm of SiO_2 coating. The 0.5 aspect ratio NRs were grown using nanosphere lithography [128] and CBD, and the 25 aspect ratio NRs were grown using CTRVPT and are those shown in the top row.

3.6. 3D Nanostructures

Our initial investigation of medium to high heating rates in section 3.2 (Figure 3.6) alongside the results of 1 °C/min depositions with source masses above ~ 65 mg in section 3.3, showed that non-uniform, rough films could be produced with this technique. This was investigated further as a potential alternative route to producing high surface area to volume ratio nanostructured coatings that could be compared to the ZnO-SiO_2 core-shell NRs for DNA binding. To do so, the PDMS source mass was kept constant at 70 mg alongside the steady-state deposition temperature of 500 °C, and the effect of the heating rate on the resultant SiO_2 morphology was investigated. Si substrates were coated using a variety of heating rates and imaged the resultant morphologies in both plan view and cross-sectional view, and the results are shown in Figure 3.24.

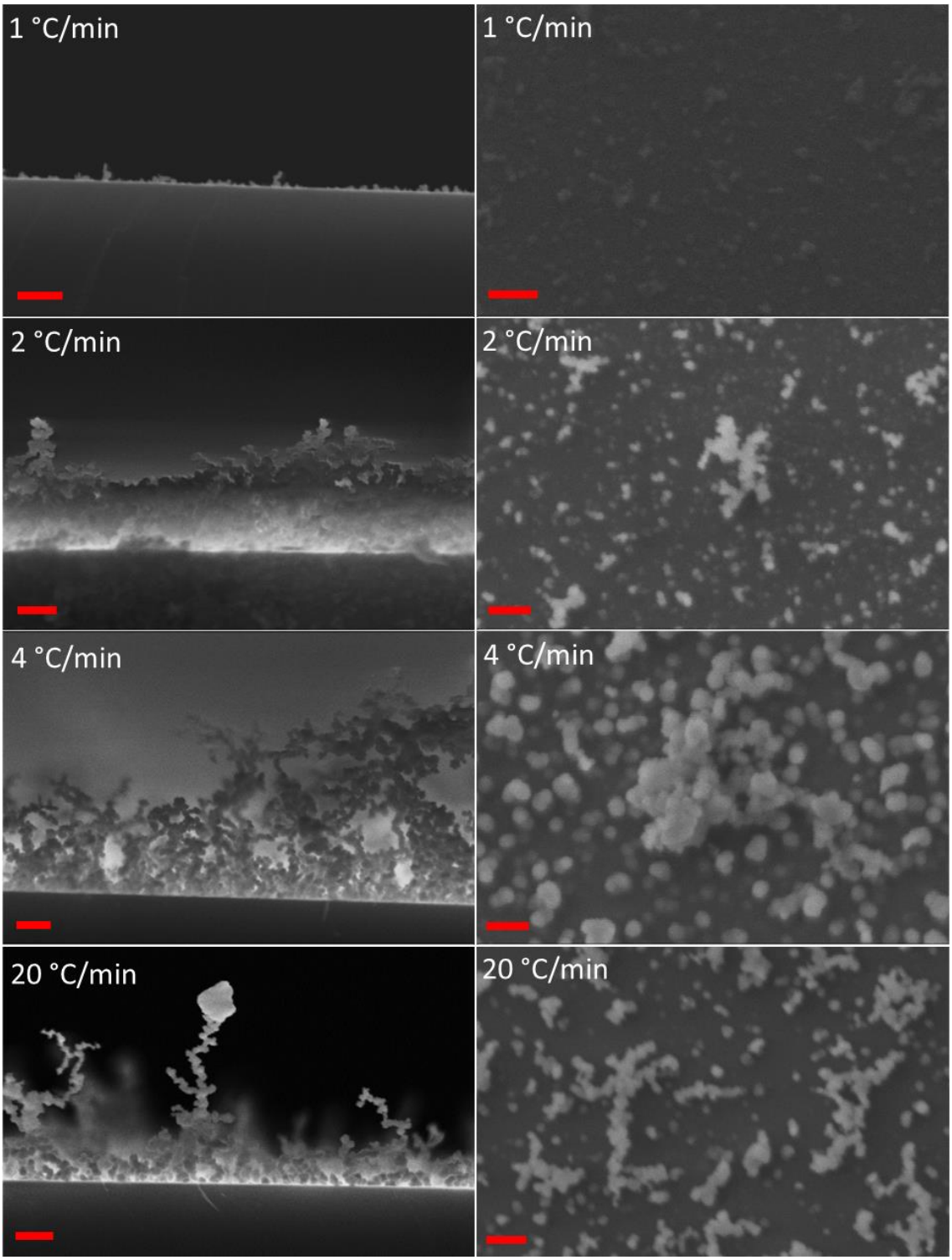

Figure 3.24: SEM data showing effects of heating rate on SiO_2 deposition morphology using a constant PDMS mass of 70 mg. Cross-sectional images are shown on the left and the corresponding plan-view image is shown on the right. The scale bar in all images represents 1 µm.

At the lowest heating rate of 1 °C/min the 2D film morphology can be seen as expected of this low heating rate regime, however with the addition of very small 3D dendritic nanostructures emerging. At a heating rate of ~2-3 °C/min however a sharp change in the deposit morphology is seen, whereby the deposited material no longer forms a thin planar

film but rather a nanoscale 3D dendritic nanostructure. Heating rates up to 40 °C/min have been explored and the dendritic morphology is observed up to the maximum heating rate obtainable in our furnace (40 °C/min). Previous studies of the thermal degradation mechanisms of PDMS report that PDMS will form ceramic silicon oxycarbide at high heating rates [112], [113]. However, EDX analysis of the SiO_2 structures shown in Figure 3.24 confirms pure SiO_2 stoichiometry, with 20 and 40 °C/min dendritic structures having Si:O ratios of 1:2.1 and 1:1.9 respectively. These high surface to volume ratio structures, particularly those obtained at 40 °C/min, are comparable in height to the CTRVPT ZnO NRs (approx. ~ 6 micron), allowing for meaningful comparison of their DNA binding capabilities.

This was a very promising result, as this could provide a desirable and effective alternative route to producing low-cost SiO_2 nanostructures in a facile, single-step manner that negates the need for the multi-step ZnO NR core. The 40 °C/min heating rate also drastically reduces the deposition time compared to the 1 °C/min heating rate required for the 2D thin films (12 minutes vs 8 hours required to reach the steady-state deposition temperature). A more comprehensive overview of these SiO_2 dendrites obtained at 40 °C/min is shown below in Figure 3.25, with SEM images of the dendrites on an Si substrate at a variety of viewing angles and magnifications to demonstrate the uniformity of the substrate coating and dendrite distribution.

Despite the relatively uncontrolled and random nature of the dendritic growth compared to the ZnO NRs, they show good surface coverage with a reasonable consistency in size and inter structure spacing. The large size and interspacing likely arises from the deposition configuration which resembles that of glancing/oblique angle deposition (GLAD) techniques [129]. These techniques are typically performed by magnetron sputtering under vacuum, and it is the high kinetic energy vapour species which do not undergo any collisions between source and substrate that give rise to well-defined, tilted nanostructure arrays. The deposition reported in this work is rather different since it is performed by evaporation in air at atmospheric pressure, giving rise to low kinetic energy vapour species. Nonetheless it was hypothesised that the large interspacing of the 3D dendritic nanostructures in Figures 3.24 and 3.25 very probably arises from the shadowing effects which are commonly seen in GLAD processes [130].

The realisation of the similarities between our technique and GLAD techniques helped provide insight into the generation of small dendritic structures even in the low heating rate regime. It is likely that ~ 65 - 70 mg of source mass is approximately the threshold at which

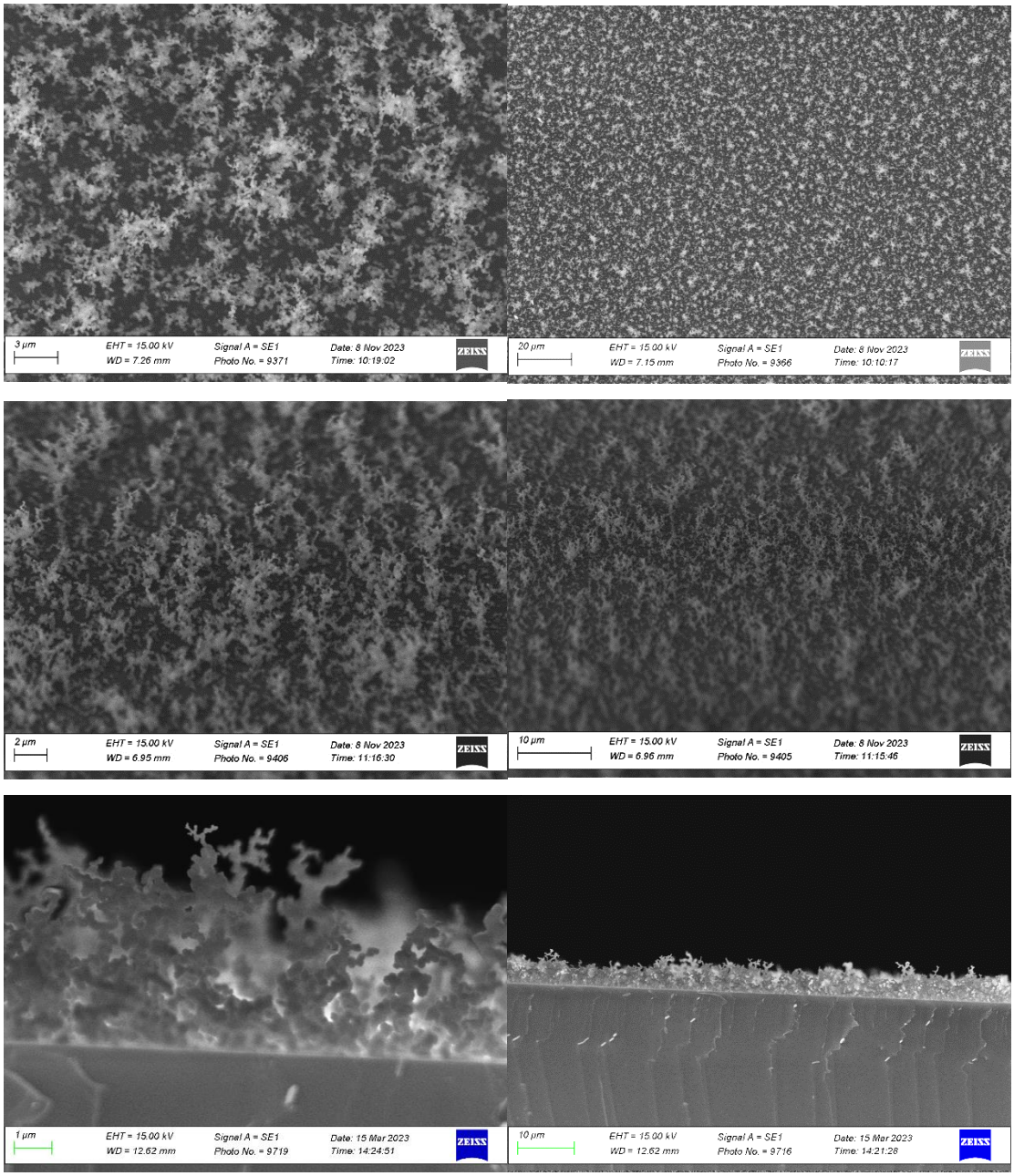

Figure 3.25: (Left) High and (right) low magnification SEM images of 40 °C/min dendrites at viewing angles of (top) 0°, (middle) 60°, and (bottom) 90° showing the uniform coverage of dendrites on the Si substrate.

enough vapour is generated such that surface trapping and shadowing effects of GLAD techniques arise. These effects would give rise to these uneven deposits akin to the larger dendrites grown under the significant amount of vapour generated at high heating rates.

Although the goal of producing ultrathin 2D films was achieved, the next step was to better understand our deposition technique and look at possible ways of overcoming the effective 18 nm limit found in section 3.3 and produce thicker 2D films without these dendritic structures. To do that, bare Si wafers and ZnO buffer layers were coated in multiple cycles of < 65 mg of PDMS in an attempt to surpass this limit. A Si substrate and a ZnO buffer were

coated in three separate deposition cycles of 6 mg each and compared to single cycles of equivalent mass (12 and 18 mg single depositions). The Si substrates were analysed using SE, and the ZnO substrates with XPS. A Si substrate was coated in two cycles of PDMS-based SiO_2 using 40.1 mg of PDMS with the aim of achieving a 20.5 nm deposition (based on the equivalent total PDMS mass used), and the results are shown in Figure 3.26.

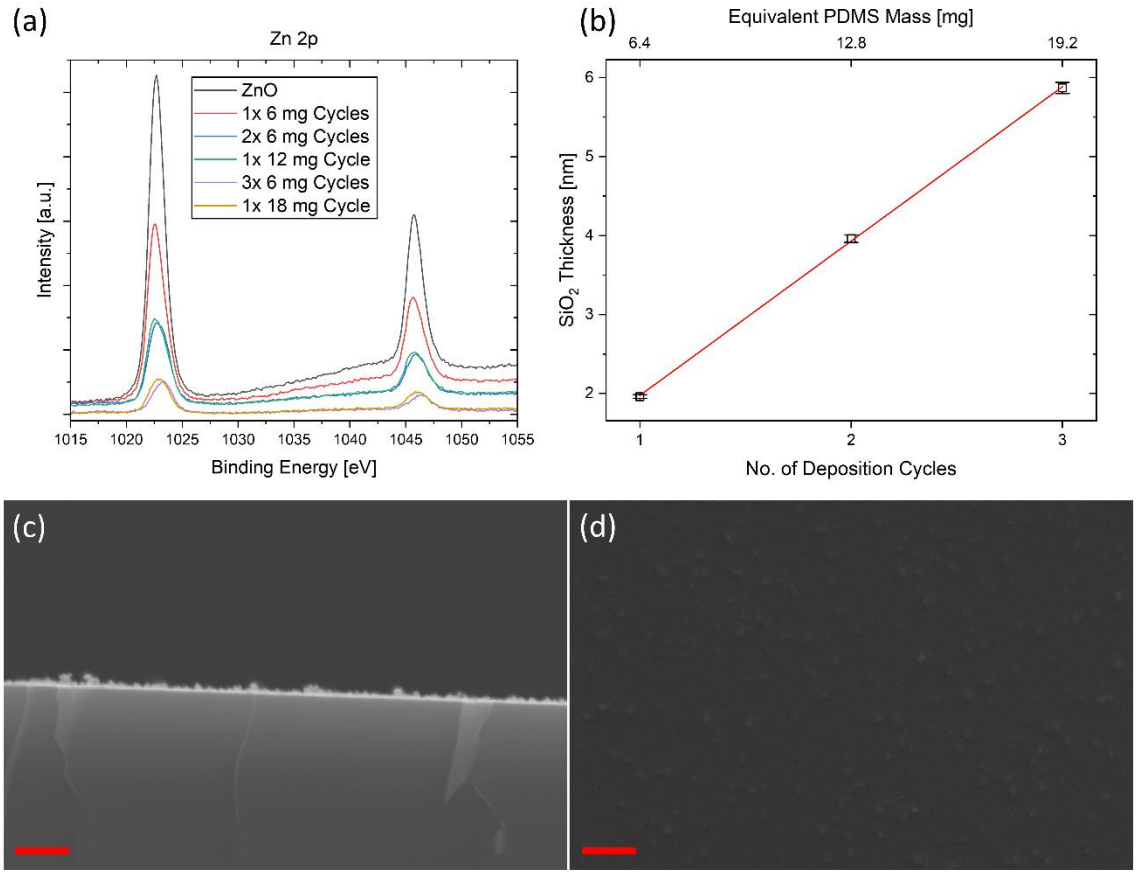

Figure 3.26: Comparison of multiple cycles of PDMS-based SiO_2 deposition and single cycles of equivalent total mass showing (a) XPS data for deposition on planar ZnO and (b) SE data for deposition on bare silicon substrates, where the straight red line is the best fit line (c) cross-sectional SEM and (d) top-down SEM images of an SiO_2 film deposited by two consecutive deposition cycles of 40.1 mg of PDMS each. The scale bars in (c) and (d) represent 1 µm.

A comparison of Zn 2p intensity of flat ZnO layers coated in one, two and three cycles of 6 mg PDMS-based depositions, with samples coated with either one cycle of 12 or 18 mg PDMS is shown in Figure 3.26a, showing excellent agreement in relative intensities, with only slightly increased coating efficiency with multiple smaller depositions, indicating that the SiO_2 vapour does not show significant preferential deposition on SiO_2 substrates. The Zn 2p peak is shown because it has a much higher relative sensitivity factor than Si 2p, and O 1s (28.72 versus 0.817 and 2.93, respectively, used in CasaXPS), allowing us to better visualise small changes in the coating thicknesses [131]. The SE data of the SiO_2 coating on an Si substrate in Figure 3.26b shows that n deposition cycles of a given mass x will return

a final thickness equal to n times x to a high degree of accuracy. The SEM data of the two 40.1 mg depositions shows a lack of features in Figure 3.26d, indicating a flat 2D film deposition. The SE fit determined a thickness of 21.4 nm, although the cross-sectional SEM shows the film is less uniform than the < 18 nm coatings of Figure 3.14 and 3.17. However, the film is more uniform than the single 70.0 mg deposition (1 °C/min images of Figure 3.24) despite the equivalent mass of this deposition being 80.2 mg. This is a promising result as it may allow flat films >18 nm thick to be achieved without creating dendritic structures.

3.7. Conclusions

In this chapter the development and optimisation of a novel and straightforward method for deposition of high-quality, nanoscale SiO_2 films and 3D SiO_2 nanostructures using thermal decomposition of polydimethylsiloxane (PDMS), in a furnace in atmospheric pressure at 500 °C was demonstrated. The temperature ramp rate is a key factor in determining the SiO_2 deposit morphology, with slower ramp rates leading to highly conformal 2D films and faster ones yielding 3D dendritic nanostructures.

Detailed characterisation using CP, SE, SEM, STEM, FESEM, FTIR, EDX, and XPS confirm that this method allows individual nanometre controllability of conformal pinhole-free layers on a variety of materials. For the 2D films the film thickness, as determined by SE data and confirmed by SEM data, is shown to correlate excellently with initial PDMS source material mass in the thickness range 0.8 – 18 nm. Depositions on high aspect ratio ZnO nanostructures are shown to be highly conformal, leading to core-shell ZnO-SiO_2 nanostructures whose shell thickness is in excellent agreement with the expected values from deposition on planar substrates. Electrical breakdown measurements confirm that the breakdown strength of the films is comparable to that of high-quality industrial thermal oxides.

At faster temperature ramp rates an abrupt morphological transition is seen to a deposit which displays a 3D nanodentritic morphology with a high surface to volume ratio. Despite the relatively uncontrolled conditions of the deposition, the nanodendrites show consistent heights and interspacing across large areas of coated substrates (1 - 4 cm^2).

The findings presented in this chapter underscore the versatility, controllability, and precision of our novel SiO_2 deposition system, allowing for high-quality SiO_2 deposition of a variety of thicknesses and morphologies in an incredibly straightforward and low-cost manner compared to current SiO_2 deposition techniques.

4. Silicon Nanoparticle Synthesis

In this chapter both ligand-free and DNA-functionalised Silicon Nanoparticles (SiNPs) were produced by Laser Ablation Synthesis in Solution (LASiS) (sometimes referred to as Pulsed Laser Ablation in Liquids (PLAL) in literature). LASiS has emerged as relatively facile technique for producing either ligand-free or functionalised NPs of a wide variety of materials without the need for environmentally harmful solvents. The previous chapter was concerned with the physical vapour deposition of SiO_2 NSs that will be employed as a proof of concept for DNA capture, with future work focused on functionalising these structures for capturing only specific DNA sequences. LASiS offers a means of functionalising the SiNPs during the synthesis step, which could be more cost-effective and efficient than post-synthesis functionalisation. However, typically LASiS produces low NP yields and functionalisation efficiencies compared to wet chemical techniques. SiNPs were produced under a variety of novel solvent flow configurations to address these issues, and their physicochemical properties were analysed. The SiNP production efficiencies of each flow configuration were measured, alongside the ligand-functionalisation efficiency using calf thymus DNA as a model biomolecule. The last section details the investigation of a drop-casting method for producing SiNP coated surfaces to be used for a variety of biomedical/biophysical applications discussed in chapter 5. The surface topography and SiNP coverage of these coatings on PLA substrates were characterised.

4.1. LASiS Growth Mechanism

LASiS is a green method for the synthesis of ligand-free and functionalised NPs [132]. It is a cost-, labor-, and time-efficient technique that does not require chemicals that potentially inhibit subsequent reactions [133]. LASiS involves immersing a solid target in a solvent and irradiating it with a high intensity pulsed laser. The laser radiation vaporises the solid surface structure and surrounding liquid environment, creating an oscillating cavitation bubble [134]. The oscillation within the highly confined conditions and subsequent induced high-pressure of the cavitation bubble by the surrounding liquid causes the ablated matter to nucleate and agglomerate, forming NPs. This nucleation site then acts as a growing centre for the adsorption of species within the liquid [135]. This technique is capable of a high degree of customization and control, as NP morphology can be precisely controlled by altering the various process parameters such as the liquid solvent and laser wavelength, power, and repetition rate [136]. These processes are schematically illustrated in Figure 4.1.

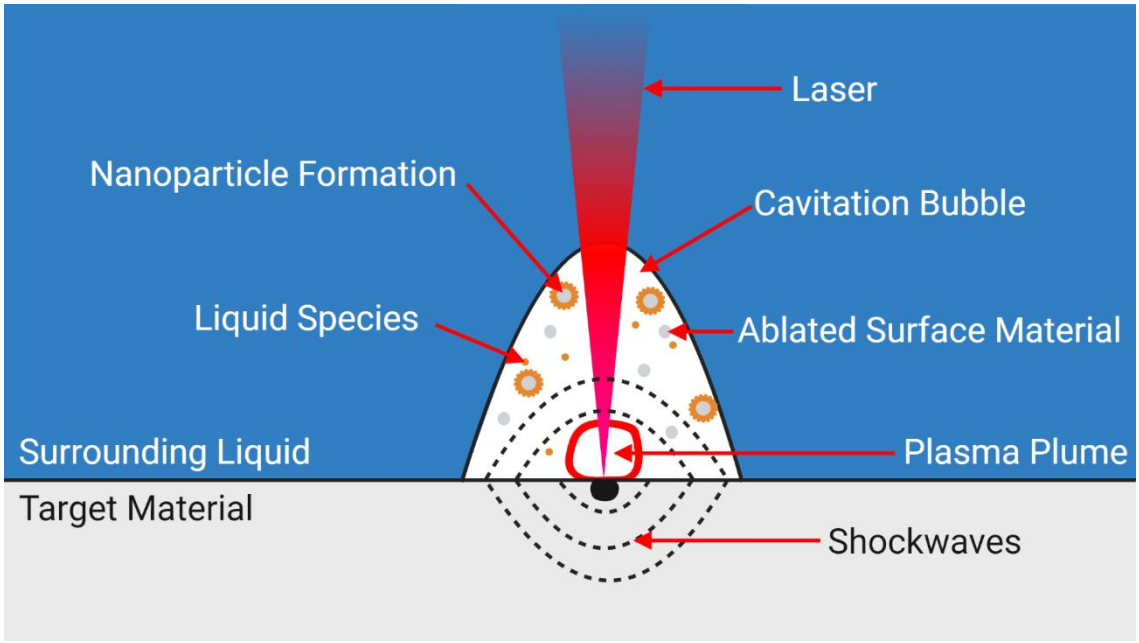

Figure 4.1: Illustration of the various components of the LASiS technique.

In this chapter, a silicon target was ablated in DI H_2O to create Si-core, SiO_2-shell SiNPs and also ablated a silicon target in a DNA solution to create SiNPs with a DNA functionalised surface, using double stranded DNA as a model biomarker for functionalisation. By ablating directly in a DNA solution, in addition to the increased binding efficiency *via in-situ* functionalisation, the scalability of this technique is increased by lowering the number of steps required to produce these functionalised NPs. Functionalisation of the SiNPs would allow for specific DNA strand capture, which is the focus of future work, beyond the scope of this thesis. The work in this thesis uses double stranded DNA as a proof of concept to demonstrate high efficiency synthesis and simultaneous single-step functionalisation. The SiNPs created in DI H_2O were used for surface coatings to compare against the ZnO-SiO_2 NRs and the SiO_2 dendrites, as Si-SiO_2 microbeads are the current state-of-the-art structure used for DNA sample preparation for PCR analysis [21]. An additional use of these SiNP coated surfaces arose in collaboration with another group within DCU, which will be discussed in section 5.3.

While LASiS has proven itself as a promising NP synthesis method, it is typically done under static flow conditions, i.e., the target material is ablated in an undisturbed petri dish or beaker filled with liquid [132]. This is a very simple technique to perform, but it is quite inefficient with low NP yields. In this work, the flow ablation process developed by Streubel *et al.* [137] and Waag *et al.* [138] was built upon, while using both the flow-cell design and recirculation configuration reported by Freeland *et al*. [139], [140], to recirculate liquid over

the target in a controlled manner to create a novel enhanced LASiS system. In doing so, the SiNPs are directed away from the ablation site, reducing the laser shielding effects created by the produced NPs, and allowing for significantly larger colloid production volumes and concentrations. The recirculation provides longer DNA-SiNP interaction times, at the site of NP creation, and under enhanced mixing conditions to further promote binding. The specifics of each setup are detailed further in section 4.2 below.

4.2. Materials & Methods

4.2.1. Laser Ablation

Previous work in our group has established the optimum parameters for SiNP generation from a silicon target [99.999% metal basis, Alfa Aesar] submerged in a liquid using a low-power micro-machining Nd: YAG laser [WEDGE HF 1064, Bright Solutions, Italy] as follows: (wavelength (λ) = 1064 nm, pulse duration (τ_p) = 100 ns, repetition rate (f_{rep}) = 10,000 Hz, fluence (F) = 1.83 J/cm^2) [81]. The beam was focused on the target, and raster scanned across the silicon surface at a speed of 2 mm/s, moving in an Archimedean spiral, using a 2D scanning galvanometer [Raylase SS-12]. This scanning process achieves a more uniform and efficient ablation compared to the cratering that occurs during stationary irradiation, and reduces the re-irradiation of previously generated NPs, which can create size

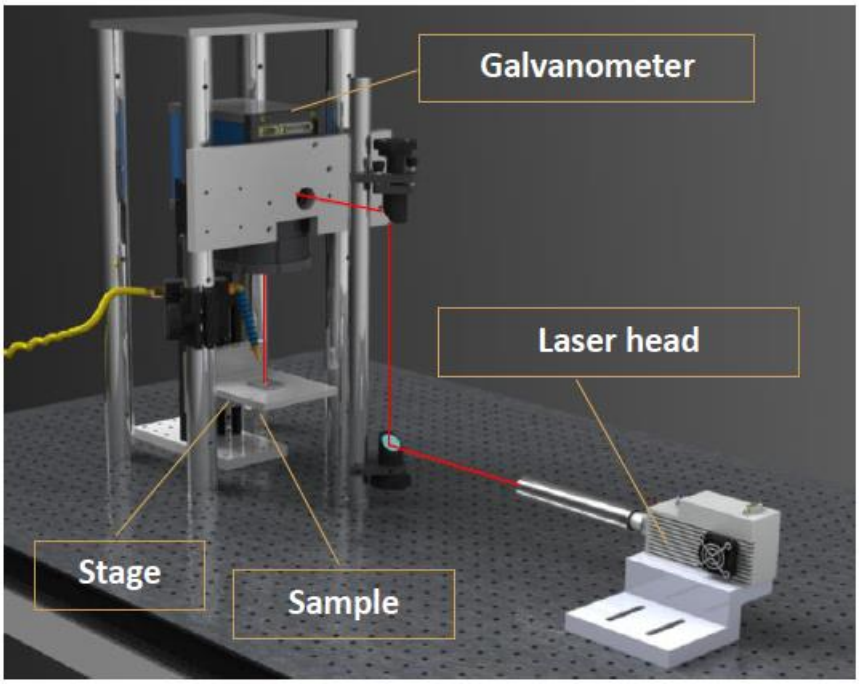

Figure 4.2: Schematic diagram of LASiS setup. The laser is directed into a galvanometer which scans the beam across the sample in a spiral pattern to increase the ablation efficiency.

heterogeneity and further reduce production efficiency [141]. The target was maintained within the laser beam-waist using an M404 4PD 1-D nanopositioning stage [PI, Germany], maintaining the laser spot size at a diameter of 100 µm. The laser beam intensity profile is Gaussian, exhibiting a near TEM_{00} mode (ellipticity 0.97) using an F-theta lens. A schematic diagram of the LASiS setup is shown in Figure 4.2.

4.2.2. DNA Preparation & Functionalisation Calculation

DNA solutions were made by dissolving calf thymus DNA [Sigma Aldrich deoxyribonucleic acid sodium salt from calf thymus) in an ionic buffer solution. The ionic buffer solution was obtained by mixing deionised water (DI H_20) and Qiagen PB binding buffer solution in a 20:1 ratio by volume, respectively. Calf thymus mass was measured gravimetrically and dissolved in the appropriate volume to achieve a stock solution concentration of 1 mg/mL. Serial dilutions of this stock were performed to achieve lower concentrations used in this work. Calf thymus was utilised for all DNA binding experiments in this work as it is a widely used strain for DNA binding studies [142], [143].

For DNA binding characterization, a 1mL aliquot of the colloid post-ablation was centrifuged [Eppendorf Centrifuge 5430R] at 17,500 rpm and 20 °C for 20 minutes. These parameters allowed for complete separation of unbound DNA from the DNA-SiNP conjugates. The DNA functionalised SiNPs formed a pellet, while unbound DNA remained in suspension. The fluorescence spectra of the supernatant was measured *via* fluorescence spectroscopy allowing for the quantification of unbound DNA. By measuring the DNA of the colloid before centrifugation (DNA_{Before}) and subtracting the DNA measurement of the separated supernatant ($DNA_{Supernatant}$), an estimate of the percentage of DNA functionalised onto the SiNPs ($DNA_{Funct.}$) could be acquired. The binding efficiency errors are calculated by propagating the standard deviations of both the colloid and supernatant fractions, with “n” denoting the number of measurements taken. This calculation is described below:

$$DNA_{Funct.} = DNA_{Before} - DNA_{Supernatant} \qquad (Eqn. 4.1)$$

An illustration of this process is shown in Figure 4.3.

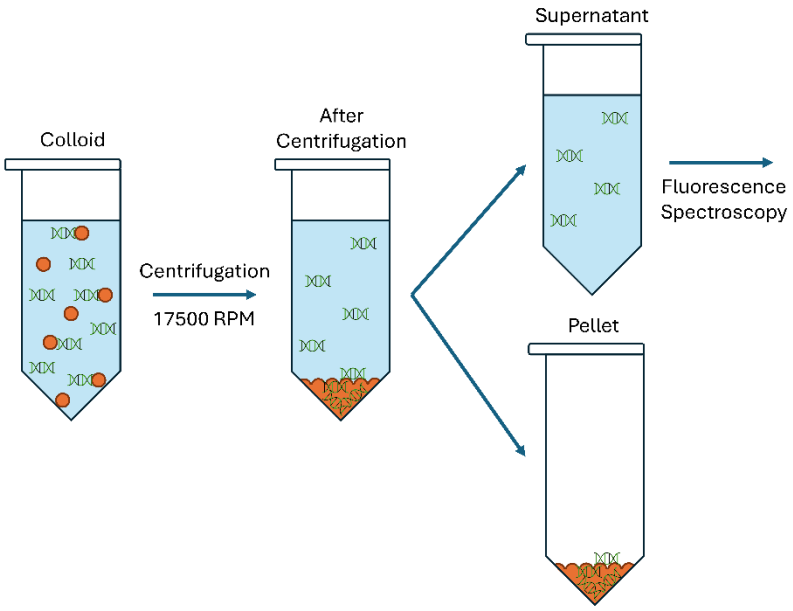

Figure 4.3: Illustration of SiNP and supernatant separation procedure to measure DNA functionalisation.

DNA binding was measured using the Quant-iT PicoGreen dsDNA Assay [Life Technologies, Dublin, Ireland]. This dye uses fluorophores which will only bind to double-stranded DNA, which not only serves as a measurement for the DNA, but it also showed that the DNA did not become denatured during the ablation process. The dye was made up of a 200-fold dilution of the concentrated dimethyl sulfoxide solution in the 1x TE buffer supplied with the PicoGreen Assay kit [10 mM Trisaminomethane-HCl, 1 mM Ethylenediaminetetraacetic acid, pH 7.5], within reflective foil covered plastic containers. The assay was performed in a 96-well plate [Nunclon MicroWell, Sigma Aldrich], where a 1:1 aliquot of sample and dye (40 µL each) was placed in each well. Other wells were filled with 40 µL of both buffer and dye to serve as the background for correction. The plate was covered in reflective foil, and the samples and dye were left to incubate for 5 minutes before being placed in a spectrofluorometer [Tecan Safire 2, Tecan Group Ltd, Switzerland]. The excitation (λ_{ex}) and emission (λ_{em}) wavelengths were 480 nm and 520 nm, respectively.

4.2.3. Flow Configurations

Typically, LASiS is performed under static conditions, that is, a metal target is ablated in a beaker containing liquid medium that is stationary and not moving. Four different ablation conditions were investigated, which are illustrated in Figure 4.4.

The first method investigated was a two-step *ex-situ* binding (Figure 4.4a). This involved ablating a silicon target in 11 mL of the ionic buffer solution without DNA for 20 minutes,

removing the sample of SiNPs and then mixing the SiNP colloid with DNA for approximately 10 s post-ablation.

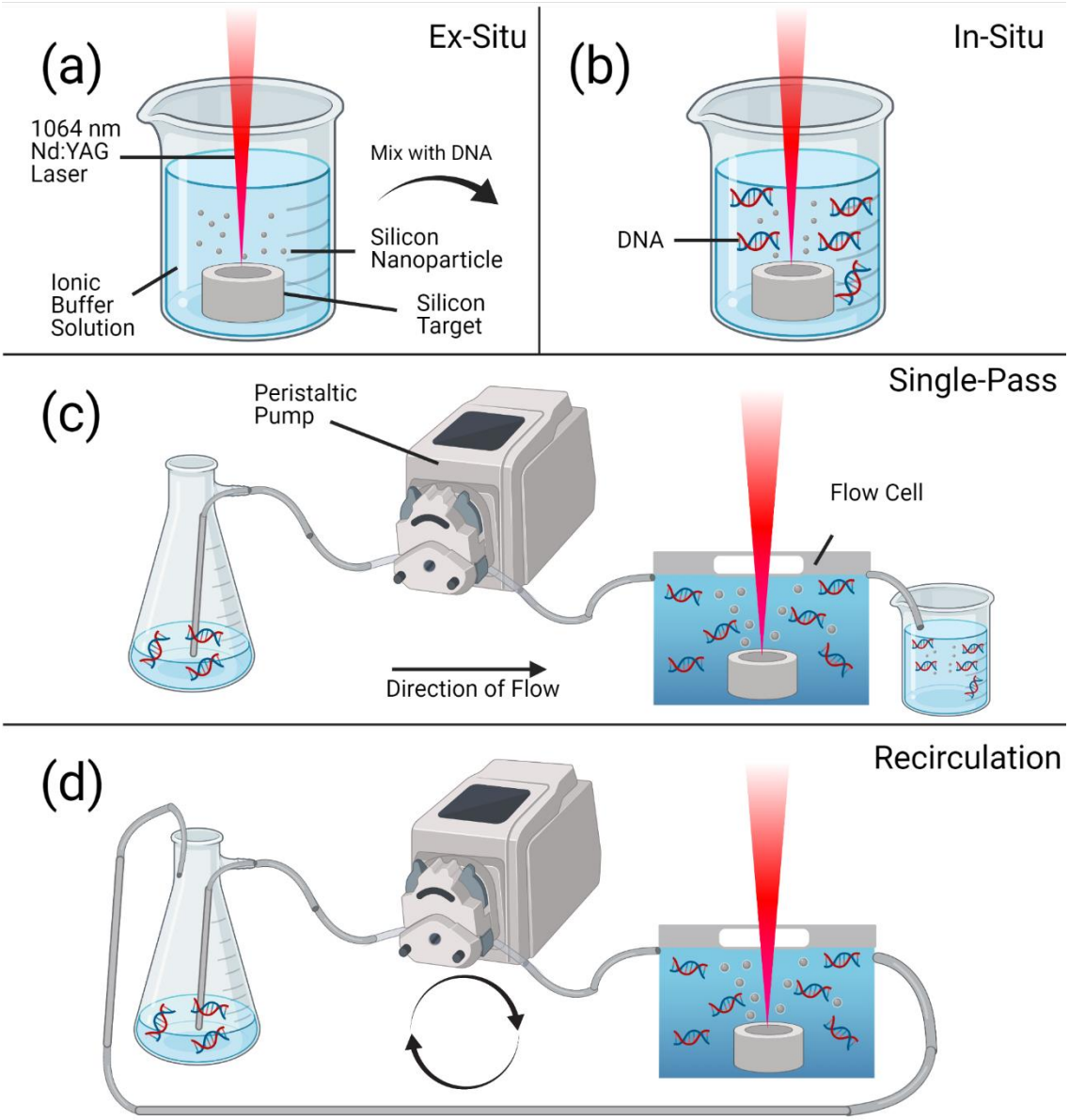

Figure 4.4: Schematic diagram of the different LASiS setups (a) Static ex-situ ablation. (b) Static in-situ ablation. (c) Single-pass flow ablation. (d) Recirculatory flow ablation. Created with BioRender.com.

For static in-situ functionalisation (Figure 4.4b), the silicon target was placed in a petri dish and submerged in 11 mL of the ionic buffer solution containing 2, 20 or 100 µg/mL DNA and ablated for 20 min.

Single-pass (non-recirculatory) flow ablations were performed using the setup shown in Figure 4.4c. Using the design reported by Freeland *et al.* a 3D-printed flow cell was custom-designed such that the liquid flow is laminar, thereby removing occluding bubbles,

particles, and debris and maintaining ablation efficiency. A reservoir was filled with 2 µg/mL DNA solution and a peristaltic pump [Isamatic MCPV510 with Millipore XX80EL005 head] passes the fluid around the tubing network [polytetrafluoroethylene tubes, total volume 22.5 mL] and into a collection beaker on the opposite end of the flow cell at three different flow rates (40, 85, and 135 mL/min]. Initially, the liquid was allowed to flow into a waste chamber for up to 10 s (this varied depending on the flow rate) before being directed into the new beaker. This was to ensure that only DNA-SiNP colloid was being collected instead of the pure DNA solution used to prime the flow system prior to ablation. The liquid is allowed to pass over the target only once during ablation before being collected. Contrary to the other methods discussed, the single-pass method was not performed for a specific time but rather 40 mL of DNA solution was placed in the reservoir, and the test was stopped after the reservoir was emptied. 15 mL was used to prime the system and the working volume was 25 mL. Considering the higher flow rates would require litres of DNA solution for a single test, and multiple repeat tests were performed, the same volume of DNA solution was used as the recirculatory ablation method discussed below. Because the SiNP concentrations during the single-pass method are time independent, this was believed to be an approach enabling meaningful comparison with other methods.

Controlled recirculatory flow ablations (Figure 4.4d) utilised the same setup as Figure 4.4c; however, the outlet tubing was placed back into the initial DNA reservoir rather than into a separate collection beaker. Here, 25 mL of the same DNA solution is circulated over the target multiple times in a closed loop at a constant flow rate of 135 mL/minute for varying ablation times (5, 10, 20, 40, and 60 min).

All samples were allowed to settle for a 12 – 16-hour period prior to centrifugation and binding analysis.

4.2.4. SiNP Characterisation

The size and morphology of the SiNPs produced were characterised *via* DLS, FESEM, and Transmission Electron Microscope (TEM) imaging. TEM was performed by collaborators[1] using a BioTwin lens with a 120 kV LaB6 emitter at 3 Å resolution limit and a Veleta 2048 × 2048 wide angle detector. Samples were prepared using a copper mesh TEM grid with 40 µL of sample applied and allowed to evaporate at room temperature.

[1] TEM was carried out by Ms. Mandy Juillerat and Dr. Michal Dabros from the School of Engineering and Architecture, HES-SO University of Applied Sciences and Arts Western Switzerland, Bd de Pérolles 80, CH-1700 Fribourg, Switzerland.

The chemical and crystallographic properties of the produced particles were characterised using EDX, FTIR, and XRD. For EDX and XRD, 100 µL of SiNPs in concentrations ranging from 3 to 8 mg/mL were pipetted onto silicon-carbide substrates (4H-SiC) and allowed to dry at room temperature. This was repeated 10 – 15 times to achieve an appropriately thick coating for each analysis. EDX spectra were obtained for an incident 5 keV electron beam. FTIR was performed by pipetting the same solutions onto the attenuated total reflection (ATR) attachment of the system. FTIR spectra were corrected for air, but the respective pure solvent spectra were recorded for comparison. EDX and transmission FTIR were also used to quantify SiNP surface coating coverage alongside SEM data.

The colloid concentration was determined using UV-Vis spectroscopy and gravimetric analysis of the cleaned silicon target before and after ablation. The spectrometer scan range was 220 – 800 nm, moving in 0.5 nm intervals. The recorded UV-Vis spectra were corrected for the solvent (DI H_2O, buffer, or DNA-buffer) contribution.

Stability and wetting properties of SiNPs were determined using zeta potential of SiNPs in solution and contact angle measurements of SiNP coated PLA discs respectively.

4.3. SiNP Synthesis

By DLS measurement, ~98 % of SiNPs produced in the DNA-Buffer solution (Figure 4.4b) were within the size range of 25 - 100 nm, with a peak distribution at 40 nm, when measured shortly after synthesis. SiNPs produced in DI water were larger (peak = 60 nm), with a broader, long-tailed size distribution (Figure 4.5.a). This DLS measurement is supported by a TEM image of SiNPs produced in DI water (Figure 4.5.c) showing the nanoscale dimensions of spherical SiNPs. It was expected that SiNPs made in DNA-buffer would be smaller compared with those in DI water due to size capping effects of ligands during LASiS. This size-capping phenomenon has been demonstrated numerous times using biomolecules [133], [144], [145], [146], [147], [148]. While it is expected that SiNPs produced in DNA would exhibit ultrasmall diameters (5 - 20 nm), the larger apparent sizes seen in the DLS measurement may be due to the fact that the hydrodynamic diameter of the conjugated particles is measured, rather than a direct measurement of the core NP diameter. DNA ligands on the surface of the core NPs may also be interfering with the measurement, indicating a larger particle size. It is well known that hydrodynamic-based measurement techniques such as DLS report larger particle diameter sizes compared with direct imaging techniques such as TEM for conjugated and unconjugated NPs, as reported

widely in literature [133], [134], [145], [149], [150], [151]. Agglomeration effects for SiNPs made in DNA were also directly observed. Time delays between synthesis and measurement of these samples lead to distinct changes in the measured sizes, shown in

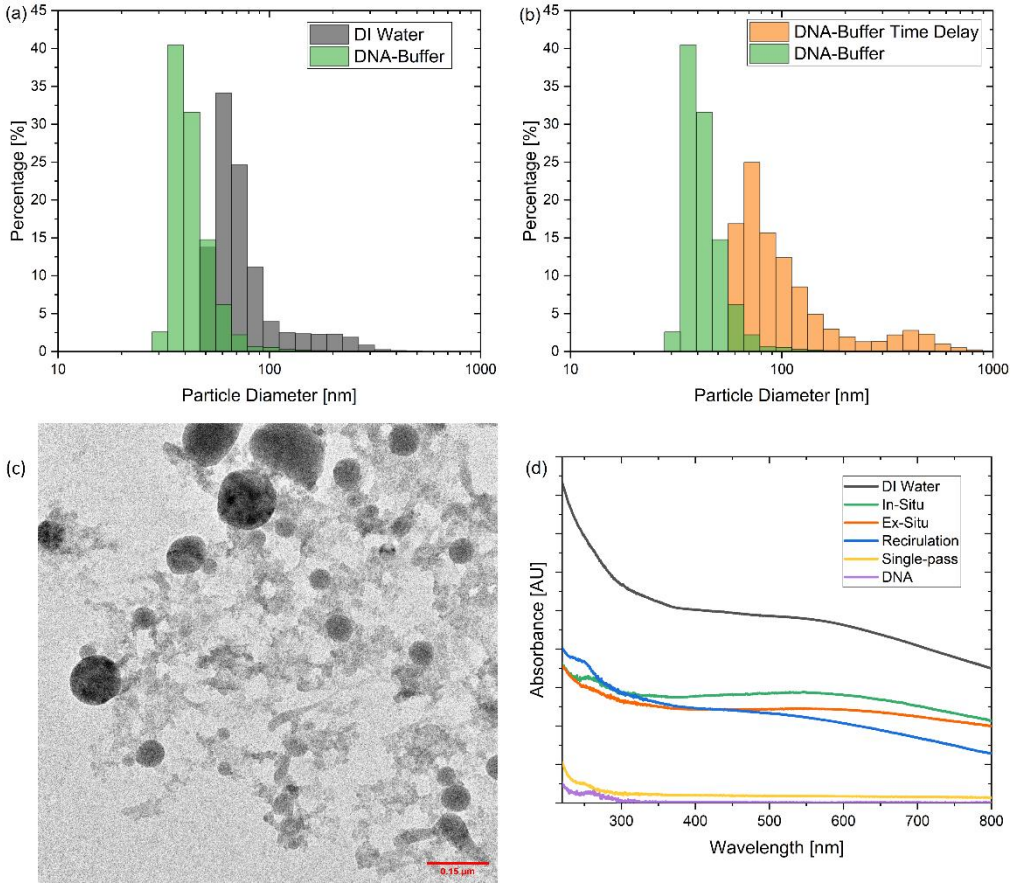

Figure 4.5: (a) Size distribution of SiNPs with largest peaks between 25 and 100 nm in diameter (n = 3) (b) Size distribution of SiNPs produced in DNA-Buffer, showing the agglomeration effects over time due to a time delay between synthesis and measurement (c) TEM image of SiNPs with 150 nm scale bar (d) UV-Vis spectra for SiNPs ablated under each flow condition for 20 minutes in 2 µg/mL of DNA alongside a pure DNA sample for reference. (n = 3) (Single-pass ablations are time independent and DI Water and Ex-Situ ablations are free from DNA).

Figure 4.5b. NPs tend to agglomerate over time, so for a true size comparison, the time delay between synthesis and measurement must be kept constant for all NP samples [134]. By performing synthesis in a DNA solution, followed by immediate DLS measurement, a reduction in size beyond that of SiNPs produced in DI water was observed. Thus, size capping effects of the DNA ligands were observed. However, the fact remains, that DLS measurement doesn't indicate the diameter of the core SiNP, but rather its hydrodynamic diameter.

Furthermore, it was observed that the peak diameter of DNA-functionalised SiNPs increased with ablation time during recirculatory ablation testing 20-minute recirculatory ablation tests reported DNA-functionalised SiNPs with hydrodynamic diameters of 80 - 150

nm, whereas 60-minute ablations produced NPs with diameters of 100 - 500 nm. The DLS size distributions for SiNPs synthesised in each flow configuration are shown in Figure 4.6.

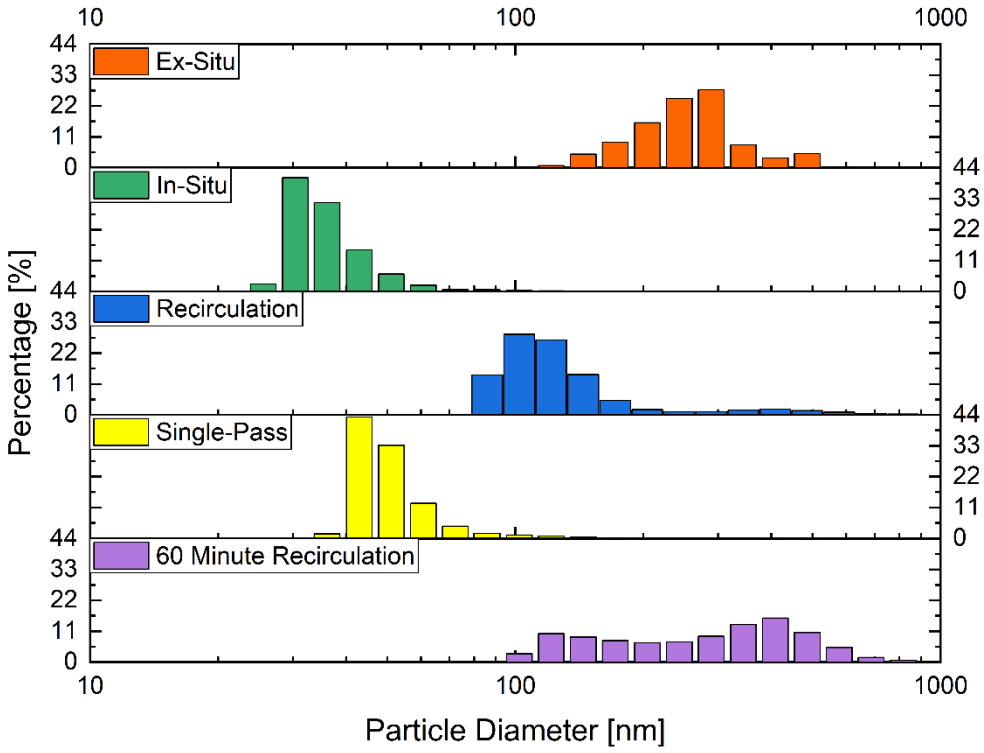

Figure 4.6: Hydrodynamic diameters of SiNPs synthesised under the various flow configurations shown in Figure 4.4.

Bare metallic NPs size reduction with increased ablation time under recirculatory flow conditions has been reported previously [152]. The authors reported that the size reduction was due to reirradiation of the metallic particles, however DNA functionalised NPs have been observed to perform differently in this work. The hydrodynamic size increase observed Figure 4.6 may be due to increased DNA binding on the surface of the SiNPs, leading to larger particle diameters measured by DLS. Indeed, increased DNA binding with ablation time is observed in this work (shown in section 4.4.2.). Additionally, the influence of ionic salts and/or DNA which may cause SiNPs to aggregate more quickly over longer time durations cannot be ruled out, the latter of which likely explains the large hydrodynamic diameters seen in the ex-situ DLS data of. Additionally, any SiNPs not functionalised with ionic salts could be attracted to and subsequently bind to salt functionalised SiNPs, leading to larger overall particle behaviour. These effects cannot be quantitatively measured using zeta potential measurements. However, zeta potential measurements were performed on ligand-free SiNPs produced in DI water under recirculatory flow conditions, indicating strong stability with a zeta potential of -31.02 ± 0.45 mV (Figure 4.7) [153].

Ultrasmall SiNPs are known to have excitation and emission wavelengths (λ_{ex} and λ_{em}) in the near UV and blue-green regions of electromagnetic spectrum, respectively, which is indicated by the steepness of the shoulder seen in the UV-Vis absorption spectra shown in

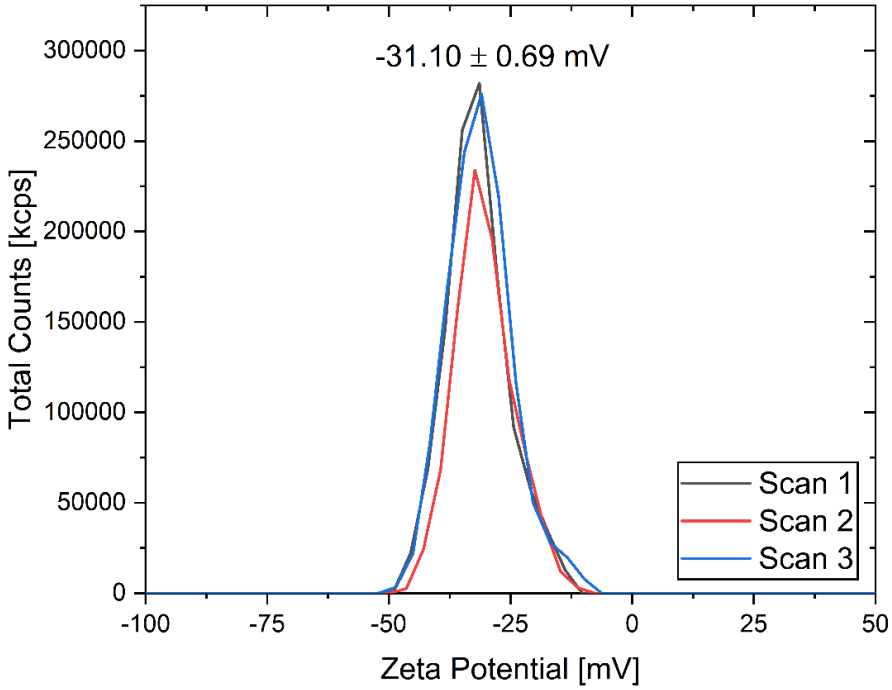

Figure 4.7: Zeta potential measurements of three different 50 mL SiNP samples, indicating strong stability of ligand-free SiNPs (i.e. < - 30 mV).

Figure 4.5d [154]. Since PicoGreen fluorophores (λ_{ex} = 480 nm, λ_{em} = 520 nm) were used, it was first verified that the fluorophores did not bind to the SiNPs on their own and that the SiNPs themselves are not fluorescent at these wavelengths given that the shoulder occurs around the emission-excitation band (Figure 4.5d). The UV-Vis absorption spectra in Figure 4.5d shows the clear presence of DNA and SiNPs (or lack thereof) in the colloids, indicated by the characteristic DNA absorption peak at 260 nm and the broadband absorption of all wavelengths associated with SiNPs. While the UV-Vis data shows qualitatively the presence of SiNPs and functionalised DNA, it cannot be used to quantify the functionalisation as one cannot distinguish the relative contributions from the DNA and SiNPs to the 260 nm peak of the colloid. Therefore, fluorescence spectroscopy was used for the quantification of captured DNA as it provides a measurement of only DNA and not the SiNPs.

Composition and crystallographic data for the produced SiNPs were obtained using XRD, FTIR, and EDX. The XRD data (Figure 4.8a) for SiNPs in water indicates a polycrystalline deposit, with peaks in excellent agreement with theoretical angles for the cubic structure silicon crystal planes (JCPDS 27-1402), typical for SiNPs in literature [155], [156]. The SiNPs

in DNA solution similarly show the Si (111) peak (which is expected to be the most intense peak in a powder pattern), albeit with a significantly reduced intensity. This reduced intensity may be due to the smaller particle sizes/volumes, because of the size capping of

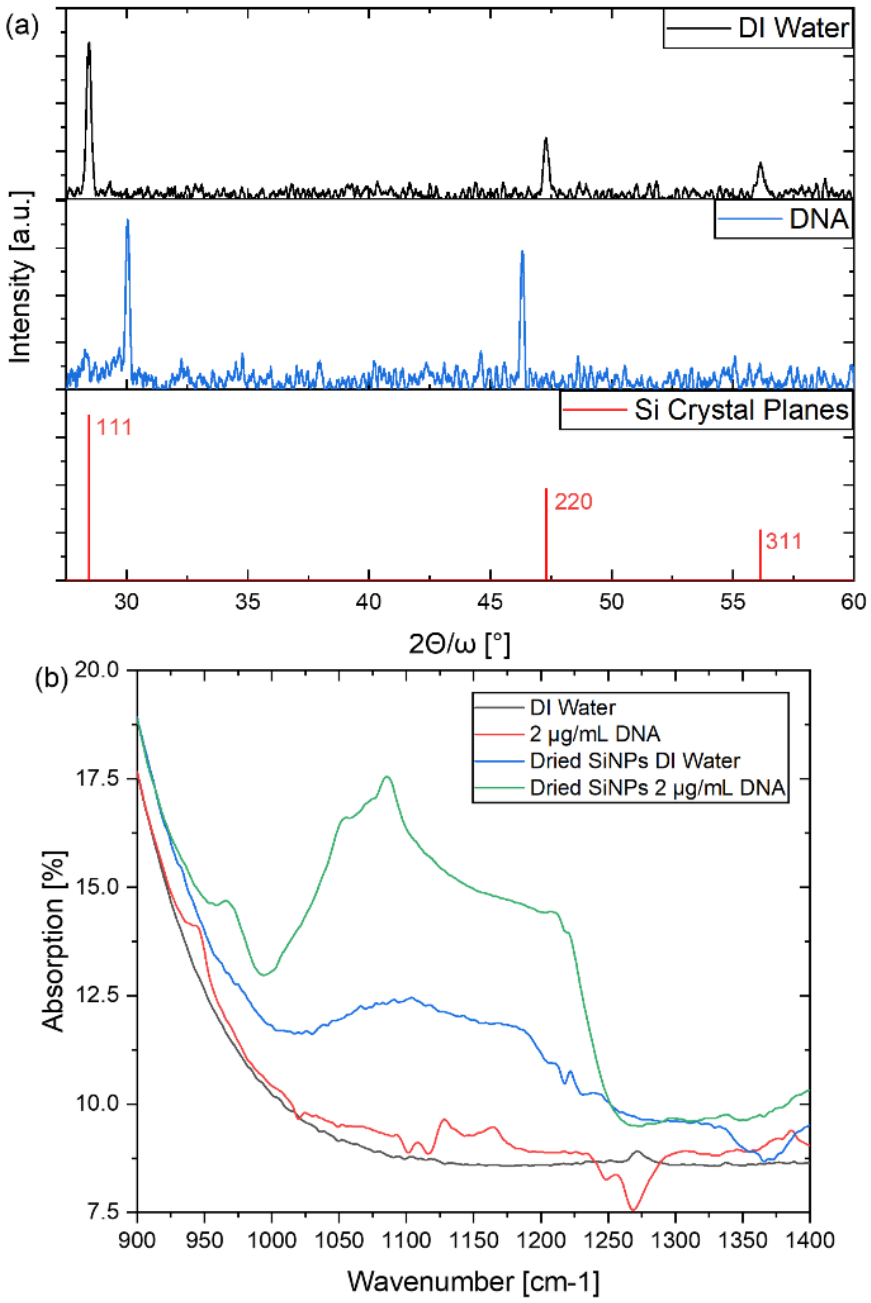

Figure 4.8: (a) XRD patterns obtained for SiNPs made in DI water and DNA alongside the locations of theoretically calculated silicon crystal planes. (b) FTIR Spectra obtained for the same SiNP samples alongside their respective solvents.

ligands, since powder pattern XRD intensities are proportional to volume [157]. The two other peaks present in the DNA-SiNP spectra are likely due to some remnant chloride salts from the ionic buffer solution. Given the reduced (111) peak intensity, the (220) and (311)

peaks are likely below the limit of detection. These XRD data confirm the presence of crystalline Si material in the NPs, as the core of the SiNPs. FTIR data (Figure 4.8b) shows a broad and distinct peak at 1104 cm^{-1} and 1086 cm^{-1} for SiNPs in DI water and DNA, respectively. These peaks correspond to the characteristic asymmetric stretching vibrations of the Si-O-Si bond of silica [153], [155], [158]. A smaller peak in the DNA SiNP spectra was observed at 966 cm^{-1}, potentially indicative of the Si-OH bond [155] However, this could be a shifted peak from the DNA spectra as a similar peak was seen around 944 cm^{-1}. To obtain stronger FTIR signals, 60-minute recirculatory ablations were performed in 50 mL of DI water to obtain a larger volume and concentration of colloid, and 20 mL was taken and centrifuged to produce a final concentration of 1.52 mg/mL. By taking 5 µL of this concentrated solution and allowing it to evaporate on the ATR crystal, significantly better signals were obtained, revealing more silica peaks that were previously hidden by the leftover DI water peaks of Figure 4.9.

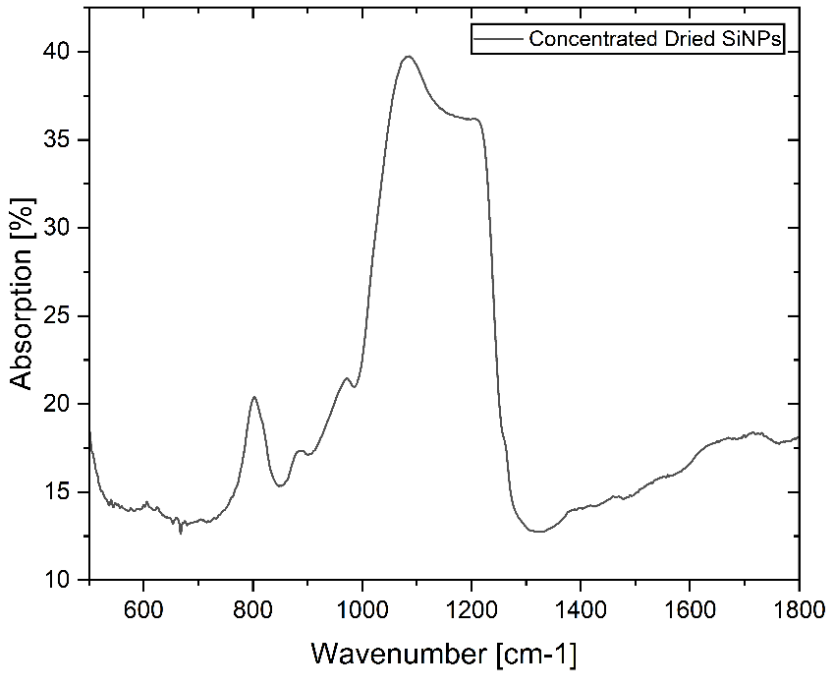

Figure 4.9: FTIR spectra of concentrated SiNP colloid revealing absorption peaks that were masked by adsorbed H_2O in Figure 4.8b.

These hidden peaks are the Si-OH bond at 970 cm^{-1}, and another Si-O-Si bond at ~800 cm^{-1}. This FTIR data confirms the presence of silica in the NPs, and the combined XRD and FTIR results provide strong evidence of silicon-core, silica-shell SiNP structures, which is in agreement with previous reports of SiNPs made by LASiS [133], [159]. This oxide shell is of particular importance as previous groups have discovered that the binding of DNA to SiNPs during LASiS occurs at defect sites in the silica layer, which is likely to also be the

functionalisation mechanism for our NPs [133]. Using Raman scattering, the chemical bonding between SiNPs and the DNA backbone was identified as a stretching vibration of Si-C/Si-CH ($H_xC4-_x-SiO_x$, x = 1-3). These results are supported by EDX analysis, which show the predominance of silicon and oxygen in the SiNP samples. The atomic percentages of each are shown in Table 4.1.

Table 4.1: EDX data for SiNPs synthesised in DI H_2O and DNA-buffer showing the atomic percentages of Si and O.

Element	DI-H2O SiNPs	DNA-Buffer SiNPs
Silicon	82.08 ± 8.41 %	55.12 ± 27.95 %
Oxygen	17.99 ± 8.42 %	44.76 ± 27.36 %

The DNA-SiNPs also contained signals from chlorine from the ionic buffer but, in both solutions, silicon and oxygen signals dominated the emissions.

While Figure 4.5 shows the difference in concentration for each method during a common 20-minute ablation, the differences in productivity and efficiency with time for each method is illustrated in Figure 4.10. Single-Pass concentrations were time independent and not calculated gravimetrically due to the unmeasurable differences in weight after such short ablations in the more viscous DNA-Buffer, as well as the large volumes required to perform experiments for such a time that the weight difference could be measured. Figure 4.10a shows the production efficiency plateauing due to shielding of the target by the ablated species after around 10 minutes in both static ablations, whereas dynamic flow ablation shows a close to linear relationship over the one-hour region tested, demonstrating a key advantage of the recirculatory set-up. It takes longer for the plateau to develop in the buffer compared to DI water due to their relative viscosities. The buffer is much more viscous than DI water, which reduces the ablation efficiency [160]. Therefore, it takes longer to synthesize enough SiNPs to shield the target from the laser beam. This is further shown by the similarities of static and dynamic ablation in buffer (& DNA buffer). They remain quite similar and linear up until ~20 minutes, at which point the SiNPs begin to significantly interact with the laser. This plateauing effect is comparable to previously published findings [103]. Under static conditions the SiNPs remain within the line of sight of the laser and shield the target, whereas under dynamic flow they move away from the target surface allowing a continuing and linear increase of ablation products with time. Single-pass SiNP concentrations are constant regardless of ablation time due to the flushing nature of the

technique, which has been previously characterised by Freeland *et al*. [161]. The relative concentrations can be visualised by the UV-Vis data in Figure 4.5d.

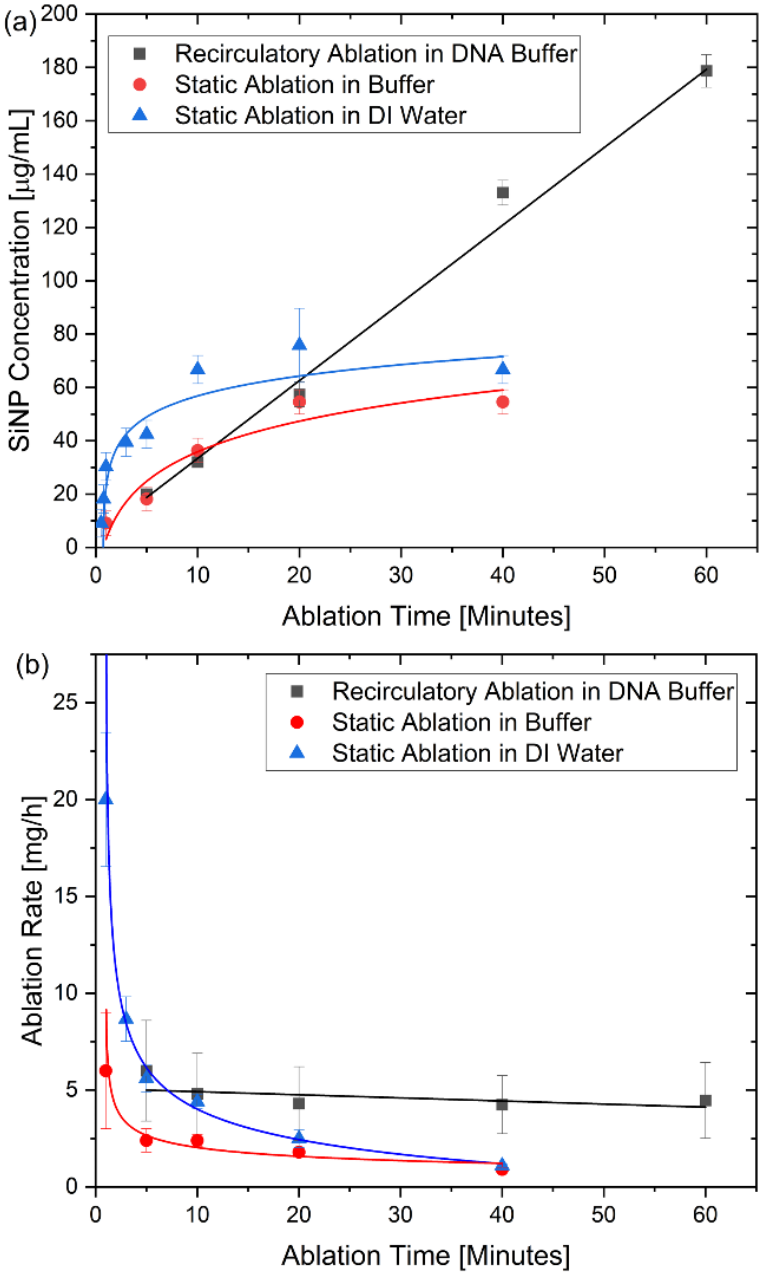

Figure 4.10: a) SiNP colloid concentration vs time for varying liquid media under static and flow conditions. Both static ablations plateau in growth whereas the recirculatory flow shows a linear relationship with a slope of 2.9999 and R2 = 0.9918. (n = 3 ± SD) (b) Ablation Rate vs Ablation Time for the same data showing the increased productivity of LASiS under dynamic flow conditions.

4.4. DNA Functionalisation

4.4.1. Ex-Situ vs. In-Situ

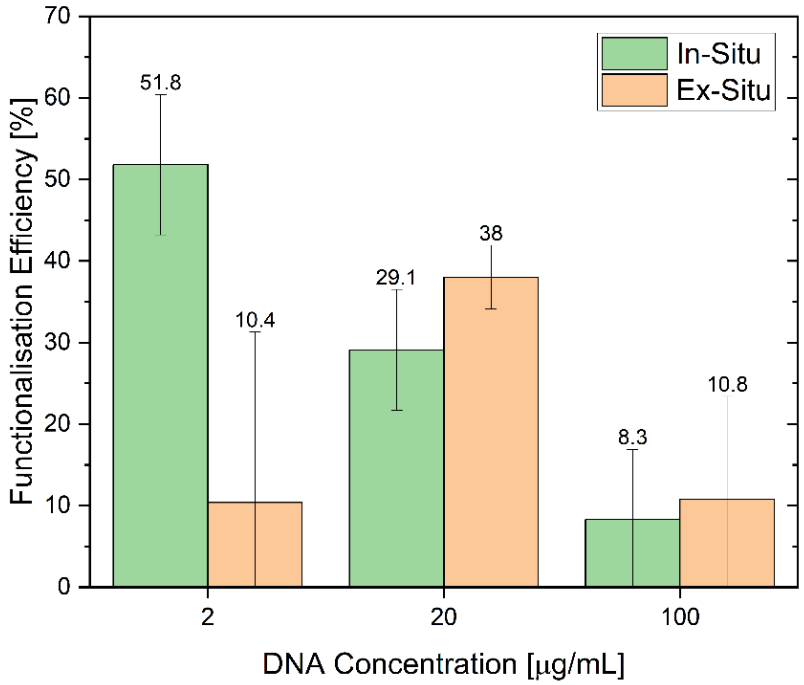

Figure 4.11: Normalised fluorescence intensity of the DNA captured at each DNA solution concentration (2, 20 and 100 µg/ml). The in-situ data shows the efficiency of capture is highest at low concentrations of DNA and that the SiNPs are becoming saturated with DNA at high concentrations. The ex-situ method shows large variations in efficiency at the high and low DNA concentrations. (n = 9 for 2 µg/ml and 100 µg/ml and n = 3 for 20 µg/ml)

Initially, the functionalisation efficiency when ablating silicon in solutions of varying DNA concentrations for 20 minutes was investigated, which can be seen in Figure 4.11. Significant binding of DNA to the SiNPs was achieved across the range of concentrations tested, with a maximum average efficiency of 52% achieved with the 2 µg/ml DNA concentration using the static in-situ set-up. The *ex-situ* (Figure 4.4a) results also showed significant binding across the same range of DNA concentrations, however, with far more variation compared to the in-situ (Figure 4.4b) results. Figure 4.11 suggests that the SiNPs become saturated as the DNA concentration increases. The *in-situ* method exhibits higher binding efficiency at lower concentrations whereas the ex-situ method exhibits slightly higher binding efficiency at higher concentrations, though the repeatability of the technique decreases at the highest concentration of DNA (100 µg/ml). The results at 2 µg/mL suggest that the state of the NPs either during or immediately after ablation (*in-situ*) is more conducive to functionalisation than long after ablation which is the case in *ex-situ* conditions. The comparable binding efficiencies at higher concentrations are likely due to the sheer amount of DNA available to bind. Here there is no need for the added benefits of

laser ablation, as the surfaces become quickly saturated with no more available binding sites *via* physical adsorption under chaotropic conditions. Silica surfaces are terminated with silanol groups which provide active positions for DNA under these conditions, allowing relatively large ex-situ binding to occur [21], [162]. The in-situ produced SiNPs, therefore, benefit from this binding mechanism post-ablation combined with the aforementioned chemical bond between SiNP and DNA backbone of Si-C/Si-CH during/shortly after ablation. The 20 and 100 µg/ml samples were diluted to 2 µg/ml prior to measurement, as they were previously outside the linear detection range of the PicoGreen dye (a calibration curve from 2-2000 ng/mL was generated to validate this linearity). Significant ex-situ binding is to be expected at these large concentrations, given silicon's desirable surface properties for physical adsorption of proteins and DNA/RNA [21], [163]. In addition, our in-situ binding efficiency of 29.1% at 20 µg/ml is comparable to the work of Bagga *et al*, who achieved a binding efficiency of 26% of Protein A from Staphylococcus aureus when ablating in 25 µg/ml [164].

4.4.2. Recirculation

In order to improve upon these binding efficiencies further, the recirculatory dynamic flow conditions of the design from Freeland *et al*. (Figure 4.4c) were incorporated [140]. The dynamic flow cell setup not only provides higher SiNP ablation efficiency/productivity but enhances mixing/interaction mechanisms which were hypothesised to further improve DNA-SiNP binding.

Figure 4.12 shows the binding efficiencies for recirculatory flow (Figure 4.4d) after five ablation times. Lower ablation times were investigated compared to the static ablation methods due to the increased volumes and NP productivity, as well as the enhanced mixing in the flow which could potentially increase binding on shorter timescales. It was expected that as SiNP concentration increases, the DNA binding efficiency would follow, due to the addition of free SiNP surfaces available for functionalisation. This trend is broadly illustrated in Figure 4.12, however the 10-minute ablation shows lower binding efficiency compared with 5 minute and 20-minute ablations, even though the SiNP concentration has been seen to increase linearly (Figure 4.10a). This indicates that either the single-step functionalisation has not reached a steady state of operation or factors including localised DNA aggregation, or the heat of the recirculated colloid and plasma plume stabilises after 10 minutes recirculatory ablation. In both cases, the binding efficiencies were significantly increased compared to the traditional static LASiS, going from 52% (for the static system)

to 65% (for the recirculatory system) binding efficiencies for the same ablation time. The small relative increase in binding efficiency vs time for each recirculatory ablation suggests

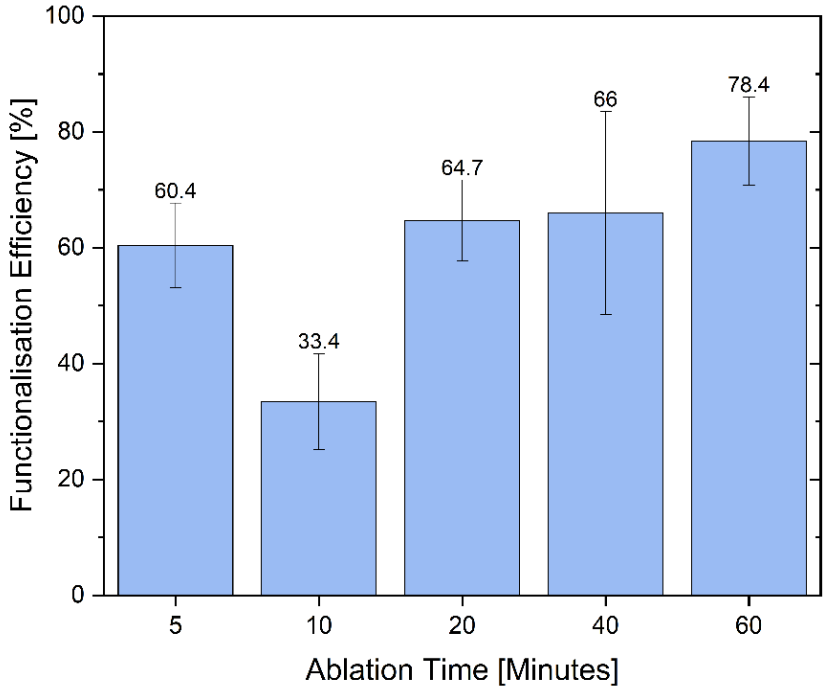

Figure 4.12: Functionalisation efficiency vs ablation time for 2 µg/mL DNA under dynamic flow conditions in recirculatory flow. A small increase in functionalisation efficiency occurs as ablation time is increased. (n = 9)

an inhibiting factor limiting binding efficiency increase, such as electrostatic repulsion within the DNA itself and between SiNPs due to their strong zeta-potentials [16].

We decided to investigate the thermal activity of the system by placing a thermocouple probe on the surface of the silicon target during a 60-minute ablation, to capture real-time temperature data in order to better understand the unexpected results obtained for 10-minute ablations. A hole was drilled through the underside of the flow cell and threaded a thermocouple wire through it. The wire was held in place with, and the hole filled by, an epoxy-based glue. This ensured that the flow cell remained watertight, and that the thermocouple would not move significantly during the experiment. Due to the lateral positioning of the thermocouple (away from the inlet and outlets), the flow was not impeded by the thermocouple, and its presence did not induce bubble generation above the silicon target. The beam was positioned such that the nearest point on the ablation site was 0.6 mm away from the thermocouple (see Figure 4.13b). Corresponding infrared images were taken with an FLIR One Pro camera, but the camera's inability to measure

through glass resulted in temperature measurements of the borosilicate glass laser window rather than the ablation site itself.

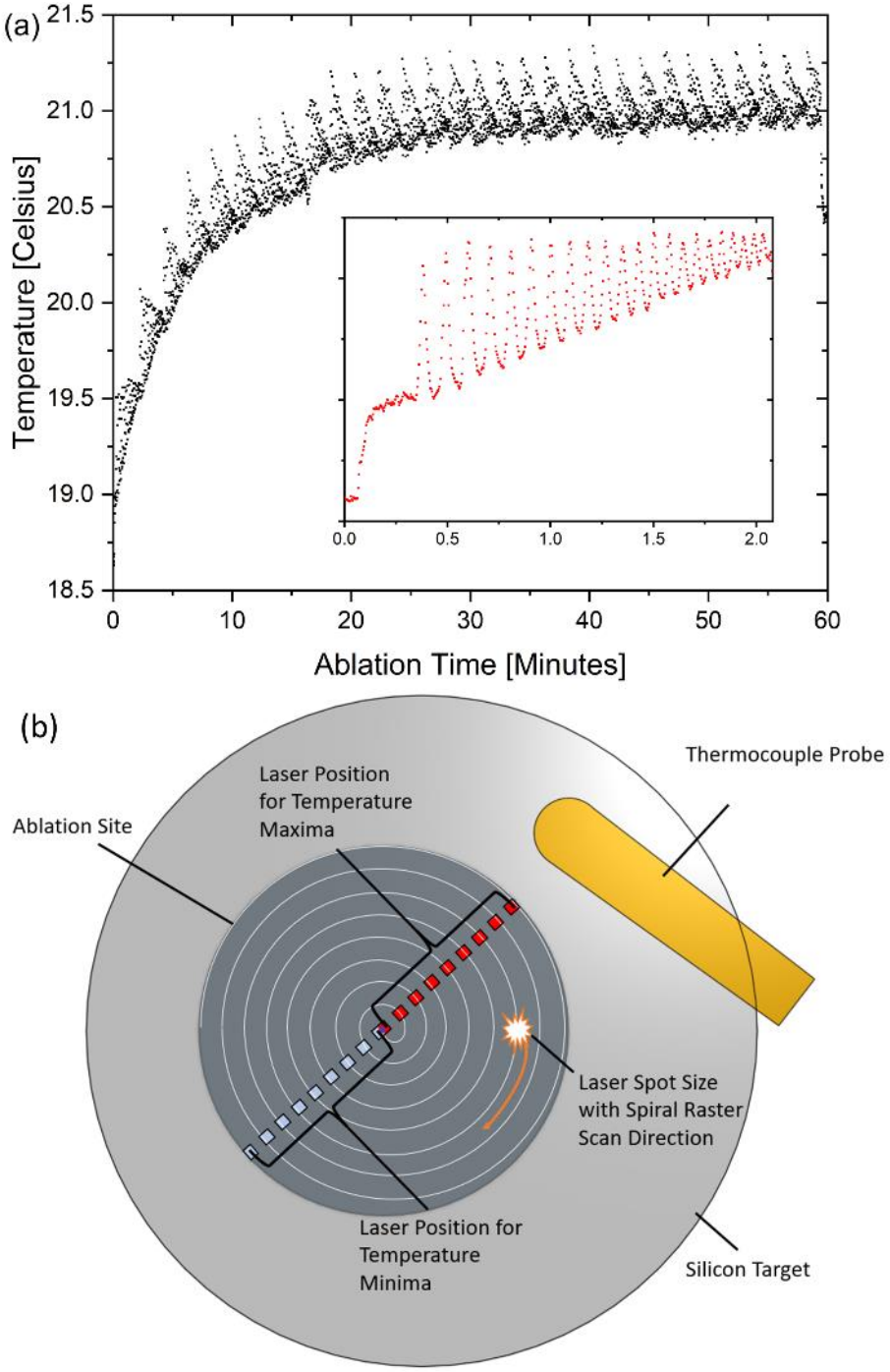

Figure 4.13: a) Temperature of the solution adjacent to the ablation site during a 60-minute recirculatory ablation in DNA-Buffer with 1 s sampling (Inset: first two minutes of the ablation with faster, 0.24 s sampling). (b) AutoCAD illustration of the ablation site showing the position of the thermocouple to scale. The silicon target diameter is 8.28 mm.

The results in Figure 4.13a show the temperature increases initially but starts to plateau after ~30 minutes, but with a recurring pattern with a 2-minute period shown in greater detail in the inset. The thermocouple probe was sampled once every second, but to further

understand the periodic pattern observed, the first two minutes of the experiment were repeated with 0.24 s delay between measurements (which was the smallest obtainable delay) to obtain a more accurate representation of the temperature fluctuations. Intense local changes in temperature were observed due to the laser's position relative to the thermocouple. The peaks and troughs are due to the laser spot spiral alternately approaching and receding from the thermocouple. The highest temperature differences were seen initially, as the spiral diameter/circumference is at its largest. The time difference between the first two peaks is 6.7s, and the maximum circumference of our spiral pattern is 14.2 mm. Our laser spot travels at 2 mm/s which means it would take 7.1 s to complete one full rotation, so it was expected to see the first peak after this time, consistent with the measured data. Slight discrepancies are likely due to the sampling intervals not exactly lining up with positions closest or furthest from the thermocouple. Additionally, the first outermost spiral was not seen as this occurs during the initial rise in temperature after ~1 s, just prior to the cyclical pattern. Not only do the temperature differences decrease over time, but so do the periods between peaks. This is due to the decreasing spiral diameter/circumference, meaning the difference in the distance to the thermocouple probe along all points of the spiral also decreases. A smaller circumference means less distance and therefore time, to make a full revolution, and the period was seen to decrease to 0.5 s before the smaller sampling measurements were stopped.

We see on the 1 s sampling data that the temperature pattern approximately converges to a final value without noticeable peaks and troughs as the spiral radius reaches zero. Thereafter the spiral pattern resets to the maximum 4.5 mm diameter and the cycle repeats again. While these results did not help definitively establish the cause of our 10-minute ablation result, these results were believed to be of interest on its own merits, since the dramatic temperature differences on a macroscopic scale could warrant more studies on a micro/nanoscopic scale.

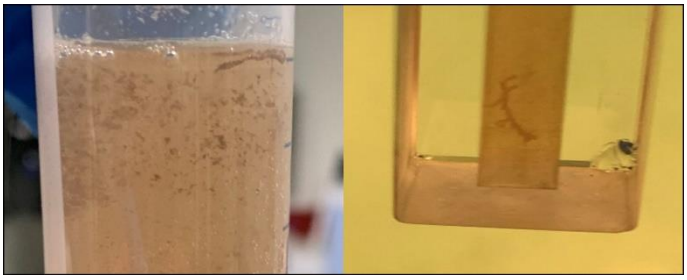

Figure 4.14: (Left) SiNP instability after 60-minute ablation indicated by visible agglomerated macroparticles of Si alongside SiNP coated DNA strands, (Right) SiNPs binding together along long strands of DNA.

Another important point to note is the adapted approach required to measure the binding efficiency for the longer ablation times of the dynamic flow cell tests compared to the static tests. It was assumed that when ablating in 2 µg/mL of DNA, the collected colloid still contained 2 µg/mL DNA but as a combination of bound and unbound DNA. The colloid fluorescence values were compared to the fluorescence of the pure 2 µg/mL DNA solution to ensure this was the case. However, it was found that the colloids of the 60-minute ablations displayed only ~25% of the pure DNA fluorescence. This is believed to be due to a combination of the greatly increased SiNP concentration, and the perceived lack of stability of SiNPs at this higher ablation time. SiNPs are remarkably stable in DI water and can remain in suspension for months, whereas they are noticeably less stable in DNA buffer and fall out of suspension in a matter of weeks. The SiNPs made during the dynamic 60-minute recirculatory ablation fell out of suspension within the 60 minute period, indicating a drastically reduced (almost non-existent) stability. It is believed that the SiNPs falling out of suspension and agglomerating as macroparticles may cover or hide DNA rather than become functionalised by the DNA, making it undetectable. This may also block the binding sites for the PicoGreen fluorophores, resulting in the lower signals. Evidence to support these claims is shown in Figure 4.14. Therefore, the recirculatory flow supernatants were subtracted from the pure DNA fluorescence rather than their corresponding colloid fluorescence values.

4.4.3. Single-Pass

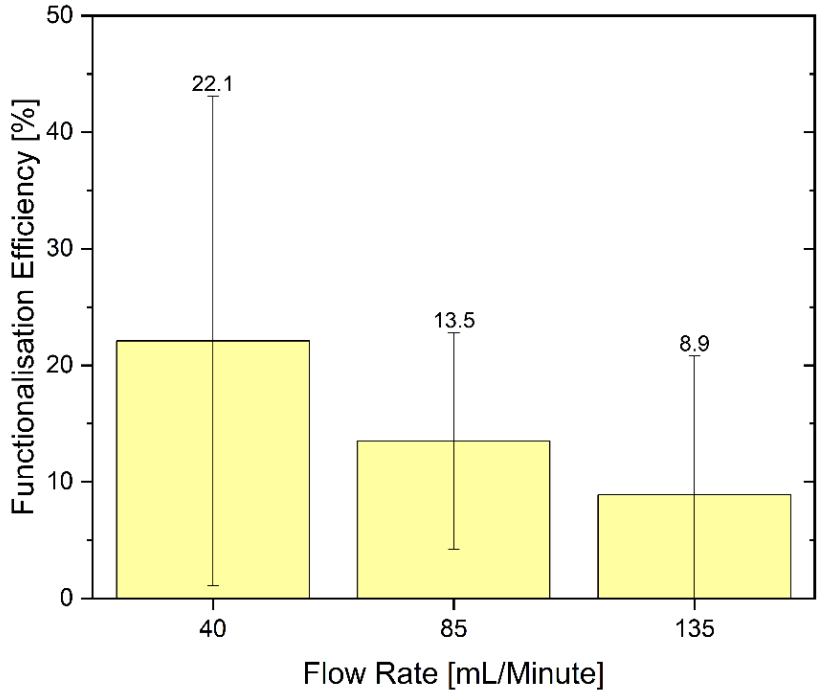

Figure 4.15: Functionalisation efficiency vs flow rate for 2 µg/mL DNA under single-pass flow conditions. A small but clear decrease in binding efficiency is seen as the flow rate is increased. (n = 9)

Figure 4.15 shows the binding efficiencies during single-pass (Figure 4.4c) ablation for three different flow rates. The largest average binding efficiency of 22% occurs at 40 mL/min, with the average efficiencies decreasing with flow rate. This is expected as the slower the flow is above the ablation site, the larger the interaction time for DNA-SiNP interactions. Slower flow rates produce higher NP concentrations, but lower productivity compared to higher flow rates. For a given volume of liquid, as one decreases the flow rate one consequently prolongs the ablation time, resulting in a denser colloidal solution as one ablates for longer in the same volume. Therefore, while higher flowrates are ideal for producing large volumes of pure colloids, lower flowrates are required for higher binding efficiencies. However, each result displays notably large error bars, especially when compared to the previous ablation methods used in this investigation. This method can be loosely compared to the *ex-situ* binding, in that there is a short and somewhat random mixing/interaction between DNA and SiNPs, leading to large inconsistencies in binding efficiencies. It is believed that this method is optimised for the processing of pure colloids, but that more work is need in terms of the investigation of the generation of functionalised colloids. The flow rate range tested correspond to the maximum and minimum flow rates that could be achieved without introducing bubbles into the system. Bubbles significantly impact colloid generation and should be avoided at all costs. The flow system is stable and will not generate bubbles

within these flow rates when using the ionic buffer, with the range being dependent on the solvent used.

4.4.4. Flow Comparison

Lastly, as shown in Figure 4.16, recirculatory ablation achieves the highest degree of functionalisation. While this efficiency was increased by ablating for 60 minutes, the aforementioned stability issues require further investigation. A maximum average efficiency of 78% was achieved when ablating in the flow cell, which is much greater than the 52% achieved with the in-situ method, the 22% achieved with the single-pass method, and the 10% achieved with the ex-situ method. There are also much smaller error bars associated with the recirculatory and batch/static *in-situ* measurements, leading us to believe these are more consistent techniques. This was hypothesised to be due to the low DNA to SiNP ratio alongside the much-longer mixing time of these method. During the in-situ and recirculatory tests, the binding process essentially occurs over 20 minutes and 5 - 60 minutes respectively, while the silicon is being ablated, compared to the approximately 10 s hand mixing binding method of the ex-situ test, and the short interaction time during single-pass ablations. The smaller number of steps taken in the in-situ test further reduces the possible errors as the *ex-situ* method has significantly larger error bars. The dynamic recirculatory ablation having a larger efficiency than the static in-situ is to be expected given the increased ablation efficiency and mixing effects of the recirculatory flow conditions.

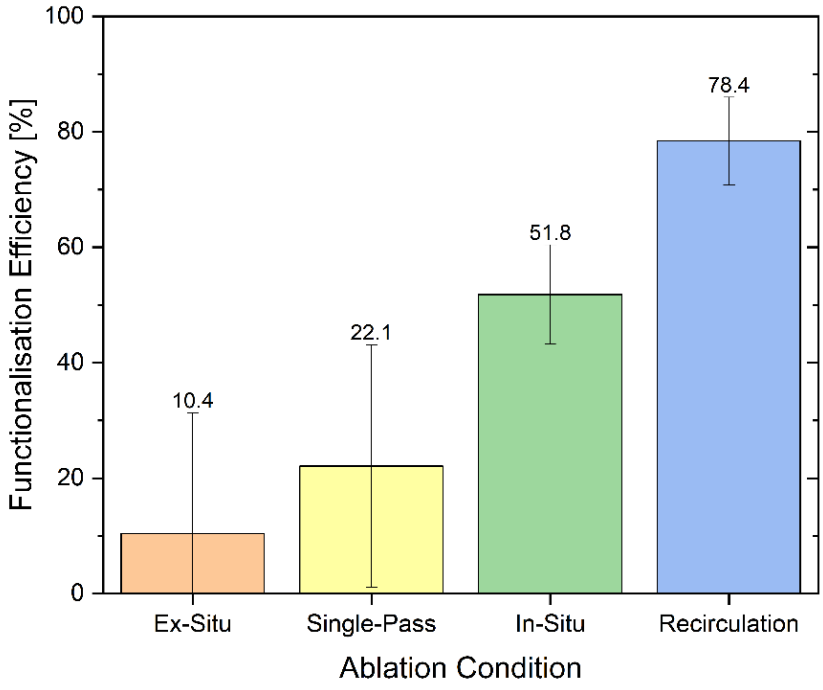

Figure 4.16: Maximum functionalisation efficiencies of each method in 2 µg/mL of DNA. (n = 9)

Lastly, as shown in Figure 4.16, recirculatory ablation achieves the highest degree of functionalisation. While this efficiency was increased by ablating for 60 minutes, the aforementioned stability issues require further investigation. A maximum average efficiency of 78% was achieved when ablating in the flow cell, which is much greater than the 52% achieved with the in-situ method, the 22% achieved with the single-pass method, and the 10% achieved with the ex-situ method. There are also much smaller error bars associated with the recirculatory and batch/static *in-situ* measurements, leading us to believe these are more consistent techniques. This was hypothesised to be due to the low DNA to SiNP ratio alongside the much-longer mixing time of these method. During the in-situ and recirculatory tests, the binding process essentially occurs over 20 minutes and 5 - 60 minutes respectively, while the silicon is being ablated, compared to the approximately 10 s hand mixing binding method of the ex-situ test, and the short interaction time during single-pass ablations. The smaller number of steps taken in the in-situ test further reduces the possible errors as the *ex-situ* method has significantly larger error bars. The dynamic recirculatory ablation having a larger efficiency than the static in-situ is to be expected given the increased ablation efficiency and mixing effects of the recirculatory flow conditions.

Preliminary tests with lower concentrations (0.5 mg/mL) have also been carried out, which show close to 100% binding efficiency (99.6 ± 6.7 %) of the DNA in solution, which was believed to be the highest reported functionalisation efficiency by any variation of the LASiS technique at the time of writing. This preliminary data suggests that further explorations may be worthwhile in this concentration range. Our results show significantly higher binding efficiencies compared to previous reports of in-situ DNA functionalisation at similar concentrations, with previously reported maximum efficiencies of 20% for unmodified DNA binding to SiNPs [133], and 40.3% efficiency for DNA modified with thiol for improved binding to gold NPs [151]. There have been reports of very high binding efficiencies (over 90%) for some other types of modified ligands and NPs in flow systems, but our results for binding efficiencies appear to be the highest reported for unmodified DNA binding to SiNPs [165]. This work provides a promising route for rapid NP synthesis and functionalisation for specific DNA strand targeting.

4.5. SiNP Surface Coatings

The SiNPs synthesised by LASiS were also considered as a potential immobilised capture medium for DNA isolation, and therefore a novel drop casting method to produce SiNP-coated surfaces was investigated. Due to the straightforward nature of the LASiS and the mild solvent used (SiNPs in Di H_2O), the coating was not reliant on monocrystalline Si wafers as suitable substrates as there were no high temperatures required for SiNP coatings compared to the SiO_2 and ZnO growth methods. Instead, polylactic acid (PLA) substrates manufactured and polished by Mr. Dylan Doherty from the Grain-4-Lab project were used. PLA serves as a potential new material for low-cost, biodegradable laboratory consumables, such as petri dishes and microwell plates, the latter of which are commonly coated in functionalised NPs to perform various enzyme linked immunosorbent assays (ELISAs) and other assay techniques [166]. In this subsection, SiNPs of various concentrations were drop cast onto these PLA surfaces and studied the resultant surface morphology and SiNP adhesion.

PLA discs were obtained by 3D printing and from laser cutting injection-moulded PLA petri-dishes [166]. PLA is relatively hydrophobic and the discs were therefore first treated with an air plasma (Henniker Plasma HPT-200 benchtop plasma treater) for six minutes to increase their surface hydrophilicity to promote a more uniform SiNP coating. 1 mL of SiNP solution was pipetted onto each disc immediately following plasma treatment. The discs were then dried at 60 °C for two hours. The discs were coated in SiNP concentrations of either 76, 380, or 1520 µg/mL. 76 µg/mL was obtained by a 60-minute recirculatory ablation in 50 mL of Di-H_2O, and the higher concentrations were achieved by centrifugation.

To create the higher concentrations, 1, 5, and 20 mL solutions of 76 µg/mL of SiNPs were pelleted *via* centrifugation and the supernatant was removed, and then the pellets were resuspended in a final volume of 1 mL of DI H_2O. A photograph of the PLA discs before and after coating in shown in Figure 4.17.

Figure 4.17: Photograph of (left) uncoated PLA discs and (right) SiNP-coated PLA discs. The SiNP concentration increases from 76 µg/mL (top right), 380 µg/mL (middle right) and 1520 µg/mL (bottom right).

The SiNPs were imaged by FESEM after centrifugation and resuspension to ensure no major changes to morphology or agglomeration occurred. 1 µL of SiNPs was drop casted onto a formvar-on-copper TEM grid and imaged in SE mode, and their data is shown in Figure 4.18. Most SiNPs were in the range of 80-120 nm in diameter, measured using the ImageJ software.

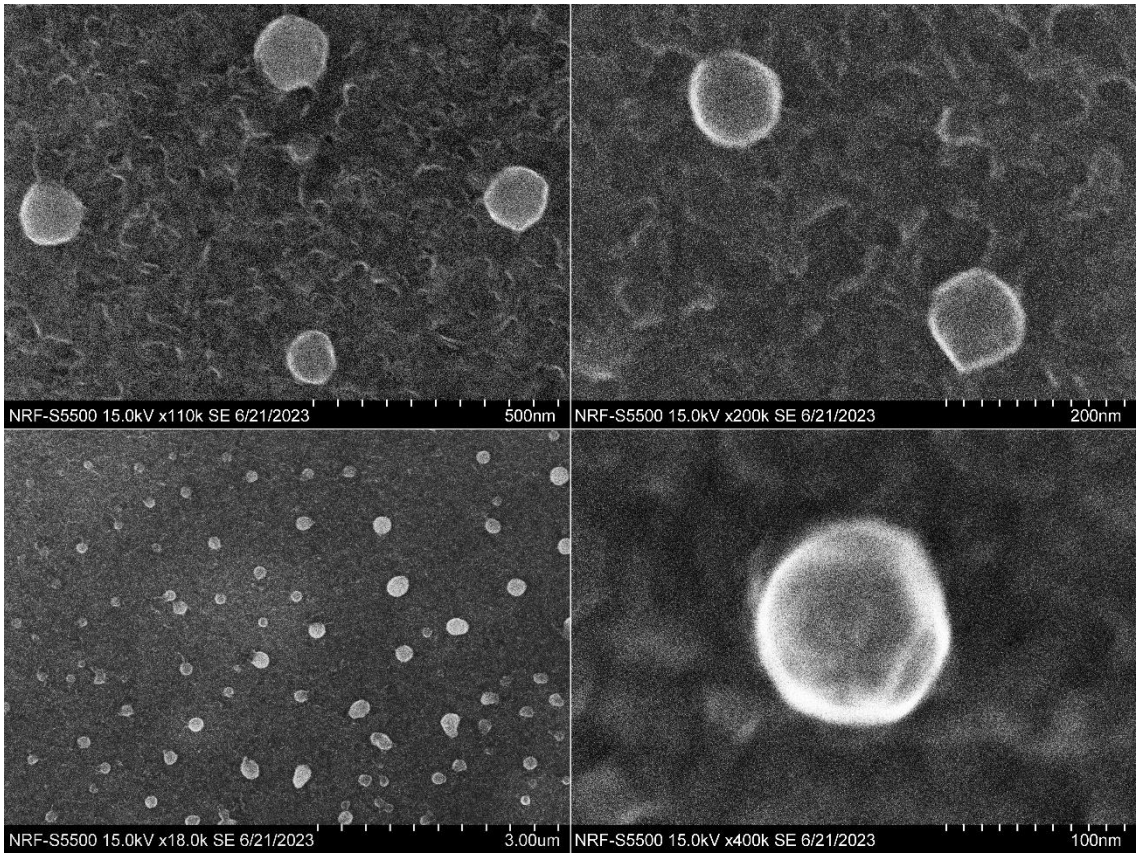

Figure 4.18: FESEM on SiNPs on formvar-Cu TEM grids after centrifugation at various magnifications.

ATR-FTIR data for SiNPs in solution and PLA powder, alongside transmission FTIR data for SiNP-coated PLA discs is shown in Figure 4.19. The ATR-FTIR data shows the three characteristic peaks of silica, which are much more indicative of the silica shell surface structure on silicon core NPs determined in section 4.3. The large peak at 1080 cm^{-1} corresponds to the characteristic asymmetric vibration of the Si-O-Si bond in silica. The small peak at 970 cm^{-1} arises from the Si-OH stretching bond. These are single non-bridging bonds, likely to be dangling silanol bonds on the SiNP surface, which act as binding sites for water [153], [167] . The final peak at 800 cm^{-1} results from the symmetric stretching vibration of the Si-O-Si bond, which is commonly masked when performing FTIR measurements in water or other solutions [153]. The small peak at 1650 cm^{-1} and broad peak at ~3400 cm^{-1} (ranging from 2000-4000 cm^{-1}) correspond to the surface silanol O-H stretching and bending vibrations, respectively [168], [169].

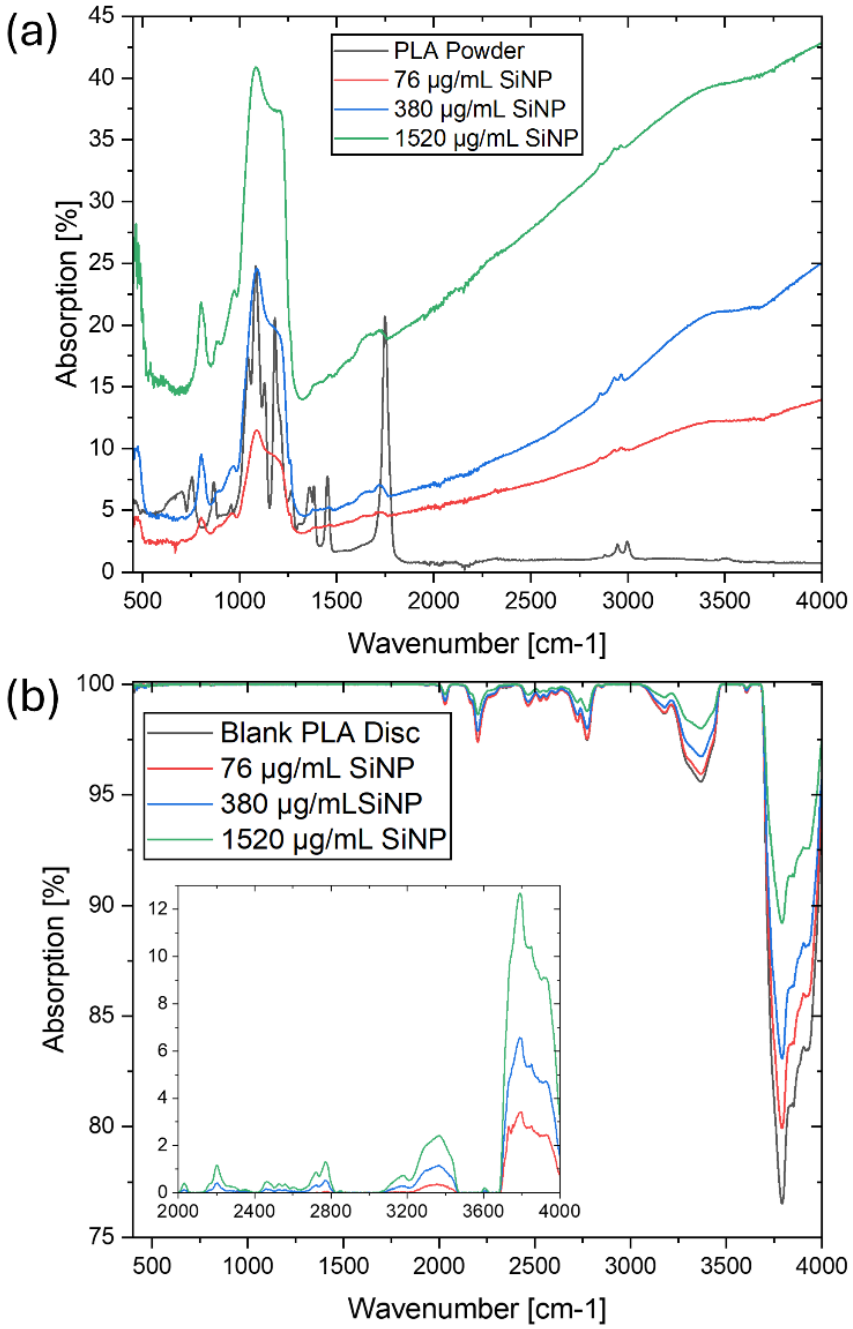

Figure 4.19: (a) FTIR spectra of SiNP colloids dried on the ATR crystal of the FTIR instrument. (b) Transmission FTIR spectra of PLA discs coated with varying amounts of SiNPs (Inset: FTIR spectra of SiNP coated discs corrected for the PLA contribution).

Unfortunately, as shown in Figure 4.19a, PLA has many strong and distinct peaks within the same region as Si/SiO_2, i.e., from 600-2000 cm^{-1}, making it difficult to identify the SiNPs by their characteristic vibrations [170], [171]. The presence of SiO_2 among PLA can be identified by the symmetric stretching vibration peak at 800 cm^{-1} (see Figure 4.19a), however, due to the relative thickness of the PLA discs (~ 1.5 mm), 100% absorption was seen within this region, arising from C-O stretching, C-H bending, and C=O stretching

vibrations. The presence of these vibration signatures, alongside the large thickness of PLA, causes broadband absorption of 800 cm^{-1}. Absorption outside of this region occurs at 2900 and 3600 cm^{-1}, corresponding to -CH and -OH stretching vibrations. However, PLA is transparent to IR wavelengths outside of these values, allowing us to measure the impact of the SiNPs through the broad absorption of the OH bonds of the SiNPs seen in Figure 4.19a, compared to the sharp absorption peak of OH vibrations observed in PLA. The much broader OH vibration peak of the SiNPs from 2000 - 4000 cm^{-1} allows us to see decreased transmission at the wavelengths within this region that PLA is transparent to. Figure 4.19b shows the absorption at these PLA transparent wavelengths, i.e., 2200, 2800, 3360, and 3790 cm^{-1}, increases greatly with increasing SiNP concentration, indicating an increased deposit of Si/SiO_2 on the surface of the discs.

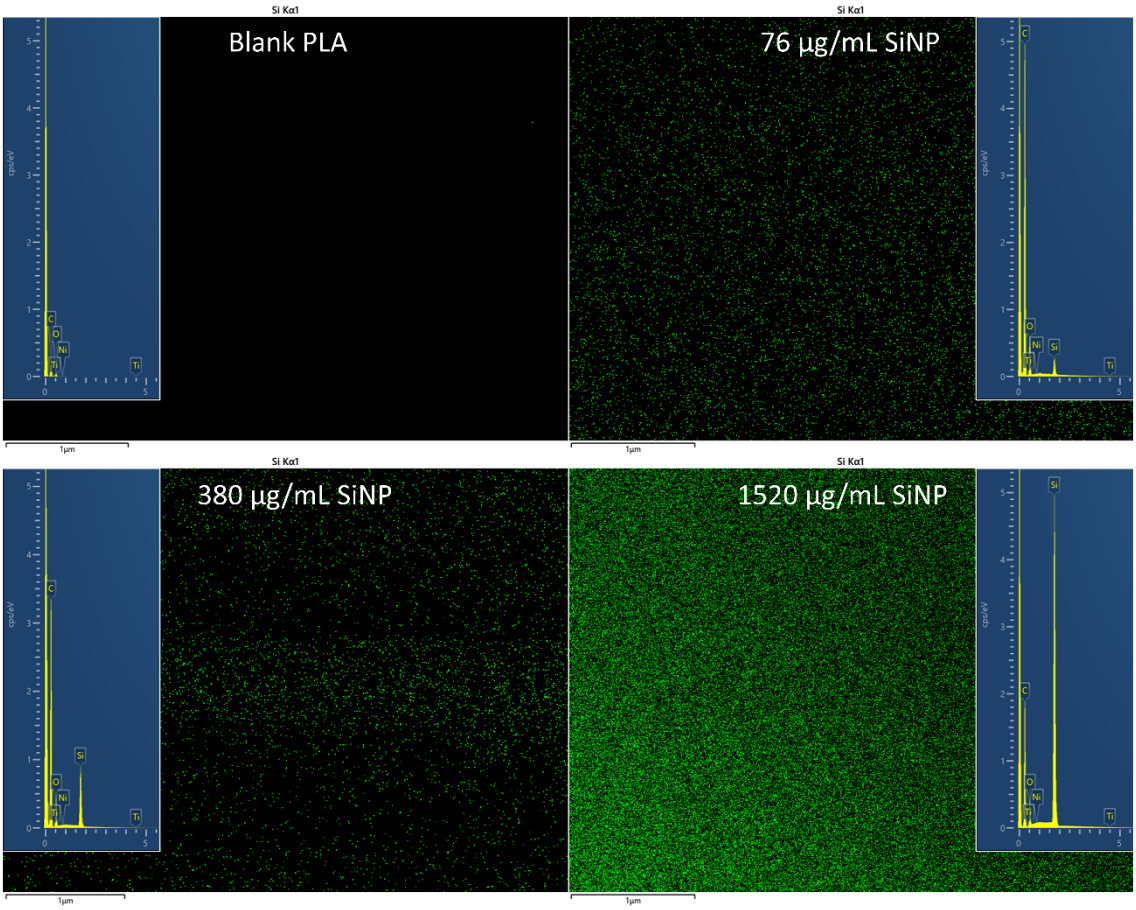

Figure 4.20: Si $K\alpha_1$ EDX images of each SiNP coated disc, with the corresponding EDX spectra overlaid on each image. The EDX spectra show the increasing percentage of Si and decreasing percentage of C as SiNP concentration increases. Low x-ray emission is seen in the bare PLA disc, likely due to excessive charging effects as the disc was not coated in a conductive layer. The SiNPs act as a semiconducting coating which would likely reduce charging effects to some degree.

EDX measurements were performed to further quantify the relative amounts of SiNPs on each disc, with Figure 4.20 showing the characteristic Si $K\alpha_1$ x-ray emission of the various

discs. The bare PLA disc shows no signs of Si on the surface, with the relative Si intensity of each coated disc being 0.26 cps/eV, 0.89 cps/eV, and 4.97 cps/eV. These intensities are directly proportional to the relative SiNP concentrations of each disc (1:5:20). The unexpectedly low intensity of the 380 ug/mL sample (1:3.4 instead of 1:5.0) is likely due to unevenness of the coating in the area measured, which can be seen in Figure 4.20 with the sample having more Si x-ray emission across the compared to the tops of bottoms of the image. SEM imaging of each of the discs was performed at a low magnification (250x) to visualise the SiNP distribution over a wide area (Figure 4.21). These discs were imaged without a conductive coating using the variable pressure mode of the Jeol JSM-IT 100 InTouchScope SEM. The discs were irradiated by the electron beam at the lowest possible magnification at a chamber pressure of 40 Pa for three minutes, at which point the chamber was evacuated to high vacuum of ~<0.001 Pa and samples were imaged in SE mode.

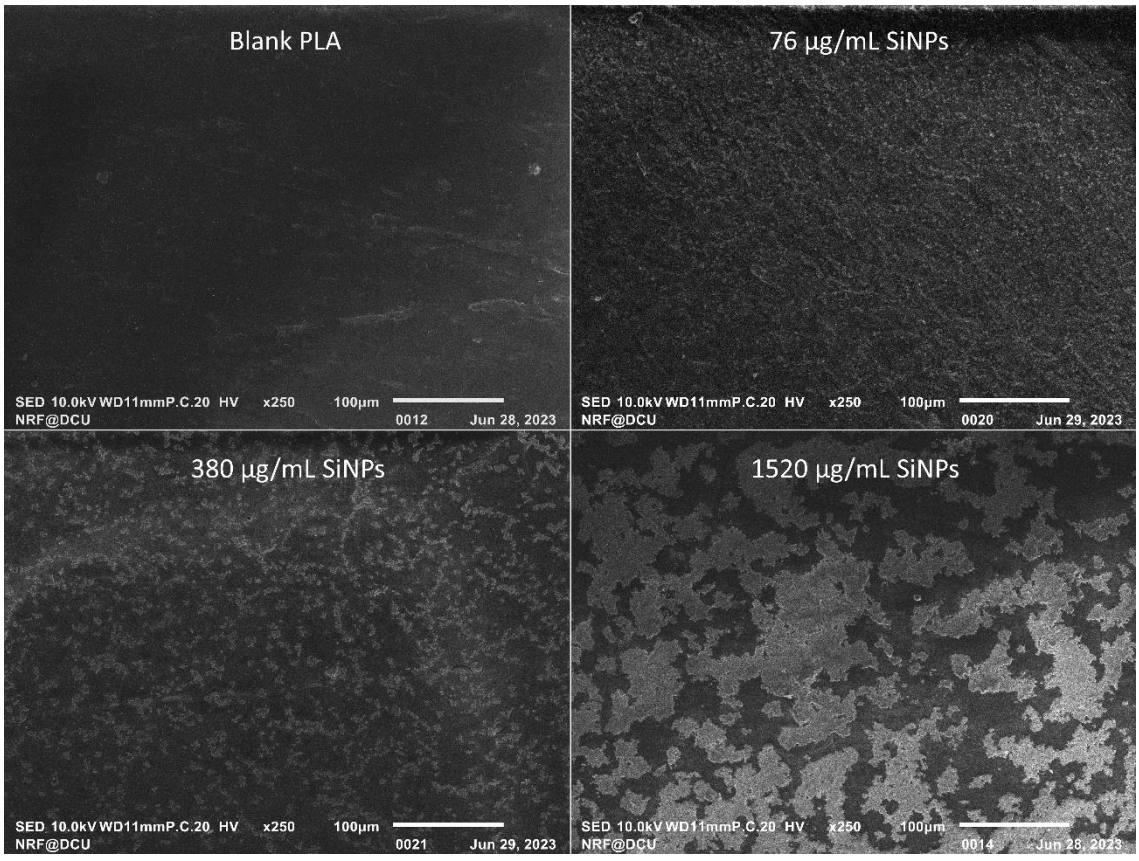

Figure 4.21: SEM images of PLA discs coated in varying amounts of SiNPs at 250x magnification.

Figure 4.21 shows the coverage efficiency of the various SiNP concentration on the PLA discs. A completely uniform increase in coverage with increasing concentration was not observed due to the SiNPs tendency to aggregate with increasing concentration which leaves seemingly large areas of uncoated PLA. However, these images in conjunction with the EDX images of Figure 4.20 show that surface coverage clearly increases with increasing

SiNP concentration. Higher magnification SEM images of the SiNPs embedded within the PLA can be seen in Figure 4.22. These sites of SiNP agglomeration are quite large and porous, which may provide many preferential sites for biomolecule binding.

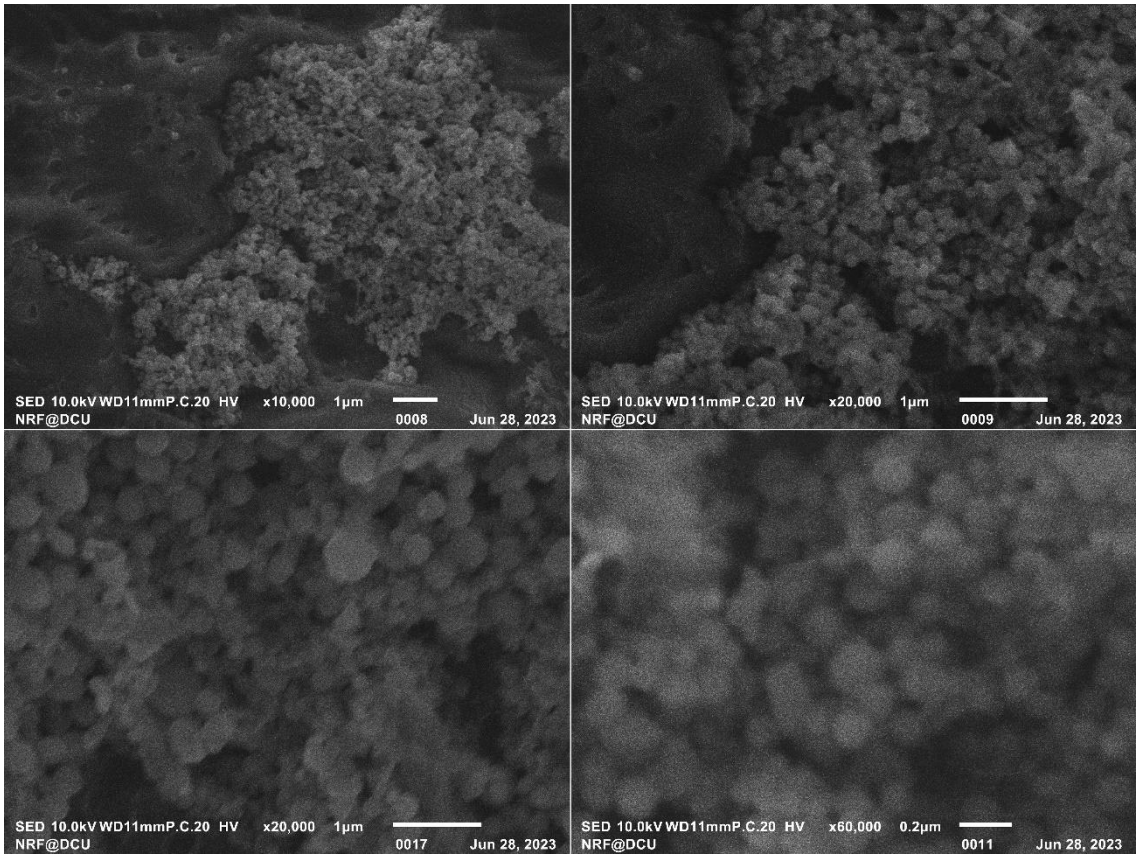

Figure 4.22: SEM images of the 1520 µg/mL SiNP coating on PLA at various magnifications. The SiNPs tend to aggregate within small cavities of the PLA matrix.

CP was performed on each of these discs using minimal force to quantify their roughness and the heights of these SiNP agglomerations, and the results are shown in Figure 4.23. The rms roughness values of each disc are 30.7, 53.9, 58.9, and 227.7 nm respectively, with the results being in excellent agreement with the EDX and SEM data. The 76 µg/mL shows a very uniform coating across the PLA surface, with large peaks in height equal to the diameter of 1 - 2 SiNP particles. On the other hand, the 380 µg/mL disc shows quite an uneven coating, with some regions showing no SiNPs on the surface (i.e. equal surface topography to that of bare PLA) and other regions showing height and width increases of multiple SiNP particles which is a sign of agglomeration. Expectedly, the 1520 µg/mL sample shows a more uniform coverage with much greater roughness, with some SiNP agglomeration sites reaching over 1000 nm in height. These structures could be somewhat comparable to our SiO_2 NRs and dendrites.

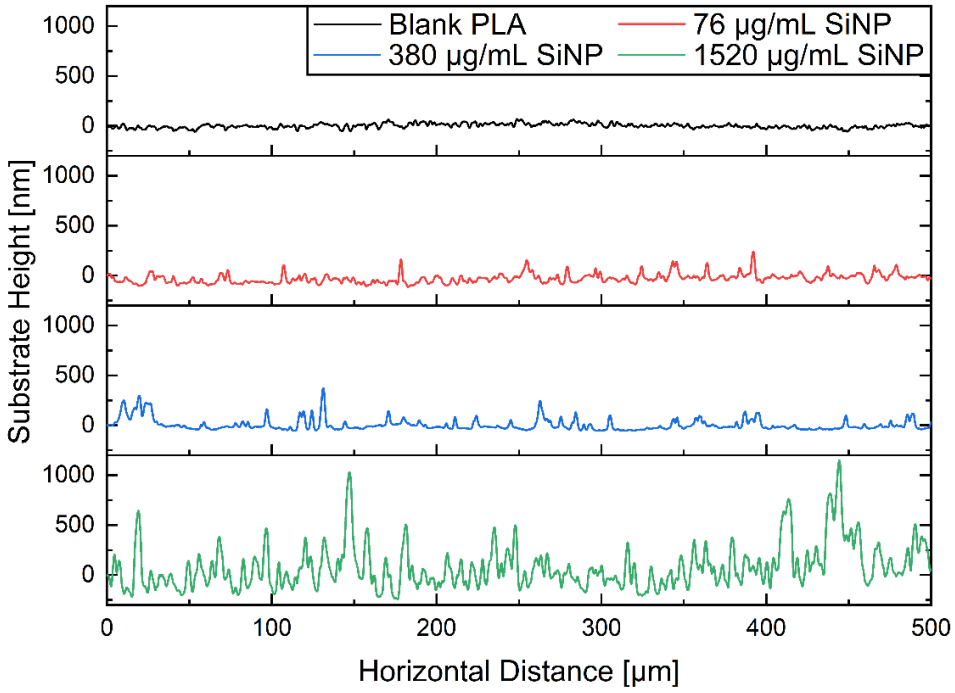

Figure 4.23: CP scans of each SiNP coated PLA disc, showing the high uniformity and coverage of the 76 µg/mL coating, the non-uniform coverage of the 380 µg/mL coating, and the large, aggregated deposits of the 1520 µg/mL coating.

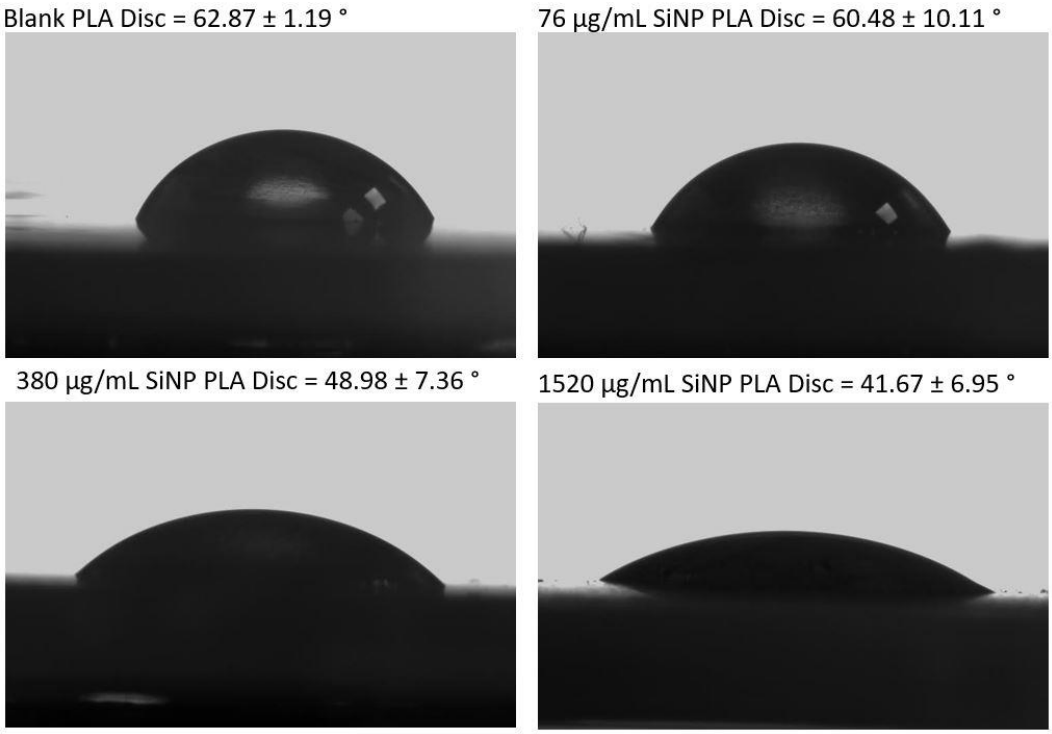

Figure 4.24: Images of a 7 µL drop of DI water used to measure contact angle of PLA discs coated in different concentrations of SiNPs.

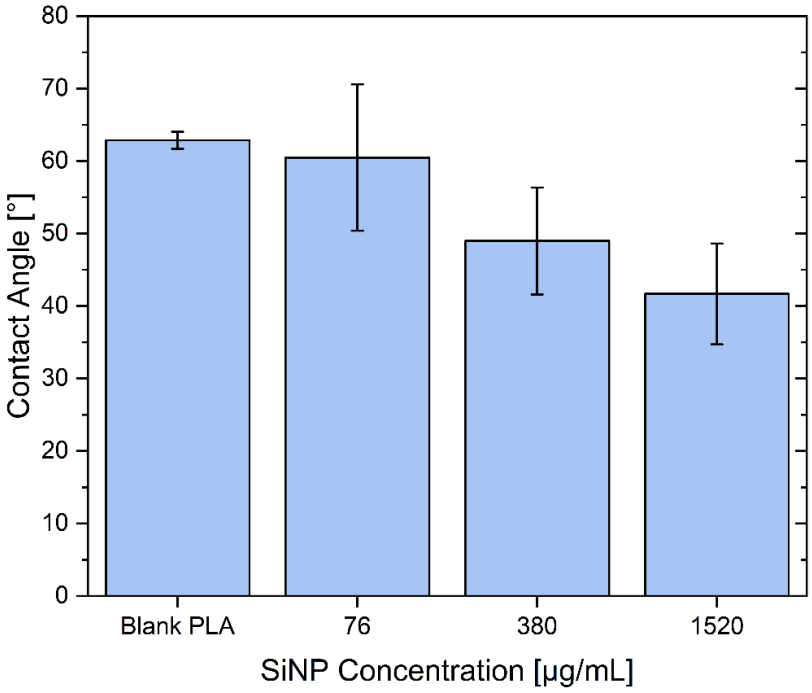

Figure 4.25: Average contact angle measurements taken from three different positions on the surface of the SiNP coated polylactic acid discs.

Lastly, the contact angles of each disc was measured, as the hydrophilicity of surfaces has been known to be an important parameter for biomolecule binding [172]. Contact angle images and results can be seen in Figure 4.24 and Figure 4.25. These figures show the clear effects of SiNP coatings on PLA discs, with the hydrophilicity increasing with increasing SiNP concentration. The larger uncertainties of the SiNP coated discs likely emerges from some variation in SiNP area density across the macroscopic disc surface (seen in SEM data of Figure 4.21), compared to the more uniform polished surface of the blank discs.

4.6. Conclusions

In this chapter a high-efficiency method for producing ligand-free SiNPs and DNA-functionalised SiNPs under dynamic flow conditions was described. By ablating under flow conditions, a 50% relative increase in DNA-functionalisation is achieved compared to what was possible with static ablations while also producing significantly more functionalised NPs per unit time. By reducing the stock DNA concentration, 100% functionalisation efficiency was achieved by recirculation ablation, the highest reported in literature to our knowledge at the time of writing.

Recirculatory ablation enables the production of large volumes of concentrated colloids which can be used to create SINP surface coatings. Detailed characterisation using SEM,

EDX, FTIR, CP, and contact angle confirms the facile drop-casting method produces uniform monolayer coatings as well as highly porous coatings depending on the SiNP concentration used.

Static ablation serves well as a mechanism for LASiS research, but the introduction of controlled recirculating flow makes the technique suitable for industrial scale production due to the large volumes and higher functionalisation efficiencies that can be produced, making it a more desirable NP synthesis technique for functionalised nanomaterials.

5. Bioapplications of SiO_2 Nanostructures

The results presented in this chapter focus on the bioapplications of the different types of SiO_2 NS synthesised in chapters 3 and 4. The chapter is split into three sections based on the different analysis techniques used and application domains.

First, in section 5.1, traditional fluorescence spectroscopy techniques were used to compare the DNA binding capabilities of planar SiO_2 surfaces, SiNPs, ZnO NRs, SiO_2 nanodendrites, and ZnO-SiO_2 NRs (i.e those discussed in chapter 3 and 4). The amount of DNA binding was investigated for substrates submerged in microwell plates under static solution flow/incubation as well as microfluidic chips under dynamic solution flow. The former condition was to ensure DNA could bind to each NS morphology, and the latter to measure the DNA capture capabilities more akin to real-world Point-of-Care (POC) device conditions.

Section 5.2 follows the work of section 5.1 by means of an investigation into the coating of QCM surfaces with SiO_2 thin films and nanodendrites and a comparison of their DNA capture and detection capabilities by monitoring of their resonance frequency in real-time *via* the piezoelectric effect.

This chapter concludes with preliminary work in section 5.3 investigating the use of SiNP coated PLA surfaces as a model prototype for increased functionality of biocompatible implants. Epithelial lung cells and primary vascular cells were grown on bare and SiNP coated PLA surfaces, and their biocompatibility and cell adhesion abilities were investigated.

5.1. Comparison of Nanostructure DNA Binding in Microfluidic Chips

5.1.1. Introduction

As previously discussed, the incorporation of SiO_2 microbeads, which are the current state of the art for DNA isolation and purification for detection, into microfluidic chips leads to highly varied and irreproducible results [173]. This is a major roadblock of achieving true DNA point-of-care diagnostics, as the ability to efficiently and reproducibly capture and isolate the target molecule is a fundamental requirement of a diagnostic device. SiO_2 micropillars have been fabricated and demonstrated to be able to capture significant quantities of DNA reproducibly within microfluidic devices, although requiring highly

specialised, complex fabrication procedures such as photolithography, etching, and CVD [53], [54]. This chapter demonstrates the application of a variety of SiO_2 NSs synthesised using facile, low-cost techniques as reproducible and reliable DNA capture mechanisms within microfluidic chips.

5.1.2. Materials & Methods

5.1.2.1. Microfluidic Chip Fabrication

Microfluidic chips were assembled using the Si substrates as the base, alongside 1.5 mm thick polymethylmethacrylate (PMMA) and 86 µm thick pressure sensitive adhesive (PSA) to create the microfluidic channels. PMMA layers were created using an Epilog Zing 16 laser cutter and served to seal the microfluidic channels created by the PSA layer, and to provide the inlets and outlets. The PSA layers were cut using a Graphtec Craft Robo Pro knife cutter. First the PSA was bonded to the PMMA top layer using a manual roller, and then the NS coated substrates were bonded to the other side of the PLA layer, ensuring that the NSs were facing the PSA and PMMA layers. The microfluidic channels within the chips were 14 x 3 x 0.086 mm in size (l x w x h) and the schematic can be seen in Figure 5.1.

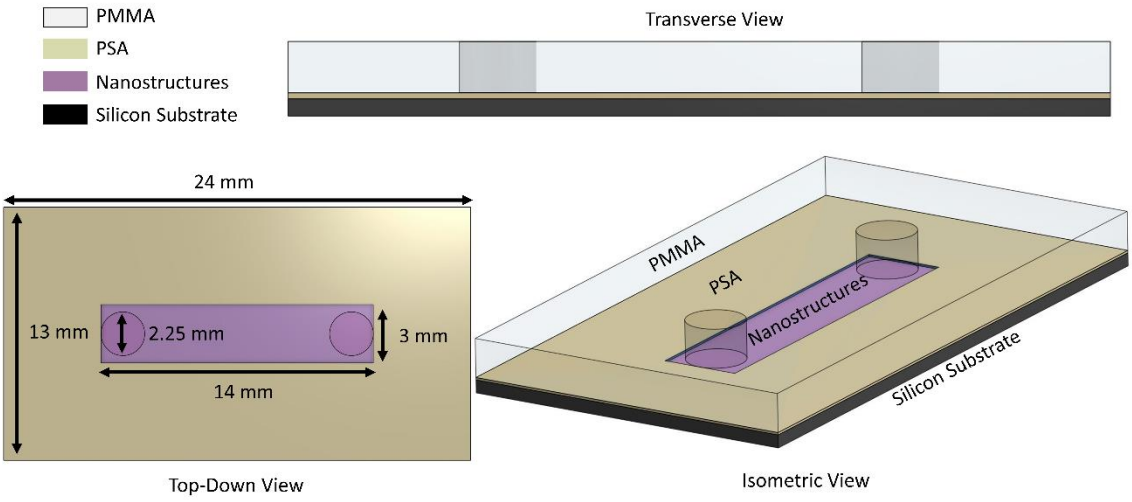

Figure 5.1: Schematic diagram of the microfluidic device design utilised for DNA binding studies.

5.1.2.2. DNA Preparation & Binding Protocol

Before incorporating the various SiO_2 NSs into the microfluidic chips, their DNA capture capabilities within 96-well plates were investigated to confirm that DNA could bind to these novel NSs. To do so, each NS was grown on a silicon wafer substrate and the silicon was cleaved into six pieces with a diamond tipped scribe to the dimensions of the microwells (~ 0.6 cm^2), and each piece was placed at the bottom of a microwell. Then 80 µL of 500 ng/mL of calf thymus DNA, prepared as described in chapter 4 section 4.2.2, was pipetted into

each well and allowed to incubate at room temperature for 30 minutes. Afterwards, the DNA solution was removed from each well and placed into a new well containing no substrate, and this solution is known as the supernatant. The substrates were then removed from their original wells and placed into new wells in case any DNA had bound to the microwell walls. Then 80 µL of PicoGreen solution was added to each well. The supernatant ($DNA_{supernatant}$) and original well (DNA_{well}) fluorescence values were added together and subtracted from the fluorescence of a stock 500 ng/mL DNA solution ($DNA_{500ng/mL}$) to calculate the amount of DNA that had been captured by each NS morphology ($DNA_{captured}$). The calculation is described by the following equation:

$$DNA_{captured} = DNA_{\frac{500ng}{mL}} - \left(DNA_{well} + DNA_{supernatant}\right) \qquad (Eqn. 5.1)$$

For DNA binding measurements within microfluidic chips, 1 mL of DNA solutions of various concentrations (10, 100, and 1000 ng/mL) was flowed over the NSs at a rate of 30 µL/min and then into a beaker for collection. Fluorescence spectroscopy before and after flowing through the microfluidic chips allows us to calculate the amount of DNA captured by the NSs by the following equation:

$$DNA_{captured} = DNA_{initial} - DNA_{final} \qquad (Eqn. 5.2)$$

The fluorescence measurements were performed in a 96-well plate, where a 1:1 aliquot of sample and dye (100 µL each) was placed in each well, with the binding buffer serving as the background. The plate was covered in reflective foil, and the samples and dye were left to incubate for 5 min before measurement.

5.1.3. Results

5.1.3.1. Preliminary Comparison in 96-Well Plates

The results in Figure 5.2 show the clear effect of the physicochemical properties of the NSs on the DNA binding efficiencies. Not only does it show that higher aspect- and surface-to-volume- ratios increase the binding efficiencies, but also further emphasises the requirement of SiO_2 surface chemistry to achieve any DNA binding at all under the ionic and pH conditions used in this work. The only difference between the ZnO NR and ZnO-SiO_2 NR samples was a 10 nm thick coating of SiO_2, yet that causes an increase from essentially 0% binding to an average binding efficiency of 62 ± 11 %. The SiO_2 dendrites and ZnO-SiO_2 NRs show approximately equal binding efficiencies within their respective errors, with the dendrites showing a slightly lower average (51 ± 17 %) with a wider standard deviation. The

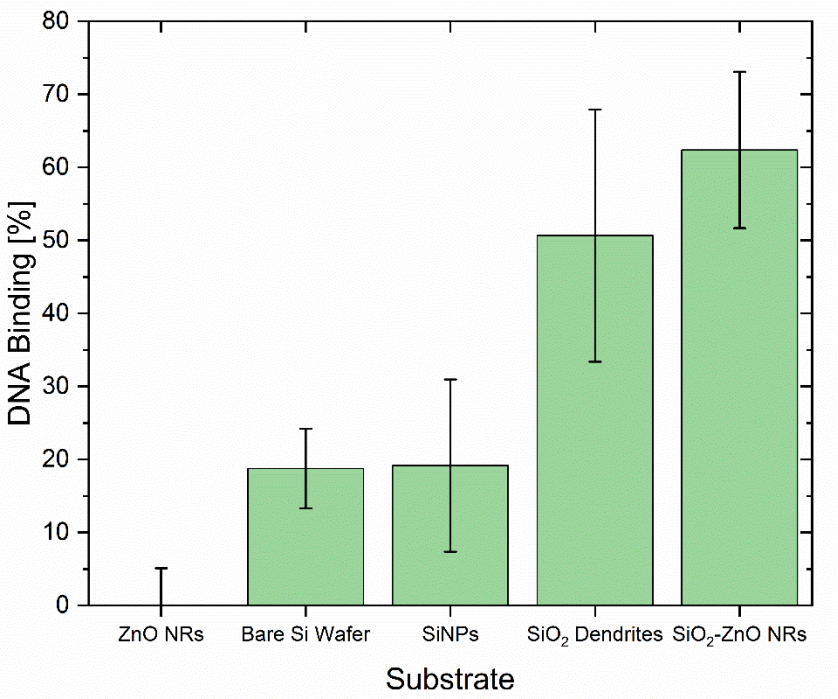

Figure 5.2: DNA binding efficiency of each NS morphology within microwells of a 96-microwell plates. The results represent the average and standard deviation of 6 independent measurements.

smaller errors associated with the ZnO-SiO_2 NRs is likely due to the more controlled NR height and dimensions compared to the SiO_2 dendrites.

The results in Figure 5.2 show the clear effect of the physicochemical properties of the NSs on the DNA binding efficiencies. Not only does it show that higher aspect- and surface-to-volume- ratios increase the binding efficiencies, but also further emphasises the requirement of SiO_2 surface chemistry to achieve any DNA binding at all under the ionic and pH conditions used in this work. The only difference between the ZnO NR and ZnO-SiO_2 NR samples was a 10 nm thick coating of SiO_2, yet that causes an increase from essentially 0% binding to an average binding efficiency of 56%. The negative binding efficiency observed likely arises from some variation in the stock DNA concentration. Errors of ± 5% in the stock concentration fluorescence have been consistently observed throughout this work. The SiO_2 dendrites and ZnO-SiO_2 NRs show approximately equal binding efficiencies within their respective errors, with the dendrites showing a slightly lower average (46%) with a wider standard deviation. The smaller errors associated with the ZnO-SiO_2 NRs is likely due to the more controlled NR height and dimensions compared to the SiO_2 dendrites.

We still see notable DNA binding to silicon substrates without any nanostructure growth at the lower concentrations. This occurs due to the native oxide of the silicon wafer which is essentially a flat layer of SiO_2 that therefore has an affinity for DNA binding. The SiNP coated

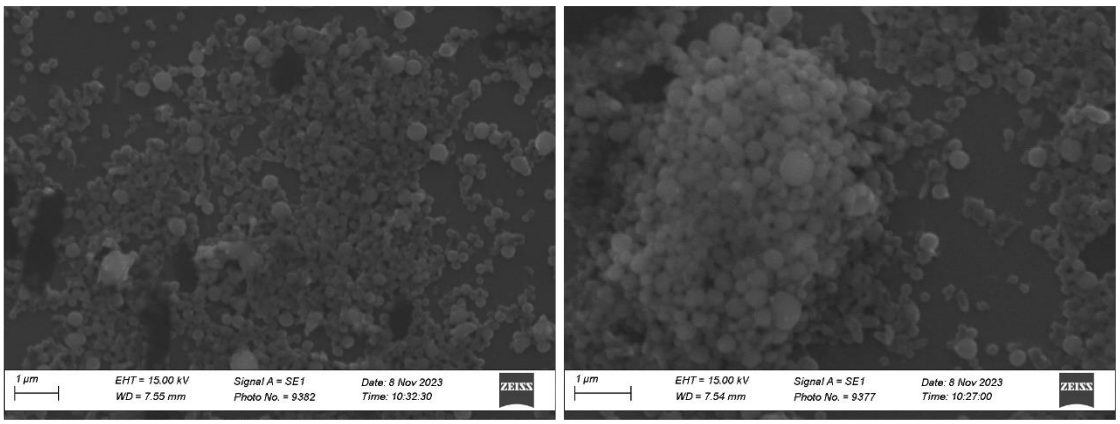

Figure 5.3: SEM image of Si substrate coated in 1520 µg/mL of SiNPs showing regions of (left) uniform coatings and (right) large SiNP agglomeration.

substrate shows the same average binding efficiency, but with error bars two times larger than the uncoated substrate. The larger errors could be attributed to simultaneously increased binding to the higher surface area of the SiNPs, but also from SiNPs coming loose from the surface during incubation or supernatant removal and subsequently reducing the amount of bound DNA. An SEM image of an SiNP coated Si substrate is shown in Figure 5.3.

The Si substrates coated in 1520 µg/mL of SiNPs show regions of uniform coatings alongside regions of large SiNP agglomeration. The former likely contributes to the larger binding efficiencies, and the latter likely contributes to the lower binding efficiencies of the SiNP coated substrate compared to the uncoated Si substrate. Further evidence of this was obtained by submerging the various SiNP coated PLA substrates in the Qiagen PB buffer. PLA substrates were used as the SEM images in section 4.3 show the SiNPs were embedded within the PLA matrix, which were hoped to help the SiNPs remain bound to the substrate surface. The 76, 380, and 1520 µg/mL coated PLA substrates were submerged in 3 mL of Qiagen PB buffer for 24 hours, after which the substrate was removed, and FTIR spectroscopy was performed on the remaining buffer. 13 mg of a fine PLA powder was also poured into a PB buffer sample to provide a reference for possible PLA-PB binding. The results are shown in Figure 5.4.

The results show the spectra of the pure PB buffer alongside the PB buffer in contact with various forms of PLA and SiNP-coated PLA substrates. The uncoated PLA substrate sample seems to suggest that PLA is leeching from the substrate into the PB solution, as its spectra has identical absorption peak positions as the PB sample containing a fine PLA powder, with new peaks emerging compared to that of the pure PB solution. However, the 76 and 380 µg/mL SiNP coated substrate supernatants show vastly reduced absorption across the

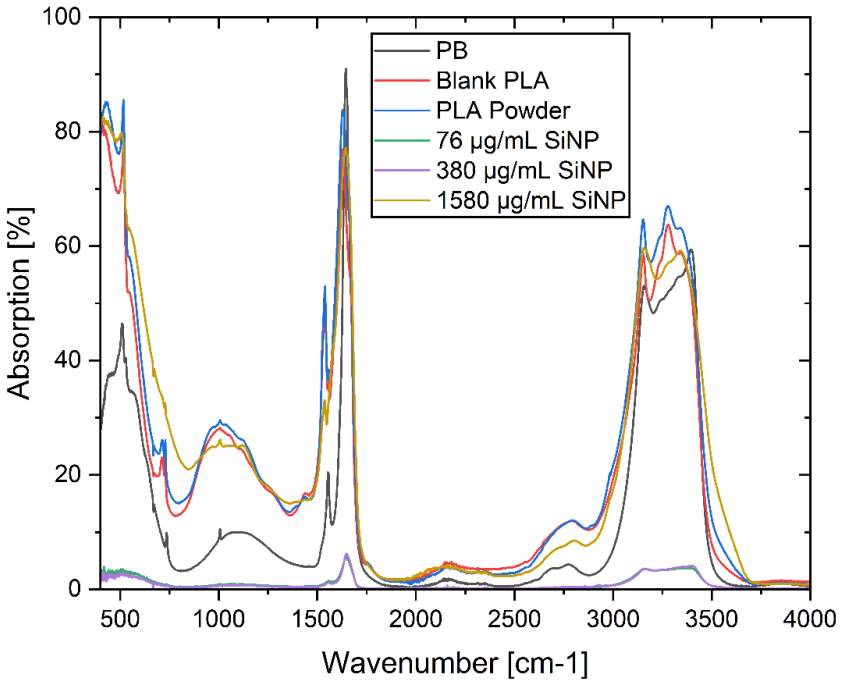

Figure 5.4: ATR-FTIR spectra of PB buffer solutions in contact with PLA substrates with varying SiNP surface coatings, and a PB-PLA powder mixture for reference.

entire wavenumber range tested. The significantly reduced absorption of these samples compared to the pure PB spectra suggests that the SiNPs have captured and extracted the ionic salts present in the buffer, with the remaining supernatant solution comprised mostly of DI H_2O (as the PB buffer is a 1:20 dilution of PB solution and DI H_2O respectively). This agrees with the known mechanism of DNA binding to SiO_2 under the ionic conditions of the PB buffer. The positively charged salts of the buffer first bind to negatively charged SiO_2 surfaces, creating an ionic bridge which the negatively charged DNA backbone can bind to. For this reason, it is expected that immobilised SiNPs would capture and extract these ions from the PB solution, which is seen in Figure 5.4. However, a unique spectrum is obtained for the 1520 µg/mL coated substrate. The absorption intensities increase back to similar levels to those of the pure PB and PLA-PB supernatants but with altered intensity ratios and peak positions. This is hypothesised to be evidence of SiNPs being removed from the PLA surface for several reasons. The first direct evidence of SiNPs being present in the supernatant is the blue-shift seen in the local minimum absorption at 800 cm^{-1} seen in the pure PB and PLA-PB samples. This local minimum is shifted from 800 cm^{-1} to 850 cm^{-1} in the 1520 µg/mL SiNP sample, as SiNPs have a characteristic absorption of 800 cm^{-1} due to the symmetric stretching vibrations of Si-O-Si bonds. The second piece of evidence is the presence of an additional local maximum at 1100 cm^{-1} seen in the sample compared to the other PB/PLA samples which only show a single local maximum at 1010 cm^{-1}. This is the

characteristic absorption of the asymmetric Si-O-Si bonds, further confirming the presence of SiNPs. The indirect evidence of SiNP removal is the return of the strong absorption peaks of the ionic salts seen in the previous PLA/PB spectra compared to the 76 and 380 µg/mL samples. For this reason, the 1520 µg/mL SiNP coated substrates are likely unsuitable for the type of immobilisation and binding studies investigated in this work. Given the need for high aspect-ratios and surface-to-volume ratios, the lower concentration coatings were not used for further DNA binding tests. However, the biocompatibility properties of the SiNP-coated PLA substrates were investigated, as they showed evidence of enhancing ionic salt binding in solution which could be beneficial for increased functionality biocompatible implants. The cell culture work was carried out by Dr. Keith Rochefort in the School of Biotechnology and is discussed in section 5.3.

Taking these results into consideration, only the bare Si substrate, the ZnO-SiO_2 NRs, and the SiO_2 dendrite binding capabilities were tested within microfluidic chips.

5.1.3.2. Microfluidic Chip Testing

Figure 5.5. shows the DNA capture efficiency of the SiO_2 nanodendrites, the ZnO-SiO_2 NRs, and uncoated silicon substrates under three different DNA concentrations. Notable binding to silicon substrates was observed without any NS growth at the lower concentrations. This occurs due to the native oxide of the silicon wafer which is essentially a flat layer of SiO_2 that

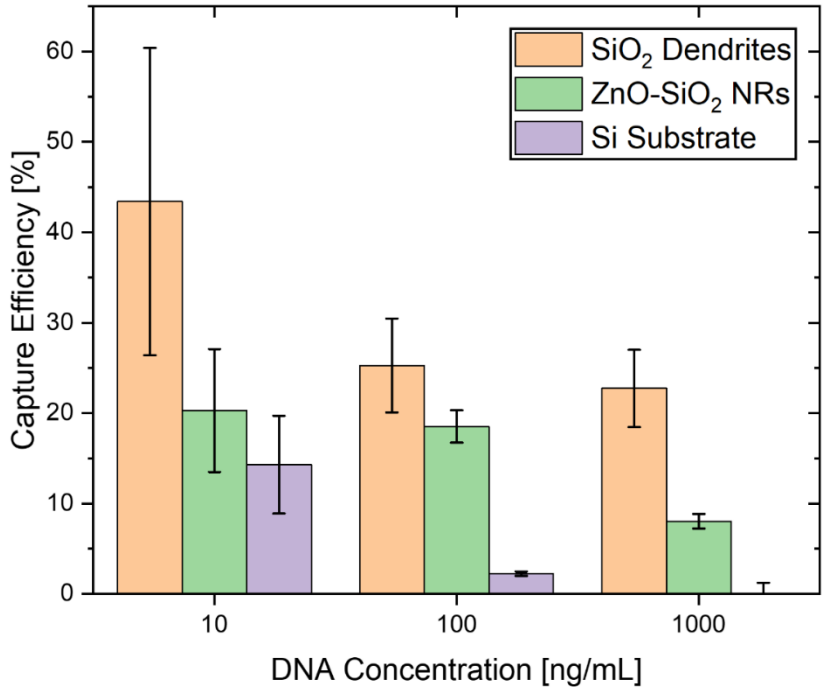

Figure 5.5: DNA capture efficiency of three different SiO_2 surface morphologies under various concentrations of DNA within microfluidic chips. The error bars represent the standard deviation of five independent measurements.

therefore has an affinity for DNA binding. However, significantly increased DNA capture is achieved by both SiO_2 dendrites and SiO_2 coated ZnO NRs at the larger DNA concentrations, with a much larger capture efficiency achieved by the dendrites at a concentration of 1000 ng/mL of DNA. Despite the decreased capture efficiencies of the nanostructures with increasing input concentrations of DNA, these values correspond with large amounts of DNA, with the dendrites and NRs capturing 227.3 ± 42.7 ng and 80.4 ± 8.0 ng of DNA respectively from 1000 ng. These quantities far exceed the typical thresholds required for the detection of DNA using quantitative PCR to diagnose disease [174].

Our hypothesis is that the significantly increased binding efficiencies of the dendrites is related to the combination of high surface to volume ratio and the presence of quite large void regions in the nanodendrite structures, which enable DNA ingress and subsequent capture, compared to the closer packed structure of the SiO_2 coated ZnO NRs. Both plan- and cross-sectional-view SEM images of each NS are shown in Figure 5.6.

Both nanostructures have similar height (6000 nm), but the NRs are much more tightly packed with an interrod spacing of 200 – 500 nm compared to the 2000–4000 nm dimension of the voids of the nanodendrite structures. The DNA strands utilised in this study were ~ 3400 nm long (10,000 base pairs) which is much larger than the SiO_2 coated ZnO NR interrod spacing, but comparable to the voids of the nanodendrite structures. The capture efficiency of the NRs might be increased with a decrease in the channel height of the microfluidic chip from 86 µm to a height similar to that of the NRs which could force the solution through the NR array, however this was not achievable within the timeframe of this work. Despite this, both nanostructure morphologies (SiO_2 nanodendrites and ZnO-SiO_2 NRs) can capture significant quantities of DNA compared to planar Si surfaces under a variety of conditions and using low-cost synthesis and device fabrication technologies.

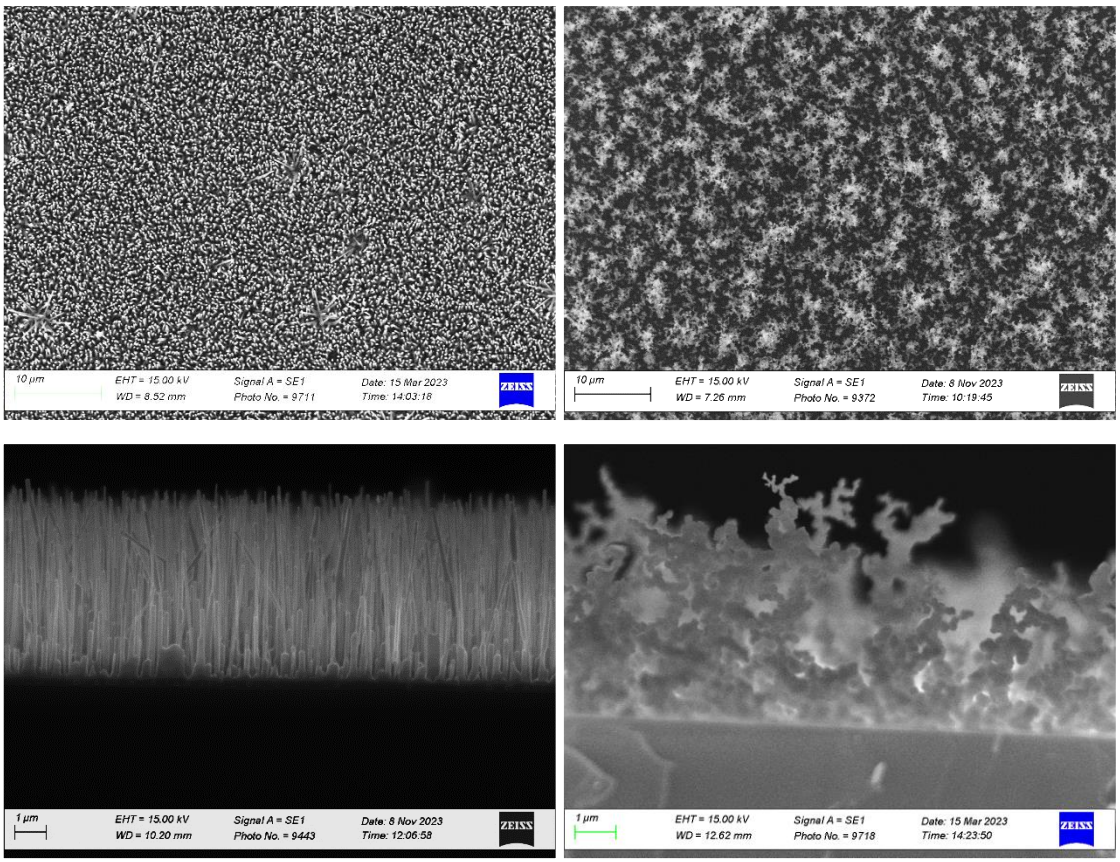

Figure 5.6: (Top row) plan-view and (bottom row) cross-section-view of (left column) ZnO NRs and (right column) SiO_2 dendrites.

5.1.4. Conclusions

By systematically growing various NS on Si substrates and evaluating their DNA binding capabilities, it was identified that the surface chemistry of ZnO is incompatible with commercial reagents for DNA binding, and that immobilised SiNPs are ineffective in enhancing DNA capture compared to planar surfaces. In contrast, high aspect-ratio and surface-to-volume ratio SiO_2 nanodendrites and ZnO-SiO_2 NRs significantly improved DNA binding both in static conditions within 96-well plates akin to ELISA, and dynamic flow conditions within a microfluidic chip akin to real world point-of-care devices. The low-cost, reproducibility, and facile nature of both nanodendrite and NR synthesis and their enhanced DNA capture abilities highlight their potential for integration into true point-of-care devices. These NSs can serve as immobilised capture mechanisms for DNA or other biomolecules, providing a reliable platform for isolation and subsequent purification and detection.

5.2. Nanostructured Deposits on QCMs

5.2.1. Introduction

While SiO_2 NSs have a high affinity for DNA binding, allowing for isolation and purification of target molecules, they simply act as filters to capture DNA which is quantified by indirect means of measuring the amount of DNA that has not bound. As previously discussed in section 2.3.2., QCM sensors are widely utilised for studying biomolecular interactions, providing high-sensitivity, real-time, and label-free measurements. This chapter first details the growth of SiO_2 nanodendrites and thin films on QCM sensors. As demonstrated in section 5.1.3.2., the nanodendrites capture much more DNA than flat, planar surfaces. By growing these nanodendrites on a QCM, they can capture and directly detect DNA bound to the NSs without the need for specialised equipment and reagents involved with traditional DNA detection methods like fluorescence spectroscopy. Changes in resonance frequency and dissipation of NS-coated QCMs was monitored to determine if DNA binding events had occurred.

5.2.2. Materials & Methods

The SiO_2 coatings on QCMs were achieved in an identical manner to those on Si substrates. The QCM crystals were suspended on supporting Si pieces that were wider than the 14 mm diameter of the QCMs to mask the underside from SiO_2 deposition, limiting the growth to only the top electrode and preventing issues with the underlying electrical contacts.

The openQCM Q-1 hardware was powered and monitored by openQCM NEXT python software installed on a Dell Latitude 5530 laptop.

The SiO_2 coated QCMs were placed in the openQCM Q-1 holder between a pair of O-rings so that the SiO_2 coated side was exposed to the DNA samples. The internal volume above the sensing area was 50 µL. First, the PB buffer solution was injected into the flow cell using syringes connected to a syringe infusion pump (Sunnymed) until a stable baseline was obtained, which takes approximately 15 - 30 minutes. Next, DNA solutions of varying concentrations were injected into the flow cell for 30 minutes. After this the PB buffer was flowed over the QCM to remove any loosely bound material. The amount of DNA bound to the QCM was calculated by subtracting the resonance frequency after this wash step from the stable baseline frequency in PB buffer obtained before the DNA injection. This change in frequency was inserted into the Sauerbrey equation to calculate the amount of captured.

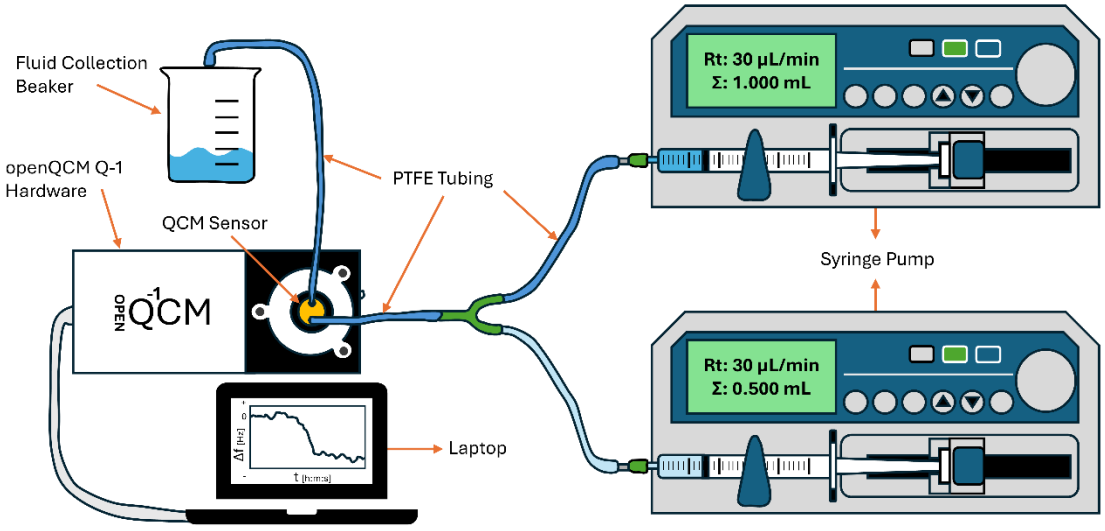

Figure 5.7: Schematic diagram of experimental setup used to investigate DNA binding to NS coated QCMs.

To avoid bubble formation, two syringe pumps were connected to the inlet of the Q-1 flow cell simultaneously, one holding the PB buffer, and the other holding the DNA solutions. These syringes were connected to the two arms of a Y-junction by 3 mm diameter polytetrafluorethylene (PTFE) tubing, with the single outlet of the Y-junction connected to the inlet of the Q-1 flow cell. The tubing for both syringes were primed with their respective solutions up to the intersection of the Y-junction. A schematic diagram of this setup is shown in Figure 5.7. Once a stable baseline was reached in PB buffer, the flow of PB was stopped and the flow of DNA solution was started simultaneously to prevent frequency shifts due to changing flowrates while also preventing air bubble formation within the Q-1 flow cell chamber.

5.2.3. Results

5.2.3.1. Nanostructure Growth & Characterisation on QCMs

Before growing NSs on the QCM surfaces, they were first subjected to the NS growth conditions without the NS precursors present to investigate the temperature and heating rate effects on resonator function. QCMs were subjected to the same conditions used to grow the 40 °C/min dendrites and the CTRVPT ZnO NRs reported in section 3.2 and 2.14, and their resonant frequencies before and after heating were measured. The QCM subjected to SiO_2 deposition conditions appears relatively unaffected by the growth conditions, with the resonant frequency remaining unchanged at ~ 10 MHz and retaining a stability/noise level of ≤ ± 1 Hz. Even after SiO_2 deposition the resonant properties remain unaffected. Figure 5.8 shows the resonant frequency in air of QCMs subjected to 500 °C,

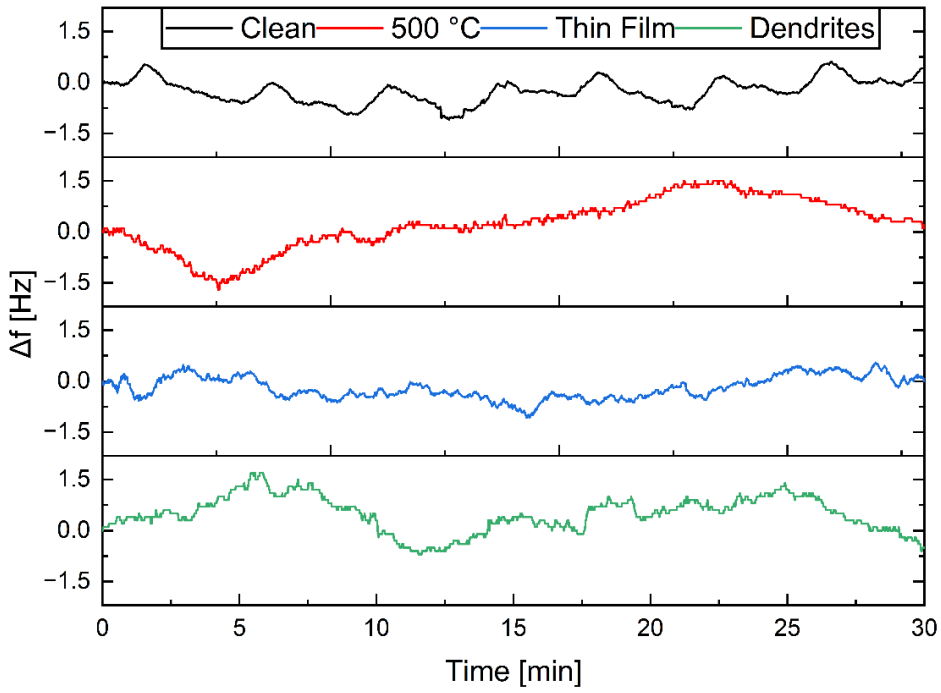

Figure 5.8: Resonant frequencies in air of QCMs that have been untreated, heated to 500 °C, subjected to SiO_2 thin film deposition, and SiO_2 dendrite deposition.

thin film deposition, and dendrite deposition, of which the latter two will be discussed in more details in the following subsection.

Unfortunately, the performance of the QCM subjected to CTRVPT conditions decreased drastically. The resonant frequency increased from 9.999760 MHz to 14.747000 MHz initially, but for the first hour of testing this increased by a further 1 kHz. This frequency increase eventually began to plateau, but for the following two hours would drift upwards by 1 Hz/min with no clear indication of an eventual plateau. Additionally, the resonant frequency would sometimes spike to 16.0 MHz for up to 10 minutes before returning to 14.748 MHz. This 16.0 MHz is the upper limit that can be measured by the Pierce Oscillator circuit driving the QCM which could have been caused by instabilities in the oscillating characteristics of the QCM or issues with the connecting electrodes. An older openQCM housing unit was used for these tests, which was incapable of overtone monitoring hence the plateau of 16 MHz. All subsequent tests were carried out with the newer openQCM Q-1 unit. The same test was repeated the following day and the QCM behaved identically as described above. CP of each QCM was performed alongside an untreated QCM for reference, and the results are shown in Figure 5.9. The 500 °C treatment does not noticeably affect the Au surface topography, however, the 925 °C treatment drastically increases the roughness of the Au electrode by 2 orders of magnitude compared to the untreated and 500 °C treated QCMs (± 1 nm versus ± 100 nm).

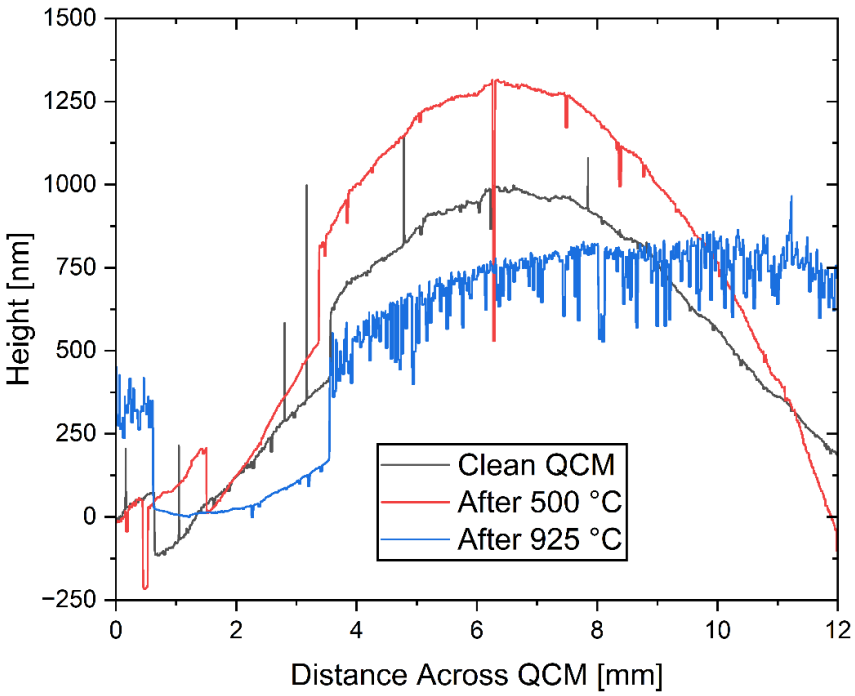

Figure 5.9: CP scans across the top surface of a clean QCM, and QCMs heated to 500 °C and 925 °C without the presence of a NS growth precursor.

The reason for the loss of stable resonator function is likely caused by the α-quartz phase transitions that occur at 573 °C, and possibly 873 °C. At 573 °C, α-quartz undergoes a reversible change in crystal structure from its tetrahedral arrangement to form β-quartz, a hexagonal crystal structure [175], [176]. At 873 °C, β-quartz can form into tridymite, an orthorhombic structure, which is a non-reversible change [177]. However, this tridymite transition should only occur when trace amounts of impurities are present within the quartz, which should be absent in our QCM crystal structure and our experimental chamber. While the phase transition from β-quartz back to α-quartz is reversible, it is known to induce thermal shock faults at cooling rates above 50 °C/hour, which would affect the resonant properties of the QCM [178]. Given the manual controller used for the CTRVPT system, this was not feasible as our system cools naturally at a rate of ~ 750 °C/hour. Another type of piezoelectric resonator was identified, $GaPO_4$, which can not only withstand, but also operate under high temperatures, which would allow us grow ZnO NRs for label-free piezoelectric detection [179], [180], [181]. However, due to costs and lead-times, exploration of this type of resonator was not feasible at the time of writing and will be the focus of future work. However, the SiO_2 dendrites allow us to circumvent the need for the ZnO scaffolds, and, under flow conditions similar to those required for QCM testing, showed greater DNA capture efficiencies.

In our first growth test, Si substrates were placed on top of the top facing electrodes either side of the QCM, to mask them from insulating SiO_2 coverage. However, this had the negative effect of removing Au from the QCM surface resulting in a loss of conductivity at the QCM edge confirmed with digital multimeter electronic testing. Some of the Au would adhere to the Si masking piece, but there was also evidence of the Ti coating underneath the Au layer (which is used to better adhere to Au electrode to the quartz crystal) diffusing to the surface and forming TiO_2, which is discussed later in this section. This was an issue in our initial testing as the first generation openQCM hardware was being used, which required electrical contacts on the top and bottom of the QCM crystal. With the newer openQCM Q-1 hardware, which only contacts the electrodes on the underside of the QCM, this was not an issue. SEM images of SiO_2 dendrites grown on a QCM crystal are shown in Figure 5.10.

The dendrites vary in size from 4 - 8 µm in height, with an inter-structure spacing of 1 - 2 µm. The dendrites appear similar to those grown on Si substrates, further emphasising that the NS growth is not strongly dependent on the substrate material. Despite the highly intricate and delicate features of the dendrites, particularly the straggly branching ends, the dendrites remain upright and retain their original morphology after multiple passes of ionic, DNA, and DI H_20 solutions within the sealed, pressurised microfluidic environment of the openQCM Q-1. SEM images of the dendrites on both Si and QCM substrates after withstanding DNA-Buffer flow at 100 µL/min is shown in Figure 5.11. This demonstrates the stability and robustness of the dendrites.

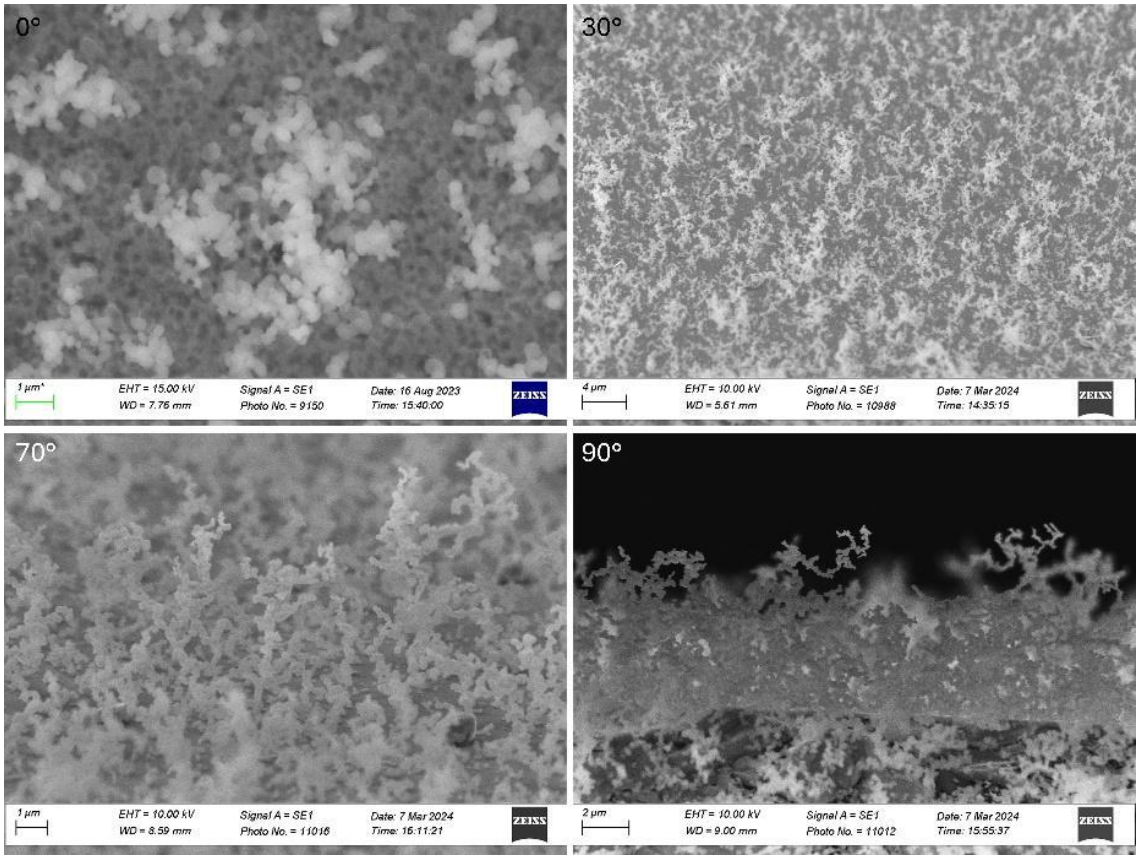

Figure 5.10: SEM data showing SiO_2 dendrites grown on a QCM at substrate tilt angles of (a) 0°, (b) 30°, (c) 70°, and (d) 90°.

We also coated some QCMs in 10 nm thick 2D SiO_2 films using the same technique (using a 1 °C/min heating rate rather than 40 °C/min) to serve as a point of reference to quantify the effect of the NSs compared to planar surfaces. The bare, 500 °C treated, 10 nm thick 2D thin film coated, and dendrite coated QCMs were analysed with XPS, SEM, CA, and CP.

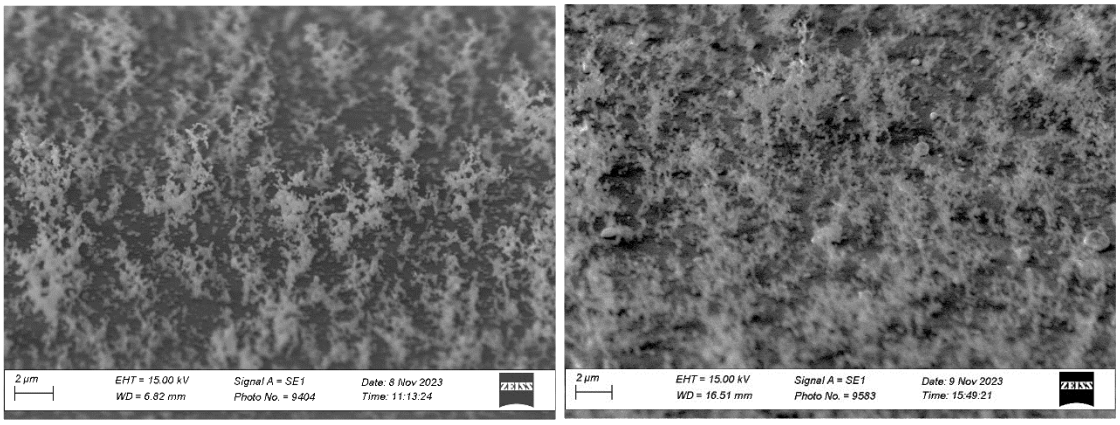

Figure 5.11: SEM images of dendrites grown on (left) Si and (right) QCM substrates after withstanding DNA-Buffer flow within the openQCM flow cell at a rate of 100 µL/min.

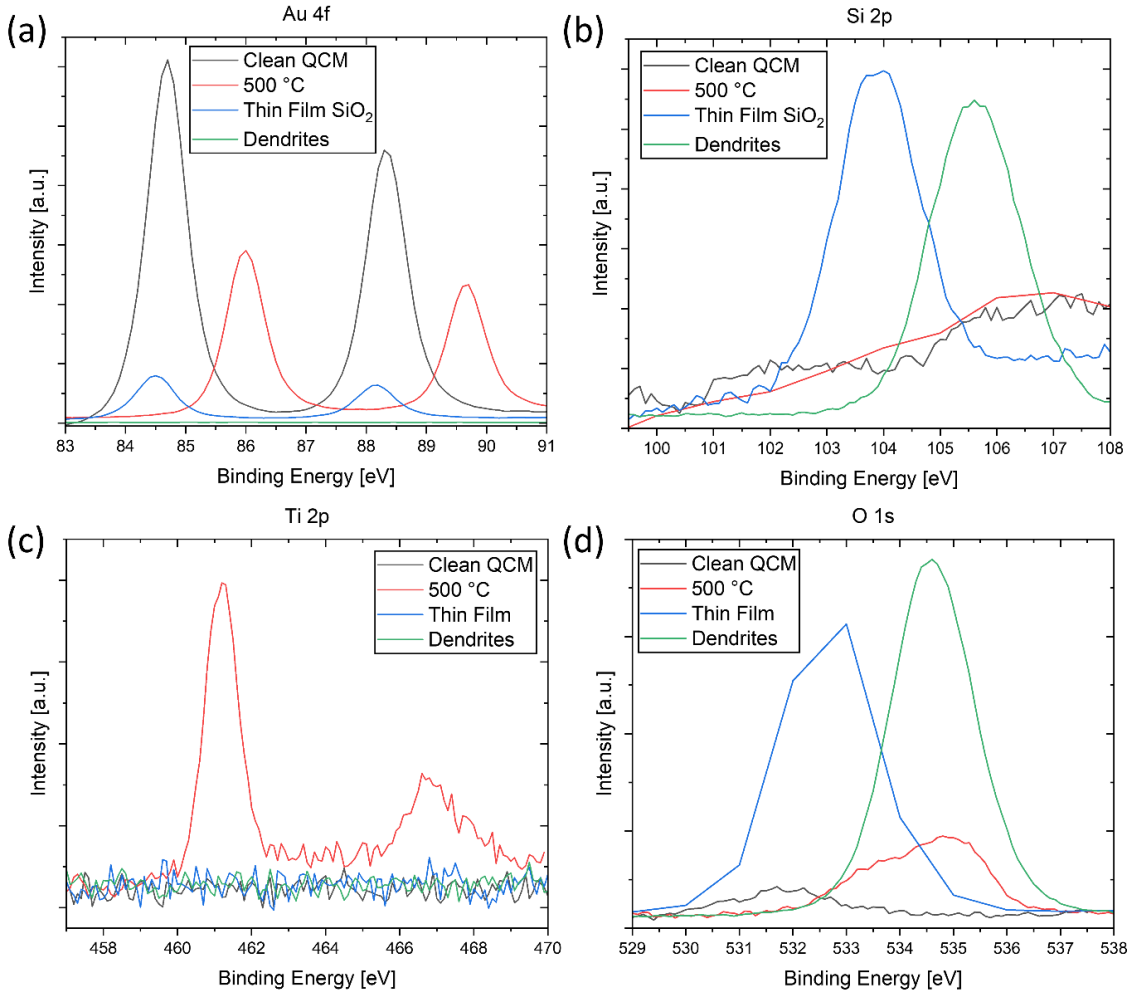

Figure 5.12: XPS Spectra of the (a) Au 4f, (b) Si 2p, (c) Ti 2p, and (d) O 1s orbital regions of QCMs with no treatment, heated to 500 °C, with a nominal 10 nm thick 2D SiO_2 film, and SiO_2 dendrites.

XPS analysis (Figure 5.12) confirms that for both dendrite and thin film coated QCMs, the Au electrode is almost completely coated in pinhole free SiO_2 layers. Small Au peaks can be seen in the thin film sample, but composition analysis reveals that there is only 1.3% Au in the first 10 nm of the sample. This could arise from areas of the thin film that are just below 10 nm in thickness, or from the beading of the Au electrode during heating exposing some additional Au. CP and SEM images confirm Au beading occurring on the surface. The complete suppression of the characteristic 4f peaks of Au at 86 and 90 eV were seen with the Dendrite coating, with the characteristic oxidised Si 2p peak appearing at 104+ eV. The larger positive shift in binding energy observed between the thin film and dendrite sample is due to the increased charging effects resulting from the increased SiO_2 deposition of the dendrites. This is supported by a similar shift seen in the O 1s spectra. The large background intensities of the fresh QCM seen in the Si 2p region are due to satellite peaks and increased background photoemission from Au 4f orbitals due to the lack of an overlying SiO_2 coating.

The Ti 2p is also shown due to the tendency of Ti to diffuse through Au at temperatures above 200 °C [182]. When the QCMs are heated to 500 °C without the presence of PDMS, the underlying Ti adhesion layer, which helps the Au electrode better adhere to the QCM surface, diffuses through the 200 nm thick Au layer and is detectable on the electrode surface. Evidence of oxidised Ti was observed due to the large positive shift in expected binding energy from the expected metallic Ti peak. The charging effects were neutralised using a low energy flood gun, so this shift can likely be attributed to the increased binding energy from Ti-O bonding or from Ti-Au intermetallic mixing.

Figure 5.13 shows top-down SEM images of each type of treated QCM. The untreated QCM is featureless, but when heated to 500 °C, faceted nanoislands can be seen on the surface compared to the more spherical structures typically observed with pure Au beading. On the other hand, the QCM with the 10 nm thin film, despite also being heated to 500 °C for the same length of time, does not show these faceted structures, and there is significantly less beading on the electrode surface. This seems to suggest that the SiO_2 thin film significantly reduces the Au beading and prevents Ti diffusion to the top surface.

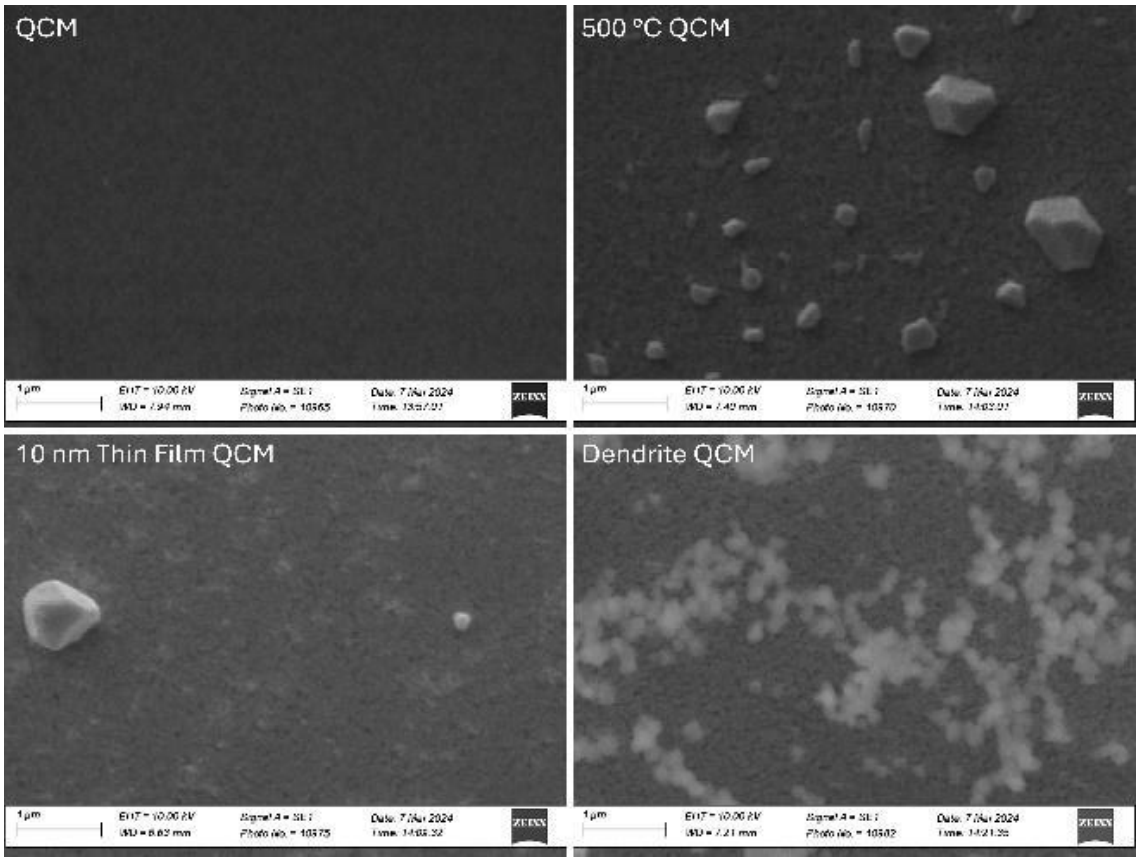

Figure 5.13: Top-down SEM data of (a) a bare QCM, (b) a QCM heated to 500 °C without PDMS, (c) a 2D thin film coated QCM, and (d) a dendrite coated QCM at the same magnification.

Figure 5.14: Contact angle results for each treated QCM. 10 µL droplets were used and the quoted values were taken from 3 independent measurements on each sample surface.

The contact angle results in Figure 5.14 show the clear effect the SiO_2 coatings have on the hydrophilicity of the QCM surfaces. Not only do the dendrites result in the most hydrophilic surfaces, but their wettability is within the realm of superhydrophilicity according to the literature [183]. The dendrite-QCM surface requires only 1 µL to coat the entire 3.14 cm^2 sensing area, needing only 0.32 $\mu L.cm^{-2}$ to fully wet the surface. On the other hand, the uncoated QCMs required 240 µL, or 76.43 $\mu L.cm^{-2}$. Superhydrophilicity has been previously reported to be a key factor in increasing the sensing response of QCMs [172]. This has the additional effect of allowing less sample volume to be used, a key factor in point-of-care diagnostic applications. One of the three assumptions of the Sauerbrey equation (discussed in chapter 2 section 2.3.2) is that the deposited mass must be evenly distributed across the entire sensing region. The superhydrophilicity ensures this underlying assumption of the Sauerbrey equation remains valid under low sample volumes. Lastly, the roughness of each surface was investigated using CP, and the results are shown in Figure 5.15.

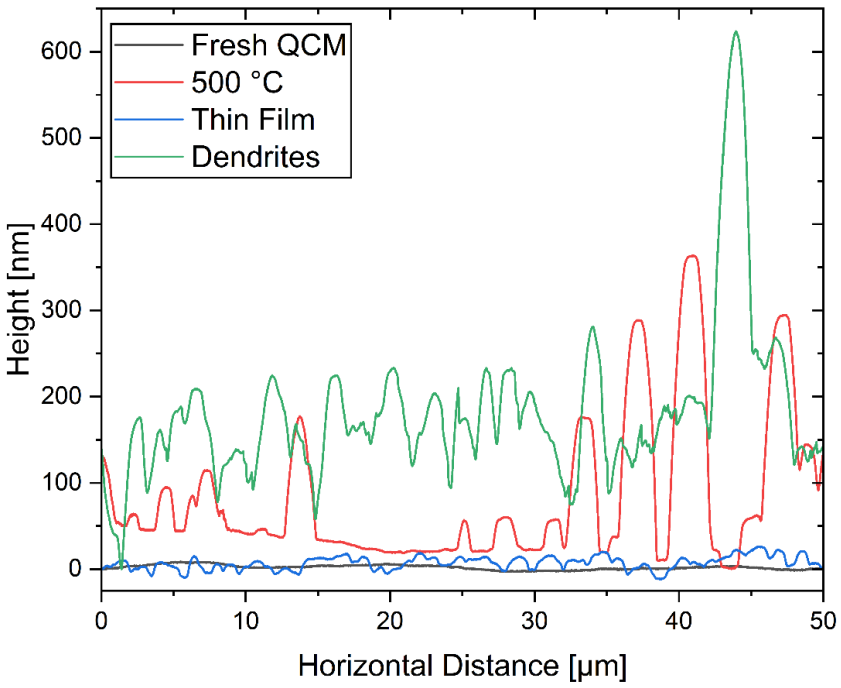

Figure 5.15: CP scans of each treated QCM surface.

These CP results in Figure 5.15 show clear difference in surface roughness between each of the different samples, which is supported by the corresponding SEM images. The RMS roughness values are 3.4, 120.0, 10.5, and 204 nm from top to bottom respectively. An unexpected result appears to be that the thin film coated QCM has a much lower roughness than the QCM heated to 500 °C without the presence of PDMS. This data agrees with the SEM data shown in Figure 5.13, further suggesting that the SiO_2 coating may reduce the amount of Au beading/nanoisland formation. The CP results of the Dendrite QCM are not a true representation of the surface, as CP is a potentially destructive technique, and the probe is likely destroying the dendrites as it scans across them. However, the remaining SiO_2 in this case is clearly much rougher than the other samples and is an indicator of the enhanced surface area.

5.2.3.2. Piezoelectric DNA Detection

The frequency response of each QCM at various concentrations is shown in Figure 5.16. The results indicate that the dendrite QCM has significantly enhanced biomolecule capture capabilities compared to planar QCM surfaces, shown by the strong frequency response seen at each DNA concentration, which is in excellent agreement with our previous results comparing NS grown on Si substrates. The high surface-to-volume ratios provide a

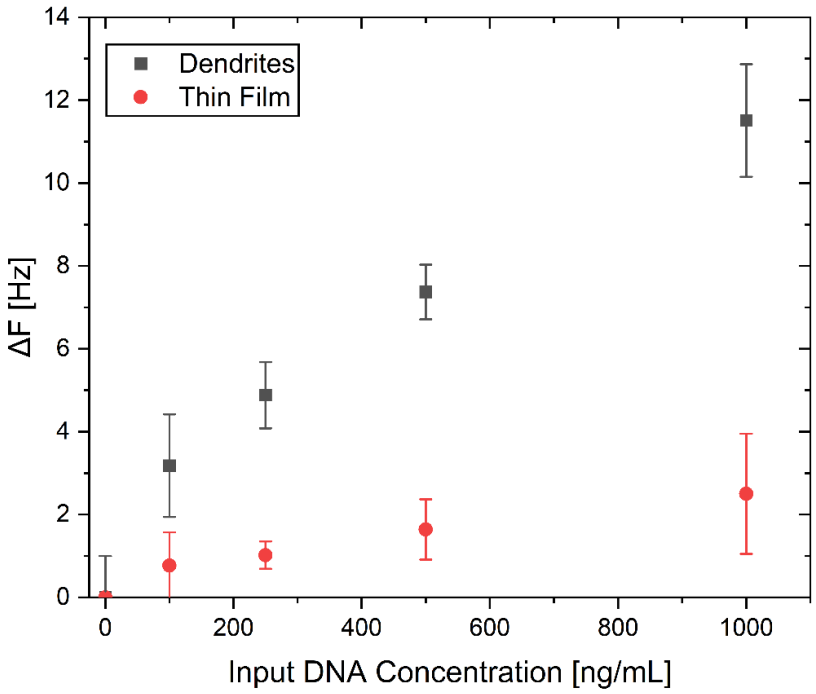

Figure 5.16: Frequency response of nanostructured QCM vs flat QCM under various DNA concentrations.

substantially greater surface area for DNA adsorption compared to the planar surfaces. The increased surface area enhances the probability of DNA molecules interacting with the surface, facilitating extensive DNA adsorption, and improving the overall binding capacity of the QCM sensor. The high sensitivity, demonstrated by the limit of detection of 100 ng/mL of DNA (signal to noise ratio of ≥ 3 (3.1 ± 1.0 Hz), highlights the effectiveness of nanostructured surfaces in capturing and detecting biomolecules with high precision. In contrast, the planar 2D films exhibited minimal frequency response except at the highest DNA concentration tested. This suggests that the flat surface of the 2D films offers limited interaction sites for DNA molecules, resulting in lower adsorption efficiency. The reduced surface area restricts the number of binding events, leading to a weaker signal that only becomes significant at high DNA concentrations. Evidence of this can be found in the frequency and complementary dissipation response of both QCMs shown in Figure 5.17.

An example of the real-time frequency and dissipation response of a dendrite coated, and thin film coated QCM to 1000 ng/mL of DNA is shown in Figure 5.17. The frequency response of both QCMs showed a similar initial decrease, indicating DNA absorption on both surfaces. However, the post-wash (from t = 40 minutes onwards) frequency behaviour of both QCMS differed significantly between one another. There is a slight frequency increase after the dendrite wash, stabilising shortly afterwards at ~ 11.5 Hz. This residual

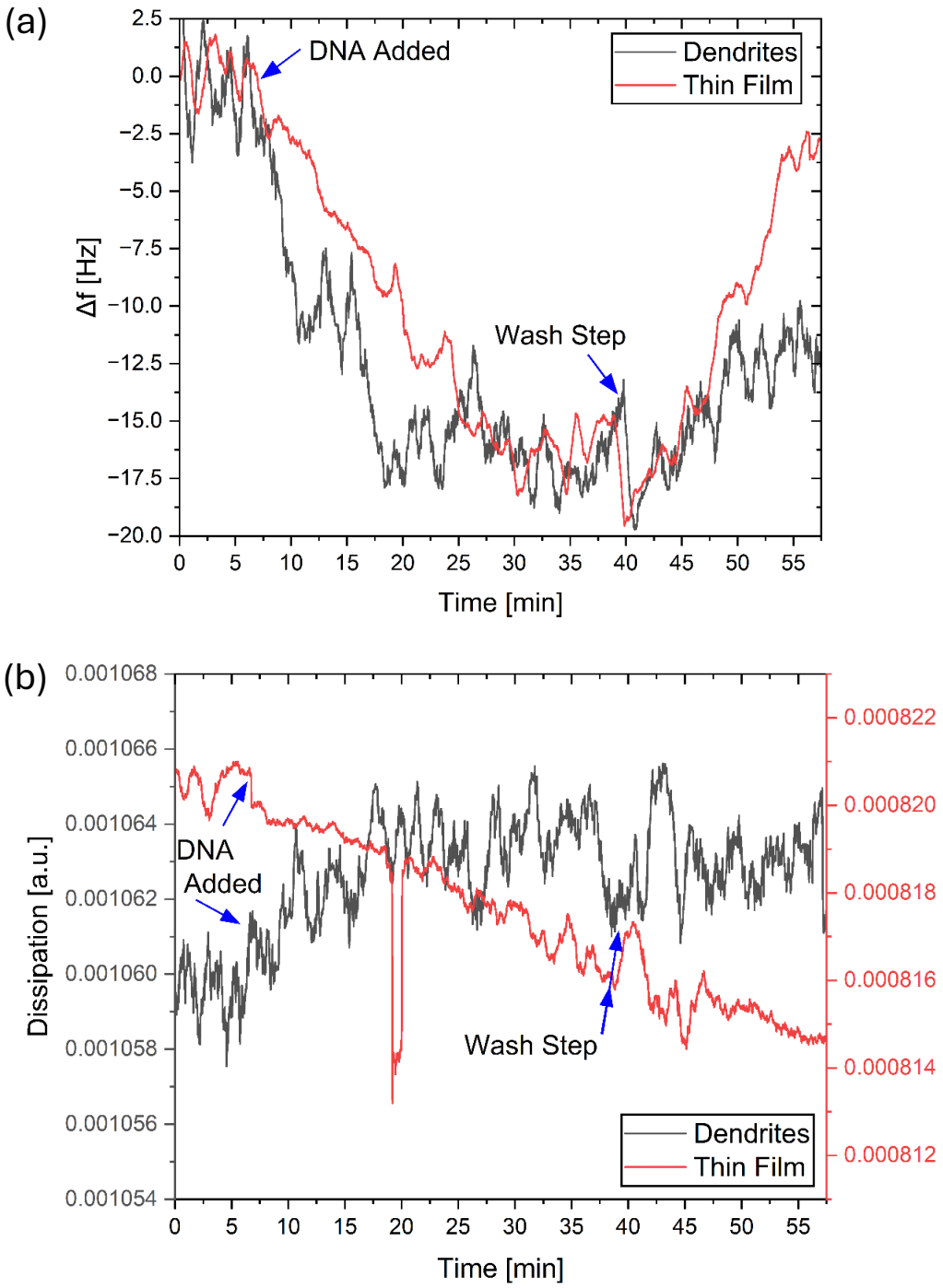

Figure 5.17: (a) Frequency and (b) dissipation response of dendrite-coated and thin film-coated QCMs to 1000 ng/mL of DNA. The arrows indicate the time at which the DNA solution and the PB solution washing step are introduced.

frequency shift indicates a significant amount of DNA remains bound to the dendrites and the QCM after washing. The slight increase suggests a small amount of desorption has occurred, likely due to removal of loosely bound DNA. In contrast, the thin film coated QCM returned almost entirely to baseline after the wash, stabilising at ~ 2.5 Hz. This minimal residual frequency shift suggests that most of the DNA adsorbed initially was removed

during the wash step, indicating weak binding. However, the frequency shift observed during DNA flow cannot be solely attributed to DNA binding. The frequency response of a QCM is not only sensitive to changes in the surface mass loading but also the viscoelastic properties of the medium in contact with the QCM surface as described in section 2.3.2 by the Kanazawa-Gordon equation. When a viscoelastic layer or viscous liquid is in contact with the QCM, the resonance frequency can also decrease due to energy dissipation in the viscoelastic layer or due to viscous drag from the liquid.

The sensitivity of the QCM to both mass loading and liquid properties highlights the need for the wash step and dissipation monitoring to truly quantify binding events. In the case of the thin film QCM, the observed frequency returning close to baseline after washing suggests that the frequency decrease might not be primarily due to stable DNA binding. Instead, it could also be influenced by the transient presence of the DNA solution with higher viscosity and density than the pure PB buffer. Once the wash step removes the DNA solution and replaces it with the original PB buffer, the frequency returns to near baseline, indicating that most of the observed frequency shift was not solely due to permanent mass loading (DNA binding) but rather to the temporary change in the contacting medium's properties. This can be further unravelled by analysing the complementary dissipation data. The difference in absolute dissipation values arises from the two difference NS coatings. The thin films show much lower absolute dissipation due to the much lower amount of SiO_2 deposited and the increased compactness and uniformity of the film compared to dendrites.

In the case of the dendrite coated QCM, the characteristic dissipation response expected of stable biomolecular binding was seen [184], [185], [186]. That is, a small but noticeable increase in dissipation as the DNA solution contacts the QCM. This increased dissipation arises from the viscoelastic nature of DNA. The DNA bound to the dendrites increases the amount of energy lost during QCM oscillations due to mechanical losses in its flexible mass. This type of energy loss could arise from transient interactions with the DNA solution as mentioned above; however, the dissipation value remains constant after the PB wash step, indicating that energy losses are due to stably bound DNA which has remained after removing the DNA solution. These frequency and dissipation results, pre- and post-wash, confirm that the DNA is strongly and stably bound to the dendrites, enabling meaningful capture and detection.

The dissipation results observed with the thin film QCM suggest a complex interaction between the QCM, the PB buffer ions, and the DNA. The continuous decrease suggests dynamic changes occurring on the QCM surface. This has been attributed in literature to dynamic reorganization or gradual desorption of adsorbed layers. Given the decreasing resonance frequency, the latter can likely be ruled out. The occasional small increases in dissipation could be attributed to transient binding events or structural rearrangements of the weakly bound DNA, or adsorbed ion reorganisation influenced by transient DNA interactions as adsorbed layer reorganisation is known to reduce the dissipation [187]. Weakly bound DNA could be stripping the adsorbed salts from the QCM surface after desorption. Additionally, the DNA can organise the adsorbed salt ions into a more compact, rigid structure, reducing the overall damping affects. Unravelling these interactions would require additional characterisation techniques beyond the scope of this work, but the fact remains that regardless of interactions during DNA flow, the DNA does not remain bound to the planar QCM after washing. This behaviour indicates that the planar surfaces provide insufficient binding sites and stability for DNA adsorption, underscoring the advantages of nanostructured surfaces. DNA may be binding, but if it does not sufficiently remain post-wash, it cannot be used with more complex and crude real-world samples which require thorough washing before detection.

5.2.3.3. Conclusions

By growing SiO_2 dendrites on QCM sensors, their ability to capture and detect DNA is significantly enhanced. The resonator properties of QCMs were shown to be unaffected by the growth conditions and the growth itself, and the binding of DNA to these NSs was shown to be highly stable, withstanding washing steps which are of extreme importance when working with crude, real world samples. Further work is now required to functionalise these nanodendrites to enable specific DNA strand capture and detection from complex samples.

These nanostructured QCM present a viable platform for POC based testing in environments where initial investment needs to be minimised, and moderate to low volumes of testing are expected, such as a general practitioner's office. Right now, the initial setup cost is low, but the per-test cost is higher than PCR as the fabrication of QCMs is quite limited and specialised at the time of writing. The initial start-up costs for PCR testing involve the purchase of the combined amplification and detection apparatus (€13000 to €81000 (depending on degree of automation)), the centrifuge (€480), and a micropipette for reagent handling (~€200) [188]. This gives a set-up cost range of ~ €14000 – €82000.

Whereas the QCM has a much lower startup cost, with the commercial housing unit costing €1800 (required for dissipation monitoring for research purposes, but a lower cost system (€1000) could be used for only frequency monitoring), and two syringe pumps (€400 each), giving the QCM a much more affordable set-up cost of ~ €1800 – €2600. PCR is more affordable per test (on a per 10-test basis), with material costs as follows; fluorophores (€740 for 200 assays, €37 per 10 tests), SiO_2 spin columns (€550 for 250 columns, €22 per 10 tests), and PCR primers (~€50 per 10 tests). On the other hand, QCM crystals cost €230 per 10 crystals/tests. The nanodendrites are deposited using 0.07 g of PDMS from a 1100 stock solution costing ~ €190, so the cost per 10 depositions is €0.12 which is negligible. Therefore, ignoring common reagents, materials, and manual labour costs, the brief running costs of PCR is ~ €110 per 10 tests, while the QCM method costs ~ €230 for 10 tests. The hope is that as research into QCM technology advances and manufacturing scales up, increased competition and production efficiency will drive down costs, as currently only a limited number of companies produce these devices. The time to run a PCR test and a QCM test is roughly similar, at ~ 40 – 60 minutes per test, but PCR has the added benefit of being able to run multiple samples (30+) at the same time, whereas our current system can only test one sample at a time. QSense, a leading company in the development of QCM technology, are developing advanced systems for multiplex sensing. Their QCM-D systems allow for simultaneous testing of 4 to 8 samples, enabling high-throughput analysis in a fully automated manner, bringing QCM technology one step closer to competition with PCR-like technologies [189].

5.3. Biocompatible SiNP Coated PLA

5.3.1. Introduction

PLA is a widely used biopolymer due to its sustainable and renewable synthesis, general abundance, compostability, and biodegradability [190]. PLA has gained significant attention in biomedical applications such as tissue regeneration, scaffolding, and surface coatings on medical implants and drug delivery systems [191]. However, these advantages come with drawbacks when it comes to biomedical implantation, as PLA is relatively hydrophobic which can impact cell growth and reduce the rate it degrades into CO_2 and H_2O (which are eliminated from the body by normal metabolism), hindering the growth of new bone [192]. Much work has been done to modify this degradation behaviour and increase the hydrophilicity of PLA by applying protective surface coatings. However, for

biomedical implants, the surface chemistry and topology of the implant material plays a crucial role in the interaction between implant and neighbouring host cells and tissues [193]. SiNPs have been widely employed in the literature for biomedical applications due to their biocompatibility, however, limited studies have explored their use as PLA surface coatings. In this chapter, the biocompatibility of PLA and SiNP-coated PLA surfaces was investigated, as well as their impact on two types of cell growth and adhesion.

5.3.2. Materials & Methods

5.3.2.1. Acknowledgments

Cell culture and biocompatibility studies were carried out by Dr. Keith Rochfort at the School of Biotechnology in Dublin City University. The PLA stent was designed and printed by Dr. Jennie O'Loughlin at the School of Physical Sciences in Dublin City University. I performed the SINP coating and physicochemical characterisation of each PLA substrate and provided the SiNP coated discs for Dr. Rochfort's testing.

5.3.2.2. Cell Culture

A549 cells were used as a model to investigate the cytotoxicity of the SiNPs. Briefly, A549 cultures were cultured in Dulbecco's modified Eagle's medium (Gibco TM, Cat. No. 11885084) supplemented with Fetal Bovine Serum (10% v/v) (Gibco TM, Cat. No. 10500064), penicillin (100 $U.mL^{-1}$) and streptomycin (100 $\mu g.mL^{-1}$) (Gibco TM , Cat. No. 15140122). A549 cells were seeded at a density of 3000 cells/cm^2 and maintained in 5% CO_2/95% humidity at 37 °C. The culture media was removed and replaced with fresh media every 2-3 days, with the cells passaged at 90% confluency.

Additionally, human aortic endothelial cells (HAEC) were isolated from a human aorta and were subjected to the same growth conditions and biomarker testing. The cell culture conditions were identical to those of A549 culture, except the media used was C-22020 from Promocell.

5.3.2.3. Treatment Conditions

Following SiNP coating as described in section 4.3, the PLA discs were placed at the bottom of 6-well plates before being then packaged and sterilised by vaporised hydrogen peroxide (VHP, 30% H_2O_2 concentration, 65 °C, ambient pressure, 6-9 hours). The sterility of PLA plastics after this sterilization technique has previously been examined by Doherty *et al.* [194]. A549 cells were tested on PLA discs coated with 76, 380, and 1520 µg/mL of SiNPs, whereas aortic cells were tested on discs coated only in 76 µg/mL. Cells were seeded to confluence in each well containing a disk at a density of 300,000 cells/cm^2. Following 12

hours, the culture media and any unadhered cells were removed and fresh culture media. The cells were then incubated in 5% CO_2/95% humidity at 37 °C with assays carried out at 24, 48 and 72 hours.

5.3.2.4. Lactate Dehydrogenase Release

The release of lactate dehydrogenase (LDH); a biomarker of cell stress, was measured using the Cytotoxicity Detection Kit (LDH) (Merck, Cat. No. 11644793001) following the culturing of the cells on SiNP-coated PLA disks. The protocol followed the manufacturer's instructions with minor modifications. Briefly, following subculture onto the SiNP-coated PLA disks for the designated amount of time (24-72 hours), 100 µl of culture media was removed from each well and transferred to a 96-well plate in triplicate. 100 µl of Reaction Mixture was then added to each well, and the plate was left to incubate for 30 minutes at room temperature. 50 µl of Stop Solution was then added to each well and the plate was shaken gently for 10 seconds. The plate was then read at 490 nm on a TECAN Infinite 200 PRO Microplate Reader. Values are represented as fold change to a polystyrene 6-well surface at each respective timepoint.

5.3.2.5. MTS Assay

The viability of the cells was measured using the CellTiter 96 Aqueous Assay (Promega, Cat. No. G3582) following the culturing of the cells on SiNP-coated PLA disks. The protocol followed the manufacturer's instructions with minor modifications. Briefly, following subculture onto the SiNP-coated PLA disks for the designated amount of time (24-72 hours), 200 µl of CellTiter 96 Aqueous Assay reagent was added to each well, with the plate returned to the incubator for 4 hrs. 100 µl of culture media was removed from each well and transferred to a 96-well plate in triplicate, and the absorbance was then read at 490 nm on a TECAN Infinite 200 PRO Microplate Reader. Values are represented as fold change to a polystyrene 6-well surface at 24 hours.

5.3.2.6. Cell Density

The cell density was measured by utilising a crystal violet-based assay as described by Geoghegan *et al*. with minor modifications following the culturing of the cells on SiNP-coated PLA disks [195]. Briefly, following subculture onto the SiNP-coated PLA disks for the designated amount of time (24-72 hours), all culture media was removed from each respective well before 2 mL of sterile phosphate buffered saline (PBS) was added. Following a gentle wash, the PBS was removed and 1 mL of 3.75% formaldehyde solution was added. Following 15 minutes incubation at room temperature, the formaldehyde solution was removed, and 1 mL of a crystal violet solution (5 mg/mL) was added to the fixed cells for 5

minutes. The crystal violet solution was then gently washed from the wells using deionised water until all excess stain was removed, and the plates were left to air dry overnight. 500 µl of a 2% (w/v) sodium dodecyl sulphate solution was added to each well, and the plate was gently agitated by placing it on a shaker to assist in cell solubilisation for approximately 30 minutes. 100 µl of culture media was removed from each well and transferred to a 96-well plate in triplicate, and the absorbance was then read at 560 nm on a TECAN Infinite 200 PRO Microplate Reader. Values are represented as fold change to a polystyrene 6-well surface at 24 hours.

5.3.2.7. Orbital Shear

HAEC cultured discs were subjected to laminar shear stress testing using an orbital rotator (Stuart Scientific Mini Orbital Rotator) as described in [196]. 4 mL of cell culture media was added onto each disc in each well, and they were rotated at 200 rpm for 24 hours.

5.3.2.8. Stent Coating

A model PLA stent was printed with length and diameter of 63.3 mm and 11.0 mm respectively, and each strand was 0.5 mm in diameter. The stents were coated in 76 ug/mL of SiNPs in the same way as the PLA discs described in section 4.4.

5.3.3. Results

Direct contact of A549 Cells with SiNP-functionalised surfaces has no significant impact on cell viability.

The biocompatibility and cytotoxicity of the SiNPs for surface functionalisation purposes was first examined utilising A549 cell cultures. Briefly, A549 cells were seeded to confluence on SiNP-functionalised polylactic acid disks placed in 6-well dishes (Figure 5.18a). From the time of seeding, indices of cell health were measured every 24 hrs up to 72 hours. Cell culture media was harvested every 24 hours and assayed for levels of LDH. There were no significant changes in LDH levels of the culture medium over the 72 hours incubation period at the examined concentrations of SiNPs (Figure 5.18b). Similarly, there were no significant changes in cell metabolism as measured by MTT assay (Figure 5.18c) or cell adhesion/number (Figure 5.18d) up to 72 hours. This data was supported by bright field microscopy observations in which no obvious perturbations to cell morphology were observed (Figure 5.18e).

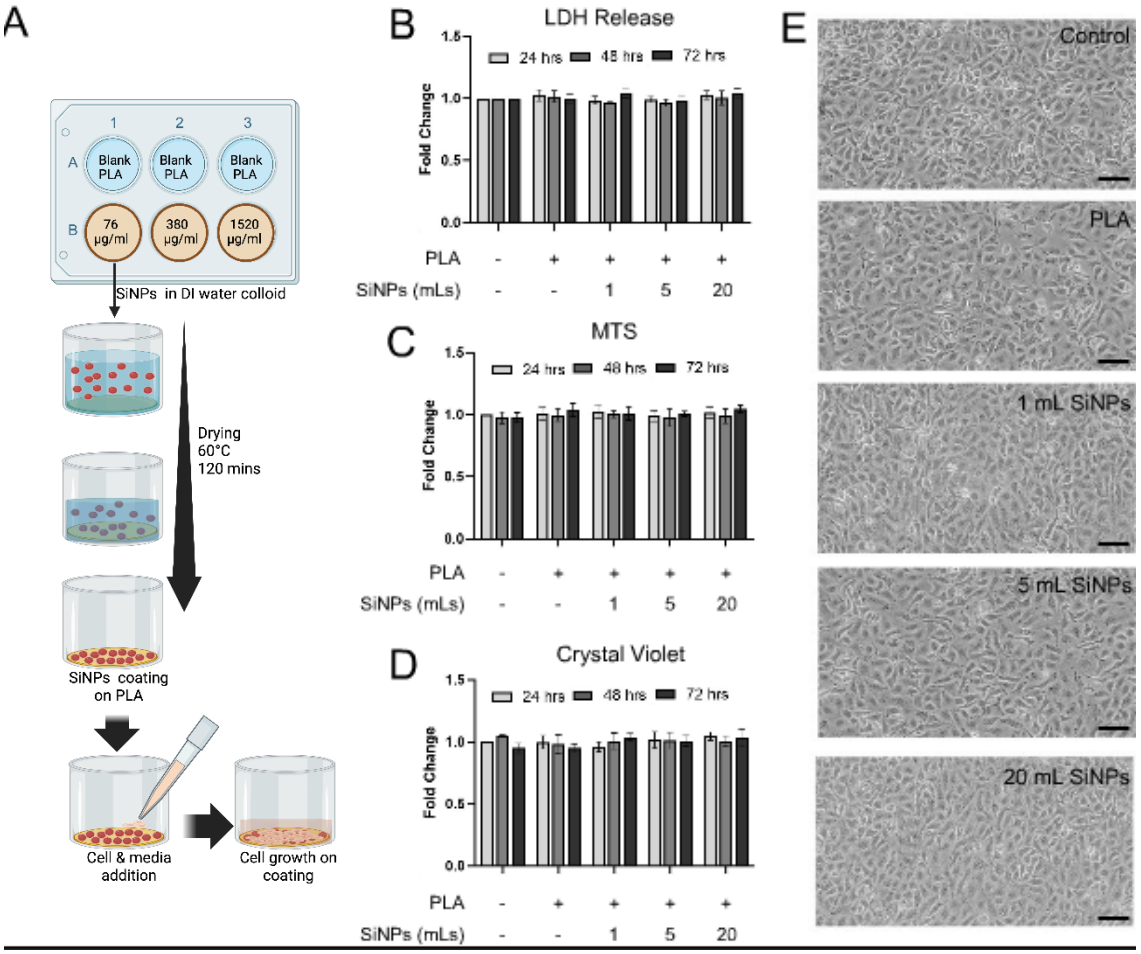

Figure 5.18: Biocompatibility and cell adhesion results for A549 cells grown on SiNP-coated PLA discs. (A) Illustration of the SiNP coating and cell growth procedures. (B) LDH release fluorescence results. (C) MTS assay results. (D) Crystal Violet assay results. (E) Bright field microscopy images of A549 cells grown on PLA discs coated in varying concentrations of SiNPs.

Observing no effect of SiNP concentration of cell growth, only the lower SiNP concentration of 76 µg/mL was used for testing HAECs. The results are shown below in Figure 5.19. Figure 5.19.a shows the change in cell proliferation by increased absorbance of crystal violet stain (i.e. more cells meaning more stains and subsequently more absorbance). Figure 5.19.b shows an increase in MTS enzyme activity, but this is likely due to the increased cell number rather than a change in each cells respective level of the enzyme, supported by Figure 5.19.a. The LDH levels in Figure 5.19 indicate the SiNPs are not adversely affecting the aortic cells, as LDH is an enzyme that leaks from injured cells (the measurable LDH levels observed come from cells being turned over and replaced). These results indicate that the SiNPs increase HAEC proliferation compared to uncoated PLA discs while also remaining biocompatible. However, to verify this, additional tests were required. The cells could grow faster if they were provoked or inflamed by the SiNP presence, which can temporarily cause a spike in growth levels.

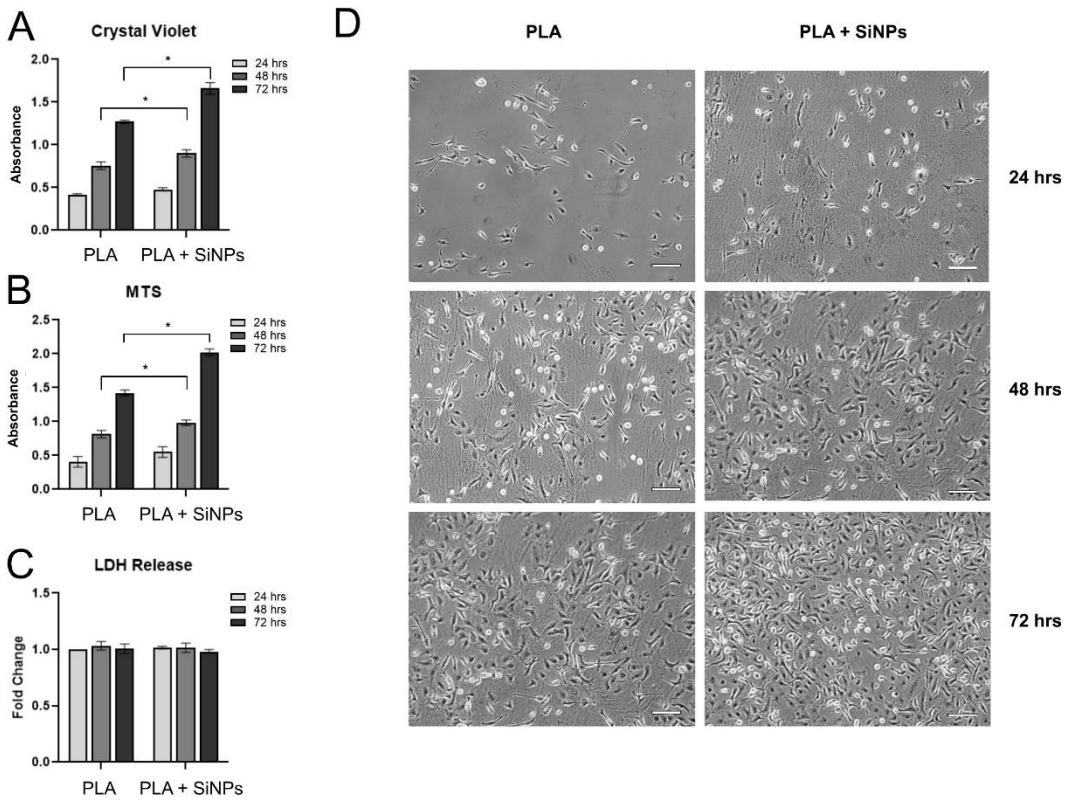

Figure 5.19: Biocompatibility and cell adhesion results for HAECs grown on SiNP-coated PLA discs. (B) Crystal Violet assay results. (C) MTS assay results. (D) LDH release fluorescence results. (E) Bright field microscopy images of aortic cells grown on PLA discs coated in 76 µg/mL of SiNPs taken every 24 hours.

Repeat tests were conducted on fully confluent cell monolayers that reflect that which is seen in a blood vessel. If the cells are inflamed in this confluent state, cell death will occur which will be indicated by drops in crystal violet and MTS signal, alongside a simultaneous increase in LDH release. These results are shown in Figure 5.20.

Figure 5.20a-c shows no statistical significance between the control PLA disc and the SiNP-coated PLAS disc, indicating the SiNPs are driving cell growth but seemingly not through an inflammation-driven mechanism. This is supported by brightfield microscopy of the fully confluent monolayers as a reference, showing minimal change between both samples. Inflammation would result in cell morphology changes, alongside gaps in the monolayer floating dead cells. Figure 5.20e shows images of the cells subjected to flow forces typical of those seen in a vessel and therefore a stent. The left panels show static cells as grown on the SiNP-disc, while the right panels show the alignment of the cells in the direction of fluid flow (indicated by the white arrow). The green signal represents the acting cytoskeleton which is a common maker used to show cell realignment under flow conditions. These results show that cells can still grip to the SiNP-coated PLA under expected flow conditions in biomedical implants.

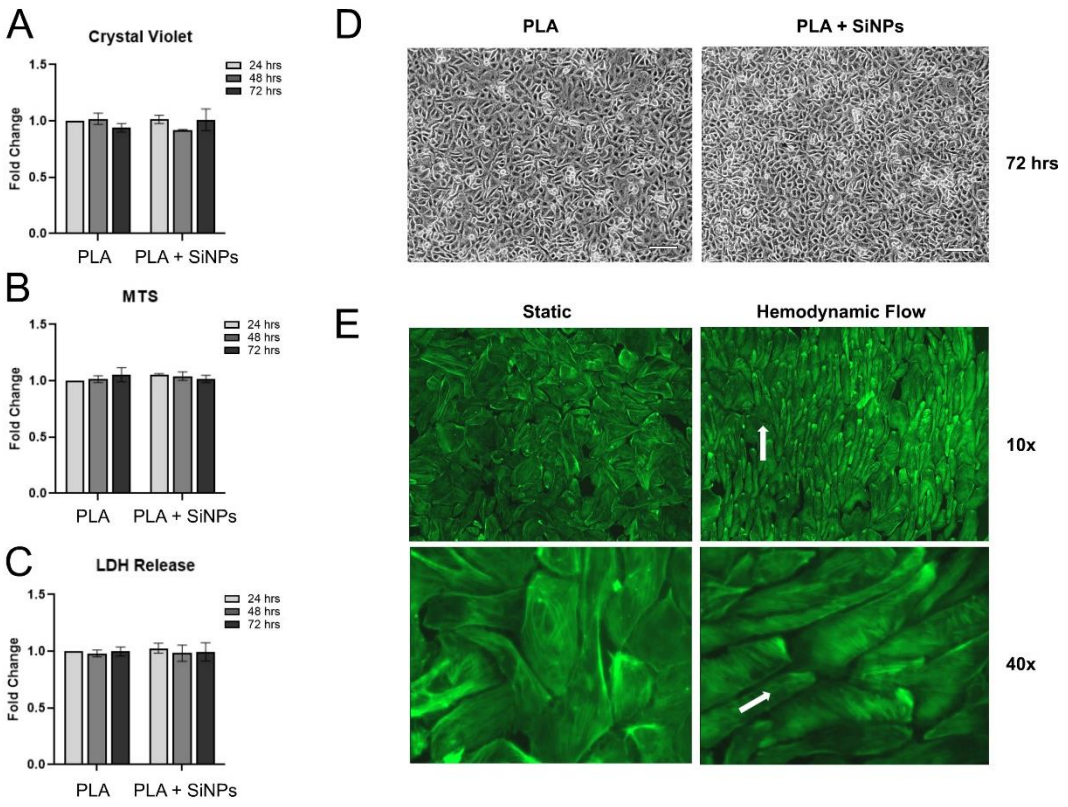

Figure 5.20: Biocompatibility and cell adhesion results for human aortic cells grown on SiNP-coated PLA discs to determine if increased cell proliferation is driven by an inflammation-drive mechanism. (A) Crystal Violet assay results. (B) MTS assay results. (C) LDH release fluorescence results. (D) Bright field microscopy image of fully confluent monolayers of aortic cells grown on PLA discs coated in 76 µg/mL of SiNPs and (E) fluorescence microscopy image of aortic cells grown on SiNP-coated PLA while subjected to flow conditions expected within blood vessels.

These results are highly promising, highlighting the potential benefits of SiNP coated biomedical implants with future optimization. As a proof of concept, a model PLA stent was 3D printed, and the ability to coat a complex 3D structure in a uniform manner like the previously discussed PLA disc was investigated. The results are shown below in Figure 5.21.

The stent was printed with scaffolding between the strands to increase stability, because the stent required Au coating for imaging since the Au coater can reach temperatures of 100-150 °C depending on the current and deposition time required. The scaffolding is shown as the vertically orientated parallel structures in Figure 5.21 a-b. Scaffolding was left absent from either side of a single strand, to obtain representative images of a true stent structure, shown in Figure 5.21 c-d. Higher magnification images of SiNPs on the PLA substrate could not be obtained, possibly due to overcoating by the Au layer. Due to the complex size and 3D structure of the stent, it could not be imaged under variable pressure mode like the previous SiNP coated discs due to substrate size restrictions of the Jeol JSM-IT 100 InTouch Scope SEM. There is some evidence of nanoscale features on the stent

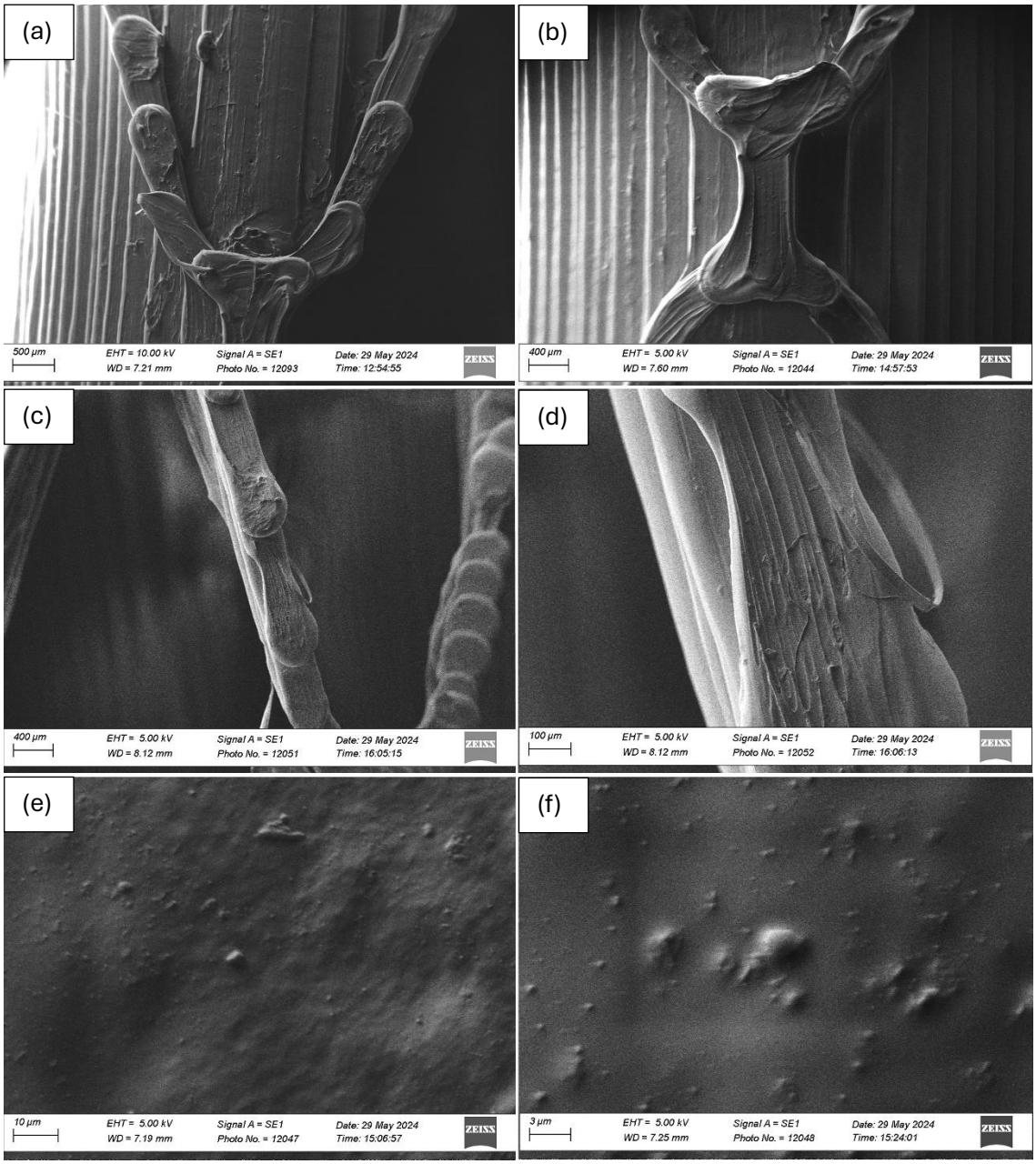

Figure 5.21: SEM images of an SiNP coated PLA stent at various magnifications.

surface (Figure 5.21e-f), but whether these are from SiNPs or PLA was not determined. However, EDX confirms the uniform coverage of SiNPs, which is shown below in Figure 5.22.

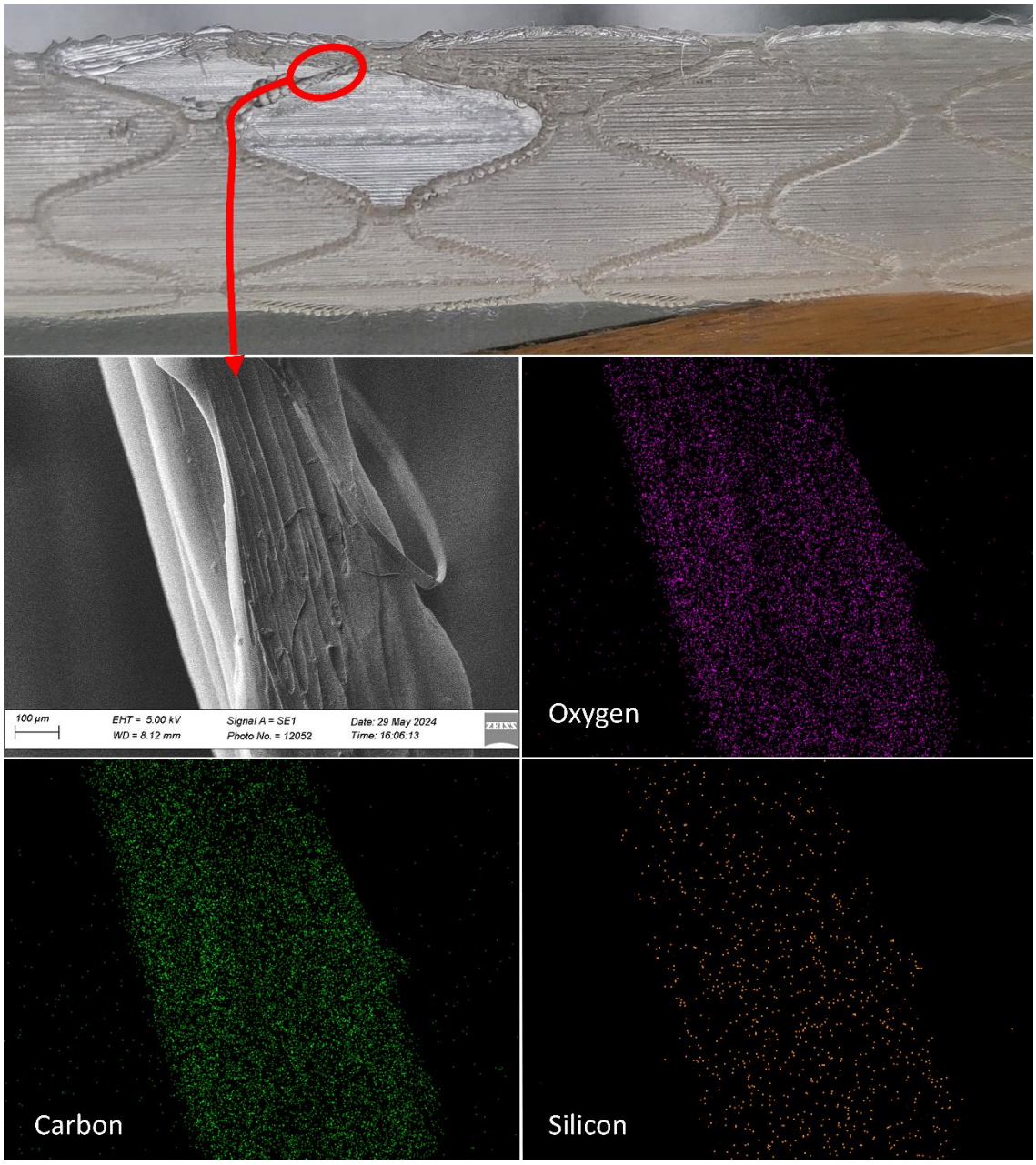

Figure 5.22: EDX of a SiNP-coated PLA stent. (Top) Photograph of stent highlighting the region that the SEM image and EDX spectra were obtained from.

5.3.4. Conclusions

The coating of PLA surfaces has demonstrated that SiNP-functionalised surfaces do not significantly impact cell viability. The comprehensive analysis of cell health, metabolism, and adhesion through LDH release, MTT assays, and cell density tests suggest that, at the concentrations examined, that SiNPs exhibit biocompatibility and low cytotoxicity, while also promoting HAEC proliferation, making them suitable as surface coatings for biomedical applications such as stents, promoting vascular cell-proliferation compared to uncoated surfaces.

5.4. Conclusions

The application of SiO_2 NSs for DNA capture and detection and as biocompatible surface coatings has been shown and the potential of these approaches clearly demonstrated. For the first time, a new method for the growth of high surface-to-volume ratio SiO_2 NSs on QCM sensors was showcased, and their significantly enhanced DNA capture capabilities compared to planar QCMs. The ease of synthesis and the label-free detection mechanism provided by the QCM opens new avenues for point-of-care DNA detection. Future work should include the post-synthesis functionalisation of the SiO_2 NSs for specific target DNA strand detection. Similarly, the SiNPs techniques require only facile synthesis and coating methods and provide highly biocompatible surface coatings that show much potential for use in biocompatible implants. Further work should include additional cell biomarker studies to fully verify the range of biocompatibility and possible cytotoxicity.

6. Conclusion and Future Work

6.1. Conclusions

This thesis has systematically explored the fabrication, characterization, and application of SiO_2 NSs for various biomedical applications. The work has demonstrated novel methodologies and significant advancements in the efficient, low-cost production and functionalisation of these nanomaterials, and an effective label-free DNA detection method was demonstrated.

The ability to produce low-cost SiO_2 NSs could lower the barriers preventing SiO_2 incorporation into microfluidic devices for DNA capture, isolation and purification, which is a major bottleneck in the development of true DNA detecting point-of-care devices. The second major bottleneck is the requirement for techniques like amplification and fluorescence spectroscopy for DNA detection.

To that end, the work demonstrated in this thesis reported a method to provide simultaneous capture, isolation and detection of DNA. To address the challenge of SiO_2 incorporation into microfluidic devices, we developed and optimised a novel and straightforward method for the deposition of high-quality, nanoscale SiO_2 films and 3D SiO_2 nanostructures through the thermal decomposition of polydimethylsiloxane (PDMS). This process was optimised to control the morphology of the SiO_2 deposits, where slower ramp rates produced conformal 2D films and faster rates yielded 3D nanodendritic structures. Detailed characterization confirmed the precise control over film thickness and uniformity, achieving conformal coatings on high aspect NSs demonstrating comparable electrical breakdown strengths to industrial thermal oxides. The 3D nanodendritic morphology, consistent in height and interspacing across large areas, offers a high surface-to-volume ratio beneficial for various applications, in our case the efficient and reproducible capture and isolation of NAs in microfluidic channels. The mild growth conditions and substrate-independent nature allow these NSs to be grown on a wide variety of substrates, and makes them applicable for use in label-free detection of NAs.

The latter bottleneck concerning label-free detection was addressed by growing these high-surface-to-volume ratio SiO_2 nanodendrites on quartz crystal microbalance (QCM) sensors. In doing so, the frequency response of the QCM sensors was significantly enhanced compared to planar QCMs when subjected to the same DNA concentrations. This label-free detection mechanism, combined with the ease of synthesis, positions these

NSs as promising tools for POC diagnostics, with limits of detection below those listed for established techniques like ELISA (100 ng/mL versus 250 ng/mL).

A high efficiency method for producing ligand-free and DNA-functionalised SiNPs using laser synthesis and dynamic flow conditions was investigated. While the SiNPs did not provide enhanced capture efficiencies when immobilised in microfluidic channels compared to the SiO_2 nanodendrites and NRs, the SiNPs would be more suited to enhancing standardised techniques like ELISA or incorporated into more advanced diagnostic devices that can enable better SiNP and target DNA interaction. A 100% DNA-functionalisation efficiency, the highest reported in literature to date, was achieved using flow conditions during the LASiS procedure, which opens the avenue for more efficient, industrial scale production of functionalised NPs for a variety of biomedical applications. Finally, SiNP surface coatings were demonstrated, and their biocompatibility was demonstrated, suggesting their potential use in biocompatible implants like stents.

Considering the work in its entirety, the research demonstrated the reproducibility, scalability, and low-cost production of a variety of SiO_2 NSs, making them highly suitable for practical applications in diagnostics, biosensing, and biomedical implants.

6.2. Future Work

6.2.1. Further Characterisation of PDMS-Based SiO_2 Deposition System

The novel PDMS-based SiO_2 deposition system developed in this thesis has shown significant promise, but there are several avenues for further characterization and optimization that warrant exploration. Future work should focus on a comprehensive investigation of the deposition parameters to fully understand and enhance the capabilities of this system, and to address the issue of scalability for sample size in a physically larger system.

6.2.1.1. Expanded Heating Rate Investigation

While this thesis explored heating rates from 1 to 40 °C/min, the thermal degradation mechanism of PDMS, as studied by Camino *et al.*, indicates that additional degradation pathways occur at heating rates of 50 °C/min and beyond. Future studies should extend the range of heating rates to include these higher values not achievable using our furnace, to identify any new and potentially useful morphologies. Additionally, examining very low

heating rates, down to 0.0167 °C/min allowed by our system, could reveal gradual morphological transitions and finer control over film characteristics.

6.2.1.2. High-Temperature Depositions

Exploring higher deposition temperatures could lead to the discovery of other unique SiO_2 NS morphologies. By increasing the temperature beyond 500 °C, it may be possible to influence the deposition kinetics in ways that produce novel morphologies.

6.2.1.3. Substrate Angle and Distance Variations

The comparison of our PDMS-based deposition setup to glancing angle deposition techniques suggests that the angle of the substrate relative to the incoming SiO_2 vapour flux could significantly affect the morphology of the deposited SiO_2. Future experiments should investigate a range of substrate angles to determine their impact on film uniformity, thickness, and NS formation. This could also be influenced by the distance between PDMS source and substrate, which was fixed at 5.5 cm in this study.

6.2.1.4. Advanced Dielectric Characterisation

The dielectric properties of the 2D SiO_2 films were assessed using current-voltage sweeps, but a broader range of dielectric characterization techniques should be applied. Techniques such as capacitance-voltage (C-V) measurements, and inert atmosphere annealing treatments to reduce leakage currents could be employed.

6.2.2. Functionalisation of SiO_2 Nanostructures

While this work demonstrated the enhanced capture efficiencies of the SiO_2 nanodendrites, it used double stranded DNA as a model biomolecule. As shown in this thesis, the nanodendrites act as effective filters for isolation and purification, however they have only been used for capturing any and all types of DNA without specificity, which is comparable to the SiO_2 membranes and microbeads used for PCR sample preparation. Future studies should focus on nanodendrite functionalisation to capture only specific target NA strands and detect particular NA sequences, broadening the scope of their application in biomolecular diagnostics. Similarly, the SiNPs should be functionalised with specific NA strands during synthesis, and their ability to capture strands of interest in other applications should be investigated, such as ELISAs.

6.2.3. High Temperature Piezoelectric Resonator

The promising DNA capture results obtained from the ZnO-SiO_2 NRs within microfluidic devices showcase their potential for highly reproducible isolation and purification of DNA. However, the temperatures required for growth made them incompatible with QCMs. As

highlighted in Chapter Five, gallium orthophosphate resonators have emerged as a promising alternative due to their ability to withstand and operate at high temperatures. Future work should focus on leveraging these properties of $GaPO_4$ to enable the integration of high-temperature-grown ZnO-SiO_2 NRs for label-free DNA detection similar to the nanodendrite coated QCM showcased in this work. A detailed comparative analysis between the ZnO-SiO_2 NRs on $GaPO_4$ sensors and SiO_2 nanodendrites on QCMs would provide a comprehensive understanding of the benefits and limitations of each system.

6.2.4. Further Biocompatibility Studies

We investigated the biocompatibility of SiNP coated PLA using lung cells and vascular cells, demonstrating promising biocompatibility, indicating that SiNP coatings do not induce cytotoxic effects and are conducive to cell proliferation. Further tests could be performed to unravel the growth promoting mechanism. Given the successful application PLA-based implants in promoting bone growth, further research should explore the use of SiNP-coated PLA in orthopaedic implants, as well as in vascular stents as demonstrated in this work.

7. References

[1] P. Yager, G. J. Domingo, and J. Gerdes, 'Point-of-care diagnostics for global health', *Annu. Rev. Biomed. Eng.*, vol. 10, pp. 107–144, 2008, doi: 10.1146/annurev.bioeng.10.061807.160524.

[2] O. Clerc and G. Greub, 'Routine use of point-of-care tests: usefulness and application in clinical microbiology', *Clin. Microbiol. Infect.*, vol. 16, no. 8, pp. 1054–1061, Aug. 2010, doi: 10.1111/J.1469-0691.2010.03281.X.

[3] D. Van De Beek, M. Brouwer, R. Hasbun, U. Koedel, C. G. Whitney, and E. Wijdicks, 'Community-acquired bacterial meningitis', *Nat. Rev. Dis. Primer 2016 21*, vol. 2, no. 1, pp. 1–20, Nov. 2016, doi: 10.1038/nrdp.2016.74.

[4] M. T. Fitch and D. van de Beek, 'Emergency diagnosis and treatment of adult meningitis', *Lancet Infect. Dis.*, vol. 7, no. 3, pp. 191–200, Mar. 2007, doi: 10.1016/S1473-3099(07)70050-6.

[5] B. Spaeth *et al.*, 'Point-of-care testing for sepsis in remote Australia and for First Nations peoples', *Nat. Med.*, pp. 1–2, May 2024, doi: 10.1038/s41591-024-03034-2.

[6] D. Mabey, R. W. Peeling, A. Ustianowski, and M. D. Perkins, 'Diagnostics for the developing world', *Nat. Rev. Microbiol.*, vol. 2, no. 3, pp. 231–240, 2004, doi: 10.1038/nrmicro841.

[7] G. Cappon, G. Acciaroli, M. Vettoretti, A. F. Id, and G. Sparacino, 'Wearable continuous glucose monitoring sensors: a revolution in diabetes treatment', *mdpi.com*, 2017, doi: 10.3390/electronics6030065.

[8] J. R. L. Ehrenkranz, 'Home and Point-of-Care Pregnancy Tests: A Review of the Technology', *Epidemiology*, vol. 13, no. 3, pp. S15–S18, May 2002.

[9] T. Peto *et al.*, 'COVID-19: Rapid antigen detection for SARS-CoV-2 by lateral flow assay: A national systematic evaluation of sensitivity and specificity for mass-testing', *EClinicalMedicine*, vol. 36, pp. 100924–100924, Jun. 2021, doi: 10.1016/J.ECLINM.2021.100924/ATTACHMENT/421A092F-BA7C-4570-8D24-6A1B02A1412A/MMC3.XLSX.

[10] N. Khehra, I. S. Padda, and C. J. Swift, 'Polymerase Chain Reaction (PCR)', in *StatPearls*, Treasure Island (FL): StatPearls Publishing, 2024. Accessed: Jun. 13, 2024. [Online]. Available: http://www.ncbi.nlm.nih.gov/books/NBK589663/

[11] A. C. Anselmo and S. Mitragotri, 'Nanoparticles in the clinic: An update', *Bioeng. Transl. Med.*, vol. 4, no. 3, Sep. 2019, doi: 10.1002/BTM2.10143.

[12] 'Coronavirus (COVID-19) Update: FDA Authorizes First Antigen Test to Help in the Rapid Detection of the Virus that Causes COVID-19 in Patients | FDA', [Online]. Available: https://www.fda.gov/news-events/press-announcements/coronavirus-covid-19-update-fda-authorizes-first-antigen-test-help-rapid-detection-virus-causes

[13] K. Chen *et al.*, 'Applications and regulatory of nanotechnology-based innovative in vitro diagnostics', *View*, vol. 2, no. 2, pp. 20200091–20200091, Apr. 2021, doi: 10.1002/VIW.20200091.

[14] D. T. N. Tram *et al.*, 'Advances in nanomaterials and their applications in point of care (POC) devices for the diagnosis of infectious diseases', *Biotechnol. Adv.*, vol. 34, no. 8, pp. 1275–1275, Dec. 2016, doi: 10.1016/J.BIOTECHADV.2016.09.003.

[15] D. Quesada-González and A. Merkoçi, 'Nanomaterial-based devices for point-of-care diagnostic applications', *Chem. Soc. Rev.*, vol. 47, no. 13, pp. 4697–4709, Jul. 2018, doi: 10.1039/C7CS00837F.

[16] R. Gupta *et al.*, 'Nanotechnology-Based Approaches for the Detection of SARS-CoV-2', *Front. Nanotechnol.*, vol. 2, pp. 6–6, Dec. 2020, doi: 10.3389/FNANO.2020.589832/BIBTEX.

[17] C. S. S. R. Kumar, *Microfluidic devices in nanotechnology: Applications*. Wiley, 2010, p. 407.

[18] S. Minchin and J. Lodge, 'Understanding biochemistry: structure and function of nucleic acids', *Essays Biochem.*, vol. 63, no. 4, pp. 433–433, 2019, doi: 10.1042/EBC20180038.

[19] M. G. Ghannam and M. Varacallo, 'Biochemistry, Polymerase Chain Reaction', in *StatPearls*, Treasure Island (FL): StatPearls Publishing, 2024. Accessed: Jun. 13, 2024. [Online]. Available: http://www.ncbi.nlm.nih.gov/books/NBK535453/

[20] Roberts, R.J., 'nucleic acid', Encyclopedia Britannica. Accessed: Jun. 13, 2024. [Online]. Available: https://www.britannica.com/science/nucleic-acid

[21] R. Boom, C. J. A. Sol, M. M. M. Salimans, C. L. Jansen, P. M. E. Wertheim-Van Dillen, and J. Van Der Noordaa, 'Rapid and simple method for purification of nucleic acids', *J. Clin. Microbiol.*, vol. 28, no. 3, pp. 495–503, 1990.

[22] B. Shi, Y. K. Shin, A. A. Hassanali, and S. J. Singer, 'DNA Binding to the Silica Surface', *J. Phys. Chem. B*, vol. 119, no. 34, pp. 11030–11040, Aug. 2015, doi: 10.1021/acs.jpcb.5b01983.

[23] A. N. 59 Analytical Methods Committee, 'PCR – the polymerase chain reaction', *Anal. Methods*, vol. 6, no. 2, pp. 333–336, Dec. 2013, doi: 10.1039/C3AY90101G.

[24] T. C. Lorenz, 'Polymerase Chain Reaction: Basic Protocol Plus Troubleshooting and Optimization Strategies', *J. Vis. Exp. JoVE*, no. 63, p. 3998, May 2012, doi: 10.3791/3998.

[25] A. Hoose, R. Vellacott, M. Storch, P. S. Freemont, and M. G. Ryadnov, 'DNA synthesis technologies to close the gene writing gap', *Nat. Rev. Chem.*, vol. 7, no. 3, pp. 144–161, Mar. 2023, doi: 10.1038/s41570-022-00456-9.

[26] 'PCR -Principle, Steps, Types, Components And Applications Of PCR', BYJUS. Accessed: Jun. 16, 2024. [Online]. Available: https://byjus.com/biology/pcr/

[27] J. Li and N. Wu, *Biosensors Based on Nanomaterials and Nanodevices - 1st Edition - Jun*, 1st Edition. CRC Press, 2017, p. 517. [Online]. Available: https://www.routledge.com/Biosensors-Based-on-Nanomaterials-and-Nanodevices/Li-Wu/p/book/9781138073258

[28] A. Albanese, P. S. Tang, and W. C. W. Chan, 'The Effect of Nanoparticle Size, Shape, and Surface Chemistry on Biological Systems', *Httpdxdoiorg101146annurev-*

Bioeng-071811-150124, vol. 14, pp. 1–16, Jul. 2012, doi: 10.1146/ANNUREV-BIOENG-071811-150124.

[29] B. Cojocaru, D. Avram, V. Kessler, V. Parvulescu, G. Seisenbaeva, and C. Tiseanu, 'Nanoscale insights into doping behavior, particle size and surface effects in trivalent metal doped SnO2', *Sci. Rep.*, vol. 7, no. 1, Dec. 2017, doi: 10.1038/S41598-017-09026-2.

[30] L. Li *et al.*, 'Surface doping for photocatalytic purposes: Relations between particle size, surface modifications, and photoactivity of SnO2:Zn 2+ nanocrystals', *Nanotechnology*, vol. 20, no. 15, 2009, doi: 10.1088/0957-4484/20/15/155706.

[31] C. Jagadish and V. A. Colemna, *Zinc Oxide Bulk, Thin Films and Nanostructures*. in Zinc Oxide Bulk, Thin Films and Nanostructures. Elsevier Ltd, 2006. doi: 10.1016/B978-0-08-044722-3.X5000-3.

[32] M. Law, L. E. Greene, J. C. Johnson, R. Saykally, and P. Yang, 'Nanowire dye-sensitized solar cells', *Nat. Mater. 2005 46*, vol. 4, no. 6, pp. 455–459, May 2005, doi: 10.1038/nmat1387.

[33] D. Byrne, 'The growth and characterisation of ordered arrays of zinc oxide nanostructures and optical studies of defects in zinc oxide', pp. 207–207, 2012.

[34] S. State, *Crystal structure of ZnS (wurtzite) with coordination polyhedra*. 2008. Accessed: Jun. 04, 2024. [Online]. Available: https://commons.wikimedia.org/wiki/File:Wurtzite_polyhedra.png

[35] 'SiO2 (alpha)'. Accessed: Jun. 04, 2024. [Online]. Available: http://www.ciss.iis.u-tokyo.ac.jp/theme/multi/material/periodic_detail/examples/SiO2_alpha_gga/SiO2_alpha_ggapbe.html

[36] M. L. Huggins, 'The Crystal Structure of Quartz', *Phys. Rev.*, vol. 19, no. 4, pp. 363–363, Apr. 1922, doi: 10.1103/PhysRev.19.363.

[37] Y. Saigusa, 'Quartz-Based Piezoelectric Materials', in *Advanced Piezoelectric Materials*, Woodhead Publishing, 2017, pp. 197–233. doi: 10.1016/B978-0-08-102135-4.00005-9.

[38] A. Bonyár, 'Label-Free Nucleic Acid Biosensing Using Nanomaterial-Based Localized Surface Plasmon Resonance Imaging: A Review', *ACS Appl. Nano Mater.*, vol. 3, no. 9, pp. 8506–8521, Sep. 2020, doi: 10.1021/acsanm.0c01457.

[39] R. Funari, K. Y. Chu, and A. Q. Shen, 'Detection of antibodies against SARS-CoV-2 spike protein by gold nanospikes in an opto-microfluidic chip', *Biosens. Bioelectron.*, vol. 169, pp. 112578–112578, Dec. 2020, doi: 10.1016/j.bios.2020.112578.

[40] H. Hassan, P. Sharma, M. Hasan, S. Singh, D. Thakur, and J. Narang, 'Gold nanomaterials – The golden approach from synthesis to applications', *Mater. Sci. Energy Technol.*, vol. 5, Sep. 2022, doi: 10.1016/j.mset.2022.09.004.

[41] S. Bhat, A. Qurashi, and F. Khanday, 'ZnO nanostructures based biosensors for cancer and infectious disease applications: Perspectives, prospects and promises', *TrAC Trends Anal. Chem.*, vol. 86, Oct. 2016, doi: 10.1016/j.trac.2016.10.001.

[42] X. Ren *et al.*, 'Zinc oxide nanoparticles/glucose oxidase photoelectrochemical system for the fabrication of biosensor', *J. Colloid Interface Sci.*, vol. 334, no. 2, pp. 183–187, Jun. 2009, doi: 10.1016/j.jcis.2009.02.043.

[43] J. X. Wang *et al.*, 'Zinc oxide nanocomb biosensor for glucose detection', *Appl. Phys. Lett.*, vol. 88, no. 23, pp. 233106–233106, Jun. 2006, doi: 10.1063/1.2210078.

[44] N. Tripathy and D.-H. Kim, 'Metal oxide modified ZnO nanomaterials for biosensor applications', *Nano Converg.*, vol. 5, no. 1, p. 27, Oct. 2018, doi: 10.1186/s40580-018-0159-9.

[45] H. Beitollahi, S. Tajik, F. G. Nejad, and M. Safaei, 'Recent advances in ZnO nanostructure-based electrochemical sensors and biosensors', *J. Mater. Chem. B*, vol. 8, no. 27, pp. 5826–5844, Jul. 2020, doi: 10.1039/D0TB00569J.

[46] A. Boisen and T. Thundat, 'Design & fabrication of cantilever array biosensors', *Mater. Today*, vol. 12, no. 9, pp. 32–38, Sep. 2009, doi: 10.1016/S1369-7021(09)70249-4.

[47] R. McKendry *et al.*, 'Multiple label-free biodetection and quantitative DNA-binding assays on a nanomechanical cantilever array', *Proc. Natl. Acad. Sci.*, vol. 99, no. 15, pp. 9783–9788, Jul. 2002, doi: 10.1073/pnas.152330199.

[48] A. Paliwal, M. Tomar, and V. Gupta, 'Refractive Index Sensor Using Long-Range Surface Plasmon Resonance with Prism Coupler', *Plasmonics*, vol. 14, no. 2, pp. 375–381, Apr. 2019, doi: 10.1007/s11468-018-0814-3.

[49] S. Jain, A. Paliwal, V. Gupta, and M. Tomar, 'Refractive index tuning of SiO2 for Long Range Surface Plasmon Resonance based biosensor', *Biosens. Bioelectron.*, vol. 168, p. 112508, Nov. 2020, doi: 10.1016/j.bios.2020.112508.

[50] S. Jain, A. Paliwal, V. Gupta, and M. Tomar, 'Smartphone integrated handheld Long Range Surface Plasmon Resonance based fiber-optic biosensor with tunable SiO2 sensing matrix', *Biosens. Bioelectron.*, vol. 201, p. 113919, Apr. 2022, doi: 10.1016/j.bios.2021.113919.

[51] X. Zhao, R. Tapec-Dytioco, and W. Tan, 'Ultrasensitive DNA detection using highly fluorescent bioconjugated nanoparticles', *J. Am. Chem. Soc.*, vol. 125, no. 38, pp. 11474–11475, Sep. 2003, doi: 10.1021/ja0358854.

[52] K. A. Wolfe *et al.*, 'Toward a microchip-based solid-phase extraction method for isolation of nucleic acids', *ELECTROPHORESIS*, vol. 23, no. 5, pp. 727–733, 2002, doi: 10.1002/1522-2683(200203)23:5<727::AID-ELPS727>3.0.CO;2-O.

[53] N. C. Cady, S. Stelick, and C. A. Batt, 'Nucleic acid purification using microfabricated silicon structures', *Biosens. Bioelectron.*, vol. 19, no. 1, pp. 59–66, Oct. 2003, doi: 10.1016/S0956-5663(03)00123-4.

[54] J. Wen, L. A. Legendre, J. M. Bienvenue, and J. P. Landers, 'Purification of nucleic acids in microfluidic devices', *Anal. Chem.*, vol. 80, no. 17, pp. 6472–6479, Sep. 2008, doi: 10.1021/ac8014998.

[55] W. Tian, S. Liu, L. Deng, N. Mahmood, and X. Jian, 'Synthesis and growth mechanism of various SiO 2 nanostructures from straight to helical morphologies', *Compos. Part B Eng.*, 2018, doi: 10.1016/J.COMPOSITESB.2018.05.025.

[56] K. Govender, D. S. Boyle, P. B. Kenway, and P. O'Brien, 'Understanding the factors that govern the deposition and morphology of thin films of ZnO from aqueous solution', *J. Mater. Chem.*, vol. 14, no. 16, pp. 2575–2591, Aug. 2004, doi: 10.1039/B404784B.

[57] M. N. R. Ashfold, R. P. Doherty, N. G. Ndifor-Angwafor, D. J. Riley, and Y. Sun, 'The kinetics of the hydrothermal growth of ZnO nanostructures', *Thin Solid Films*, vol. 515, no. 24 SPEC. ISS., pp. 8679–8683, Oct. 2007, doi: 10.1016/J.TSF.2007.03.122.

[58] D. Byrne, E. McGlynn, K. Kumar, M. Biswas, M. O. Henry, and G. Hughes, 'A study of drop-coated and chemical bath-deposited buffer layers for vapor phase deposition of large area, aligned, zinc oxide nanorod arrays', *Cryst. Growth Des.*, vol. 10, no. 5, pp. 2400–2408, May 2010, doi: 10.1021/CG100231U/SUPPL_FILE/CG100231U_SI_001.PDF.

[59] M. Biswas, E. McGlynn, and M. Henry, 'Carbothermal reduction growth of ZnO nanostructures on sapphire-comparisons between graphite and activated charcoal powders', *Microelectron. J.*, vol. 40, pp. 259–261, Feb. 2009, doi: 10.1016/j.mejo.2008.07.013.

[60] L. E. Greene *et al.*, 'General Route to Vertical ZnO Nanowire Arrays Using Textured ZnO Seeds', *Nano Lett.*, vol. 5, no. 7, pp. 1231–1236, Jul. 2005, doi: 10.1021/nl050788p.

[61] A. N. Red'kin, A. N. Gruzintsev, E. E. Yakimov, O. V. Kononenko, and D. V. Roshchupkin, 'Vapor-phase synthesis of aligned zinc oxide nanorod arrays on various substrates', *Inorg. Mater.*, vol. 47, no. 7, pp. 740–745, Jul. 2011, doi: 10.1134/S0020168511070181.

[62] '(PDF) Effect of Seed Layer on Structural Properties of ZnO Nanorod Arrays Grown by Vapor-Phase Transport'. Accessed: Jun. 12, 2024. [Online]. Available: https://www.researchgate.net/publication/231644255_Effect_of_Seed_Layer_on_Structural_Properties_of_ZnO_Nanorod_Arrays_Grown_by_Vapor-Phase_Transport

[63] K. Harsha, *Principles of vapor deposition of thin films*. 2005. [Online]. Available: https://books.google.com/books?hl=en&lr=&id=k8fI2BH1KVEC&oi=fnd&pg=PP1&ots=m7gDMRuJKk&sig=XPP7tVSPIkNzInUUYq8n1pp8taQ

[64] G. Zhang, R. Pitchimani, and B. Weeks, 'A simple and flexible thin film evaporating device for energetic materials', *Rev. Sci. Instrum.*, vol. 79, p. 096102, Oct. 2008, doi: 10.1063/1.2978390.

[65] Y. Xiang, W. Chengbiao, L. Yang, Y. Deyang, and X. Tingyan, 'Recent Developments in Magnetron Sputtering', *Plasma Sci. Technol.*, vol. 8, no. 3, p. 337, May 2006, doi: 10.1088/1009-0630/8/3/20.

[66] L. Reimer, *Scanning Electron Microscopy*, Second Edition. in Springer Series in Optical Sciences. Berlin, Heidelberg: Springer Berlin Heidelberg, 1998. doi: 10.1007/978-3-540-38967-5.

[67] B. J. Inkson, 'Scanning electron microscopy (SEM) and transmission electron microscopy (TEM) for materials characterization', *Mater. Charact. Using Nondestruct. Eval. NDE Methods*, pp. 17–43, Jan. 2016, doi: 10.1016/B978-0-08-100040-3.00002-X.

[68] A. Muller and J. Grazul, 'Optimizing the environment for sub-0.2 nm scanning transmission electron microscopy', *J. Electron Microsc. (Tokyo)*, vol. 50, no. 3, pp. 219–226, May 2001, doi: 10.1093/jmicro/50.3.219.

[69] J. Goldstein *et al.*, *Scanning Electron Microscopy and X-ray Microanalysis ISBN: 0306472929*, vol. XIX. 2003. doi: 10.1007/978-1-4615-0215-9.

[70] J. A. Venables, *Introduction to Surface and Thin Film Processes*. Cambridge: Cambridge University Press, 2000. doi: 10.1017/CBO9780511755651.

[71] K. Christmann, 'D. P. Woodruff, T. A. Delchar: Modern Techniques of Surface Science, Cambridge Solid State Science Series, Cambridge University Press 1986. 453 Seiten, brosch., Preis: £ 15.–.', *Berichte Bunsenges. Für Phys. Chem.*, vol. 93, no. 1, pp. 104–105, 1989, doi: 10.1002/bbpc.19890930129.

[72] B. D. Ratner and D. G. Castner, 'Electron Spectroscopy for Chemical Analysis', in *Surface Analysis – The Principal Techniques*, John Wiley & Sons, Ltd, 2009, pp. 47–112. doi: 10.1002/9780470721582.ch3.

[73] M. P. Seah and W. A. Dench, 'Quantitative electron spectroscopy of surfaces: A standard data base for electron inelastic mean free paths in solids', *Surf. Interface Anal.*, vol. 1, no. 1, pp. 2–11, Feb. 1979, doi: 10.1002/SIA.740010103.

[74] J. N. Hilfiker and J. A. Woollam, 'INSTRUMENTATION | Ellipsometry', in *Encyclopedia of Modern Optics*, R. D. Guenther, Ed., Oxford: Elsevier, 2005, pp. 297–307. doi: 10.1016/B0-12-369395-0/00833-2.

[75] G. E. Jellison, 'Ellipsometry', in *Encyclopedia of Spectroscopy and Spectrometry*, J. C. Lindon, Ed., Oxford: Elsevier, 1999, pp. 402–411. doi: 10.1006/rwsp.2000.0070.

[76] G.W. Stachowiak, A.W. Batchelor, and G.B. Stachowiak, *Experimental methods in tribology*, 1st ed., vol. 44. Elsevier, 2004.

[77] 'Quantifying and qualifying surface changes on dental hard tissues in vitro - ScienceDirect'. Accessed: Jun. 12, 2024. [Online]. Available: https://www.sciencedirect.com/science/article/pii/S030057121000014X

[78] F. J. Giessibl, 'Advances in atomic force microscopy', *Rev. Mod. Phys.*, vol. 75, no. 3, pp. 949–983, Jul. 2003, doi: 10.1103/RevModPhys.75.949.

[79] 'Practical Aspects of STM and AFM Measurements', in *Surface Analysis with STM and AFM*, John Wiley & Sons, Ltd, 1995, pp. 47–63. doi: 10.1002/9783527615117.ch4.

[80] H. Hölscher, 'AFM, Tapping Mode', in *Encyclopedia of Nanotechnology*, B. Bhushan, Ed., Dordrecht: Springer Netherlands, 2012, pp. 99–99. doi: 10.1007/978-90-481-9751-4_33.

[81] 'Tip - Sample Interactions', in *Surface Analysis with STM and AFM*, John Wiley & Sons, Ltd, 1995, pp. 135–149. doi: 10.1002/9783527615117.ch8.

[82] A. Dujardin, P. De Wolf, F. Lafont, and V. Dupres, 'Automated multi-sample acquisition and analysis using atomic force microscopy for biomedical applications', *PLoS ONE*, vol. 14, no. 3, p. e0213853, Mar. 2019, doi: 10.1371/journal.pone.0213853.

[83] J.-J. Rousseau, *Basic Crystallography*. J. Wiley, 1998.

[84] B. D. Cullty and S. R. Stock, 'Elements of X-Ray Diffraction: Third Edition', *FEBS Lett. Educ. Ltd.*, vol. 108, no. 2, pp. 495–500, 2014.

[85] D. F. Swineharf, E. The, and B.-L. Law, 'The Beer-Lambert Law', *J. Chem. Educ.*, vol. 39, no. 7, pp. 333–335, 1962, doi: 10.1021/ED039P333.

[86] F.-X. Schmid, 'Biological Macromolecules: UV-visible Spectrophotometry', in *Encyclopedia of Life Sciences*, John Wiley & Sons, Ltd, 2001. doi: 10.1038/npg.els.0003142.

[87] 'Infrared Spectroscopy', in *ACS Reagent Chemicals*, in ACS Reagent Chemicals. , American Chemical Society, 2017. doi: 10.1021/acsreagents.2008.

[88] Stuard, B.H., *Infrared Spectroscopy: Fundamentals and Applications*. John Wiley & Sons, 2004.

[89] B. C. Smith, *Fundamentals of Fourier Transform Infrared Spectroscopy*, 2nd ed. Boca Raton: CRC Press, 2011. doi: 10.1201/b10777.

[90] W. Weibull, 'A Statistical Distribution Function of Wide Applicability', *J. Appl. Mech.*, vol. 18, no. 3, pp. 293–297, Apr. 2021, doi: 10.1115/1.4010337.

[91] R. M. Hill and L. A. Dissado, 'Examination of the statistics of dielectric breakdown', *J. Phys. C Solid State Phys.*, vol. 16, no. 22, p. 4447, Aug. 1983, doi: 10.1088/0022-3719/16/22/018.

[92] R. O'Connor, 'Electrical and chemical characterisation of ultrathin transistor gate dielectric layers', doctoral, Dublin City University, 2005. Accessed: Jun. 12, 2024. [Online]. Available: https://doras.dcu.ie/18132/

[93] K. Kumar, 'Effect of ranking on reliability prediction using Weibull analysis', *Reliab. Eng. Syst. Saf.*, vol. 24, no. 3, pp. 257–265, Jan. 1989, doi: 10.1016/0951-8320(89)90043-4.

[94] Young, Thomas, 'III. An essay on the cohesion of fluids', *Philos. Trans. R. Soc. Lond.*, vol. 95, pp. 65–87, 1805, doi: https://doi/.org10.1098/rstl.1805.0005.

[95] F. Staniscia, H. V. Guzman, and M. Kanduč, 'Tuning Contact Angles of Aqueous Droplets on Hydrophilic and Hydrophobic Surfaces by Surfactants', *J. Phys. Chem. B*, vol. 126, no. 17, pp. 3374–3384, May 2022, doi: 10.1021/acs.jpcb.2c01599.

[96] B. E. Dahneke, 'Measurement of suspended particles by quasi-elastic light scattering, Barton E. Dahneke, Ed., Wiley, New York, 1983, 570 pp. Price:$39.95', *J. Polym. Sci. Polym. Lett. Ed.*, vol. 21, no. 12, pp. 1020–1020, Dec. 1983, doi: 10.1002/POL.1983.130211210.

[97] M. Kaszuba, D. McKnight, M. T. Connah, F. K. McNeil-Watson, and U. Nobbmann, 'Measuring sub nanometre sizes using dynamic light scattering', *J. Nanoparticle Res.*, vol. 10, no. 5, pp. 823–829, May 2008, doi: 10.1007/s11051-007-9317-4.

[98] P. M. Williams, 'Zeta Potential', *Encycl. Membr.*, pp. 2063–2064, 2016, doi: 10.1007/978-3-662-44324-8_612.

[99] E. Joseph and G. Singhvi, 'Multifunctional nanocrystals for cancer therapy: a potential nanocarrier', *Nanomater. Drug Deliv. Ther.*, pp. 91–116, Jan. 2019, doi: 10.1016/B978-0-12-816505-8.00007-2.

[100] S. Samimi, N. Maghsoudnia, R. B. Eftekhari, and F. Dorkoosh, 'Lipid-Based Nanoparticles for Drug Delivery Systems', *Charact. Biol. Nanomater. Drug Deliv. Nanosci. Nanotechnol. Drug Deliv.*, pp. 47–76, Jan. 2019, doi: 10.1016/B978-0-12-814031-4.00003-9.

[101] Ashutosh. Sharma and S. G. (Stephen G. Schulman, *Introduction to fluorescence spectroscopy*. Wiley, 1999, p. 173.

[102] A. I. Dragan, J. R. Casas-Finet, E. S. Bishop, R. J. Strouse, M. A. Schenerman, and C. D. Geddes, 'Characterization of PicoGreen Interaction with dsDNA and the Origin of Its Fluorescence Enhancement upon Binding', *Biophys. J.*, vol. 99, no. 9, pp. 3010–3019, Nov. 2010, doi: 10.1016/j.bpj.2010.09.012.

[103] R. G. Ballas, 'The Piezoelectric Effect – an Indispensable Solid State Effect for Contemporary Actuator and Sensor Technologies', *J. Phys. Conf. Ser.*, vol. 1775, no. 1, p. 012012, Jan. 2021, doi: 10.1088/1742-6596/1775/1/012012.

[104] *Applications of Piezoelectric Quartz Crystal Microbalances*. 1984. Accessed: Jun. 12, 2024. [Online]. Available: https://shop.elsevier.com/books/applications-of-piezoelectric-quartz-crystal-microbalances/lu/978-0-444-42277-4

[105] G. Sauerbrey, 'Use of Oscillating Crystals for Weighing Thin Layers and for Micro-Weighing', *Mag. Phys.*, vol. 155, no. 2, pp. 206–222, 1959, doi: 10.1007/BF01337937.

[106] M. C. Dixon, 'Quartz Crystal Microbalance with Dissipation Monitoring: Enabling Real-Time Characterization of Biological Materials and Their Interactions', *J. Biomol. Tech. JBT*, vol. 19, no. 3, pp. 151–158, Jul. 2008.

[107] M. Rodahl and B. Kasemo, 'A simple setup to simultaneously measure the resonant frequency and the absolute dissipation factor of a quartz crystal microbalance', *Rev. Sci. Instrum.*, vol. 67, no. 9, pp. 3238–3241, Sep. 1996, doi: 10.1063/1.1147494.

[108] 'Frequency of a quartz microbalance in contact with liquid | Analytical Chemistry'. Accessed: Jun. 12, 2024. [Online]. Available: https://pubs.acs.org/doi/10.1021/ac00285a062

[109] H. J. Lim, T. Saha, B. T. Tey, W. S. Tan, and C. W. Ooi, 'Quartz crystal microbalance-based biosensors as rapid diagnostic devices for infectious diseases', *Biosens. Bioelectron.*, vol. 168, p. 112513, Nov. 2020, doi: 10.1016/j.bios.2020.112513.

[110] X. Huang, J. Xu, H. F. Ji, G. Li, and H. Chen, 'Quartz crystal microbalance based biosensor for rapid and sensitive detection of maize chlorotic mottle virus', *Anal. Methods*, vol. 6, no. 13, pp. 4530–4536, Jun. 2014, doi: 10.1039/C4AY00292J.

[111] R.-Z. Hao *et al.*, 'DNA probe functionalized QCM biosensor based on gold nanoparticle amplification for *Bacillus anthracis* detection', *Biosens. Bioelectron.*, vol. 26, no. 8, pp. 3398–3404, Apr. 2011, doi: 10.1016/j.bios.2011.01.010.

[112] C. Camino, S. M. Lomakin, and M. Lazzari, 'Polydimethylsiloxane thermal degradation Part 1. Kinetic aspects', *Polymer*, vol. 42, no. 6, pp. 2395–2402, Mar. 2001, doi: 10.1016/S0032-3861(00)00652-2.

[113] G. Camino, S. M. Lomakin, and M. Lageard, 'Thermal polydimethylsiloxane degradation. Part 2. The degradation mechanisms', *Polymer*, vol. 43, no. 7, pp. 2011–2015, Mar. 2002, doi: 10.1016/S0032-3861(01)00785-6.

[114] T. H. Thomas and T. C. Kendrick, 'Thermal analysis of polydimethylsiloxanes. I. Thermal degradation in controlled atmospheres', *J. Polym. Sci. Part -2 Polym. Phys.*, vol. 7, no. 3, pp. 537–549, 1969, doi: 10.1002/pol.1969.160070308.

[115] N. Grassie and I. G. Macfarlane, 'The thermal degradation of polysiloxanes—I. Poly(dimethylsiloxane)', *Eur. Polym. J.*, vol. 14, no. 11, pp. 875–884, Jan. 1978, doi: 10.1016/0014-3057(78)90084-8.

[116] V. V. Korshak, *The Chemical Structure and Thermal Characteristics of Polymers*. New York: Halsted Press, 1971.

[117] Y. Hu, J. Ge, and Y. Yin, 'PDMS rubber as a single-source precursor for templated growth of silica nanotubes', *Chem. Commun.*, no. 8, pp. 914–916, Feb. 2009, doi: 10.1039/B820755K.

[118] Z. Favors, W. Wang, H. H. Bay, A. George, M. Ozkan, and C. S. Ozkan, 'Stable Cycling of SiO2 Nanotubes as High-Performance Anodes for Lithium-Ion Batteries', *Sci. Rep. 2014 41*, vol. 4, no. 1, pp. 1–7, Apr. 2014, doi: 10.1038/srep04605.

[119] M. K. Gunde, 'Vibrational modes in amorphous silicon dioxide', *Phys. B Condens. Matter*, vol. 292, no. 3–4, pp. 286–295, 2000.

[120] A. G. Milekhin *et al.*, 'Infrared spectroscopy of bonded silicon wafers', *Semicond. Struct. Interfaces Surf.*, vol. 40, no. 11, pp. 1138–1348, 2006.

[121] B. El-Kareh, 'Thermal Oxidation and Nitridation', *Fundam. Semicond. Process. Technol.*, pp. 39–85, 1995, doi: 10.1007/978-1-4615-2209-6_2.

[122] G. H. Baek *et al.*, 'Atomic layer chemical vapor deposition of SiO2 thin films using a chlorine-free silicon precursor for 3D NAND applications', *Ceram. Int.*, vol. 47, no. 13, pp. 19036–19042, Jul. 2021, doi: 10.1016/j.ceramint.2021.03.249.

[123] M. Sometani, R. Hasunuma, M. Ogino, H. Kuribayashi, Y. Sugahara, and K. Yamabe, 'Suppression of Leakage Current of Deposited SiO 2 with Bandgap Increasing by High Temperature Annealing', *ECS Trans.*, vol. 19, no. 2, pp. 403–413, May 2009, doi: 10.1149/1.3122105/XML.

[124] S. Garry, É. McCarthy, J. P. Mosnier, and E. McGlynn, 'Influence of ZnO nanowire array morphology on field emission characteristics', *Nanotechnology*, vol. 25, no. 13, pp. 135604–135604, Mar. 2014, doi: 10.1088/0957-4484/25/13/135604.

[125] R. T. Rajendra Kumar *et al.*, 'Control of ZnO nanorod array density by Zn supersaturation variation and effects on field emission', *Nanotechnology*, vol. 18, no. 21, pp. 215704–215704, Apr. 2007, doi: 10.1088/0957-4484/18/21/215704.

[126] 'NIST Standard Reference Database 71 | NIST', doi: 10.18434/T48C78.

[127] F. A. Stevie and C. L. Donley, 'Introduction to x-ray photoelectron spectroscopy', *J. Vac. Sci. Technol. Vac. Surf. Films*, vol. 38, no. 6, Dec. 2020, doi: 10.1116/6.0000412.

[128] D. Byrne, E. McGlynn, J. Cullen, and M. O. Henry, 'A catalyst-free and facile route to periodically ordered and c-axis aligned ZnO nanorod arrays on diverse substrates.', *Nanoscale*, vol. 3, no. 4, pp. 1675–1682, 2011, doi: 10.1039/c0nr00919a.

[129] M. T. Taschuk, M. M. Hawkeye, and M. J. Brett, 'Glancing Angle Deposition', *Handb. Depos. Technol. Films Coat. Sci. Appl. Technol.*, pp. 621–678, Jan. 2010, doi: 10.1016/B978-0-8155-2031-3.00013-2.

[130] C. Lopez-Santos *et al.*, 'Nanocolumnar association and domain formation in porous thin films grown by evaporation at oblique angles', *Nanotechnology*, vol. 27, no. 39, pp. 395702–395702, Aug. 2016, doi: 10.1088/0957-4484/27/39/395702.

[131] N. Fairley *et al.*, 'Systematic and collaborative approach to problem solving using X-ray photoelectron spectroscopy', *Appl. Surf. Sci. Adv.*, vol. 5, pp. 100112–100112, Sep. 2021, doi: 10.1016/J.APSADV.2021.100112.

[132] D. Zhang, B. Gökce, and S. Barcikowski, 'Laser Synthesis and Processing of Colloids: Fundamentals and Applications', *Chem. Rev.*, vol. 117, no. 5, pp. 3990–4103, 2017, doi: 10.1021/acs.chemrev.6b00468.

[133] R. Intartaglia *et al.*, 'Bioconjugated silicon quantum dots from one-step green synthesis', *Nanoscale*, vol. 4, no. 4, pp. 1271–1274, 2012, doi: 10.1039/c2nr11763k.

[134] S. Barcikowski *et al.*, *Handbook of Laser Synthesis of Colloids*, 1st ed. Essen, 2016. doi: 10.17185/duepublico/41087.

[135] V. Amendola and M. Meneghetti, 'What controls the composition and the structure of nanomaterials generated by laser ablation in liquid solution?', *Phys. Chem. Chem. Phys.*, vol. 15, no. 9, pp. 3027–3046, Mar. 2013, doi: 10.1039/c2cp42895d.

[136] H. Zeng *et al.*, 'Nanomaterials via laser ablation/irradiation in liquid: A review', *Adv. Funct. Mater.*, vol. 22, no. 7, pp. 1333–1353, Apr. 2012, doi: 10.1002/adfm.201102295.

[137] B. Gökce, R. Streubel, and S. Barcikowski, 'Continuous multigram nanoparticle synthesis by high-power, high-repetition-rate ultrafast laser ablation in liquids', *Opt. Lett. Vol 41 Issue 7 Pp 1486-1489*, vol. 41, no. 7, pp. 1486–1489, Apr. 2016, doi: 10.1364/OL.41.001486.

[138] F. Waag, B. Gökce, and S. Barcikowski, 'Ablation target cooling by maximizing the nanoparticle productivity in laser synthesis of colloids', *Appl. Surf. Sci.*, vol. 466, pp. 647–656, Feb. 2019, doi: 10.1016/J.APSUSC.2018.10.030.

[139] B. Freeland *et al.*, 'Real-time monitoring and control for high-efficiency autonomous laser fabrication of silicon nanoparticle colloids', *Int. J. Adv. Manuf. Technol. 2021 1141*, vol. 114, no. 1, pp. 291–304, Mar. 2021, doi: 10.1007/S00170-021-06772-6.

[140] B. Freeland, R. McCann, G. Alkan, B. Friedrich, G. Foley, and D. Brabazon, 'Stable nano-silver colloid production via Laser Ablation Synthesis in Solution (LASiS) under laminar recirculatory flow', *Adv. Mater. Process. Technol.*, pp. 1–9, Mar. 2020, doi: 10.1080/2374068X.2020.1740877.

[141] V. Amendola *et al.*, 'Room-Temperature Laser Synthesis in Liquid of Oxide, Metal-Oxide Core-Shells, and Doped Oxide Nanoparticles', *Chem. - Eur. J.*, vol. 26, no. 42, pp. 9206–9242, Jul. 2020, doi: 10.1002/chem.202000686.

[142] P. Mercier and R. Savoie, 'Interaction of DNA with Silica Particles: A Vibrational Spectroscopic Study', John Wiley & Sons, Inc, 1997. doi: 10.1002/(SICI)1520-6343(1997)3:4.

[143] F. Ahmadi, N. Jamali, R. Moradian, and B. Astinchap, 'Binding studies of pyriproxyfen to DNA by multispectroscopic atomic force microscopy and molecular modeling methods', *DNA Cell Biol.*, vol. 31, no. 2, pp. 259–268, Feb. 2012, doi: 10.1089/dna.2011.1303.

[144] G. Compagnini, A. A. Scalisi, O. Puglisi, and C. Spinella, 'Synthesis of gold colloids by laser ablation in thiol-alkane solutions', *J. Mater. Res.*, vol. 19, no. 10, pp. 2795–2798, Oct. 2004, doi: 10.1557/JMR.2004.0401.

[145] S. Petersen and S. Barcikowski, 'In Situ Bioconjugation: Single Step Approach to Tailored Nanoparticle-Bioconjugates by Ultrashort Pulsed Laser Ablation', *Adv. Funct. Mater.*, vol. 19, no. 8, pp. 1167–1172, Apr. 2009, doi: 10.1002/ADFM.200801526.

[146] S. Petersen, J. Jakobi, and S. Barcikowski, 'In situ bioconjugation-Novel laser based approach to pure nanoparticle-conjugates', *Appl. Surf. Sci.*, vol. 255, no. 10, pp. 5435–5438, Mar. 2009, doi: 10.1016/j.apsusc.2008.08.064.

[147] S. Petersen, A. Barchanski, U. Taylor, S. Klein, D. Rath, and S. Barcikowski, 'Penetratin-conjugated gold nanoparticles - Design of cell-penetrating nanomarkers by femtosecond laser ablation', *J. Phys. Chem. C*, vol. 115, no. 12, pp. 5152–5159, Mar. 2011, doi: 10.1021/JP1093614/SUPPL_FILE/JP1093614_SI_001.PDF.

[148] V. Amendola and M. Meneghetti, 'Controlled size manipulation of free gold nanoparticles by laser irradiation and their facile bioconjugation', *J. Mater. Chem.*, vol. 17, no. 44, pp. 4705–4710, Nov. 2007, doi: 10.1039/B709621F.

[149] C. L. Sajti, A. Barchanski, P. Wagener, S. Klein, and S. Barcikowski, 'Delay time and concentration effects during bioconjugation of nanosecond laser-generated nanoparticles in a liquid flow', *J. Phys. Chem. C*, vol. 115, no. 12, pp. 5094–5101, Mar. 2011, doi: 10.1021/JP1093405/SUPPL_FILE/JP1093405_SI_001.PDF.

[150] C. L. Sajti, S. Petersen, A. Menéndez-Manjón, and S. Barcikowski, 'In-situ bioconjugation in stationary media and in liquid flow by femtosecond laser ablation', *Appl. Phys. 2010 1012*, vol. 101, no. 2, pp. 259–264, Jun. 2010, doi: 10.1007/S00339-010-5813-Y.

[151] J. G. Walter, S. Petersen, F. Stahl, T. Scheper, and S. Barcikowski, 'Laser ablation-based one-step generation and bio-functionalization of gold nanoparticles conjugated with aptamers', *J. Nanobiotechnology*, vol. 8, no. 1, pp. 1–11, Aug. 2010, doi: 10.1186/1477-3155-8-21/FIGURES/8.

[152] S. S. Pavithran *et al.*, 'Silver and Copper nano-colloid generation via Pulsed Laser Ablation in Liquid: Recirculation nanoparticle production mode', *https://popups.uliege.be/esaform21*, Apr. 2021, doi: 10.25518/ESAFORM21.2239.

[153] C. O. Metin, L. W. Lake, C. R. Miranda, and Q. P. Nguyen, 'Stability of aqueous silica nanoparticle dispersions', *J. Nanoparticle Res.*, vol. 13, no. 2, pp. 839–850, Feb. 2011, doi: 10.1007/S11051-010-0085-1.

[154] R. Intartaglia, K. Bagga, M. Scotto, A. Diaspro, and F. Brandi, 'Luminescent silicon nanoparticles prepared by ultra short pulsed laser ablation in liquid for imaging applications', *Opt. Mater. Express*, vol. 2, no. 5, pp. 510–510, May 2012, doi: 10.1364/ome.2.000510.

[155] P. Sahu and D. Das, 'Synthesis and characterization of organic ligand capped luminescent silicon nanoparticles', *Mater. Today Proc.*, Mar. 2022, doi: 10.1016/J.MATPR.2022.02.398.

[156] A. Y. Kharin, Y. V. Kargina, and V. Y. Timoshenko, 'Evolution of nanocrystal size distribution in porous silicon nanoparticles during storage in aqueous media: X-ray diffraction analysis', *J. Nanoparticle Res.*, vol. 21, no. 2, pp. 1–7, Feb. 2019, doi: 10.1007/S11051-019-4466-9/FIGURES/5.

[157] C. F. Holder and R. E. Schaak, 'Tutorial on Powder X-ray Diffraction for Characterizing Nanoscale Materials', *ACS Nano*, vol. 13, no. 7, pp. 7359–7365, Jul. 2019, doi: 10.1021/ACSNANO.9B05157/ASSET/IMAGES/MEDIUM/NN-2019-051577_0009.GIF.

[158] D. Das and S. Samanta, 'Advanced nanocrystallinity with widened optical gap realized via microstructural control in P-doped silicon oxide thin films used as window layer in nc-Si solar cells', *Mater. Chem. Phys.*, vol. 243, pp. 122628–122628, Mar. 2020, doi: 10.1016/J.MATCHEMPHYS.2020.122628.

[159] R. Intartaglia *et al.*, 'Optical properties of femtosecond laser-synthesized silicon nanoparticles in deionized water', *J. Phys. Chem. C*, vol. 115, no. 12, pp. 5102–5107, Mar. 2011, doi: 10.1021/JP109351T/ASSET/IMAGES/LARGE/JP-2010-09351T_0002.JPEG.

[160] M. R. Kalus, R. Lanyumba, S. Barcikowski, and B. Gökce, 'Discrimination of ablation, shielding, and interface layer effects on the steady-state formation of persistent bubbles under liquid flow conditions during laser synthesis of colloids', *J. Flow Chem. 2021*, pp. 1–20, Mar. 2021, doi: 10.1007/S41981-021-00144-7.

[161] B. Freeland, R. McCann, G. Foley, and D. Brabazon, 'High-efficiency generation of nanomaterials via laser ablation synthesis in solution with in-situ diagnostics for closed-loop control', *https://doi.org/10.1117/12.2545878*, vol. 11269, pp. 53–58, Mar. 2020, doi: 10.1117/12.2545878.

[162] D. Knopp, D. Tang, and R. Niessner, 'Review: bioanalytical applications of biomolecule-functionalized nanometer-sized doped silica particles', *Anal. Chim. Acta*, vol. 647, no. 1, pp. 14–30, Aug. 2009, doi: 10.1016/J.ACA.2009.05.037.

[163] M. C. Coen, R. Lehmann, P. Gröning, M. Bielmann, C. Galli, and L. Schlapbach, 'Adsorption and bioactivity of protein A on silicon surfaces studied by AFM and XPS', *J. Colloid Interface Sci.*, vol. 233, no. 2, pp. 180–189, Jan. 2001, doi: 10.1006/jcis.2000.7240.

[164] K. Bagga *et al.*, 'Laser-assisted synthesis of Staphylococcus aureus protein-capped silicon quantum dots as bio-functional nanoprobes', *Laser Phys. Lett.*, vol. 10, no. 6, pp. 065603–065603, Jun. 2013, doi: 10.1088/1612-2011/10/6/065603.

[165] S. Petersen and S. Barcikowski, 'Conjugation efficiency of laser-based bioconjugation of gold nanoparticles with nucleic acids', *J. Phys. Chem. C*, vol. 113, no. 46, pp. 19830–19835, 2009, doi: 10.1021/jp905962f.

[166] D. Doherty *et al.*, 'Assessing the viability of 3D-printed poly(lactic acid) petri dishes: A sustainable alternative for laboratory use', *Sustain. Mater. Technol.*, vol. 40, p. e00899, Jul. 2024, doi: 10.1016/j.susmat.2024.e00899.

[167] G. Spiekermann, M. Steele-Macinnis, C. Schmidt, and S. Jahn, 'Vibrational mode frequencies of silica species in SiO2-H2O liquids and glasses from ab initio molecular dynamics', *J. Chem. Phys.*, vol. 136, no. 15, pp. 154501–154501, Apr. 2012, doi: 10.1063/1.3703667.

[168] R. Abd Aziz and I. Sopyan, 'Synthesis of TiO2-SiO2 powder and thin film photocatalysts by sol-gel method', *Indian J. Chem.*, vol. 48, pp. 951–957, 2009.

[169] D. Arun Kumar, J. Merline Shyla, and F. P. Xavier, 'Synthesis and characterization of TiO2/SiO2 nano composites for solar cell applications', *Appl. Nanosci. Switz.*, vol. 2, no. 4, pp. 429–436, Dec. 2012, doi: 10.1007/S13204-012-0060-5.

[170] W. H. Hoidy, M. B. Ahmad, E. A. J. Al-Mulla, and N. A. B. Ibrahim, 'Preparation and characterization of polylactic acid/polycaprolactone clay nanocomposites', *J. Appl. Sci.*, vol. 10, no. 2, pp. 97–106, 2010, doi: 10.3923/JAS.2010.97.106.

[171] H. W. Lee, R. Insyani, D. Prasetyo, H. Prajitno, and J. Sitompul, 'Molecular weight and structural properties of biodegradable PLA synthesized with different catalysts by direct melt polycondensation', *J. Eng. Technol. Sci.*, vol. 47, no. 4, pp. 364–373, 2015, doi: 10.5614/J.ENG.TECHNOL.SCI.2015.47.4.2.

[172] Z. Zhang, H. Chen, J. Zhong, Y. Chen, and Y. Lu, 'ZnO nanotip-based QCM biosensors', *Proc. IEEE Int. Freq. Control Symp. Expo.*, pp. 545–549, 2006, doi: 10.1109/FREQ.2006.275444.

[173] M. A. Dineva, L. Mahilum-Tapay, and H. Lee, 'Sample preparation: A challenge in the development of point-of-care nucleic acid-based assays for resource-limited settings', *Analyst*, vol. 132, no. 12, pp. 1193–1199, 2007, doi: 10.1039/b705672a.

[174] A. Szpechcinski, M. Dancewicz, P. Kopinski, J. Kowalewski, and J. Chorostowska-Wynimko, 'Real-time PCR quantification of plasma DNA in non-small cell lung cancer patients and healthy controls', *Eur. J. Med. Res.*, vol. 14, no. SUPPL.4, pp. 237–240, Dec. 2009, doi: 10.1186/2047-783X-14-S4-237/TABLES/2.

[175] M. L. Huggins, 'The Crystal Structure of Quartz', *Phys. Rev.*, vol. 19, no. 4, p. 363, Apr. 1922, doi: 10.1103/PhysRev.19.363.

[176] E. G.-C. International and undefined 1982, 'The structure of SiO2—Current views', *ElsevierE GörlichCeramics Int. 1982•Elsevier*.

[177] P. J. Heaney, 'Structure and chemistry of the low-pressure silica polymorphs', in *Silica*, vol. 29, De Gruyter Mouton, 2019, pp. 1–40. doi: 10.1515/9781501509698.

[178] V. Singh, V. Tathavadkar, M. B. Denys, and R. Venugopal, 'Application of quartz inversion phenomenon in mineral processing - A case study of siliceous manganese ores', *Miner. Eng.*, vol. 32, pp. 8–11, May 2012, doi: 10.1016/j.mineng.2012.03.010.

[179] H. Thanner, P. W. Krempl, R. Selic, W. Wallnöfer, and P. M. Worsch, 'GaPO4 high temperature crystal microbalance demonstration up to 720°C', *J. Therm. Anal. Calorim. 2003 711*, vol. 71, no. 1, pp. 53–59, 2003, doi: 10.1023/A:1022249713714.

[180] J. W. Elam and M. J. Pellin, 'GaPO4 sensors for gravimetric monitoring during atomic layer deposition at high temperatures', *Anal. Chem.*, vol. 77, no. 11, pp. 3531–3535, Jun. 2005, doi: 10.1021/AC050349A/ASSET/IMAGES/LARGE/AC050349AF00004.JPEG.

[181] F. Krispel *et al.*, 'Properties and Applications of Singly Rotated GaPO4 Resonators', *Proc. Annu. IEEE Int. Freq. Control Symp.*, pp. 668–673, 2003, doi: 10.1109/FREQ.2003.1275172.

[182] W. E. Martinez, G. Gregori, and T. Mates, 'Titanium diffusion in gold thin films', *Thin Solid Films*, vol. 518, no. 10, pp. 2585–2591, Mar. 2010, doi: 10.1016/j.tsf.2009.07.187.

[183] J. Drelich and E. Chibowski, 'Superhydrophilic and superwetting surfaces: Definition and mechanisms of control', *Langmuir*, vol. 26, no. 24, pp. 18621–18623, Dec. 2010, doi: 10.1021/LA1039893/ASSET/IMAGES/LARGE/LA-2010-039893_0001.JPEG.

[184] M. C. Dixon, 'Quartz Crystal Microbalance with Dissipation Monitoring: Enabling Real-Time Characterization of Biological Materials and Their Interactions', *J. Biomol. Tech. JBT*, vol. 19, no. 3, p. 151, Jul. 2008.

[185] C. Tonda-Turo, I. Carmagnola, and G. Ciardelli, 'Quartz crystal microbalance with dissipation monitoring: A powerful method to predict the in vivo behavior of bioengineered surfaces', *Front. Bioeng. Biotechnol.*, vol. 6, no. OCT, p. 158, Oct. 2018, doi: 10.3389/FBIOE.2018.00158/BIBTEX.

[186] A. D. Easley, T. Ma, C. I. Eneh, J. Yun, R. M. Thakur, and J. L. Lutkenhaus, 'A practical guide to quartz crystal microbalance with dissipation monitoring of thin polymer films', *J. Polym. Sci.*, vol. 60, no. 7, pp. 1090–1107, Apr. 2022, doi: 10.1002/POL.20210324.

[187] T. K. Lind and M. Cárdenas, 'Understanding the formation of supported lipid bilayers via vesicle fusion—A case that exemplifies the need for the complementary method approach (Review)', *Biointerphases*, vol. 11, no. 2, Jun. 2016, doi: 10.1116/1.4944830/164495.

[188] M. Johnson, 'PCR Machines', *Mater. Methods*, Apr. 2023, Accessed: Aug. 18, 2024. [Online]. Available: https://www.labome.com/method/PCR-Machines.html

[189] 'QSense Pro | QSense | QCM-D'. Accessed: Aug. 18, 2024. [Online]. Available: https://www.biolinscientific.com/qsense/instruments/qsense-pro

[190] B. Freeland *et al.*, 'A Review of Polylactic Acid as a Replacement Material for Single-Use Laboratory Components', *Mater. 2022 Vol 15 Page 2989*, vol. 15, no. 9, p. 2989, Apr. 2022, doi: 10.3390/MA15092989.

[191] P. Saini, M. Arora, and M. N. V. R. Kumar, 'Poly(lactic acid) blends in biomedical applications', *Adv. Drug Deliv. Rev.*, vol. 107, pp. 47–59, Dec. 2016, doi: 10.1016/j.addr.2016.06.014.

[192] P. Feng, J. Jia, M. Liu, S. Peng, Z. Zhao, and C. Shuai, 'Degradation mechanisms and acceleration strategies of poly (lactic acid) scaffold for bone regeneration', *Mater. Des.*, vol. 210, Nov. 2021, doi: 10.1016/j.matdes.2021.110066.

[193] W. F. de Oliveira *et al.*, 'Pharmaceutical applications of chitosan on medical implants: A viable alternative for construction of new biomaterials?', *Carbohydr. Polym. Technol. Appl.*, vol. 7, Jun. 2024, doi: 10.1016/j.carpta.2023.100407.

[194] D. Doherty *et al.*, 'Assessing the viability of 3D-printed poly(lactic acid) petri dishes: A sustainable alternative for laboratory use', *Sustain. Mater. Technol.*, vol. 40, Jul. 2024, doi: 10.1016/j.susmat.2024.e00899.

[195] N. Geoghegan *et al.*, 'Controlled degradation of polycaprolactone-based micropillar arrays', *Biomater. Sci.*, vol. 11, no. 9, pp. 3077–3091, May 2023, doi: 10.1039/D3BM00165B.

[196] K. D. Rochfort, 'Characterisation of anti-inflammatory and pro-inflammatory influences on blood-brain barrier phenotype using an in vitro human brain microvascular endothelial model', doctoral, Dublin City University, 2013. Accessed: Jun. 14, 2024. [Online]. Available: https://doras.dcu.ie/19467/